



Max-Planck-Institut für Intelligente Systeme
(ehemals Max-Planck-Institut für Metallforschung)
Stuttgart

Internal precipitation of nitrides in Iron-based alloys

Tobias Steiner

Dissertation
an der
Universität Stuttgart

Bericht Nr. 255
März 2016

Internal precipitation of nitrides in Iron-based alloys

Von der Fakultät Chemie der Universität Stuttgart zur Erlangung der
Würde eines Doktors der Naturwissenschaften (Dr. rer. nat.)
genehmigte Abhandlung

vorgelegt von

Tobias Steiner

aus Hamburg/Deutschland

Hauptberichter: Prof. Dr. Ir. E. J. Mittemeijer

Mitberichter: Prof. Dr. J. Bill

Prüfungsvorsitzender: Prof. Dr. T. Schleid

Tag der Einreichung: 16.12.2015

Tag der mündlichen Prüfung: 18.03.2016

MAX-PLANCK-INSTITUT FÜR INTELLIGENTE SYSTEME, STUTTGART

(ehemals MAX-PLANCK-INSTITUT FÜR METALLFORSCHUNG)

INSTITUT FÜR MATERIALWISSENSCHAFT DER UNIVERSITÄT SUTTGART

Table of Contents

Chapter 1: Introduction.....	1
1.1 General introduction	1
1.2 Nitriding.....	2
1.3 Microstructure of the nitrided zone.....	3
1.4 Morphology of nitrides in steel	5
1.5 Micro- and macro-structural effects on X-ray diffraction lines.....	7
1.6 Outline of the thesis	8
Chapter 2: Lattice-parameter change induced by accommodation of precipitate/matrix misfit; misfitting nitrides in ferrite	11
2.1 Introduction	11
2.2 Elastic strain field in a misfitting system: lattice-parameter changes.....	12
2.2.1 Change of the lattice parameter of the matrix	13
2.2.2 Change of the lattice parameter of the misfitting phase.....	14
2.2.3 Change of the lattice parameter of the assembly (matrix plus misfitting phase) ...	15
2.2.4 Coherent vs. incoherent diffraction of matrix and misfitting precipitates; consequences for interpretation of lattice-parameter changes.....	15
2.3 Experimental.....	17
2.3.1 Specimen preparation.....	17
2.3.2 Nitriding and de-nitriding experiments.....	18
2.3.3 Specimen characterization.....	19
2.4 Results and Evaluation.....	22
2.5 Discussion	25
2.6 Conclusions.....	31
Chapter 3: Misfit induced changes of lattice parameters in two-phase systems: coherent/incoherent precipitates in a matrix.....	33

3.1	Introduction; micro-and macrostrains; coherent and incoherent diffraction	33
3.2	Lattice-parameter changes due to elastically accommodated misfit	35
3.2.1	Change of the lattice parameter of the matrix	35
3.2.2	Change of the lattice parameter of the misfitting phase.....	36
3.2.3	Change of the lattice parameter of the assembly (matrix plus misfitting phase) ...	36
3.2.4	The misfit parameter.....	36
3.3	Observations and discussion	37
3.3.1	Coherent diffraction by the assembly matrix plus second phase particles; transformation misfit	39
3.3.2	Incoherent diffraction of the matrix and second phase particles; transformation misfit	42
3.3.3	Incoherent diffraction of the matrix and second phase particles; thermal misfit...	45
3.4	Conclusions.....	47
Chapter 4: Diffraction-line shifts and broadenings in continuously and discontinuously coarsening precipitate-matrix systems; coarsening of initially coherent nitride precipitates in a ferrite matrix		
		49
4.1	Introduction	49
4.2	Experimental procedures	51
4.2.1	Specimen preparation.....	51
4.2.2	Nitriding experiments	52
4.2.3	Specimen characterization.....	52
4.3	Results.....	54
4.3.1	Fe-2.0 at.%Cr alloy.....	54
4.3.2	Fe-4.5 at.%Cr alloy.....	60
4.4	Discussion	66
4.4.1	Initial state.....	66
4.4.2	Continuous Coarsening	68
4.4.3	Discontinuous Coarsening.....	69

4.5	Conclusions.....	70
Chapter 5: Alloying element nitride stability in nitrided iron-based alloys; denitridding of nitrided Fe-V alloys		
		73
5.1	Introduction.....	73
5.2	Experimental.....	76
5.2.1	Specimen preparation.....	76
5.2.2	Nitriding and denitridding experiments.....	77
5.2.3	Microstructural characterization	77
5.3	Results and discussion	79
5.3.1	Hydrogen reduction of nitrided Fe-V alloys.....	79
5.3.2	Strategy for denitridding; stabilization of nitrided microstructure	84
5.4	Conclusions.....	90
Chapter 6: Continuous and discontinuous precipitation in Fe-1 at.%Cr-1 at.%Mo alloy upon nitriding; crystal structure and composition of ternary nitrides		
		93
6.1	Introduction.....	93
6.2	Experimental.....	94
6.2.1	Specimen Preparation and Nitriding.....	94
6.2.2	Microstructural Characterization	95
6.2.3	Atom Probe Tomography.....	97
6.3	Results and evaluation.....	98
6.3.1	Continuously precipitated nitrides; initial stages	98
6.3.2	Discontinuously precipitated nitrides; later stages	105
6.4	Discussion	117
6.4.1	Continuous precipitation.....	119
6.4.2	Discontinuous precipitation	121
6.5	Conclusions.....	125
Chapter 7: Nitriding of ternary Fe-Cr-Mo alloys; role of the Cr/Mo-ratio.....		
		127
7.1	Introduction.....	127

7.2	Experimental.....	129
7.2.1	Specimen preparation and nitriding	129
7.2.2	Microstructural characterization	130
7.3	Results and discussion	132
7.3.1	Morphology	132
7.3.2	Nitrogen uptake	139
7.3.3	X-ray diffraction and residual stress evolution	145
7.4	General discussion	148
7.4.1	Nitriding of binary Fe-Cr and Fe-Mo alloys	148
7.4.2	Nitriding of ternary Fe-Cr-Mo alloys	149
7.5	Conclusions	153
	Summary	155
	Zusammenfassung in deutscher Sprache.....	161
	References.....	167
	Supplements.....	183
	Danksagung	191
	Curriculum Vitae.....	193
	List of Publications	195

Chapter 1

Introduction

1.1 General introduction

Social demands, such as lower fuel consumption and CO₂ emissions for public traffic, lead to a sustainable demand for more effective, less expensive and lighter engineering components. For example in combustion engines, optimized operational parameters can only be realized by targeted research investigations to produce stronger and tougher materials.

Due to its relatively low cost of production, world-wide availability, and widely tailorable properties, steel is the most utilized material for manufacturing of technical parts [1]. Numerous studies were and are performed on the influence of the material chemistry (alloying) to create new steels with yet unreached properties (see, e.g., Ref. [2]), and new ways of component design are being developed based on the understanding of the mechanisms operating on a micro- or even nanoscopic level (e.g. Ref. [3]).

Especially their surface properties are responsible for the performance of technical components. This appears obvious for surface-dependent deterioration processes such as corrosion and wear. However, the surface quality of the part also strongly influences, e.g., the fatigue resistance [4]. Therefore, a number of specialized treatments have been devised that are based on altering the materials chemistry at the surface. Among these, those that rely on the introduction of alloying elements at elevated temperature and in a suitable environment (e.g. gas, plasma, salt bath, or powder pack) are termed as thermochemical surface treatments [5]. Among the most widely employed of these processes are carburizing, which introduces (additional) C in the surface adjacent region in the austenitic temperature range, and nitriding, which introduces N at usually moderate temperatures into the ferritic or martensitic phases [5]. The main advantages of nitriding for a technical application are the low distortion, as hardening is achieved without the need for quenching (see below), and the very high hardness that can be achieved after the treatment [6].

This thesis aims at gaining a deeper understanding of the nitriding process. On one hand, investigations are performed that enable correlation of the microstructural changes occurring upon nitriding and the shape and position of X-ray diffraction peaks. On the other hand, as alloy steels are comprised of several alloying elements, the developing nitride phases and the evolution and properties of the nitrided zone of ternary Fe-Cr-Mo model alloys are characterized.

1.2 Nitriding

Nitriding is usually performed in the temperature range from 400 °C to 600 °C in NH₃-containing atmospheres, i.e. NH₃-N₂ or NH₃-H₂, (gaseous nitriding), in a plasma generated in a N₂-H₂-atmosphere (at lower pressure), or in salt baths containing cyanates (CN⁻) [5]. Also high temperature processes exist that introduce N directly from N₂ gas at high pressure into austenite, a process that involves quenching to form hard N-martensite at the surface. Common nitriding times reach from a few hours up to 100 h if very thick nitrided layers are required [6].

Gaseous nitriding; thermodynamics

Of the above nitriding processes, gaseous nitriding in NH₃-H₂-atmospheres is the only one where the thermodynamics can be precisely controlled by employing a flowing (continuously renewed) atmosphere in a furnace with inert inner surface of the furnace walls, such as fused silica, so that the unwanted thermal decomposition of NH₃ can be minimized (reaction (1.1) below).

The nitriding reaction in an NH₃-H₂-atmosphere can be conceived as the sum of the following two reactions [5]:



Where $[\text{N}]_\alpha$ represents N dissolved in α -Fe. The combined reaction gives:



Upon establishment of local equilibrium between the gas phase and the specimen surface and choosing the same reference state for N (usually pure N₂ gas at 1 atm) in the solid phase and the gas phase, the chemical potential of N in the gas phase $\mu_{\text{N}_2,\text{gas}}$ becomes equal to the chemical potential of N in the solid $\mu_{\text{N},\alpha}$, thus giving (with the definition of the chemical potential $\mu = \mu^0 + RT\ln(a_{\text{N}})$):

$$\frac{1}{2}\mu_{\text{N}_2,\text{gas}}^0 + \frac{1}{2}RT\ln\left(\frac{p_{\text{N}_2}}{p^0}\right) = \mu_{\text{N},\alpha}^0 + RT\ln(a_{\text{N}}) \quad (1.4)$$

Where p^0 is the total pressure and p_{N_2} the partial pressure of N_2 gas. The activity of N, a_{N} , is then given by:

$$a_{\text{N}} = \sqrt{\frac{p_{\text{N}_2}}{p^0}} \quad (1.5)$$

The equivalent pressure of N_2 imposed by the $\text{NH}_3\text{-H}_2$ -atmosphere is obtained from equation (1.1) as:

$$p_{\text{N}_2} = (K_{\text{N}} \cdot r_{\text{N}})^2 \quad (1.6)$$

with

$$r_{\text{N}} = \frac{p_{\text{NH}_3}}{p_{\text{H}_2}^{3/2}} \quad (1.7)$$

where r_{N} is the so called nitriding potential determined from the partial pressures p of NH_3 and H_2 as given in relation (1.7), and K_{N} is the equilibrium constant of reaction (1.1). At the common nitriding temperatures in the usual $\text{NH}_3\text{-H}_2$ -mixtures, the equivalent pressure of N_2 corresponds to several hundred atmospheres.

1.3 Microstructure of the nitrated zone

At the high activities of N imposed by the nitriding atmosphere, in addition to the dissolution of a small amount of N on the octahedral interstices of ferrite (see section 1.4) (up to about 0.4 at.% [7]), also iron nitrides $\gamma\text{-Fe}_4\text{N}$, and $\epsilon\text{-Fe}_{2.3}\text{N}$, can start to form at the specimen surface where the highest activity of N can be achieved first [8]. Such an outer iron-nitride layer grown in iron substrate is called as “compound layer” or “white layer”. Below the compound layer a so-called “diffusion zone” develops which consist of ferrite matrix with dissolved N and/or alloying-element nitrides provided the iron is alloyed with strong nitride forming elements like Cr, Ti, V (Fig. 1.1a). In general, N can be bound in three ways in the diffusion zone of alloy specimens: (i) strongly bound in alloying element nitrides, (ii) adsorbed at the interface of the alloying element nitride precipitates and the ferrite matrix (interface, immobile excess N [9], [10]), and (iii) interstitially dissolved in the ferrite matrix, either due to the imposed nitriding atmosphere of high

N-activity (equilibrium dissolved N, [7]) or due to the elastic expansion of the ferrite matrix by the nitride precipitates (strain dissolved, mobile excess N [9], [10]; see Chapter 2).

The nitriding potential required at a certain nitriding temperature for the formation of the various Fe-N phases is commonly represented in the so-called Lehrer diagram (Fig. 1.1b). A metastable intermediate phase α'' -Fe₁₆N₂ develops at low temperatures (even at room temperature (RT)) by ordering of N on the interstitial sites in N-supersaturated ferrite or martensite. It develops as thin platelets on the {100}_{α-Fe} planes of the N-supersaturated ferrite matrix [11]. Upon prolonged aging it transforms into the stable γ' -Fe₄N phase.

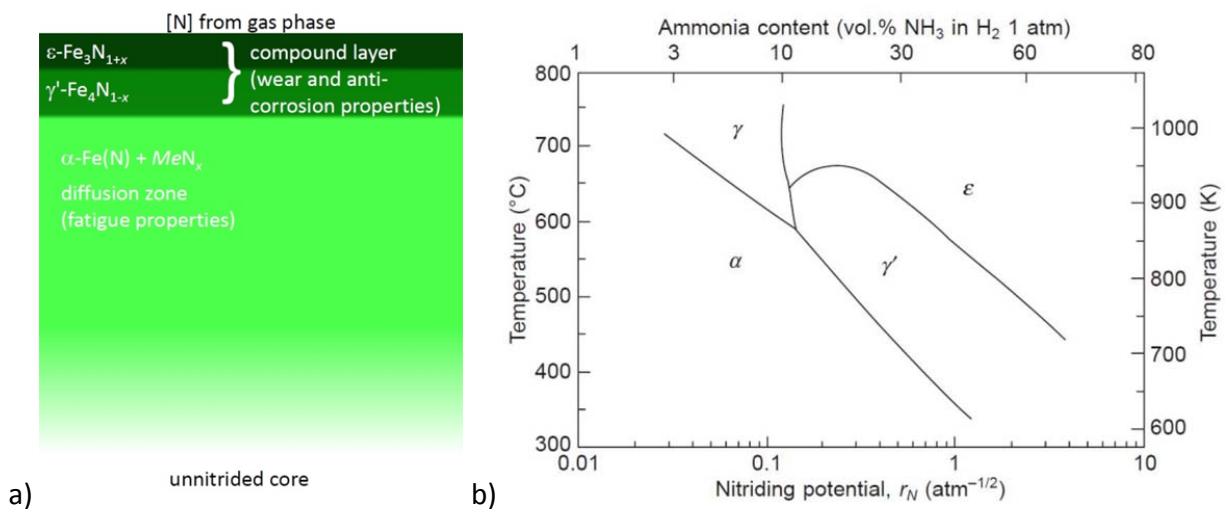


Fig. 1.1: a) Schematic drawing of the nitrided zone with the compound layer of ϵ - and γ' -nitride forming at the surface with the diffusion zone below. Material properties that are mainly affected by the respective microstructural-zones development are indicated. b) Lehrer-diagram [12], redrawn according to [5], showing the phase fields of ferrite (α), N-austenite (γ), γ' -Fe₄N_{1-x} and ϵ -Fe₃N_{1+x} iron nitrides as function of temperature and nitriding potential. The content of NH₃ in the NH₃-H₂-atmosphere is given in the upper abscissa.

The nitride forming alloying elements present in steel react with inwardly diffusing N to form alloying element nitrides in the diffusion zone; Ti [13], [14], V [15]–[19], Cr [20]–[27], Mo [28]–[31], Al [32]–[35], Si [36]–[38] and Mn [39]–[43]. Often the developed alloying-element nitrides are extremely fine (in the nanometer range) and thus lead to a considerable hardening of the nitrided surfaces and simultaneously result in the development of high residual compressive macrostresses parallel to the specimen surface. Hardening, together with the establishment of compressive residual stresses is responsible for the simultaneous improvement of both wear and fatigue resistances of treated components. Due to the much higher affinity for N of alloying

elements than that of Fe, the nitriding potentials that are required to form these alloying element nitrides are considerably smaller than that for the Fe-nitrides at the same temperature, see Chapter 5. Thus it is possible to achieve enhanced hardness, due to the development of nano-sized alloying-element nitrides without the formation of a brittle outer compound layer. Controlled treatments, which, according to thermodynamic conditions, avoid the formation of iron-nitrides but allow the development of alloying-element nitrides, i.e. development of only a diffusion zone, are referred to as internal nitriding, a term originating from oxidation of metal alloys [44]. However, although there exists a chemical driving force for the formation of alloying-element nitrides in ferrite, their development can be hindered due to their volume misfit with the matrix. In some cases this misfit can be extremely high and may considerably retard the nitride precipitation process, as e.g. in the case of Si [38]. Based on the precipitation-favoring chemical free energy and the precipitation-retarding misfit strain energy a so-called interaction parameter can be defined which indicates the relative ease of precipitation of a particular nitride in ferrite matrix. This interaction parameter is taken as the ratio of chemical free energy release upon nitride precipitation to the elastic misfit strain energy [45] associated with nitride precipitation [5].

This strength of interaction, as a measure for the nitride precipitation kinetics, has a direct impact on the N-concentration-depth profiles and thus also the achievable material properties. A classification was devised [32] to link the strength of interaction to the observed N-content-depth profiles. Strong nitride formers, as Ti, and V show a very high surface N-content and a very steep transition to the unnitrided core as N arriving at a certain depth immediately reacts with free alloying element. Weak nitride formers, as Si, Al, and Mo, show very shallow N-content-depth profiles as considerable inward diffusion of N can occur before its reaction with the alloying element. Nitride formers of intermediate strength, as Cr, lead to depth profiles that can be relatively shallow but still show precipitation mainly at the surface. In addition, nucleation of especially hexagonal (as e.g. AlN and δ -MoN) nitride phases can be severely impaired further slowing their precipitation kinetics. In the case of Si_3N_4 even the formation of an amorphous intermediate phase occurs [38].

1.4 Morphology of nitrides in steel

The nitrides of Fe and the alloying elements forming on and/or in steel can have a variety of crystal structures. Some of the most important crystal structures of common (alloying-element) nitrides have been gathered on page 182 in Supplement 1 and Supplement 2 and their unit cells are shown in Supplement 3 and Supplement 4.

The morphology of nitride phases in steels depends mainly on their mechanism of formation. While the matrix phases, i.e. ferrite and austenite, are usually comprised of equiaxed grains, N-martensite shows a characteristic lath- or plate-like microstructure (see, e.g., Refs. [43], [46], [47]). When ϵ -Fe₂₋₃N and γ' -Fe₄N form as compound layers on the surface of pure Fe, many times they show a columnar microstructure [8]. In steels, due to the generally much finer microstructure and the much larger amount of defects present this columnar structure is not observed. Furthermore, even in ferritic model alloys containing alloying elements like Al, Si or Mo, that inhibit the formation of the γ' -phase, the compound layer may (initially) consist of separate individual γ' -grains with a needle-like morphology [48]. Upon aging of N-supersaturated ferrite or martensite, the precipitation of α'' -Fe₁₆N₂ will occur in the form of very fine platelets on the {100} _{α -Fe} planes [49]. Upon further aging, this intermediate precipitates transform to γ' -Fe₄N which shows a needle-like morphology [50], a microstructural feature that is commonly observed in the diffusion zone of relatively slowly cooled (furnace cooled) nitrided steels.

The formation of the NaCl-type alloying element nitrides (CrN, ..., see Supplement 2) in ferrite and martensite occurs usually as nano-sized platelets on the {100} _{α -Fe} planes of the bcc(-based) matrix [19], [20], [51]. This precipitation morphology is driven by the favorable Baker-Nutting (BN) orientation relationship (OR) [52] that is established with the matrix. The platelets form by continuous precipitation (CP) leading to their homogeneous, fine distribution in the matrix. Due to the very fine size of the particles and the associated large interface area in this precipitation morphology, a large tendency for coarsening is present. This tendency may become sufficiently large, that the coarsening mechanism changes from the slower continuous coarsening (CC), i.e. growth of the precipitates, to a faster grain boundary discontinuous coarsening (DC) mechanism. The latter transforms the platelet morphology to a lamellar morphology, such that the microstructure after DC is comprised of alternating lamellae of ferrite and NaCl-type nitride [23]. In Fe-based alloys with high Cr-content, the precipitation of Cr can also occur as Cr₂N ahead of the main nitriding front [25]. The thus forming larger rods of Cr₂N later transform to CrN upon continued nitriding. The precipitation of hexagonal AlN occurs in the form of very small, roughly spherical particles with a Pitsch-Schrader OR [53] in ferrite [35]. In binary Fe-Mo alloys, after the initial precipitation of NaCl-type γ -Mo₂N platelets [31], hexagonal δ_3 -MoN forms by a discontinuous precipitation (DP) mechanism also resulting in a lamellar microstructure of alternating lamellae of ferrite and δ_3 -MoN with a Burgers OR [54]. In two-phase Fe-Mo alloys, containing the Fe₂Mo-Laves phase before nitriding, initially η -Fe₃Mo₃N is formed, which later transforms to γ -Mo₂N [55]. The hexagonal layered CrMoN₂-phase has now, as a result of this work, first been reported upon nitriding of ternary Fe-Cr-Mo alloys (see chapter Chapter 6).

1.5 Micro- and macro-structural effects on X-ray diffraction lines

X-ray diffraction (XRD) has become a widely employed materials characterization method [56] by which information can be gathered about the microstructure that is otherwise difficult to obtain, as e.g. the residual stress state, the grain size of nano-crystalline materials, and the texture and microstrains of the microstructure. In order to correctly quantify many of these properties, a precise, fundamental understanding of the interplay of microstructure and diffraction conditions is required.

Generally, the presence of defects in the microstructure disturbs the ideal, average lattice of the crystal. However, in most cases it is possible to identify regions in the microstructure that are sufficiently large as compared to the physical coherence length of the radiation, which then give rise to Bragg-like peaks [57]. On one hand, this allows the characterization of materials with a highly complex microstructure, as are virtually all modern steels; on the other hand it can also make the observation of small microstructural changes of the material difficult. The precipitation of small second phase particles, which is the main strengthening mechanism of (internally) nitrided parts, is many times so fine, that although the nitrides and the matrix have a completely different crystal structure (see section 1.4), they still diffract as one aggregate. This is termed as “coherent” diffraction of matrix and precipitates [58], [59]. If this occurs, the changes in the individual phases cannot directly be derived from the diffractogram and models relating the (micro-)structural changes to the diffraction effects are required.

Residual stresses are stresses present in a material in the absence of an external load [59]. They originate due to several reasons: different thermal expansion coefficients of parts of the material in contact, variations in chemical composition, or different degrees of plastic deformation. Depending on the length scale on which they are acting, they are categorized as microstress for local stresses in the order of the grain size or less, or macrostress for long ranging stresses present in extended regions of the specimen. The microstrains resulting from the locally varying stress state express themselves in a broadening of the peaks in XRD, i.e. a wider distribution of lattice spacings. Macrostress generally lead to peak shifts as the overall, average lattice spacing is changed by the stress state. Complex macroscopic stress states can require elaborate measurements for their determination [60].

1.6 Outline of the thesis

The aim of this thesis is a better fundamental understanding of the consequences and mechanisms of the interaction of alloying elements with inwardly diffusing nitrogen in the diffusion zone, i.e. the internal nitriding, of iron-based alloys.

In Chapter 2 an elastic misfit accommodation model is extended by considering the diffraction conditions of the experiment to predict the peak shifts occurring for the ferrite matrix due to the precipitation of coherent nitrides. By isolating the effect of the nitride precipitation from the various other contributions to the peak shifts, the experimental validation shows a very good quantitative agreement of an elastic misfit accommodation model and experimental data. Furthermore, a “tail of scattered intensity” at the high-angle side of the Bragg-like peaks of the aggregate originates from scattering of the distorted regions in close to the coherent precipitates.

In Chapter 3, the elastic misfit accommodation model is applied to the lattice-parameter changes reported in literature for various systems showing different origins of misfit (thermal or transformation-induced), different types of accommodation of the misfit in the system (elastic or plastic), and different diffraction conditions of the misfitting phases (coherent or incoherent). Recognizing the specific conditions of the respective systems, generally good agreement between experimental results and model predictions is found.

The effect on the X-ray diffraction peaks of the two main mechanisms of relaxation in the nitrided microstructure, continuous and discontinuous coarsening, of Fe-2.0 at.%Cr and Fe-4.5 at.%Cr alloys is presented in Chapter 4. The misfit accommodation model developed in Chapter 2 relies on the completely elastic accommodation of the precipitate/matrix misfit in the nitrided microstructure. However, upon prolonged nitriding/aging, plastic relaxation of the misfit may occur. Continuous coarsening expresses itself by a gradual back shifting of the peaks in the XRD patterns. Discontinuous coarsening leads to the immediate, full relaxation of the misfit and thus the emergence of the relaxed peak directly at its final position. In both cases, the relaxed regions begin to diffract separately. The peak evolution is correlated to the microstructural evolution and an overview of the evolution of the “ferrite” peaks upon nitriding and subsequent relaxation is presented.

In Chapter 5 the origin of the observed discrepancy of experimentally determined and expected N-content after denitriding, and consequently of the magnitude of the peak shift of XRD peaks, is exposed and a strategy is proposed and experimentally validated to improve (for relatively stable alloying element nitrides) and enable (for relatively less stable alloying element nitrides) the determination of the nitride stoichiometry.

A number of ternary Fe- Me_1 - Me_2 -alloys have previously been investigated in order to gain understanding of the simultaneous interaction of inwardly diffusing N with two alloying elements with affinity for N, see e.g. Refs. [61]–[67]. The Fe-Cr-Mo systems is not only the basis for a large variety of steel systems [68], but furthermore offers a unique combination of two nitride formers with moderate (Cr) and weak (Mo) interaction with N.

A detailed characterization of the nitrides forming in an Fe-1 at.%Cr-1 at.%Mo alloy upon nitriding is presented in Chapter 6. The sequence of developing ternary nitrides is attributed to the thermodynamic and kinetic constraints of the precipitation of these phases in the ferritic matrix. Initially, continuous precipitation of fine, coherent, cubic NaCl-type nitride platelets with their broad faces parallel to the $\{100\}_{\alpha\text{-Fe}}$ planes occurs. The platelets have a composition of $(Cr_{\frac{1}{2}}, Mo_{\frac{1}{2}})N_{\frac{3}{4}}$ in this alloy. Upon prolonged nitriding, the nitrides undergo a discontinuous precipitation reaction resulting in the formation of a coarsened microstructure consisting of lamellae of a novel, hexagonal $CrMoN_2$ nitride along $\{110\}_{\alpha\text{-Fe}}$ lattice planes and ferrite lamellae. Inside the ferrite lamellae, spherical precipitates of cubic, NaCl-type $(Cr, Mo)N_x$ occur.

In order to further understand the role of Cr and Mo during nitriding, in Chapter 7 four nitrided ternary Fe-Cr-Mo alloys, all containing a total of 2 at.% Cr+Mo but with Cr/Mo-ratios varying from 1.0 to 7.2, are investigated. Initially, ternary, “mixed”, cubic, NaCl-type $(Cr, Mo)N_y$ nitride platelets are found to precipitate continuously in the ferrite matrix. The N-concentration-depth profiles indicate that with decreasing Cr/Mo-ratio the nitriding kinetics become slightly slower. The formation of a coarsened lamellar microstructure by a discontinuous transformation mechanism shows a strong dependency on the Cr/Mo-ratio of the alloy. Additionally, in this chapter a summarizing discussion on the precipitation of “mixed” vs. separate precipitation of alloying element nitrides in ternary Fe-based systems upon nitriding is presented.

Chapter 2

Lattice-parameter change induced by accommodation of precipitate/matrix misfit; misfitting nitrides in ferrite

M. Akhlaghi, T. Steiner, S.R. Meka, A. Leineweber and E.J. Mittemeijer

Abstract

Upon nitriding of iron-based alloys, development of misfitting coherent nitride precipitates in a ferrite matrix induces an overall expansion of the ferrite lattice. This lattice expansion was quantitatively determined by X-ray diffraction from the change of the lattice parameter of ferrite of homogeneously nitrided Fe-Cr and Fe-V alloys. Adopting the experimentally verified (by X-ray diffraction and transmission electron microscopy) notion that the misfitting precipitates *diffract coherently with the matrix*, the extent of this hydrostatic lattice-strain component could be calculated, in general, as function of the precipitate/matrix misfit, the volume fraction of precipitates and the elastic properties of the matrix and precipitates. The experimentally observed and the predicted dependencies of lattice dilatation agree very well for both nitrided Fe-Cr and Fe-V alloys. This is the first time that this type of lattice expansion was experimentally identified and quantitatively explained.

2.1 Introduction

Solid-state phase transformations involving volume misfit between parent and product phases can induce unusual, non-equilibrium phenomena, such as, the establishment of metastable phases (e.g. cubic AlN in a ferrite matrix [33], [34]), non-monotonous variation of transformation rate (e.g. during austenite-ferrite and austenite-martensite transformations [69]–[71]), unusual morphologies (as octapod shaped, amorphous silicon-nitride particles in a ferrite matrix [72]). These effects are often attributed to the complex interplay of the chemical Gibbs energy change driving the transformation and the deformation energy associated with volume misfit accommodation [59], [73]. Precise understanding of the effects of misfit-strain energies on the thermodynamics and kinetics of phase transformations and on the resulting microstructure is essential to optimize the properties of engineering components [74].

The elastic strain fields surrounding individual (tiny) precipitates have been exposed by transmission electron microscope (TEM) diffraction-contrast images [75]–[77] which allow (local) determination of the sign and (approximate) magnitude of the occurring misfit. The lattice distortions associated with misfit-strain fields induce diffuse scattering in X-ray diffraction (XRD) experiments [57], which can be used to reveal characteristics of the strain fields around

(very) small precipitates [78]. The presence of misfitting inclusions of larger dimensions induces (X-ray) diffraction-line broadening, characteristic for the presence of *microstrains* [56], [57], [79].

However, it is not generally recognized that the (average, overall) lattice-parameter values of misfitting systems are different from their (misfit) strain-free values, thereby exposing the presence of a (hydrostatic) *macrostrain*. Thus, straightforward determination of the lattice parameter (e.g. from the peak position in (X-ray) diffractograms) provides important information not only on the course of a precipitation process by compositional change of the parent matrix, but also on the extent of the developing misfit-strain fields. The last feature plays a cardinal role in the present work.

The state of stress invoked by misfitting inclusions in a matrix has been dealt with largely theoretically in the literature [45], [80]–[82]. Experimental verification of such theoretical predictions is relatively rare: adopting a theory for point imperfections in a solid matrix, the effect of misfitting precipitates on the lattice distortions of the matrix, and in one case also of the precipitates, was investigated for the case of *incoherent* precipitate/matrix interfaces [83]–[85]. Since this early work, no further development and application of this approach appears to have taken place.

Against the above background, the present work is devoted to prediction and experimental verification of lattice distortions introduced upon the development of misfitting second-phase particles in a solid matrix, with (largely) *coherent* precipitate/matrix interfaces, employing X-ray diffraction. To this end, systems composed of misfitting nitride particles in a ferrite matrix, as developing during internal nitridation of iron-based alloy substrates (Fe-Cr and Fe-V alloys), have been chosen as model systems. The tiny CrN and VN precipitates are (largely) coherent with the ferrite matrix [19], [20], [23], [42] and yet exhibit pronounced volume misfit with the matrix. The coherency of the precipitate/matrix interface gives rise to peculiar diffraction effects involving coherent diffraction of the assembly precipitate plus matrix (so no precipitate reflections occur) and asymmetrically broadened diffraction-line profiles. It will be shown that the effect of misfit strain is sensitively expressed in lattice-parameter changes and that good agreement between theoretically predicted and experimentally measured data can be achieved.

2.2 Elastic strain field in a misfitting system: lattice-parameter changes

A continuum theory for the fully elastic accommodation of the misfit of a point imperfection in a matrix has been presented by Eshelby [86], [87]. The theory was developed to (also) predict the slope of the dependence of the lattice parameter of a crystalline solid solution on solute content (cf. Vegard's law [88]). However, for this application the theory failed, as electronic interaction on the atomic scale can be dominant over elastic straining effects [45]. Therefore, the theory is more likely applicable to the case of precipitation of misfitting second-phase particles. On this basis, cases of particle-matrix misfit strain for elastically anisotropic matrices could be dealt with leading to the prediction of precipitate-particle shape [80], [89]–[91].

In the following subsections, formulae are presented that describe the changes of the relative volume/lattice-parameters of the matrix (section 2.2.1), the misfitting particles (inclusions; section 2.2.2) and of the assembly, i.e. matrix plus misfitting particles (inclusions; section 2.2.3)¹.

2.2.1 Change of the lattice parameter of the matrix

Insertion of the undeformed inclusions B in the holes of the matrix A leaves the whole assembly in a state of self-stress. Considering i) a *finite* matrix A containing, in the strain-free condition, holes of radius r_A^0 and ii) particles B , of strain-free radius r_B^0 , the relative volume increase of the matrix A due to the insertion of the misfitting inclusions B into the holes of the matrix A can be written as [45]:

$$\frac{\Delta V_A}{V_A} = \frac{16}{3} \pi \frac{\mu_A}{K_A} C_6 \varepsilon (r_A^0)^3 n \quad (2.1)$$

with

$$C_6 = \frac{3K_B}{3K_B + 4\mu_A} \quad (2.2)$$

where n is number of inclusions B per unit volume and K and μ represent the bulk modulus and the shear modulus, respectively. The linear misfit parameter, ε , can be calculated from $(r_B^0 - r_A^0)/r_A^0 = (\sqrt[3]{v_B^0} - \sqrt[3]{v_A^0})/\sqrt[3]{v_A^0}$, where v_B^0 and v_A^0 are the molar volumes of the strain-free precipitate particle and the matrix, respectively. The volume fraction of inclusion y_B can be taken as $y_B = 4\pi(r_B^0)^3 n/3$. For the case of a matrix of cubic crystal structure with a

¹ In the derivations of the following formulae, in order to calculate the image force term for a *finite* matrix and a *finite* assembly, it is assumed that the volume fraction of misfitting particles is small: only the matrix elastic constants are used to calculate the image force term for matrix and assembly. Further, the matrix and the misfitting particles are taken to be elastically isotropic.

(strain-free) lattice parameter a_A , $\Delta V_A/V_A$ can be approximated by $3\Delta a_A/a_A$, and Eq. (2.1) can be rewritten as [83]:

$$\Delta a_A = \frac{4\mu_A C_6}{3K_A} \frac{\varepsilon}{(1 + \varepsilon)^3} y_B a_A \quad (2.3)$$

It is important to note that the matrix is of finite dimensions. In an *infinite* matrix, the volume change of the matrix due to the introduction of misfitting inclusions is zero (the matrix only experiences shear strains); then, the volume change of the assembly is fully confined to the precipitates. The matrix dilatation that is predicted for a matrix of *finite* size is a consequence of the image forces required to achieve a stress-free surface of the finite assembly.

2.2.2 Change of the lattice parameter of the misfitting phase

A misfitting inclusion with a radius larger or smaller than that of the hole in the matrix will experience hydrostatic compression or tension, respectively. For the case of a *finite* assembly of matrix A plus misfitting inclusions B , the fractional volume change of the inclusions can be written as [85]:

$$\frac{\Delta V_B}{V_B} = -3\varepsilon(1 - C_6) + \frac{16}{3}\pi \frac{\mu_A}{K_B} C_6 \varepsilon (r_A^\circ)^3 n \quad (2.4)$$

For the case of precipitates of cubic crystal structure with a (strain-free) lattice parameter a_B , $\Delta V_B/V_B$ can be approximated by $3\Delta a_B/a_B$, and it follows for the change of the lattice parameter, Δa_B , of the misfitting second phase:

$$\Delta a_B = \left[-\varepsilon(1 - C_6) + \frac{4\mu_A C_6}{3K_B} \frac{\varepsilon}{(1 + \varepsilon)^3} y_B \right] a_B \quad (2.5)$$

The total relative volume change of the inclusions results from the *sum* of the fractional volume change of the inclusions in an *infinite* assembly (first term in Eqs. (2.4) and (2.5)) and the fractional volume change of the inclusions due to the image forces acting (also) on the inclusions in a *finite* assembly (second term in Eqs. (2.4) and (2.5)).

2.2.3 Change of the lattice parameter of the assembly (matrix plus misfitting phase)

The relative volume change of the whole, finite assembly comprising the finite matrix and the misfitting inclusions can be given as [45]:

$$\frac{\Delta V}{V} = 4\pi C_6 \varepsilon (r_A^\circ)^3 + \frac{16}{3} \pi \frac{\mu_A}{K_A} C_6 \varepsilon (r_A^\circ)^3 n = 4\pi \frac{C_6}{C'_6} \varepsilon (r_A^\circ)^3 n \quad (2.6)$$

with

$$C'_6 = \frac{3K_A}{3K_A + 4\mu_A} \quad (2.7)$$

For an aggregate of cubic crystal structure and a (strain-free) lattice parameter a , thus approximating $\Delta V/V$ by $3\Delta a/a$, the resulting change of the lattice parameter, Δa , of the aggregate for a volume fraction y_B precipitate particles B is given by:

$$\Delta a = \frac{C_6}{C'_6} \frac{\varepsilon}{(1 + \varepsilon)^3} y_B a \quad (2.8)$$

The total relative volume change of the assembly, analogous to the case of the relative volume change of only the inclusions, results from the *sum* of the fractional volume change of the inclusions in an *infinite* assembly (first term in Eq. (2.6) (this volume change is confined to the inclusions; cf. section 2.2.1)) and the fractional volume change of the assembly due to the image forces required to achieve a stress-free surface of the *finite* assembly (second term in Eq. (2.6)).

2.2.4 Coherent vs. incoherent diffraction of matrix and misfitting precipitates; consequences for interpretation of lattice-parameter changes

The coherent or incoherent nature of the diffraction by a second phase (here precipitate particles) with the diffraction by the matrix need not coincide with the occurrence of a coherent or incoherent nature of the interfaces between the second-phase particles and the matrix. Coherency/incoherency of diffraction depends on whether or not constructive interference of waves scattered by separate parts of the diffracting material (matrix and second phase) occurs. Incoherency of diffraction is a statistical phenomenon: parts of a specimen can be considered to scatter incoherently if the phase difference (given as reduced modulo 2π) between a wave scattered in one part and a wave scattered in another part takes any value between zero and 2π with equal probability [58], [59].

Thus, because of the variability of the phase jump at an *incoherent* boundary between a second-phase particle and the matrix, due to its irregular structure, it appears likely that in this case the second-phase particles and the matrix diffract independently, i.e. incoherently, and in the diffraction pattern separate diffraction peaks of the second-phase particles and the matrix occur [58], [59].

For *coherent* (and semi-coherent) interfaces, more complicated diffraction effects can be expected. If a misfit between the second-phase particles and the matrix exists, lattice distortions, due to elastic accommodation, occur in the matrix and the second-phase particles, especially close to the particle/matrix interfaces. The phase difference between waves scattered by the matrix and waves scattered by second-phase particle depends on both the position (difference) vector from one scatterer (in the matrix) to the other one (in the particle) and the value of the diffraction angle (i.e. the length of the diffraction vector). Then, given the imperfect (strained) but (semi-)coherent crystal structure of the entity matrix/second-phase particles, it depends on the length of the diffraction vector if coherent or incoherent diffraction occurs. The occurrence of coherent diffraction implies that each peak in the diffraction pattern represents diffraction of the whole assembly of matrix plus second-phase particles [58], [59].

Provided matrix and precipitate diffract independently, i.e. incoherent diffraction of matrix and of precipitates occurs, the changes of the lattice parameters of the matrix and of the precipitates can be determined from measurements of the positions of the (separate) X-ray diffraction peaks of the matrix and of the precipitates. In that case, Eqs. (2.3) and (2.5) predict the changes of the lattice parameters of the matrix and the precipitates, respectively. If a coherent nature of the precipitate/matrix interfaces prevails, then, dependent on the length of the diffraction vector and the extent of misfit-strain variation, coherent diffraction by precipitate phase and matrix can occur, in which case the change of the lattice parameter derived from the position of the diffraction peaks is predicted by Eq. (2.8).

2.3 Experimental

To exclude the presence of macroscopic stresses, usually present in heterogeneously nitrated specimens, thin foil specimens of Fe-Cr and powder specimens of Fe-V alloys, which both can be homogeneously nitrated, were employed in this study.

2.3.1 Specimen preparation

Fe-2.0 at.%Cr and Fe-4.5 at.%Cr alloys were prepared by melting appropriate amounts of pure Fe (99.98 wt.%) and pure Cr (99.999 wt.%) in an Al₂O₃ crucible in an inductive furnace under a protective argon atmosphere (99.999 vol.%). After casting, the alloys had a cylindrical shape with a diameter of 10 mm and a length of 100 mm.

Fe-V powders of various V contents were procured from Nanoval GmbH&Co.KG, which had produced the Fe-V alloy powders from pure Fe (99.8 wt.%) and pure V (99.6 wt.%) by spray atomization of the alloy melt according to the Nanoval-process [92] under a high-velocity Ar-stream. The mean particle diameter of the Fe-0.9 at.%V powder was $d_{50} = 17.2 \mu\text{m}$, of the Fe-3.5 at.%V powder $d_{50} = 19.8 \mu\text{m}$ and of the Fe-1.8 at.%V powder $d_{50} = 9.9 \mu\text{m}$. Preliminary investigations with powders of different particle sizes of the same alloy had shown no influence of the particle size on the nitriding response.

The compositions of the cast Fe-Cr alloys and the spray-atomized Fe-V powders were determined by chemical analysis; the results have been gathered in Table 2.1. The contents of Cr, V and metal impurities (negligible) were determined by inductive coupled plasma optical emission spectroscopy (ICP-OES); the O and N contents were determined by carrier gas hot extraction and the C and S contents were determined by a combustion method.

Table 2.1: Results of chemical analysis of the massive Fe-Cr alloys and the Fe-V alloy powders

alloy	Cr, V		O (wt.%)	N (wt.%)	C (wt.%)	S (wt.%)
	(at.%)	(wt.%)				
Fe-2.0 at.%Cr	2.03±0.02	1.90±0.02	0.008	<0.001	<0.002	<0.002
Fe-4.5 at.%Cr	4.54±0.05	4.24±0.01	0.018±0.001	<0.004	0.002±0.001	<0.001
Fe-0.9 at.%V	0.90±0.01	0.82±0.01	0.020±0.003	<0.002	0.003±0.001	<0.001
Fe-1.8 at.%V	1.79±0.02	1.64±0.02	0.014±0.003	<0.002	0.004±0.002	<0.001
Fe-3.6 at.%V	3.56±0.04	3.26±0.04	0.022±0.003	<0.002	0.003±0.001	<0.001

The cast Fe-Cr alloys were cold-rolled to sheets with a thickness of 1 mm. The obtained sheets were annealed for 2h at 700 °C to get a recrystallized grain structure and further cold-rolled to foils with a thickness of 0.2 mm. Rectangular pieces of approximate lateral dimensions 10 mm × 10 mm were cut from the foil and ground to a thickness of less than 100 μm. Subsequently, the specimens were annealed at 700 °C for 2 h under flowing H₂ atmosphere to obtain a recrystallized grain structure. The average grain size measured from the optical macrographs recorded from the recrystallized specimens is 50-60 μm. Before nitriding, the thin foils were polished (last step: 1 μm diamond suspension) and cleaned with ethanol.

2.3.2 Nitriding and de-nitriding experiments

For nitriding, the Fe-Cr thin foils were suspended with a quartz fiber in a vertical quartz tube furnace and the Fe-V powders were deposited onto a quartz half-tube slider and inserted into a horizontal quartz tube furnace. The furnaces have a temperature accuracy of ±1 K. Nitriding was performed in an ammonia/hydrogen gas flux (purity: H₂: 99.999 vol. %, NH₃: >99.998 vol. %). The nitriding parameters used have been gathered in Table 2.2. All nitriding conditions have been chosen such that only a diffusion zone (ferrite with dissolved N and alloying element nitride particles) develops, i.e. other Fe-N phases such as iron-nitrides and Fe-N austenite do not develop. The applied nitriding conditions led to homogeneously nitrated Fe-2.0at. % Cr thin foils, implying that, after through nitriding, the nitrogen level at all depths in the specimen increased identically as a function of time. This leaves the specimen free of macroscopic stresses, due to the absence of a concentration-depth gradient even before full N saturation (i.e. precipitation of all Cr as CrN and saturation of the remaining ferrite matrix with dissolved N) had been attained for the foil. The Fe-V powder specimens were nitrated until the saturation level of N uptake had been realized (i.e., all V had precipitated as VN and the remaining ferrite matrix was saturated with dissolved nitrogen). Subsequently, some of the nitrated Fe-Cr thin foils and some of the Fe-V powder specimens were de-nitrated in pure H₂ at 400 °C for 16 h and then slowly cooled to the room temperature. At the employed denitriding conditions both CrN and VN are stable and the less strongly bonded dissolved N diffuses out [9], [10], [93].

Table 2.2: Applied nitriding parameters for the different Fe-Cr foils and the different Fe-V powders. For all treatments fluxes of 43 ml/min NH₃ and 456.4 ml/min H₂ were applied, which corresponds with a nitriding potential [8] of $r_N = 0.1 \text{ atm}^{-1/2}$.

composition	nitriding temperature [°C]	nitriding time [h]
Fe-2.0 at.% Cr	450	72, 144, 216, ..., 792
	500	16
Fe-4.5 at.% Cr	500	2.25
Fe-0.9 at.% V	500	4
Fe-1.8 at.% V	500	4
Fe-3.6 at.% V	500	4

2.3.3 Specimen characterization

Weight measurement

Fe-Cr thin foils were weighed before nitriding, after nitriding and after subsequent denitriding using a Mettler Toledo UMX2 microbalance with an accuracy of $\pm 1 \mu\text{g}$.

Electron probe microanalysis (EPMA)

EPMA was performed on the cross-sections of nitrated and de-nitrated Fe-4.5at.%Cr thin foils. For these measurements, a Cameca SX100 microprobe (acceleration voltage $U = 10 \text{ kV}$, current $I = 100 \text{ nA}$, spot size about $1 \mu\text{m}$) equipped with five wavelength-dispersive spectrometers was used. To obtain the element contents at each measurement point, the intensities of the characteristic X-ray emission peaks were measured and divided by the corresponding intensities obtained from standard samples of pure Fe, Cr and γ' -Fe₄N (for N-K_α). Elemental concentrations were calculated from the intensity ratios applying the $\Phi(\rho z)$ approach [94].

X-ray and synchrotron diffraction

XRD measurements were performed on the surface of unnitrided, nitrated and denitrided specimens (Fe-Cr thin foils and Fe-V powders) using a PANalytical X'Pert diffractometer with Bragg-Brentano configuration, equipped with a Co tube and a graphite monochromator in the diffracted beam to suppress the components other than CoK_α radiation. The diffraction-angle 2ϑ range of 30° - 105° 2ϑ was scanned with a step size of 0.009° 2ϑ .

The XRD patterns thus recorded were evaluated using the TOPAS software (Version 4.2, Bruker AXS). Each diffraction profile in the diffractogram recorded with Co-K α radiation is composed of an α_1 component and an α_2 component [95]. The structural broadening of each of the components was fitted by three pV-functions; one for the main reflection and two for the tail (which is also referred as diffuse, scattered intensity in the literature [78]) (for discussion, see section 2.4). The instrumental profile was obtained from a measured standard LaB $_6$ powder diffraction pattern. This instrumental broadening was incorporated into the fitting of the measured diffraction profiles by convolution with the pV-functions describing the specimen (structural) broadening. An example of the original measured data, the total fit and the corresponding fits of the α_1 and α_2 components is presented in Fig. 2.1. The 2θ -positions of the maximum intensities of the pV-profiles of the main peaks describing the specimen broadening only were then used for determination of the lattice parameters as described next.

In the case of the (de-)nitrided Fe-Cr thin foil a value of the lattice parameter and a value of the specimen displacement [96], were obtained by fitting to the 110, 200 and 211 ferrite-reflection positions determined as described above.

In the case of the (de-)nitrided Fe-V powder specimens, a powder specimen was mixed with Si-standard powder to determine, from the Si peak positions in the measured diffractograms and the known value of the Si lattice parameter [97], the instrumental zero-point 2θ offset and the specimen displacement. Then a value of the lattice parameter was obtained by fitting to the 110, 200, 211 and 220 ferrite-reflection positions determined as described above.

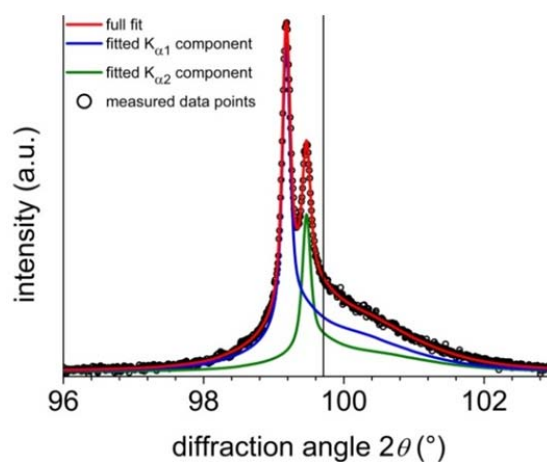


Fig. 2.1: Comparison of measured 211 diffraction peak (Co-K α radiation) of Fe-2.0 at.%Cr specimen, nitrided at 450°C for 720 h with a nitriding potential of 0.1 atm $^{-1/2}$, with the corresponding total fit and the corresponding K α_1 and K α_2 components. The K α_1 -peak position for pure, unnitrided ferrite (α -Fe) has been indicated.

High-resolution powder diffraction data from the nitrated Fe-V powders were collected on the beamline ID31 of the European Synchrotron Radiation Facility (ESRF). A Si 111 reflection was used to select an X-ray energy of 41.3 keV. The size of the beam was adjusted using slits. The wavelength was determined as $0.300715 \pm 0.000005 \text{ \AA}$ from a silicon standard of known lattice parameter (NIST SRM640c). The nitrated Fe-V powder specimen was contained in a 1.0 mm borosilicate glass capillary, which was, during measurement, rotated around its length axis in order to improve orientation randomization of the diffracting crystallites. The diffracted beam was analyzed with a nine-crystal analyzer stage (nine Ge 111 crystals separated by 2° intervals) and detected with nine Na(Tl)I scintillation counters simultaneously. The recorded data were converted to a step scan for values of 2θ from 0.5 to 33.90° in steps of 0.002° . Evaluation was performed by a simultaneous fit of a pV-function to a main peak and a pV-function to its intensity tail employing the TOPAS software. No deconvolution of the instrumental and specimen profiles was performed for these data (no precise lattice-parameter values needed to be extracted from these data; see section 2.4). Thus, the respective 2θ positions, $2\theta_1$ for each main peak and $2\theta_2$ for each intensity tail, and the corresponding peak areas I_1 and I_2 , were determined.

2.4 Results and Evaluation

Upon nitriding the Fe-Cr thin foil and Fe-V powder specimens, under the nitriding conditions described above, a homogenous N-distribution is achieved throughout the specimen. A considerable peak shift of the ferrite reflections towards lower diffraction angles occurs. This is shown exemplarily by the evolution of 211 ferrite diffraction-line profiles recorded for various Fe-Cr and Fe-V specimens in Fig. 2.2. The magnitude of peak shift increases with nitriding time for the Fe-2.0 at.%Cr specimen implying that an increased amount of CrN precipitation leads to an increased shift of the peak (Fig. 2.2a). The Fe-V powders nitrided until saturation (i.e. until precipitation of all V as VN) indicate that the higher the amount of V in the alloys, i.e. the higher the amount of VN precipitation, the larger is the shift of the ferrite reflection towards lower diffraction angles (Fig. 2.2b-d). The same is observed when comparing nitrided Fe-2.0 at.%Cr and Fe-4.5 at.%Cr alloys (not shown). Also, as shown in Fig. 2.2, an intensity tail towards higher diffraction angles is present for both the nitrided Fe-Cr and the nitrided Fe-V alloys. The N-saturated specimens (achieved after 792 h of nitriding for the Fe-2.0 at.%Cr alloy thin-foil specimens) were subsequently subjected to a denitriding treatment until no further N is lost from the specimen. After denitriding, a partial shift of the ferrite reflection (back) towards higher 2ϑ is observed.

From the synchrotron measurements, a more detailed evaluation of the intensity tail is possible because also higher order reflections are detectable (with significant intensity) within the accessible 2ϑ range, see Fig. 2.3. For each observed reflection, the refined positions $2\theta_1$ and $2\theta_2$ due to the main peak and the intensity tail (c.f. section 3.3.3), were converted into reciprocal lattice spacings, d^* , according to:

$$d_{1,2}^* = \frac{2 \sin \theta_{1,2}}{\lambda} \quad (2.9)$$

The distance between the main peak and intensity-tail positions in reciprocal space then follows from $\Delta d^* = d_2^* - d_1^*$. The value of Δd^* has been plotted as function of d_1^* in Fig. 2.4a. The indeterminacy of the refined 2ϑ positions was used to assess the error in Δd^* by error propagation, which has been indicated in Fig. 2.4a. The fraction of the intensity-tail area with respect to the total reflection area (ratio of integrated intensity of the intensity tail to the sum of the integrated intensities of main peak and intensity tail, $\left(\frac{I_2}{I_1+I_2}\right)$) is presented as function of d_1^* in Fig. 2.4b.

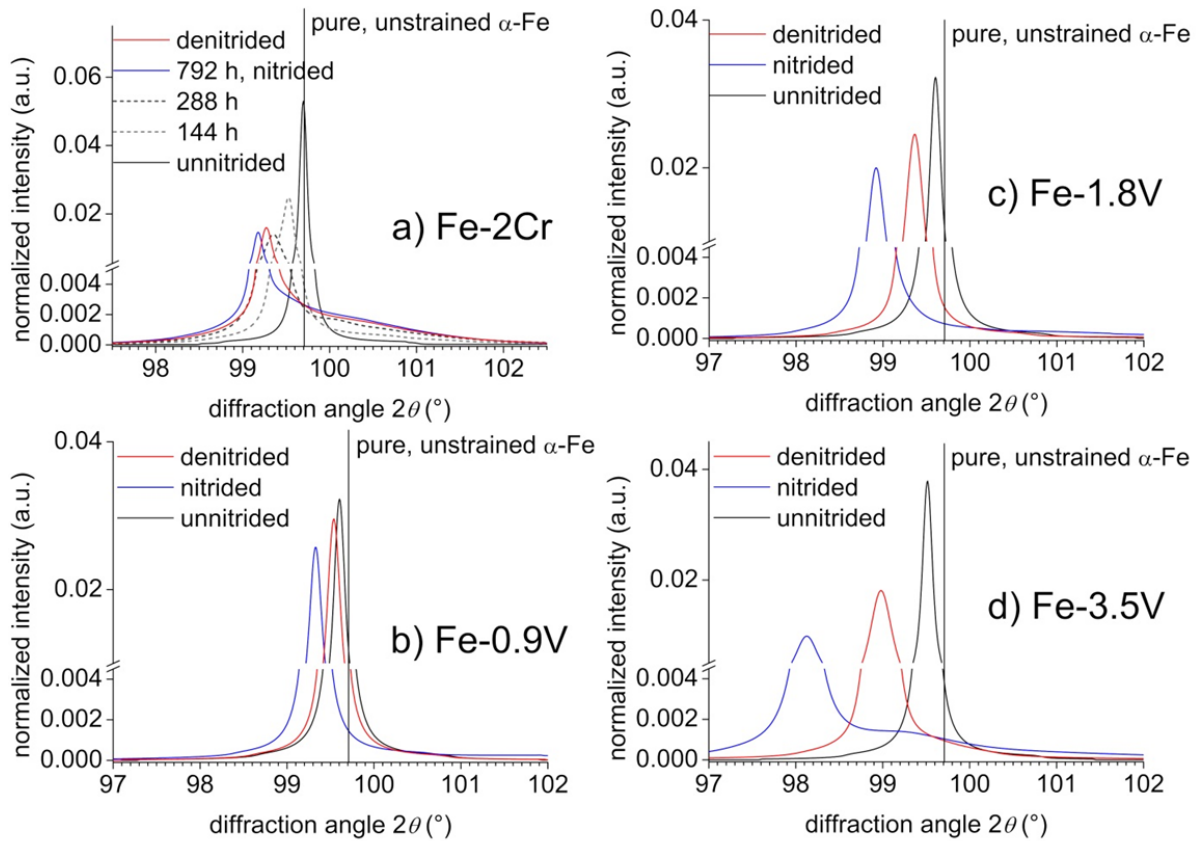


Fig. 2.2: Evolution of the ferrite 211 reflection of thin-foil Fe-Cr alloy (thickness 85 μm) specimens (a) and Fe-V alloy powder specimens (b) – d)) upon nitriding and denitriding. The shown profiles result after subtracting from the measured profile the $K_{\alpha 2}$ component as well as removing the instrumental profile as described in section 3.3.4. a) Fe-2.0 at.%Cr thin foil with a thickness of approx. 85 μm nitrided at 450 $^{\circ}\text{C}$ with a nitriding potential of 0.1 $\text{atm}^{-1/2}$ in steps of 72 h to a total of 792 h (only some of the intermediate nitriding steps are shown here). The result after a denitriding treatment in flowing H_2 atmosphere at 400 $^{\circ}\text{C}$ for 16 h is shown as well. b-d) Fe-V powders of indicated compositions, nitrided for 4 h at 500 $^{\circ}\text{C}$ with a nitriding potential of 0.1 $\text{atm}^{-1/2}$. The results after a denitriding treatment at 400 $^{\circ}\text{C}$ for 16 h in flowing H_2 atmosphere are shown as well. The profiles reveal the shifts of the diffraction-line profile towards lower diffraction angle upon (prolonged) nitriding and a partial shift back upon denitriding.

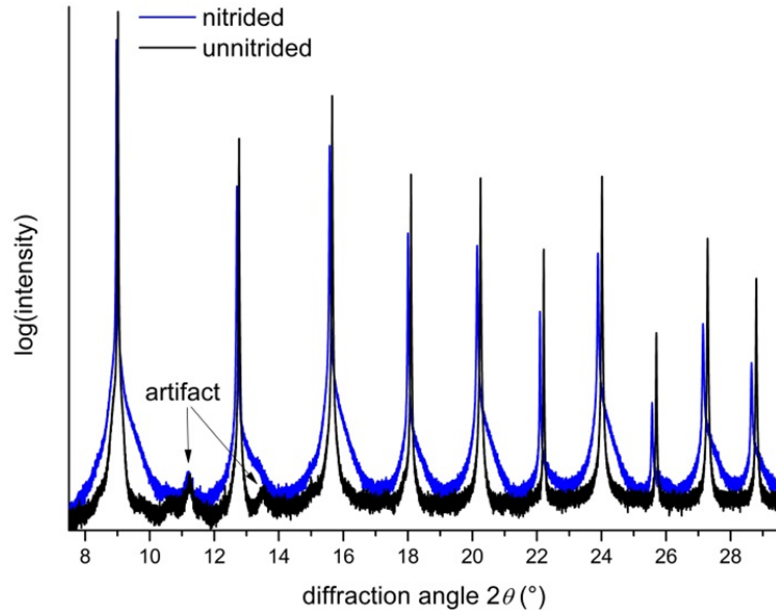


Fig. 2.3: Diffractograms (synchrotron diffraction, $\lambda=0.300715$ Å, c.f. section 3.3.3) of Fe-1.8 at.%V powder specimens before nitriding and after nitriding at 500 °C for 4 h with a nitriding potential of $0.1 \text{ atm}^{-1/2}$. Upon nitriding a distinct shift of the diffraction-line profiles towards lower diffraction angles and the development of an intensity tail towards higher diffraction angles occur. The small reflections at approx. 11 and 13.5 ° 2θ are artifacts due to irregularities in the instrumental background.

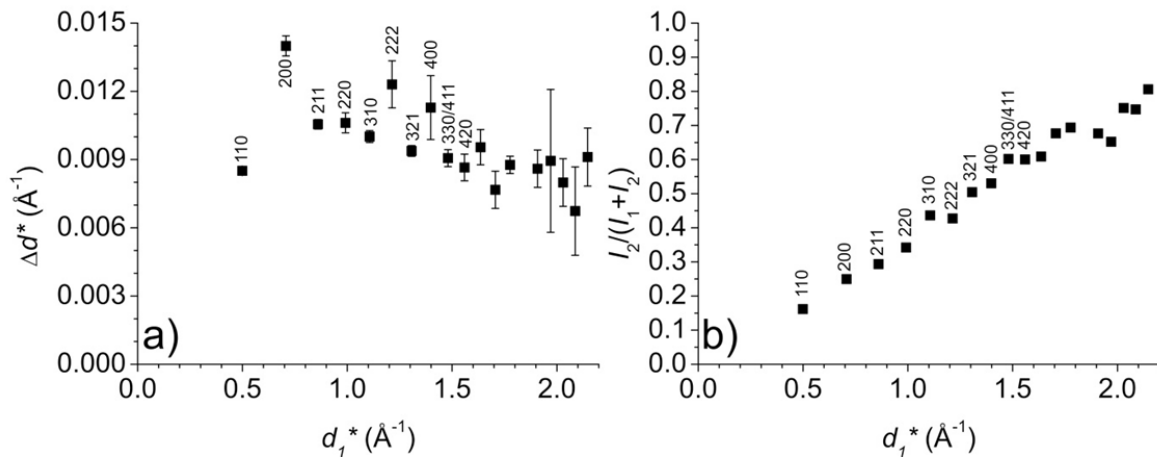


Fig. 2.4: Evaluation of the synchrotron diffraction data of nitrided Fe-1.8 at.%V powder specimens (cf. Fig. 2.3). a) The distance in reciprocal space, Δd^* , between positions of the main reflection d_1^* and the intensity tail d_2^* , as a function of the length of the diffraction vector, d_1^* ; b) The relative intensity of the tail, $I_2/(I_1+I_2)$, as a function of the length of the diffraction vector, d_1^* .

If it would be assumed that main peak and intensity tail represent incoherent diffraction by two different phases, specific relationships for Δd^* vs. d_1^* are expected. For example, if two different bcc (as ferrite) phases would be present, the dependence of Δd^* on d_1^* would be linear: a straight line of positive slope passing through the origin in Fig. 2.4a. Clearly, this is not the case. The surroundings of the nitride platelet are affected by a strain field of tetragonal symmetry and it has been suggested that this tetragonally distorted ferrite could diffract independently from the undistorted ferrite [19]. However, also in this case, Δd^* would show an overall increase with d_1^* , which is not the case. Moreover, the relative intensity of the intensity tail $\left(\frac{I_2}{(I_1+I_2)}\right)$ would be more or less constant as function of d_1^* , if incoherent diffraction of two phases would occur, as the integrated intensity of a diffraction peak is proportional to the diffracting volume. Such constancy is not observed (Fig. 2.4b). It has been suggested in Ref. [57] (see also Ref. [79]) that strong strain fields surrounding defects (e.g. misfitting precipitates) in crystals can lead to scattered intensity adjacent to the main peaks (c.f. Ref. [78]), which can be well compatible with the present experimental results. It is concluded, that the reflection lines comprised of “main peak” and “intensity tail” represent diffraction by a single, distorted phase.

2.5 Discussion

At first sight, the shift of the main, ferrite-matrix reflection to lower diffraction angles upon nitriding might be ascribed to isotropic expansion of the lattice. Substitutional solute (Cr, V) depletion of the matrix, by nitride precipitation, leads to a minor lattice-parameter *decrease* ($-0.0005 \frac{\text{\AA}}{\text{at.\%}}$ for Cr in ferrite and $-0.001 \frac{\text{\AA}}{\text{at.\%}}$ for V in ferrite in the compositional range for the alloys employed in this study [44]), as compared to the observed major lattice-parameter *increase* (e.g. approx. $+0.0109 \text{\AA}$ for fully N-saturated Fe-2.0 at.%Cr alloy, cf. Table 2.3). Interstitial dissolution of nitrogen leads to lattice-parameter increase ($+0.0079 \frac{\text{\AA}}{\text{at.\%}}$ for dissolution of N in pure ferrite [98], [99]). However, the amount of dissolved nitrogen (N not precipitated in the form of CrN or VN) is much too small to explain the observed effect (cf. Table 2.3). Moreover, after removing all dissolved N by a denitriding treatment, the ferrite lattice remains in expanded state (cf. Fig. 2.2). It will be argued below, qualitatively and quantitatively, that the observed lattice-parameter increases, as compared to the condition before nitriding, can be ascribed to the elastic accommodation of the precipitate/matrix misfit based on the model described in section 2.2.

Previous TEM, HRTEM and XRD analyses of nitrated Fe-Cr and Fe-V alloys have shown that the tiny CrN and VN platelets in the nitrated alloys are largely coherent with the surrounding finite matrix [19], [20], [23], [42], [77]: a largely elastic accommodation of the precipitates/matrix mis-

fit is likely. Then, depending on whether coherent *diffraction* of the precipitates with the matrix occurs or not, the lattice-parameter change should be compared with the theoretical prediction according to either Eq. (2.8) (for coherent diffraction of the precipitates with the matrix) or Eq. (2.3) (for incoherent diffraction of the precipitates and the matrix); see section 2.2.4.

In order to realize a quantitative comparison of predicted and measured lattice-parameter change, the amount of precipitate and the amount of dissolved nitrogen should be known for each specimen. These values were determined by the following procedure utilizing denitriding experiments.

It has been demonstrated by previous nitriding/denitriding experiments on Fe-Cr [26] and Fe-V [93] alloys that the developing nitrides form with a stoichiometry of N to *Me* of 1:1, i.e. as CrN and VN nitrides. The atomic fraction of N in the homogeneously nitrated and subsequently denitrated specimen, as determined by weighting before nitriding and after subsequent ing, x_N , corresponds to the fraction of alloying element *Me* precipitated as nitride *MeN*, x_{MeN} (i.e. $x_{MeN} = x_N$). The volume fraction of nitride precipitates, y_{MeN} , can then be determined from x_{MeN} according to:

$$y_{MeN} = \frac{x_{MeN}v_{MeN}}{x_{MeN}v_{MeN} + (1 - x_{MeN})v_{\alpha}} \quad (2.10)$$

where v_{MeN} and v_{α} are the molar volumes of *MeN* and α -Fe (which can be calculated from the corresponding lattice-parameter data [97], [100]). The thus calculated volume fractions of nitride precipitates and the deduced amounts of dissolved nitrogen after nitriding for the nitrated Fe-Cr and Fe-V specimens have been gathered in Table 2.3 and Table 2.4, respectively.

The amounts of dissolved nitrogen in both alloys for the fully nitrated (saturated) specimens are much larger than the equilibrium amount of nitrogen dissolved in pure unstrained ferrite (compare values indicated in Table 2.3 for Fe-Cr thin-foils and in Table 2.4 for Fe-V specimens with N contents obtained from the N-absorption function for pure ferrite (α -Fe) given in [7]: 0.033 at.%N at 450 °C with $r_N=0.1 \text{ atm}^{-1/2}$ and 0.075 at.%N at 500°C with $r_N=0.1 \text{ atm}^{-1/2}$). This occurrence of “excess nitrogen” is well known and can be ascribed to the (additional) uptake of nitrogen by adsorption of nitrogen at the precipitate-platelet faces and increased ferrite-lattice dilatation due to the hydrostatic stress component of the stress-field induced by the precipitate/matrix misfit [10], [26], [93], [101].

Table 2.3: N contents, volume fraction of nitride precipitates and strain-free lattice-parameters determined for Fe-Cr thin foils from nitriding and nitriding plus subsequent denitriding experiments. All thin foils contain 2 at.% Cr except the data presented in the last row which pertain to a specimen containing 4.5 at.%Cr. The volume fraction of CrN nitride was calculated using the N content after denitriding (denitriding was performed at 400°C for selected specimens). Data in the last three rows correspond to the complete precipitation of Cr as CrN. The amount of dissolved N shown in column 5 is the difference in the nitrogen content of the nitrided and denitrided specimens. The error in the lattice parameter values (columns 7 and 8) obtained after fitting the measured diffractograms is $\pm 0.0003 \text{ \AA}$.

nitriding temperature [°C]	nitriding time [h]	N content after nitriding [at.%]	N content after denitriding [at.%]	dissolved N [at.%]	volume of CrN precipitates y_{CrN} [vol.%]	a_α after nitriding [Å]	a_α after denitriding [Å]
450	0	0	0		0	2.8664	
450	72	0.330 [†]				2.8688	
450	144	0.696 [†]				2.8701	
450	216	1.092 [†]	0.798 [†]	0.294		2.8724	2.8699
450	288	1.361 [†]				2.8736	
450	360	1.615 [†]				2.8752	
450	432	1.738 [†]				2.8761	
450	504	1.777 [†]				2.8765	
450	576	1.844 [†]				2.8767	
450	648	1.899 [†]				2.8769	
450	720	1.925 [†]				2.8772	
450	792	1.949 [†]	1.691 [†]	0.258	2.366	2.8773	2.8752
500	16	2.260 [†]	1.900 [†]	0.360	2.821	2.8818	2.8767
500	2.25	4.620 [‡]	4.2 [‡]	0.42	6.022	2.8967	2.8891

[†] N-content determined by weight uptake of the specimen after treatment, [‡] N-content determined by EPMA

Table 2.4: N contents and lattice parameters determined for Fe-V powders from nitriding and nitriding plus subsequent denitriding experiments. The volume fraction of VN nitride was calculated using the N-content after denitriding, which is taken to correspond to the nominal V-content (in at.%) of the unnitrided alloy determined by chemical analysis. All V (of the respective alloy) is completely precipitated as VN in the specimens. The error in the lattice parameter values (columns 6 and 7) obtained after fitting the measured diffractograms is $\pm 0.0003 \text{ \AA}$.

alloy	nitriding temperature [°C]	N content after nitriding [at.%]	N content after denitriding (nominal V-content) [at.%]	volume of VN precipitates V_{VN} [vol.%]	a_α after nitriding [Å]	a_α after denitriding [Å]
Fe-0.9 at.%V	500	1.196	0.9	1.349	2.8744	2.8699
Fe-1.8 at.%V	500	2.539	1.8	2.686	2.8830	2.8736
Fe-3.4 at.%V	500	4.864	3.4	5.178	2.9004	2.8816

Now, for the denitrided specimens (systems of MeN precipitates in a pure ferrite matrix) the difference of their lattice parameter and that of a single-phase pure ferrite specimen (2.8664 \AA [97]) has been plotted in Fig. 2.5a, b as function of the amount of MeN precipitates for both alloys. In the same figures the predictions for this lattice-parameter difference according to Eq. (2.3) (precipitates diffract separately) and Eq. (2.8) (precipitates diffract coherently with the matrix) have been indicated as well (values for materials constants used in Eqs. (2.3) and (2.8) have been gathered in Table 2.5). Evidently, the predicted lines for expansion of the whole assembly, precipitate plus matrix (i.e. Eq. (2.8)) agree very well with the experimental data for both alloy systems in the denitrided state. The lattice-parameter shifts predicted for separate diffraction by precipitates and matrix are distinctly smaller than the experimental data for the denitrided state.

Table 2.5: Values of constants used in the model calculations of lattice dilatation

	Fe	CrN	VN
a_0 [Å]	2.8664 [97]	4.1400 [97]	4.1392 [97]
K [GPa]	166 [102]	360 [103]	300 [104]
μ [GPa]	82 [102]	(unnecessary)	(unnecessary)

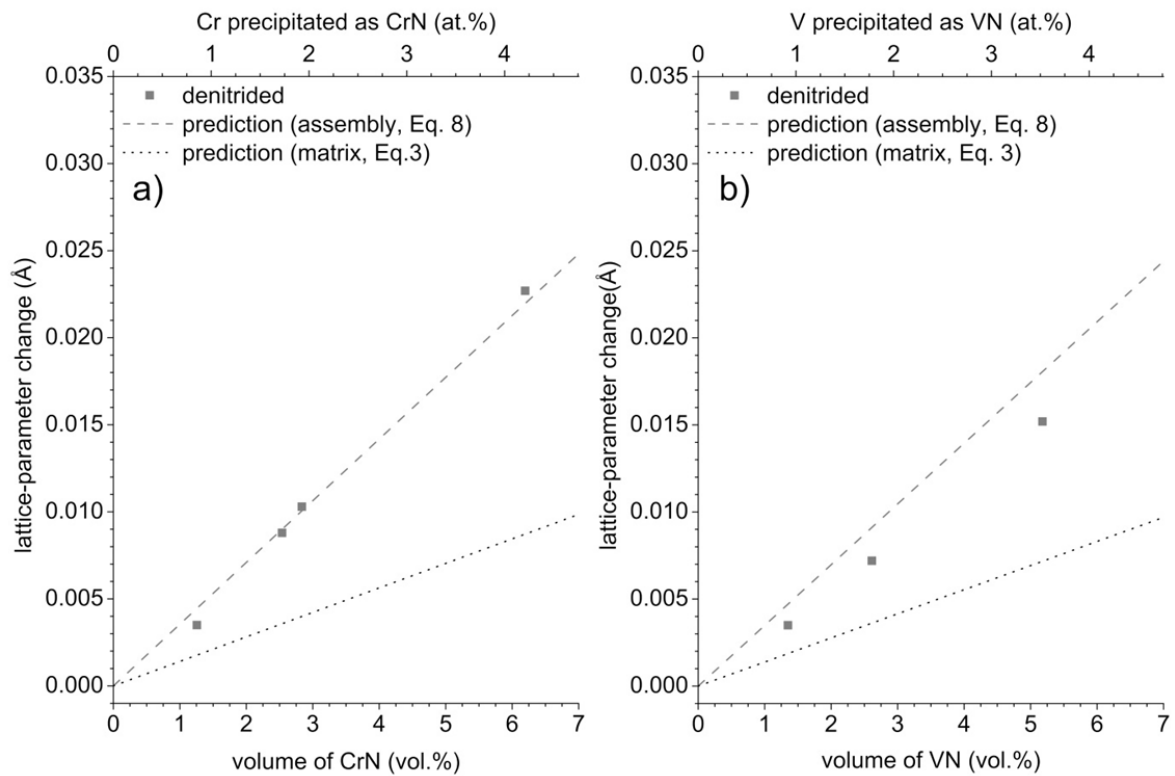


Fig. 2.5: Comparison of model predicted and experimental data for the difference of the lattice parameter of denitrided a) Fe-Cr and b) Fe-V specimens and the lattice parameter of pure, single-phase ferrite as function of the amount of precipitated nitride phase. Model predictions for the lattice expansion corresponding to coherent diffraction of the whole assembly (nitride precipitates and ferrite matrix), i.e. Eq. (2.8), and corresponding to separate (incoherent) diffraction (of nitride precipitates and ferrite matrix), i.e. Eq. (2.3), have been indicated by the dashed lines.

Considering the simplicity of the applied model (section 2.2) and because of the uncertainty about the values of the elastic constants used in the model (the elastic constants for nitrides of nanoscopic size need not be equal to those of bulk material), the good agreement between the experimental lattice dilatation for the denitrided specimens and the model prediction according to Eq. (2.8) is remarkable: the model not only well accounts for the difference in alloy systems (different extent of precipitate/matrix misfit and different elastic properties of the precipitates (cf. Table 2.5)) but also well describes the dependency on the amount (volume fraction) of precipitates.

The minor discrepancy between measured and model-predicted lattice parameters for the Fe-V powders can be attributed to (i) the small amount of V being oxidized owing to the large surface-area per unit volume of the Fe-V powders as compared to the Fe-Cr foils (see also Ref. [38]) and/or (ii) a possible relaxation of part of the elastically accommodated misfit during coarsening of VN particles upon denitriding; the chemical driving force available for the precipitation of VN is larger than for CrN [8], which results in a relatively much smaller size of the VN particles, which consequently implies a larger driving force for the coarsening of the VN particles as compared to the CrN particles.

This result is the first time demonstrating that coherent diffraction of the precipitates with the matrix is associated with a distinct lattice-parameter shift of the *assembly* compatible with elasticity theory. The only case known to us of observed lattice-parameter shift in agreement with prediction on the basis of elastic accommodation of precipitates/matrix misfit pertains to precipitates and matrix diffracting independently (i.e. Eq. (2.3) instead of Eq. (2.8) holds): a system of Si precipitates in an Al matrix [83].

In the investigation of Ref. [83] the volume misfit of Si precipitates and Al matrix, with ε_V as linear misfit parameter, was completely relaxed after the completion of precipitation at elevated temperature (in flagrant contrast with the present system). Then cooling of the specimens from annealing temperature T_A to room temperature T_{RT} resulted in a thermal misfit with linear misfit parameter $\varepsilon_T = \Delta\alpha \times (T_A - T_{RT})$ due to the difference in thermal expansion coefficients of matrix and second-phase particles, $\Delta\alpha$. This thermal-misfit effect gave rise to the change of lattice parameter of the Al matrix, measured and predicted (according to Eq. (2.3)) in Ref. [83]. Such thermal misfit is in principle also present in the current system of second-phase nitride particles in the ferrite matrix (for which Eq. (2.8) applies), but the magnitude of thermal misfit ε_T is negligible as compared to the volume misfit ε_V due to the precipitate formation: for nitrided Fe-Cr alloys, $\varepsilon_V = 0.1464$ and $\varepsilon_T = 0.0044$ for cooling from 400 °C to 25 °C, for nitrided Fe-V alloys, $\varepsilon_V = 0.1461$ and $\varepsilon_T = 0.0022$ for cooling from 400 °C to 25 °C, (employing thermal expansion coefficients from [105], [106])).

As a last note, it is remarked that for both cases (i.e. applicability of either Eq. (2.3) or Eq. (2.8)) it is essential to apply elasticity theory for a finite matrix; predictions for an infinitely large matrix do not apply at all.

2.6 Conclusions

1. *Coherent diffraction* by an assembly composed of precipitates and matrix leads, for the case of elastic accommodation of the precipitate-matrix misfit, to lattice-parameter changes, which can be well predicted adopting a theory originally developed by Eshelby for point imperfections for the case of *finite* size of the assembly.
2. The, according to the above, theoretically predicted dependences of lattice-parameter change on both degree of misfit and amount of precipitates, well agree with the experimental observations for nitrated Fe-Cr and Fe-V alloys, which exhibit a microstructure consisting of tiny, coherent nitride platelets in a severely distorted ferritic matrix.
3. The reflections recorded from the nitrated Fe-Cr and Fe-V alloys exhibit intensity tails at the high diffraction-angle side, which represent the highly tetragonally distorted regions surrounding the precipitates; the specimens diffract as a single phase.

Acknowledgements

We thank Mr. P. Kress for assistance with the nitriding experiments and Mrs. S. Haug for assistance with the EPMA experiments (both with the Max Planck Institute for Intelligent Systems). We also thank the European Synchrotron Radiation Facility (ESRF) for provision of synchrotron radiation facilities and Dr. Caroline Curfs (ESRF) and Dr. Silke Kurz (Max Planck Institute for Intelligent Systems) for assistance during use of beamline ID31.

Chapter 3

Misfit induced changes of lattice parameters in two-phase systems: coherent/incoherent precipitates in a matrix

Maryam Akhlaghi, Tobias Steiner, Sai Ramudu Meka and Eric Jan Mittemeijer

Abstract

Elastic accommodation of precipitation induced or thermally induced misfit leads to lattice-parameter changes in crystalline multi-phase systems. Formulae for calculation of such misfit induced lattice-parameter changes are presented for the aggregate (matrix + second phase particles) and for the individual matrix and second phase, recognizing the occurrence of either coherent or incoherent diffraction by matrix and second phase particles. An overview and an (re)interpretation on the above basis is presented of published lattice-parameter data, obtained by X-ray diffraction analyses of aggregates of matrix plus second phase particles. Examples for three types of systems consisting of a matrix with misfitting second phase particles are dealt with, which differ in the origin of misfit (precipitation or thermally induced) and in the type of diffraction (coherent or incoherent diffraction of matrix plus second phase particles). The experimental data are shown to be in good to very good agreement with predictions according to the current treatment.

3.1 Introduction; micro-and macrostrains; coherent and incoherent diffraction

The complex interplay of the chemical Gibbs energy change driving solid state phase-transformations and the deformation energy associated with the elastic/plastic accommodation of the misfit of parent and product phases, hinders the prediction of the course and the kinetics of phase transformations [59], [73], [107]. Accordingly, unusual, non-equilibrium phenomena can occur: occurrence of metastable phases, non-monotonous variation of transformation rate, and unusual morphologies [33], [34], [69]–[72], [108]. Therefore, it is essential to acquire fundamental understanding of the effects of developing misfit-strain energies on the thermodynamics and kinetics of phase transformations. Only thus the resulting microstructure and properties of engineering components can be optimized [74], [109], [110]. Thus the evolution of shape changes during precipitate growth in an elastically anisotropic, infinite matrix has been investigated for different two-phase systems (e.g. nickel-base alloys [111]–[114] and piezoelectric-piezomagnetic composites [115]).

The elastic strain field in the matrix surrounding very small (of the order 1 nm) misfitting particles/point defects can be investigated by high resolution transmission electron microscopy and by X-ray diffraction and diffuse scattering (static Debye-Waller factor [57]). Larger sized misfitting particles can be associated with more extended misfit-strain fields, which evoke contrast in diffraction-contrast images recorded by transmission electron microscopy [77] and broadening of diffraction lines ([58], [116], see in particular chapter 4 of [56]).

Application of continuum, elasticity theory to describe the elastic accommodation of the misfit of the (parent) matrix and the (product) second-phase particles [80], [86], [87] allows calculation of microstrains, say variance of the local strain $\langle \epsilon^2 \rangle$ [58], [116], [117], and of the average (hydrostatic) macrostrain $\langle \epsilon \rangle$ [84]. The microstrain expresses itself by (extensive) diffraction-line broadening. The hydrostatic macroscopic strain causes (distinct) change of the (average) lattice constant of a phase. Countless observations of diffraction-line broadening due to microstrain have been reported; in fact analysis of diffraction-line broadening has become a standard method of microstructural characterization [56]. However, only a few experimental works have been devoted to change of the (average) macroscopic lattice parameter by misfit strain [83], [118]–[124]. Against the above background, this manuscript presents a review of misfit induced (average, macroscopic) lattice-parameter changes, as predicted and as observed. In this context in particular the distinction of cases of coherent and incoherent diffraction by second-phase/matrix assemblies is emphasized.

The coherent or incoherent nature of the diffraction by a second phase (as precipitate particles) with the diffraction by the matrix needs not coincide with the occurrence of a coherent or incoherent nature of the interfaces between the second phase particles and the matrix: The coherency of diffraction depends not only on the specimen microstructure, but also on the diffraction conditions, as the length of the diffraction vector [58], [125]. Coherency/incoherency of diffraction depends on whether or not constructive interference of waves scattered by separate parts of the diffracting material (matrix and second phase) occurs. For a detailed discussion on the origin of coherent and incoherent diffraction of a second phase particle and the matrix the reader is referred to Ref. [58]; see also Ref. [59]. The effect of lattice-parameter variation/ the distribution of lattice spacings in a diffracting material on the occurrence of coherent or incoherent diffraction (and intermediates thereof) is considered most generally in Ref. [126].

Provided matrix and second phase particles diffract independently, i.e. incoherent diffraction of matrix and of second phase particles occurs, the changes of the lattice parameters of the matrix and of the second phase particles can be determined from measurements of the positions of the (separate) X-ray diffraction peaks of the matrix and of the second phase. If a coherent na-

ture of the second phase particles/matrix interfaces prevails, then, depending on the length of the diffraction vector and the extent of misfit-strain variation, coherent diffraction by second phase particles and matrix can occur.

3.2 Lattice-parameter changes due to elastically accommodated misfit

The continuum theory for the fully elastic accommodation of the misfit of a point imperfection in a matrix has been developed originally by Eshelby [86], [87]. This theory is more likely applicable to the case of precipitation of misfitting entities of larger dimensions, as second phase particles (i.e. a block of atoms), which are more likely to exhibit elastic characteristics as for bulk materials. The formulae presented below describe the changes of the relative volume/lattice parameters of the matrix, of the misfitting particles and of the assembly, i.e. matrix plus misfitting particles (for more information see Chapter 2):

3.2.1 Change of the lattice parameter of the matrix

For the case of an isotropic, cubic *finite* matrix A with a (strain-free) lattice parameter a_A , the change of lattice parameter, Δa_A , of the *finite* matrix due to the introduction of misfitting isotropic inclusions B can be written as [45], [83]:

$$\Delta a_A = \frac{4\mu_A C_6}{3K_A} \frac{\varepsilon}{(1 + \varepsilon)^3} y_B a_A \quad (3.1)$$

with

$$C_6 = \frac{3K_B}{3K_B + 4\mu_A} \quad (3.2)$$

where ε represents the linear misfit parameter (see below) and K and μ represent the bulk modulus and the shear modulus, respectively and y_B is the volume fraction of inclusions. It is essential to recognize that the matrix is of finite dimensions (see Chapter 2).

3.2.2 Change of the lattice parameter of the misfitting phase

For the case of isotropic second phase particles of cubic crystal structure with a (strain-free) lattice parameter a_B , the change of the lattice parameter, Δa_B , of the misfitting second phase in a finite matrix is [85]:

$$\Delta a_B = \left[-\varepsilon(1 - C_6) + \frac{4\mu_A C_6}{3K_B} \frac{\varepsilon}{(1 + \varepsilon)^3} y_B \right] a_B \quad (3.3)$$

3.2.3 Change of the lattice parameter of the assembly (matrix plus misfitting phase)

For a finite aggregate of cubic crystal structure and a (strain-free) lattice parameter of the matrix, a , the resulting change of the lattice parameter, Δa , of the aggregate for a volume fraction y_B of inclusions B is given by [45]:

$$\Delta a = \frac{C_6}{C'_6} \frac{\varepsilon}{(1 + \varepsilon)^3} y_B a \quad (3.4)$$

with

$$C'_6 = \frac{3K_A}{3K_A + 4\mu_A} \quad (3.5)$$

3.2.4 The misfit parameter

The linear misfit parameter appearing in the above equations can be given an explicit, analytical expression in the following cases:

i) Thermal misfit: This misfit originates from a change in the temperature of the two (or multi) phase composite (matrix + second phase particles) due to the difference in linear thermal expansion coefficients of matrix (α_A) and the second phase precipitate (α_B). This type of misfit can be described by the linear thermal misfit parameter, ε_T :

$$\varepsilon_T = (\alpha_A - \alpha_B)(T_h - T_r) \quad (3.6)$$

where T_h and T_r stand for elevated heat-treatment temperature and the considered, low (e.g. room) temperature, where measurements are made, respectively.

ii) Precipitation-induced misfit: This misfit originates from the different specific volumes of (solute and solvent) atoms in the second phase (precipitate) and the (solute and solvent) atoms in the matrix. This type of misfit can be described by the linear volume misfit parameter, ϵ_V :

$$\epsilon_V = \frac{\sqrt[3]{v_B^0} - \sqrt[3]{v_A^0}}{\sqrt[3]{v_A^0}} \quad (3.7)$$

where v_B^0 and v_A^0 are the volumes of the strain-free precipitate particle and the volume occupied by the atoms of the precipitate particle as previously incorporated in the matrix, respectively.

3.3 Observations and discussion

At elevated (aging/annealing) temperature (T_h), development of a misfitting, second phase can occur from a supersaturated matrix. The volume misfit (ϵ_V) of the two phases can initially be accommodated elastically under preservation of a coherent interface. Upon prolonged annealing, leading to an increasing size of the second phase particles, this misfit can no longer be accommodated fully elastically, and the interface can become semi or fully incoherent [72], [109], [127], [128].

Upon cooling from elevated temperature (T_h) to room temperature (T_r), irrespective of whether the precipitation-induced misfit at elevated temperature is accommodated elastically or plastically, thermal misfit arises which has to be accommodated either elastically [83] or plastically [129]. In many cases, upon fast cooling of the specimens, the thermal misfit accommodation occurs mainly elastically (even if an incoherent matrix/second phase particle occurs) and it can remain in that state for long time due to very slow rates of plastic relaxation processes at low (room) temperature.

As long as the (transformation or thermal) misfit is accommodated elastically, its effect on the expansion/contraction of the system consisting of matrix and misfitting second phase particle can be quantified considering the model description presented in section 3.2. Thus, in the following three types of systems consisting of a matrix with misfitting second phase particles are dealt with (see Table 3.1), which differ in the origin of misfit (transformation induced or thermally induced) and the in type of diffraction (coherent or incoherent diffraction of matrix plus second phase particles). For different systems described in the following, the values of the constants and misfit parameters used for the calculation of lattice parameter changes of the matrix

(Eq. (3.1)), the precipitate (Eq. (3.3)) and the assembly (Eq. (3.4)) are presented in Table 3.2 and Table 3.3, respectively.

Table 3.1: Types of systems consisting of a matrix with misfitting second phase particles, categorized on the basis of the type of elastically accommodated misfit (column 2) and of the type of precipitate/matrix diffraction (column 3; cf. section 3.1). Equations to be used for the calculation of lattice-parameter changes of the assembly (Eq. (3.4)), the matrix (Eq. (3.1)) and the second phase particle (Eq. (3.3)) (column 4) and system examples (column 5).

type of system	type of elastically accommodated misfit	type of precipitate/matrix diffraction	lattice-parameter change	case studies
1	transformation misfit	coherent	Eq. (3.4)	nitrided Fe-Me alloys (Chapter 2) Co clusters in decomposed Cu-Co alloy [130]
2	transformation misfit	incoherent	Eqs. (3.1) and (3.3)	aged (at RT) Fe-N alloy [118], [131], [132]
3	thermal misfit	incoherent	Eqs. (3.1) and (3.3)	aged AlSi alloy [83]–[85], [116] nitrided and aged Fe-Cr alloys (Chapter 4)

Table 3.2: Values of the physical constants used in the model calculations of lattice-parameter changes.

	lattice-constants [\AA]	K [GPa]	μ [GPa]	$\alpha * 10^{-6}$ [K^{-1}]
Fe	2.8664 (bcc) [97]	166 [102]	82 [102]	12.1 [133]
CrN	4.1400 (NaCl) [97]	360 [103]	-	2.3 [106]
VN	4.1392 (NaCl) [97]	300 [104]	-	8.1 [106]
Cu	3.6150 (fcc) [97]	140 [134]	48 [133]	17 [133]
Co	3.5442 (fcc) [135]	140 [†] [134]	-	-
Fe ₁₆ N ₂	5.7200 (bct) 6.2900 [97]	166 [†] [102]	-	-
Al	4.0494 (fcc) [97]	75 [133]	26 [133]	23.5 [133]
Si	5.4309 (diamond) [97]	98 [136]		3 [137]

[†] The bulk modulus of fcc cobalt precipitates is assumed to be the same as that of the Cu matrix and the bulk modulus of the Fe₁₆N₂ precipitates is considered to be the same as that of the Fe matrix.

Table 3.3: Values of the misfit parameters used in the model calculations of lattice-parameter changes. Values of thermal misfits are italic; the other values refer to precipitation-induced misfit.

matrix inclusion	Fe	Cu	Al
CrN	0.1464 <i>0.004 ($\Delta T = 375\text{ }^\circ\text{C}$)</i>	-	-
VN	0.1461 <i>0.002 ($\Delta T = 375\text{ }^\circ\text{C}$)</i>	-	-
Co	-	-0.0173	-
Fe ₁₆ N ₂	0.0299	-	-
Si	-	-	<i>0.003 ($\Delta T = 127\text{ }^\circ\text{C}$)</i>

3.3.1 Coherent diffraction by the assembly matrix plus second phase particles; transformation misfit

Misfitting coherent alloying element nitrides in ferrite

Upon nitriding of ferritic Fe-Me (Me: Cr, V, Ti) alloys, tiny nitride precipitates (MeN) develop [19], [22], [25], [138]. At least initially these nitrides possess coherent interfaces with the matrix. Matrix/nitride-particle misfit in this system, as considered at room temperature, originates from i) the specific volume misfit induced by nitride precipitation from a supersaturated matrix as a consequence of elastic accommodation of the misfit while the precipitate/matrix interface remains coherent and ii) the thermal misfit induced by cooling after nitriding. The specific volume misfit between MeN precipitates and the ferrite matrix can be calculated from Eq. (3.7), where v_B^0 and v_A^0 can now be taken as molar volumes of MeN precipitates and matrix, respectively. After *complete* precipitation, the molar volume of MeN precipitate can be calculated from the volume of the precipitate unit-cell divided by the number of metals atoms occupying one unit cell of the precipitate and the molar volume of matrix (in this case, containing only Fe atoms) can be calculated from the volume of matrix unit-cell divided by the number of iron atoms occupying one unit cell of the matrix. In this case the thermal misfit (corresponding to the difference of the thermal expansion coefficients of the Fe-matrix and the developed nitrides) is negligible as compared to the precipitation induced misfit (i.e. $\varepsilon_V = 0.1464$ and $\varepsilon_T = 0.004$ for cooling from 400 °C to room temperature for nitrided Fe-Cr alloy and $\varepsilon_V = 0.1461$ and $\varepsilon_T = 0.002$ for cooling from 400 °C to 25 °C for nitrided Fe-V alloys [105], [106]).

This system is an example of *coherent* diffraction by the entity matrix plus precipitates in the presence of *coherent* interfaces between the Fe matrix (of bcc crystal structure) and the MeN overall expansion of the assembly (composed of MeN nitride precipitates and ferrite matrix), expressed in terms of the change in the lattice parameter deduced from the position of the “ferritic” peak maxima, can be calculated using Eq. (3.4), as a function of the volume fraction of alloying element nitrides. Experimental values for such changes of lattice parameter upon nitriding, of Fe-Cr and Fe-V alloys, were obtained by employing X-ray diffraction on homogeneously nitrided (thus macroscopically strain-free) Fe-Me specimens (see Chapter 2²). The volume fraction of (CrN and VN) nitride precipitates was determined (by weight-change measurements) from the N content of denitrided thin foils (i.e. after removing from the specimen, by denitriding, the dissolved (excess) N and the excess N adsorbed at the nitride-platelet faces during nitriding [10], [101]). The volume fraction of precipitates was varied by varying the nitriding time (for times larger than the minimal time to achieve a homogeneously nitrided specimen) and/or varying the amount of Me (Cr,V) in the alloy (realizing full precipitation throughout the specimen). Results are shown in Fig. 3.1 (the single dots). The predictions on the basis of Eq. (3.4) (solid lines in Fig. 3.1) are in good agreement with the experimental data. Evidently, in this case Eq. (3.1) (implying incoherent diffraction of matrix and precipitates; dashed lines in Fig. 3.1) does not at all correctly predict the ferritic (X-ray) lattice-parameter changes observed for the nitrided Fe-Cr and Fe-V alloys.

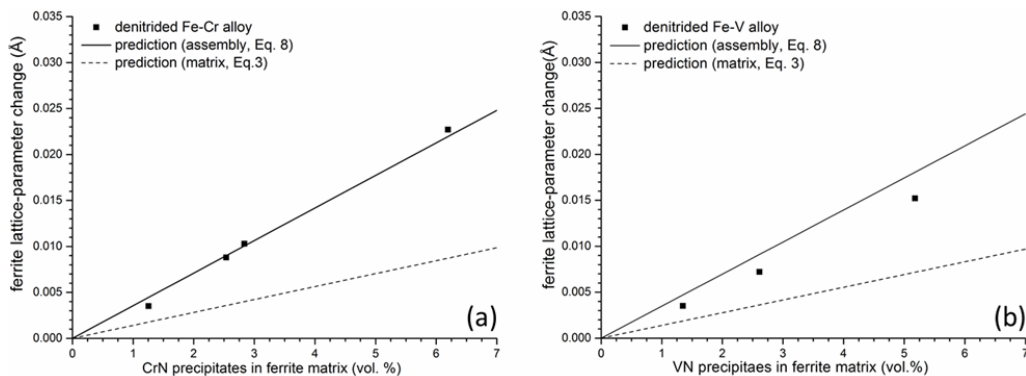


Fig. 3.1: Experimental “ferrite” lattice-parameter change (dots; data from Chapter 2) as a function of vol.% of (a) CrN precipitates and (b) VN precipitates and the predictions on the basis of Eq.(4) (solid line) and Eq. (3.1) (dashed line). The error in the experimental lattice parameter values obtained after fitting the measured diffractograms is $\pm 0.0003 \text{ \AA}$.

² Indeed no separate nitride reflections could be discerned; the strongly broadened ferritic peaks represent coherent diffraction by the distorted (by elastic misfit-strain accommodation) ferrite matrix and the nitride precipitates (for details see Chapter 2).

Misfitting coherent cobalt precipitates in copper

A thin film of a metastable Cu(Co) solid solution can be prepared by co-deposition of Cu and Co by magnetron sputtering up to a maximum of 12 at.% Co. For Co contents larger than 12 at.%, clusters/tiny precipitates of Co occur in the alloy [130], [139].

The X-ray diffraction patterns recorded from such Cu-Co alloy films of different Co concentrations show the occurrence of a single fcc Cu(Co) phase up to 65 at.% Co. Only beyond this Co-concentration, additional hcp (Co) reflections can be observed (see Fig. 5 in [130]). Evidently, the Co inclusion/particles present in the Cu-Co alloy films with more than 12 at.% Co and up to 65 at.% Co diffract coherently with the matrix.

The experimentally obtained lattice parameters of the fcc Cu(Co) films as a function of Co-concentration are shown as single dots in Fig. 3.2 for Co concentrations between 12-65 at.%. The predictions of the lattice-parameter values of the aggregate Cu matrix (Cu-12 at.% Co solid-solution) and second phase, Co particles as a function of the value percentage of Co precipitates in the Cu (12 at.% Co) matrix according to Eq. (3.4) (coherent diffraction of matrix and inclusions) and Eq. (3.1) (incoherent diffraction of matrix and inclusions) are shown in Fig. 3.2. Evidently, the experimentally determined lattice-parameter values and the predictions on the basis of Eq. (3.4) (solid black line in Fig. 3.2) are in very good agreement, implying occurrence of coherent diffraction of matrix and precipitates. In this case predictions according to Eq. (3.1) (incoherent diffraction of matrix and precipitates; (dashed line in Fig. 3.2)) are not at all in agreement with the experimental data. The prediction of the lattice parameter of fcc Cu(Co) can also be made on the basis of Vegard's law (linear interpolation between Cu and fcc Co lattice parameters as shown in Ref. [130]).

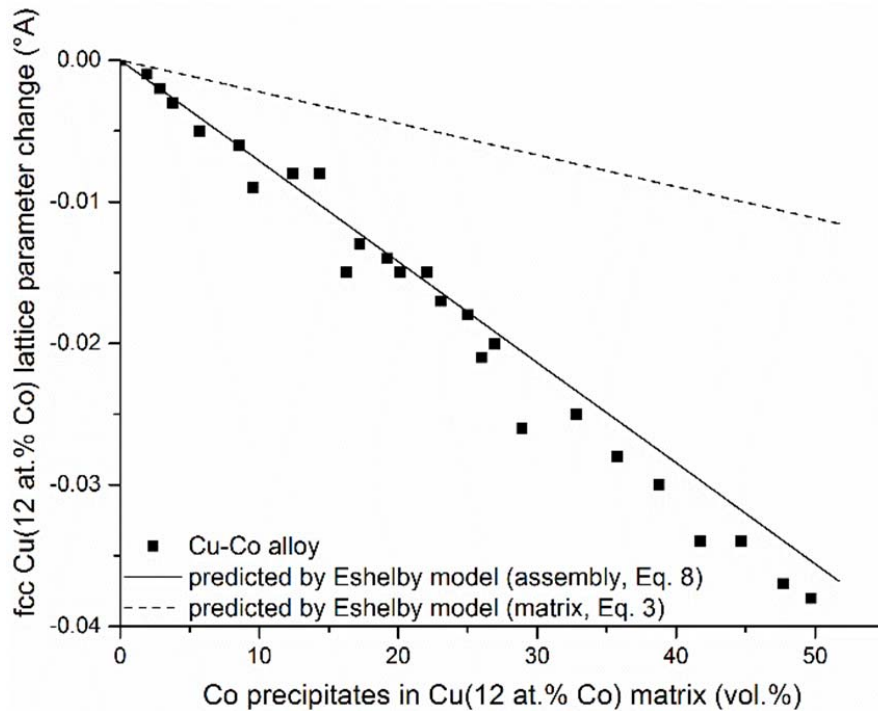


Fig. 3.2: Experimental Cu-12 at.% Co lattice-parameter change (dots; data from Ref. [130]) as a function of vol. % of Co precipitates in Cu(12 at.% Co) matrix and the predictions on the basis of Eq. (3.4) (solid line) and Eq. (3.1) (dashed line). For the application of Eq. (3.4), it is assumed that Co in the Cu matrix has precipitated as fcc Co particles.

3.3.2 Incoherent diffraction of the matrix and second phase particles; transformation misfit

Misfitting incoherent nitrides in ferrite

Upon nitriding of pure α -Fe (ferrite) in an atmosphere of a certain nitriding potential, N dissolves in the ferrite matrix. The formation of this solid solution leads to an increase of the lattice parameter of the ferrite matrix. By quenching after nitriding the solid solution can be retained. The system then is metastable. During aging of the α -Fe matrix supersaturated with dissolved N at room temperature, formation of α'' -Fe₁₆N₂ precipitates occurs in association with depletion of N from the ferrite matrix. Experimentally, a decrease of the ferrite lattice parameter is observed at room temperature during development of the α'' -Fe₁₆N₂ precipitates [98], [118], [131], [132]. Upon prolonged aging, after complete precipitation of α'' -Fe₁₆N₂, a constant lattice parameter value is established that is larger than the one expected for pure α -Fe (the equilibrium solubility of N in α -Fe at room temperature is practically nil) (see Fig. 4 in Ref. [131], Fig. 1 in Ref. [98] and Fig. 7 in Ref. [132]).

The values of the constant lattice parameter of the ferrite matrix at this stage of prolonged aging at room temperature, i.e. after all N has precipitated, as recorded from specimen containing different amounts of nitrogen, are shown as a function of the volume fraction of developed $\alpha''\text{-Fe}_{16}\text{N}_2$ precipitates in Fig. 3.3. Predictions for the change of the ferritic lattice parameter are also shown in Fig. 3.3: (i) for the case of incoherent diffraction of matrix and precipitates (Eq. (3.1); dotted line in Fig. 3.3) and (ii) for the case of coherent diffraction of the assembly matrix plus precipitates (Eq. (3.4); full line in Fig. 3.3). The experimental results very well agree with the predictions according to Eq. (3.1): Evidently, in this case of prolonged ageing, the $\alpha\text{-Fe}$ matrix and the $\alpha''\text{-Fe}_{16}\text{N}_2$ -nitrides precipitates diffract incoherently. The separate $\alpha''\text{-Fe}_{16}\text{N}_2$ reflections are very weak³, because of the small amounts of N (and thus $\alpha''\text{-Fe}_{16}\text{N}_2$) in the specimens and cannot be observed by conventional laboratory XRD (as is the case here; synchrotron radiation would be required as shown in Ref. [140]).

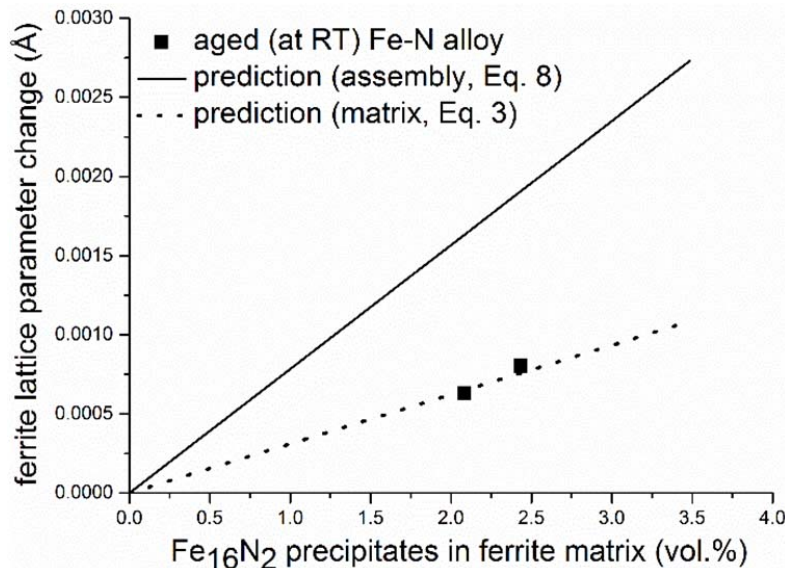


Fig. 3.3: Experimental Fe-matrix lattice-parameter change (dots; data from Refs. [118], [132]) as a function of vol.% of $\alpha''\text{-Fe}_{16}\text{N}_2$ precipitates and the predictions on the basis of Eq. (3.4) (solid line) and Eq. (3.1) (dashed line).

As mentioned above, before complete precipitation of $\alpha''\text{-Fe}_{16}\text{N}_2$, i.e. in the intermediate stages of aging, the lattice parameter of ferrite decreases continuously as the ferrite-lattice contraction by the depletion of N, dissolved on the interstitial (octahedral) sites of the ferrite matrix, is large-

³ The $\alpha''\text{-Fe}_{16}\text{N}_2$ crystal structure can be conceived as a superstructure developing in nitrogen ferrite by ordering of N on the sublattice of octahedral interstices. The intensity of the $\alpha''\text{-Fe}_{16}\text{N}_2$ structure specific super structure reflection is governed by the weak scattering power of the nitrogen atoms.

er than the ferrite-lattice expansion due to the formation of misfitting α'' - Fe_{16}N_2 precipitates diffracting either coherently or incoherently with the matrix. Thus, *during* precipitation of α'' - Fe_{16}N_2 , a (possibly occurring) change of the diffraction conditions from coherent to incoherent will only lead to a change in magnitude of the resulting lattice-parameter decrease. Corresponding calculations for the change of the ferritic-lattice parameter as a function of the fraction transformed (i.e. the precipitated fraction of N), for a fixed N-content of the specimen, are shown in Fig. 3.4: (i) for the case considering both the effect of the depletion of dissolved N from the solid-solution (Eq. (1) in Ref. [98]) and incoherent diffraction of matrix and precipitate (Eq. (3.1); dashed line in Fig. 3.4), (ii) for the case considering both the effect of the depletion of dissolved N from the solid-solution (Eq. (1) in Ref. [98]) and coherent diffraction of assembly matrix plus precipitates (Eq. (3.4); full line in Fig. 3.4) and (iii) for the case considering only the effect of the depletion of dissolved N from the solid-solution (Eq. (1) in Ref. [98]; dotted line in Fig. 3.4). Evidently, ignorance of the effect of misfit strain on lattice-parameter changes, results in a strongly erroneous (too small) precipitated fraction of N as derived from the decrease of lattice parameter.

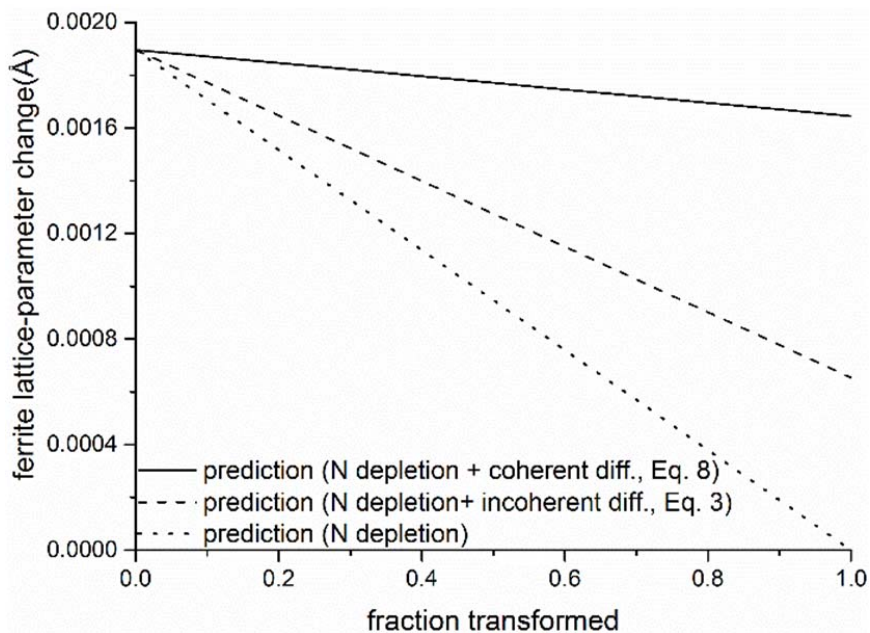


Fig. 3.4: Lattice-parameter change of the nitrated ferrite matrix upon precipitation of α'' - Fe_{16}N_2 as a function of the fraction N precipitated for a specimen of ferrite containing 0.24 at.% N. Calculations on the basis of Eq. (3.4) (solid line) and Eq. (3.1) (dashed line), with considering the effect of nitrogen depletion of the ferrite matrix. The change of the ferrite-lattice parameter due to only N depletion is also shown (dotted line; calculated using Eq. (1) in Ref. [98]).

3.3.3 Incoherent diffraction of the matrix and second phase particles; thermal misfit

Misfitting incoherent silicon in aluminium

During high temperature annealing/aging of an Al matrix supersaturated with dissolved Si, precipitation of incoherent Si occurs. Initially, lattice *expansion* of the Al matrix happens due to partially elastic accommodation of the precipitate/matrix misfit (cf. Eq. (3.1)) and depletion of Si from the solid solution (see Fig. 9 in Ref. [85]). This same process also results in lattice *contraction* for the Si precipitates (cf. Eq. (3.3); see Fig. 7 in Ref. [85]). Upon prolonged aging at high temperature, this precipitation induced misfit relaxes fully, i.e. is accommodated entirely plastically. Then a case of *incoherent* diffraction of matrix and precipitates in the presence of *incoherent* interfaces between the Al matrix (with fcc crystal structure) and the Si precipitates (with diamond cubic crystal structure) is established.

Now, upon rapid cooling of such a relaxed two phase (*pure* Al matrix + incoherent Si-particles) specimen to room temperature, thermal misfit develops, owing to the difference of the thermal expansion coefficients of Al matrix and Si precipitates; this misfit ($\varepsilon_T = 0.003$ for cooling from 152 °C to room temperature) is accommodated elastically. The changes of the lattice parameters of the matrix and the precipitates were measured as a function of the volume fraction of developed precipitates (Si), utilizing the separate diffraction peaks from matrix and precipitates as recorded from fast cooled (to suppress any relaxation of the thermal misfit during cooling) two phase specimens of different Si contents. The thus experimentally obtained lattice-parameter change for the Al-matrix is shown as a function of the volume fraction of Si precipitates in Fig. 3.5a (dots). The prediction (now) on the basis of Eq. (3.1) (dashed line in Fig. 3.5a) is in good agreement with the experimental data. Evidently, in this case Eq. (3.4) (implying coherent diffraction of matrix and precipitate; solid line in Fig. 3.5a) does not at all correctly predict the lattice-parameter change of the aluminum matrix. An only reasonable agreement occurs for the theoretical (Eq. (3.3)) and experimental values for the lattice-parameter change of the silicon precipitates (Fig. 3.5b); significant experimental errors are inherent to the determination of the minority-phase lattice parameter of the Si precipitates, in particular for the alloy of the lowest Si content of 2.8 (vol.%) (cf. Fig. 3.5b).

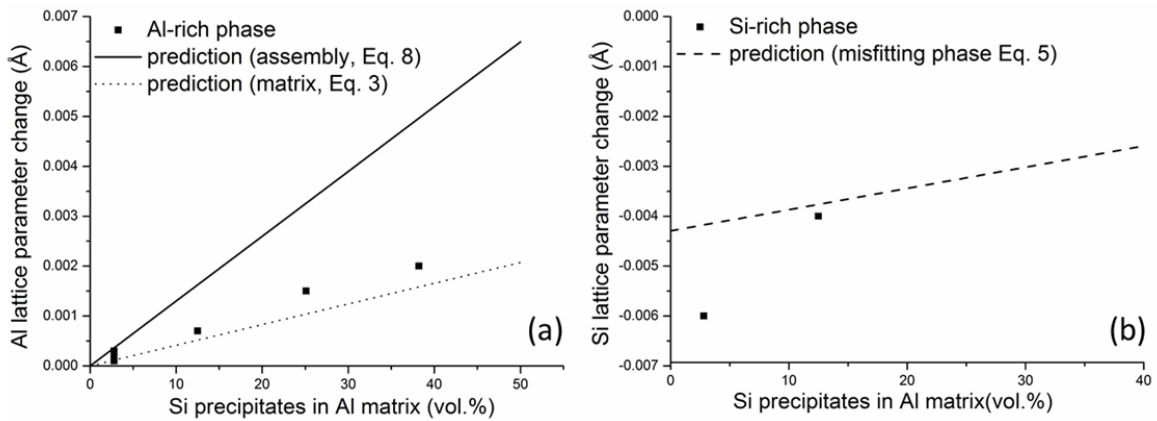


Fig. 3.5: (a) Experimental Al-matrix lattice-parameter change (dots; data from Table 1 (experiments were performed between 425-448 K) in Ref. [83]) as a function of vol.% of Si precipitates and the predictions on the basis of Eq. (3.4) (solid line) and Eq. (3.1) (dashed line) (b) Experimental Si-precipitate lattice-parameter change (dots; data from Table 1 (experiments were performed at 425 K) in Ref. [85]) as a function of vol.% of Si precipitates and the prediction on the basis of Eq. (3.3) (dashed line). The experimental lattice parameter values were determined with a precision of 1-2 parts in 40000.

Misfitting incoherent alloying element nitrides in ferrite

As described in section 3.3.1, upon nitriding Fe-Cr alloys misfitting CrN particles develop which initially have a coherent interface with the matrix leading to an overall lattice expansion as observed from the change of the “ferrite” lattice parameter (cf. Fig. 3.1). Upon aging (at the nitriding temperature), coarsening of the precipitates occurs (see Fig. 4.5) in association with the development of incoherent matrix/precipitate interfaces: plastic accommodation of the precipitation induced misfit. Consequently, the system in those conditions exhibits incoherent diffraction of matrix and precipitates (i.e. matrix and coarsened precipitates now diffract separately: indeed both matrix and precipitate reflections are detected (see Fig. 4.11).

Upon cooling of this relaxed two-phase composite (Fe matrix + incoherent CrN nitrides) to room temperature, thermal misfit develops, owing to the difference of the thermal expansion coefficients of Fe matrix and CrN nitrides; this misfit ($\varepsilon_T = 0.005$ for cooling from 500 °C to room temperature) gets accommodated elastically. The change of the lattice parameter of the *ferrite matrix* by elastic accommodation of this thermal misfit has been measured by X-ray diffraction and has been predicted on the basis of Eq. (3.1). A very good agreement occurs (Table 3.4). The change of the lattice parameter of the *precipitates* has also been measured by X-ray diffraction and has been predicted on the basis of Eq. (3.3). As predicted, the experimental change of the lattice parameter of the precipitates has a sign opposite to that of the matrix

(cf. Table 3.4). The quantitative agreement here is less good, which can be ascribed to uncertainty concerning the strain-free lattice parameter of CrN [97] and limited accuracy in the experimentally determination of the lattice parameter of the minority phase.

Table 3.4: Change of the Fe-matrix lattice parameter and that of the CrN-precipitates for a homogeneously nitrated (till saturation) Fe-4.5 at.% Cr specimen as measured after aging at 500 °C for 78 h, and as predicted on the basis of Eq. (3.1) and Eq. (3.3), respectively.

phase	Δa prediction [Å]	Δa experiment [Å]
α -Fe	+ 0.0005 (Eq. (3.1))	+ 0.0006 \pm 0.0003 (Chapter 4)
CrN	- 0.0045 (Eq. (3.3))	- 0.0020 \pm 0.0003 (Chapter 4)

3.4 Conclusions

Formulae have been presented for calculation of lattice-parameter changes induced in misfitting matrix/second phase-particles systems.

Diffraction analysis of such lattice-parameter changes requires distinction of (i) coherent diffraction by the matrix/second phase-particles aggregate and (ii) incoherent diffraction of matrix and second phase particles.

A number of examples presented for cases of precipitation induced specific volume misfit and cooling induced thermal misfit show good to very good agreement of theoretical predictions and experimental observations.

The discussed misfit induced lattice-parameter/volume-changes are often ignored in the diffraction (and also in the dilatometric) analysis of phase-transformation kinetics. The present treatment provides a direct route for correction of these effects.

Chapter 4

Diffraction-line shifts and broadenings in continuously and discontinuously coarsening precipitate-matrix systems; coarsening of initially coherent nitride precipitates in a ferrite matrix

Tobias Steiner, Maryam Akhlaghi, Sai Ramudu Meka, and Eric Jan Mittemeijer

Abstract

The initial precipitation of misfitting particles can be accompanied by elastic accommodation of the precipitate/matrix misfit leading to considerable matrix lattice dilatation/contraction and variable lattice microstrain. In this stage, the entire assembly of matrix and precipitate particles, as a whole, can diffract coherently. Upon aging of the system, relaxation of the accommodated misfit can occur by continuous and/or discontinuous coarsening of the precipitates. These processes are associated with distinctly different, characteristic diffraction phenomena, also involving a transition from coherent to incoherent diffraction of precipitates and matrix. For the case of, initially fully coherent, alloying element nitrides in a homogeneously nitrated ferrite matrix, these effects have been identified and analyzed, thus allowing tracing of misfit-relaxation processes.

4.1 Introduction

Diffraction processes are sensitive to the imperfections of the crystalline solid state and thus diffraction methods are applied extensively for the study of the microstructure of materials [56], [79], [141]–[143]. In particular, X-ray diffraction (XRD) has been employed to characterize the (micro-) structural changes in a material upon precipitation of second phases, e.g. Refs. [144]–[148].

The precipitation of finely distributed misfitting nitride platelets in a ferrite matrix leads to hydrostatic expansion of the ferrite-matrix lattice, see Chapter 2 and Ref. [10]. This lattice expansion was quantified with a model based on elastic accommodation of the misfit. The model was validated recently by comparison of its predictions for the lattice-parameter changes with the lattice-parameter changes as measured by XRD performed on homogeneously nitrated Fe-Cr and Fe-V alloys (Chapter 2).

The lattice-parameter change discussed in the above paragraph pertains to the mean, long-range strain in the precipitate-matrix system. In the vicinity of the precipitate/matrix inter-

faces pronounced, local misfit-strain variations can occur [149]: microstrains giving rise to specific diffraction-line-broadening effects [56].

It is important to distinguish the case i) of precipitate particles coherent with the matrix and the case ii) of precipitate particles incoherent with the matrix. In both cases, elastic misfit accommodation of the precipitate-matrix misfit is possible depending on the origin and magnitude of the misfit (e.g. intrinsic lattice misfit vs. extrinsic thermal misfit). This leads to the following consequences for the (X-ray) diffraction experiment: in the first case i), particles and matrix can diffract coherently, and in the second case ii) particles and matrix likely diffract incoherently (c.f. discussion in Ref. [58]).

The first described situation (case i)) pertains to the particle-matrix systems considered here: the tiny nitride particles developing in iron-based alloys upon nitriding are coherent with the matrix and can diffract coherently with the matrix. Therefore, the dilatations of matrix and precipitates contribute to the diffraction-line shifts (Chapter 2 and Ref. [58]). The microstructure of tiny, coherent precipitates in a matrix is usually referred to as *continuously precipitated* (CP) (see, e.g., Ref. [8], [24]), and the same term is used in the following to refer to the corresponding diffraction patterns.

The elastic expansion of the assembly as well as the large precipitate/matrix interfacial area associated with the nanosized platelets represent a state of elevated energy [127]. As is well known, coarsening of the microstructure, involving reduction of the interface area and loss of coherency, is a means of nature to reduce the energy of the system [59]. The enhancement of strain energy by growth of the precipitates is (partly) relaxed by the introduction of misfit dislocations, i.e. plastic misfit accommodation occurs [45], [109] (see also HR-TEM micrographs of the interfaces of aged nitrides in the Fe-V system in [19] and the formation of dislocation loops encircling the growing precipitate particles [72], [128]). As a result, remaining lattice strain is significant only in the immediate vicinity of the precipitate/matrix interface, i.e. the long-range strain has vanished. The above process of coarsening will be referred to as *continuous coarsening* (CC) as it occurs gradually throughout the entire microstructure.

Coarsening of the initial tiny, coherent precipitates in a matrix can also be realized by *discontinuous coarsening* (DC), i.e. a cellular transformation starting at a mobile interface/grain boundary, also involving relaxation of the precipitation-induced misfit strains [59], [150]–[152]. As a result, a lamellar microstructure develops composed of alternate lamellae of precipitate and matrix with an incoherent interface [19], [21], [24]. Next to (ongoing) continuous coarsening,

such discontinuous coarsening has been observed in a number of nitrided iron-based alloys: Fe-Cr [21]–[23], [25], Fe-V [18], Fe-Mo [31] and Fe-Cr-Mo⁴ (see Chapter 6).

For the study of diffraction effects corresponding with CC and DC, in this work nitrided Fe-Cr alloys were chosen as a model system for two reasons. Firstly, the finely distributed nitride precipitates present in the initial CP microstructure diffract coherently with the ferrite matrix, which leads to large peak shifts in XRD patterns. Secondly, upon aging (i.e. continued annealing at the nitriding temperature) Fe-Cr alloys with a Cr content below 2 at.% show only minimal DC, whereas alloys with higher Cr content fully transform according to DC [21]–[23], [25]. Thus, by varying the Cr-content, the diffraction consequences of CC and DC can be revealed and analyzed.

Nitriding processes usually result in a *heterogeneous* microstructure: a nitrided surface adjacent region (case) with the unnitrided matrix (core) underneath [8]. Consequently a state of residual stress, exhibiting strong and varying stress-depth gradients [153], prevails in the nitrided specimen. Residual stresses contribute to diffraction-line shift and broadening. This explains why diffraction-line shifts and broadenings due to CC and DC in the nitrided, surface-adjacent part of such specimens cannot be identified from XRD measurements performed on such specimens.

To remedy this problem, in the present study, *homogeneously* nitrided thin foils have been employed: no stress-depth and no composition-depth profiles occur in these specimens, so that diffraction-line shifts and broadenings due to CC and DC can be exposed separately for the first time.

4.2 Experimental procedures

4.2.1 Specimen preparation

Fe-2.0 at.%Cr and Fe-4.5 at.%Cr alloys were prepared by melting, in an Al₂O₃ crucible, pure Fe (99.98 wt.%) and pure Cr (99.999 wt.%) in an inductive furnace under a protective argon atmosphere (99.999 vol.%). The casts have a cylindrical shape with a diameter of 10 mm and a length of 100 mm. The composition of the cast Fe-Cr alloys was determined by chemical analysis; the results have been gathered in Table 2.1 in Chapter 2.

⁴ Note that in both Fe-Mo and Fe-Cr-Mo alloys actually a discontinuous *precipitation* (DP) reaction, from the cubic CP-nitride to the hexagonal DP-nitride, occurs. Still, as in the case of a DC reaction, the DP reaction is associated with (full) misfit-strain relaxation in the DP regions, leading to the same effects in the XRD patterns as for a DC reaction.

The cast Fe-Cr alloys were cold-rolled to sheets with a thickness of 1 mm. The obtained sheets were annealed for 2 h at 700 °C in flowing H₂ atmosphere to get a recrystallized grain structure and further cold-rolled to foils with a thickness of 0.2 mm. Rectangular pieces of lateral dimensions of approx. 10 mm × 10 mm were cut from the foil and were ground to a thickness of less than 100 μm. Subsequently, the specimens were annealed at 700 °C for 2 h under H₂ atmosphere to obtain a recrystallized grain structure. Before nitriding, the thin foils were polished (last step: 1 μm diamond suspension) and cleaned with ethanol.

4.2.2 Nitriding experiments

For nitriding, the Fe-Cr thin foils were suspended with a quartz fiber in a vertical quartz tube furnace. The furnace has a temperature accuracy of ±1 K. Nitriding was performed in an ammonia/hydrogen gas flux (purity: H₂: 99.999 vol. %, NH₃: >99.998 vol. %), with the flow rates adjusted to obtain a nitriding potential of 0.1 atm^{-½} [8]. The (total) nitriding times employed at 580 °C for the Fe-2.0 at.%Cr foils were 5 min, 15 min, 30 min, 1 h, 2 h, 6 h, 12 h, 36 h, 103 h, 175 h, 247 h, 309 h, and 385 h. Fe- 2.0 at.% Cr thin foils were homogeneously saturated with nitrogen by nitriding for 1 h at 580 °C (determined by weight uptake of the specimens, see below). Further nitriding at this temperature in this saturated stage implies aging of the nitrified microstructure⁵. Similarly, the (total) nitriding times employed at 500 °C for the Fe-4.5 at.%Cr foils were 90 min, 135 min, 150 min, 255 min, and 300 min. The Fe- 4.5 at.% Cr thin foils were homogeneously saturated with nitrogen by nitriding for 135 min at 500 °C and further nitrified/aged at this temperature. After this treatment, the alloy was further aged under the same conditions for another 72 h (78 h total). The nitriding conditions had been chosen such that only a diffusion zone (ferrite with dissolved N and alloying element nitride particles) develops, i.e. other Fe-N phases such as iron-nitrides and Fe-N austenite do not develop [12]. After the nitriding and aging treatment, the specimens were lifted into the cold zone of the furnace to allow slow cooling (in approx. 10 min) of the specimens to room temperature.

4.2.3 Specimen characterization

Weight measurement

In order to determine the amount of N lost or taken up by the specimens, thin foils were weighed before nitriding and after each nitriding/aging step using a Mettler Toledo UMX2 microbalance with an accuracy of ±1 μg.

⁵ During this effective aging treatment, the nitriding conditions were maintained in order to avoid the possible dissolution of nitrides and the escape of nitrogen from the specimens.

Light microscopy (LM)

For metallographic investigations, cross-sections of nitrided specimens were prepared by cutting pieces from the specimen with a diamond wire saw. Each cross-section was ground and polished (final polishing step: 1 μm diamond suspension) and etched with 1 % Nital (1 vol.% HNO_3 in ethanol) at room temperature for about 10 s for Fe-2.0 at.%Cr thin foils and 30 s for Fe-4.5 at.%Cr thin foils. LM micrographs were taken using a Zeiss Axiophot microscope equipped with a digital camera (Olympus ColorView IIIu).

X-ray diffraction (XRD) analysis

XRD patterns were recorded from the surface of unnitrided, and nitrided/aged Fe-Cr thin foils using a PANalytical X'Pert diffractometer in Bragg-Brentano configuration equipped with a Co tube and a graphite monochromator in the diffracted beam to select Co-K α radiation. The diffraction-angle range of 30°-110° 2θ was scanned with a step size of 0.009° 2θ . The XRD patterns thus recorded were evaluated using the TOPAS software (Version 4.2, Bruker AXS). Each diffractogram recorded with Co-K α radiation is composed of both Co-K α_1 and Co-K α_2 components [95]. In the case of the Fe-2.0 at.% Cr specimen, the structural broadening of each of the components was fitted by three pseudo-Voigt (pV) functions (for details see section 4.3.1). For the Fe-4.5 at.%Cr alloy for nitriding/aging times up to 150 min, the structural broadening of each component was also fitted by three pV-functions. For longer nitriding/aging times of this alloy, fitting was performed with only two pV-functions for each component (for details see section 4.3.2). The instrumental profile was obtained from a measured standard LaB₆ powder diffraction pattern. This instrumental broadening was incorporated into the fitting of the measured diffraction profiles by convolution with the pV-functions describing the specimen (structural) broadening. The lattice-spacing/lattice-parameter data given in this paper pertain to the diffraction profiles without instrumental broadening.

Transmission electron microscopy (TEM) analysis

Electron transparent foils for TEM investigations were prepared by cutting a small piece from the nitrided Fe-2.0 at.%Cr foils with a diamond wire saw followed by fixing it onto a copper ring and final thinning of the fixed thin foil by Ar-ion milling (3 kV, 8° ion angle of incidence, approx. 2 h, liq.-N₂ cooling). A Philips CM 200 TEM operating at an acceleration voltage of 200 kV was used.

4.3 Results

4.3.1 Fe-2.0 at.%Cr alloy

A comparison of the fitted and measured 211 diffraction profile of nitrated and aged Fe-2.0 at.%Cr alloy (36 h at 580 °C) is provided by Fig. 4.1. The specimen is in an intermediate stage of aging, such that contributions of CP-ferrite (at lower diffraction angles) and of the emerging CC-ferrite (at higher diffraction angles) are clearly present in the profile (for a detailed discussion see section 4.4.2). The results obtained by evaluation of other ferrite reflections of the Fe-2.0 at.%Cr specimen are in agreement with those obtained by evaluation of the 211 reflection. Due to the larger peak separation at higher diffraction angles, only the results of the 211 reflection are presented. Fitting of the structural broadening in the diffraction patterns with a single (symmetric or asymmetric) pV-function is not possible; three (symmetric) pV-functions are required for each $\text{Co}_{\text{K}\alpha}$ -component of the radiation. For the aged specimens these functions can be assigned to the main peak of CP ferrite, its tail towards higher diffraction angles (cf. Chapter 2), and the peak of CC ferrite. The contribution of the first two functions decreases and the contribution of the third function increases with increasing aging time. Up to an aging time of 247 h, the position of the main, CP peak can be reliably determined with the described fitting procedure as it is manifested as either a separate peak or a clear shoulder (see error bars in Fig. 4.3).

The maximum initial shift of the ferrite (XRD) reflections towards lower diffraction angles (Fig. 4.2), and correspondingly the largest ferrite-matrix lattice expansion (Fig. 4.3), i.e. just after full saturation of the Fe-2.0 at.%Cr specimen with N (i.e. precipitation of all Cr as CrN, c.f. Fig. 2.5) was observed after 1 h of nitriding at 580 °C with a nitriding potential of $0.1 \text{ atm}^{-1/2}$ (see also discussion in section 4.4.1). This implies that nitriding times longer than 1 h can be considered as aging times.

The evolution of the ferrite reflections, exemplarily presented for the 211 reflection, upon further nitriding (i.e. aging, cf. above discussion and section 4.2.2) at 580 °C reveals two processes (see Fig. 4.2): i) the main CP peak shifts (back) towards higher diffraction angles (see also Fig. 4.3) and its integrated intensity decreases with increasing treatment time until it has fully vanished at the finally observed stage after 385 h, and ii) a separate peak showing considerable broadening (as compared to the main CP peak) develops centered at approximately the position of pure, unstrained α -Fe (Fig. 4.2). This second peak subsequently increases in integrated intensity and begins to sharpen upon continued nitriding (=aging).

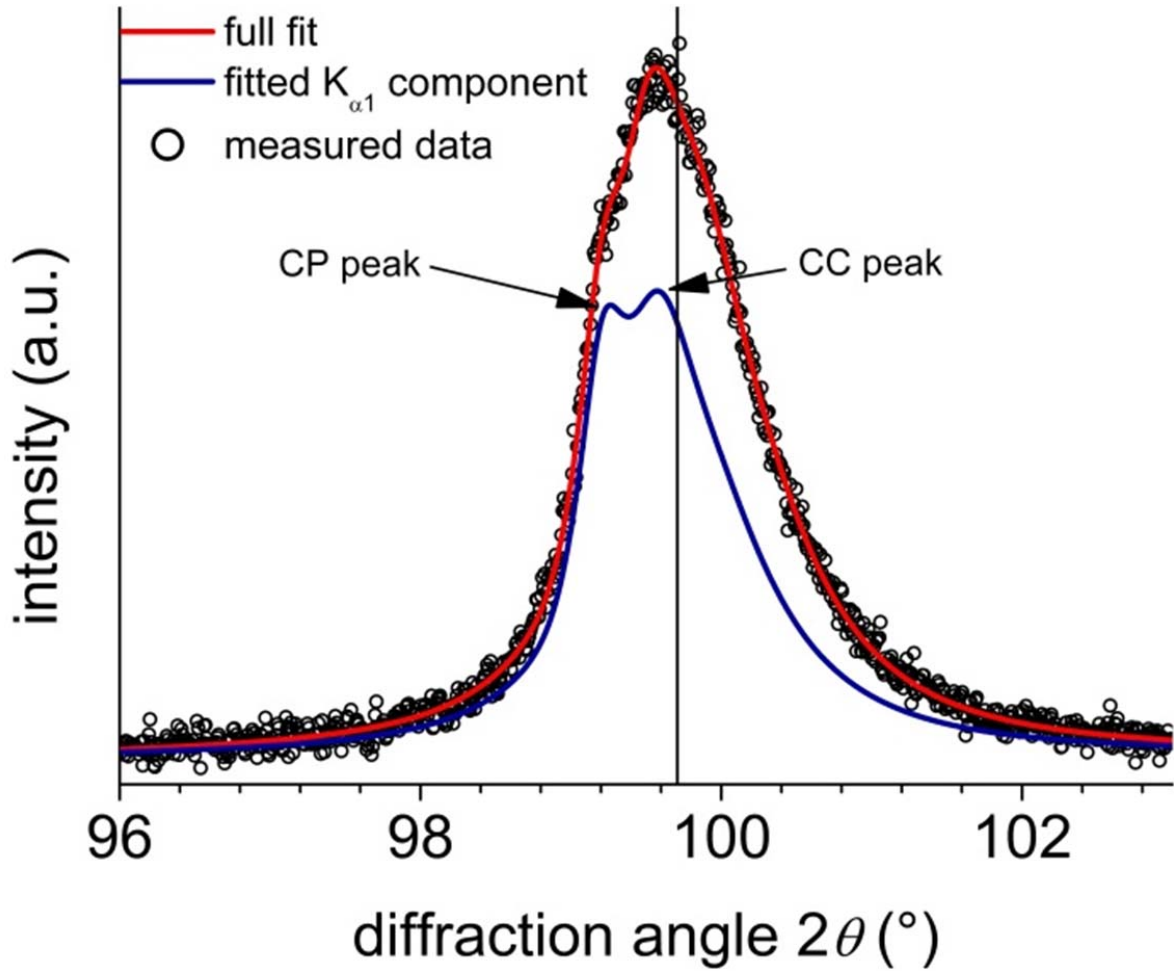


Fig. 4.1: Comparison of the measured 211 diffraction profile (Co- $K\alpha$ radiation) of an Fe-2.0 at.%Cr specimen, nitrided at 580°C for 36 h with a nitriding potential of 0.1 atm^{-1/2}, with the corresponding $K\alpha_1+K\alpha_2$ fit, and the fitted $K\alpha_1$ -component (see section 4.2.3 X-ray diffraction (XRD) analysis). The $K\alpha_1$ -peak position for pure, unstrained ferrite (α -Fe) has been indicated by a vertical line. The specimen is in an intermediate state of aging; both a CP and a CC peak are present in the diffractogram, as indicated by arrows (cf. evolution of ferrite peaks in Fig. 4.2).

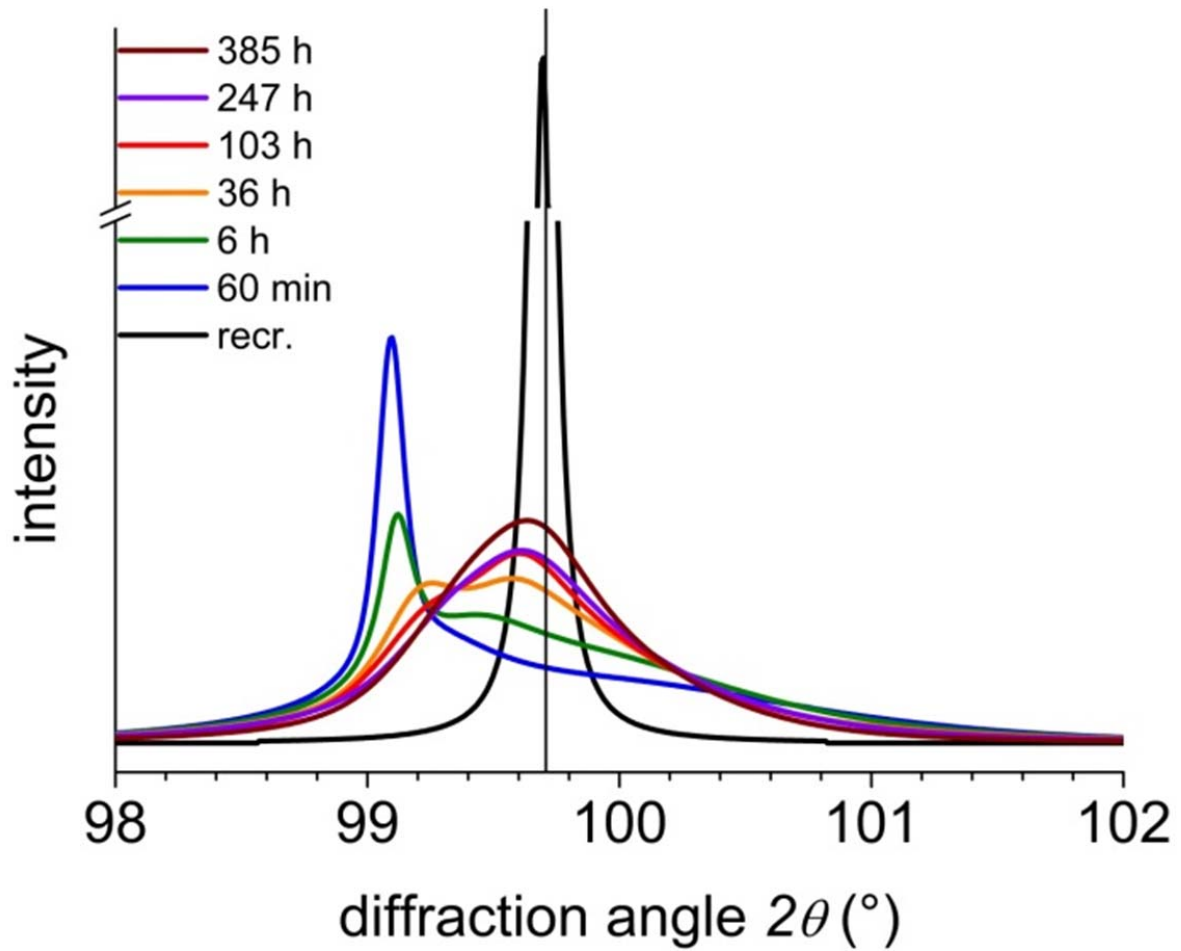


Fig. 4.2: Evolution of the $\text{CoK}\alpha_1$ -211 ferrite–matrix reflection, recorded from the surfaces of Fe-2.0 at.%Cr thin foils homogeneously nitrided at 580 °C with a nitriding potential of $0.1 \text{ atm}^{-1/2}$, for the nitriding/aging times indicated in the figure. The $K\alpha_1$ -peak position for pure, unstrained ferrite (α -Fe) has been indicated by a vertical line. The profiles were normalized with respect to their integrated intensity.

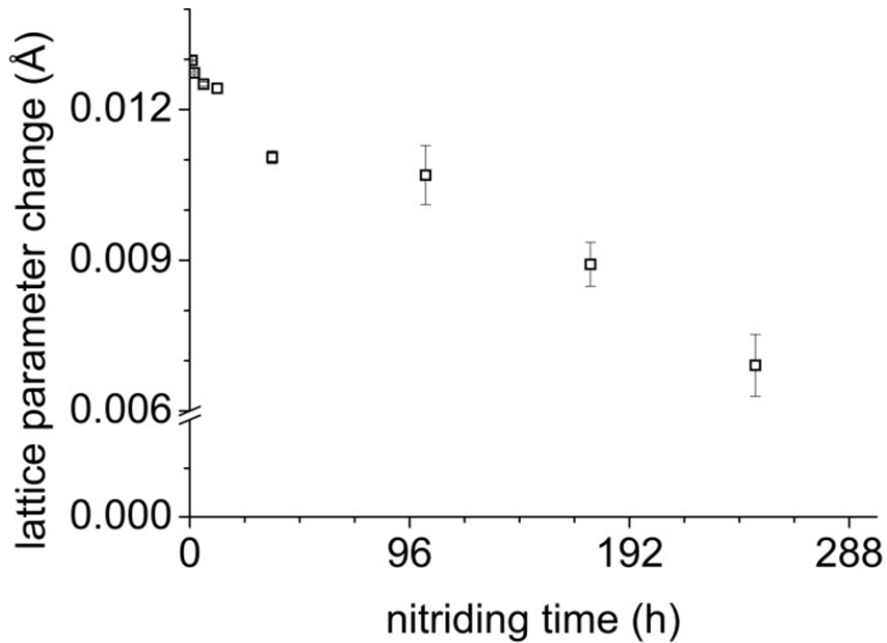


Fig. 4.3: Evolution of the lattice-parameter change, as compared to the lattice-parameter of pure, unstrained α -Fe, determined from the 211 ferrite, CP main peak position (after 103 h the peak is present as a shoulder, cf. Fig. 4.2) of Fe-2.0 at.%Cr alloy, nitrided/aged at 580 °C with a nitriding potential of $0.1 \text{ atm}^{-1/2}$, as function of nitriding/aging time. After a total of 247 h of aging, the shoulder due to the main, CP peak becomes indistinguishable/vanishes in the measured diffraction profiles (see text).

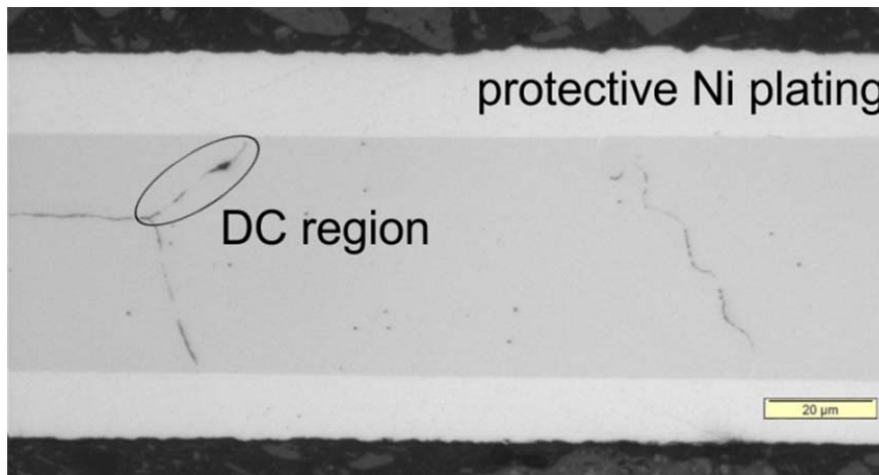


Fig. 4.4: Light optical micrograph taken from the cross-section of a Fe-2.0 at.%Cr thin foil after nitriding for 385 h at 580 °C with a nitriding potential of $0.1 \text{ atm}^{-1/2}$. Only minor DC regions occur along the grain boundaries.

The light optical micrograph taken from the cross section of the specimen after the final stage of nitriding/aging is shown in Fig. 4.4. No indication of an extended DC reaction (which would lead to more pronounced etching contrast) is observed; only very few regions close to a grain boundary may have transformed according to DC. It is concluded that the above described changes in the XRD pattern pertain to the CC process.

TEM analysis was performed on the specimen after 1 h of nitriding at 580 °C, i.e. shortly after all Cr has precipitated as CrN, as validated by no further weight gain of the specimen. At this stage, the maximum peak shift of the ferrite reflection towards lower diffraction angles has occurred (see Fig. 4.3). In this initial state, i.e. before distinct coarsening, extremely fine, coherent precipitates (platelets of approx. 5 nm diameter and less than 1 nm thickness) are present (see bright- and dark-field micrographs in Fig. 4.5a)). After pronounced aging, i.e. after 385 h of nitriding/aging at 580 °C, when only a relatively broad peak remains in the XRD pattern at the position of pure, unstrained α -Fe, the precipitates have grown considerably in diameter (to approx. 50 nm, see Fig. 4.5b) and have lost their coherency with the matrix (note the disappearance of the intensity streak through the 200-type reflections (as observed for the nitrided state; Fig. 4.5a)) and the appearance of distinct CrN spots in the selected area diffraction pattern (SADP) (Fig. 4.5b)).

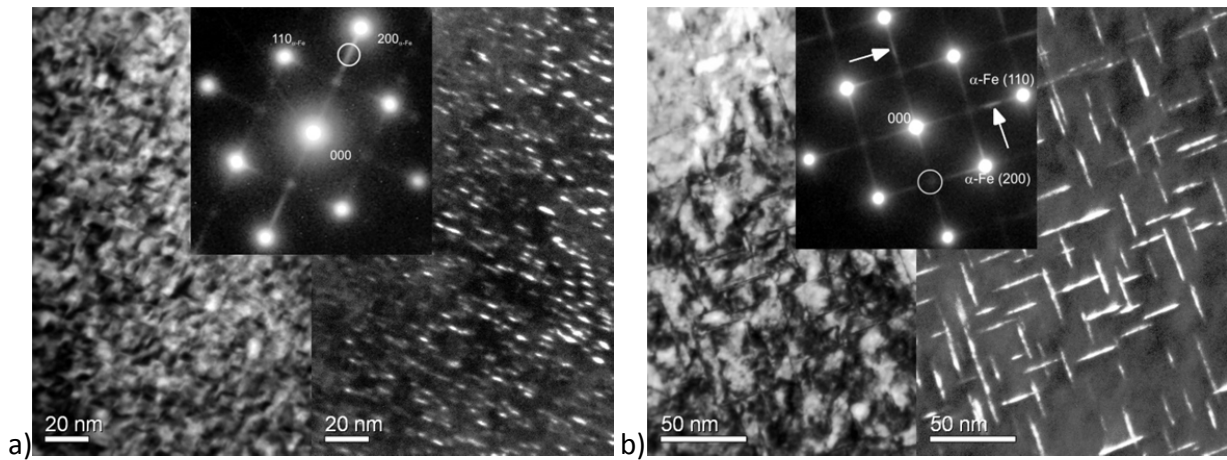


Fig. 4.5: a) TEM bright field micrograph (left) with $[001]_{\alpha\text{-Fe}}$ zone axis, SADP (inset), and dark field micrograph (right) of a Fe-2.0 at.%Cr specimen homogeneously nitrided at 580 °C for 1 h with a nitriding potential of $0.1 \text{ atm}^{-\frac{1}{2}}$. The bright and dark field micrographs show the formation of platelets along $\langle 100 \rangle_{\alpha\text{-Fe}}$ directions. The SADP (inset) is compatible with nitride platelets of NaCl-type crystal structure exhibiting a Baker-Nutting orientation-relationship with the ferrite matrix [52]. The aperture for the DF image shown at the right-hand side of a) has been indicated by a white circle in the SADP and was positioned on the streak through the $200_{\alpha\text{-Fe}}$ spot originating from one variant of the CrN precipitate platelets. b) TEM bright field micrograph (left) with $[001]_{\alpha\text{-Fe}}$ zone axis, SADP (inset), and dark field micrograph (right) of Fe-2.0 at.%Cr specimen nitrided at 580 °C for 385 h (i.e. *aged*) with a nitriding potential of $0.1 \text{ atm}^{-\frac{1}{2}}$. The aperture for the DF image has been indicated by a white circle in the SADP and was positioned on the intersection of the streaks originating from two variants of the CrN precipitates. The white arrows in the SADP indicate the position of intensity maxima along the streak which correspond to the 200_{CrN} -type spots.

4.3.2 Fe-4.5 at.%Cr alloy

A comparison of the fitted and measured diffraction patterns of nitrated and aged Fe-4.5 at.%Cr alloy is provided by Fig. 4.6. The specimen is in an initial stage of aging, such that contributions of CP ferrite (at lower diffraction angles) and DC ferrite (at higher diffraction angles) are clearly present in the profile (for a detailed discussion see section 4.4.3). The results obtained by evaluation of other ferrite reflections of the Fe-4.5 at.%Cr specimen are in agreement with those obtained by evaluation of the 211 reflection. Due to the larger peak separation at higher diffraction angles (and to allow for direct comparison with results shown for the Fe-2.0 at.%Cr alloy in Fig. 4.2), only the results of the 211 reflection are presented. Up to an aging time of 150 min., the structural broadening of each $\text{Co}_{K\alpha}$ -component was fitted with three pV-functions, as for the Fe-2.0 at.%Cr alloy: for the aged specimens these functions can be assigned to the main peak of CP ferrite, its tail towards higher diffraction angles (cf. Chapter 2), and the peak of DC ferrite. For longer aging times, two pV-functions for the structural broadening of each component sufficed for a successful fitting: the influence of the tail of the CP microstructure had vanished. The occurrence of a distinct diffraction peak of the DC ferrite, more outspoken than the CC ferrite peak in case of the Fe-2.0 at.%Cr alloy (compare Fig. 4.2 and Fig. 4.7), allows for (much) better determination of all peak parameters and thus quantitative peak data are presented for both the CP main peak and the DC peak in the following.

The maximum initial shift of the ferrite main-peak (Fig. 4.7), and correspondingly the largest ferrite matrix-lattice expansion (Fig. 4.8), occurs (just) after full saturation of the Fe-4.5 at.%Cr specimen with N, i.e. after nitriding for 135 min at 500°C with a nitriding potential of 0.1 atm^{-½} (see also discussion in section 4.4.1).

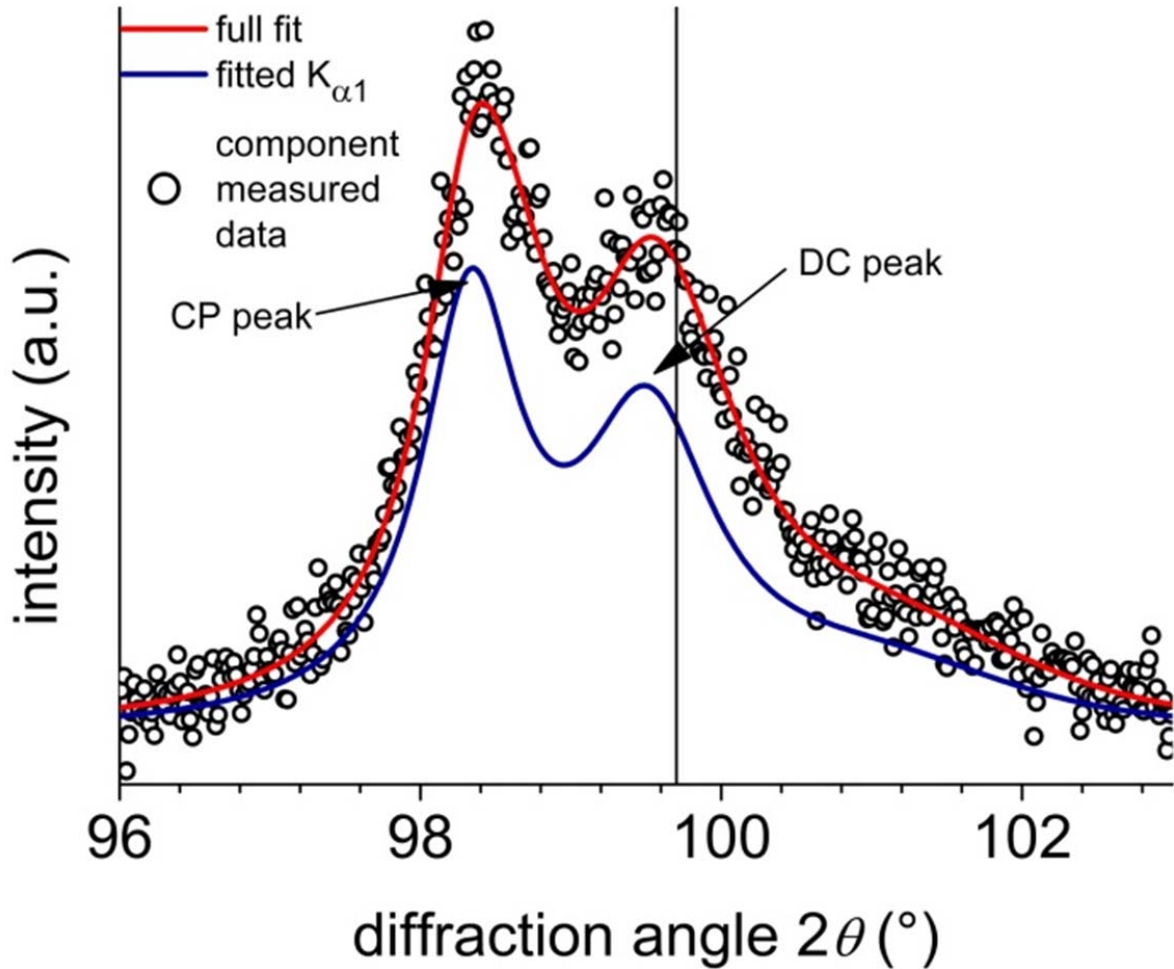


Fig. 4.6: Comparison of the measured 211 diffraction profile (Co- $K\alpha$ radiation) of an Fe-4.5 at.%Cr specimen, nitrated at 500°C for 135 min with a nitriding potential of 0.1 atm^{-1/2}, with the corresponding $K_{\alpha 1}+K_{\alpha 2}$ fit, and the fitted $K_{\alpha 1}$ -component (see section (see section 4.2.3 X-ray diffraction (XRD) analysis)). The $K_{\alpha 1}$ -peak position for pure, unstrained ferrite (α -Fe) has been indicated by a vertical line. The specimen is in an initial state of aging; both a CP and a DC peak are present in the diffractogram, as indicated by arrows (cf. evolution of ferrite peaks in Fig. 4.7). The larger noise in the measured data points as compared to the Fe-2.0 at.% Cr specimen (Fig. 4.1) is a result of the more textured nature of the Fe-4.5 at.%Cr specimen implying a lower intensity of the 211 ferrite reflection.

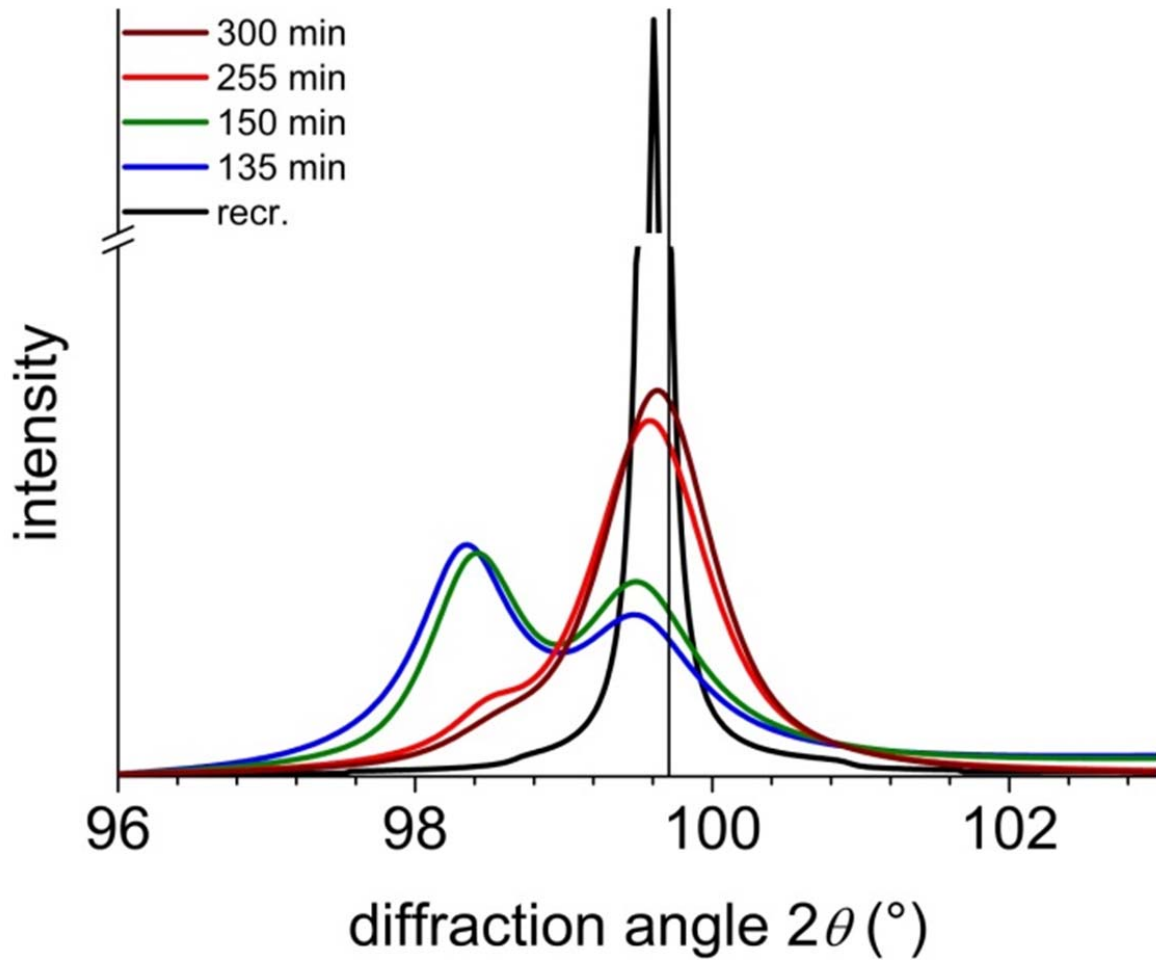


Fig. 4.7: Evolution of the $\text{CoK}_{\alpha_1-211}$ ferrite-matrix reflection, recorded from the surfaces of Fe-4.5 at.%Cr thin foils homogeneously nitrided at 500 °C with a nitriding potential of $0.1 \text{ atm}^{-1/2}$ for the nitriding times indicated in the figure. The $\text{K}\alpha_1$ -peak position for pure, unstrained ferrite ($\alpha\text{-Fe}$) has been indicated by a vertical line. The profiles were normalized with respect to their integrated intensity.

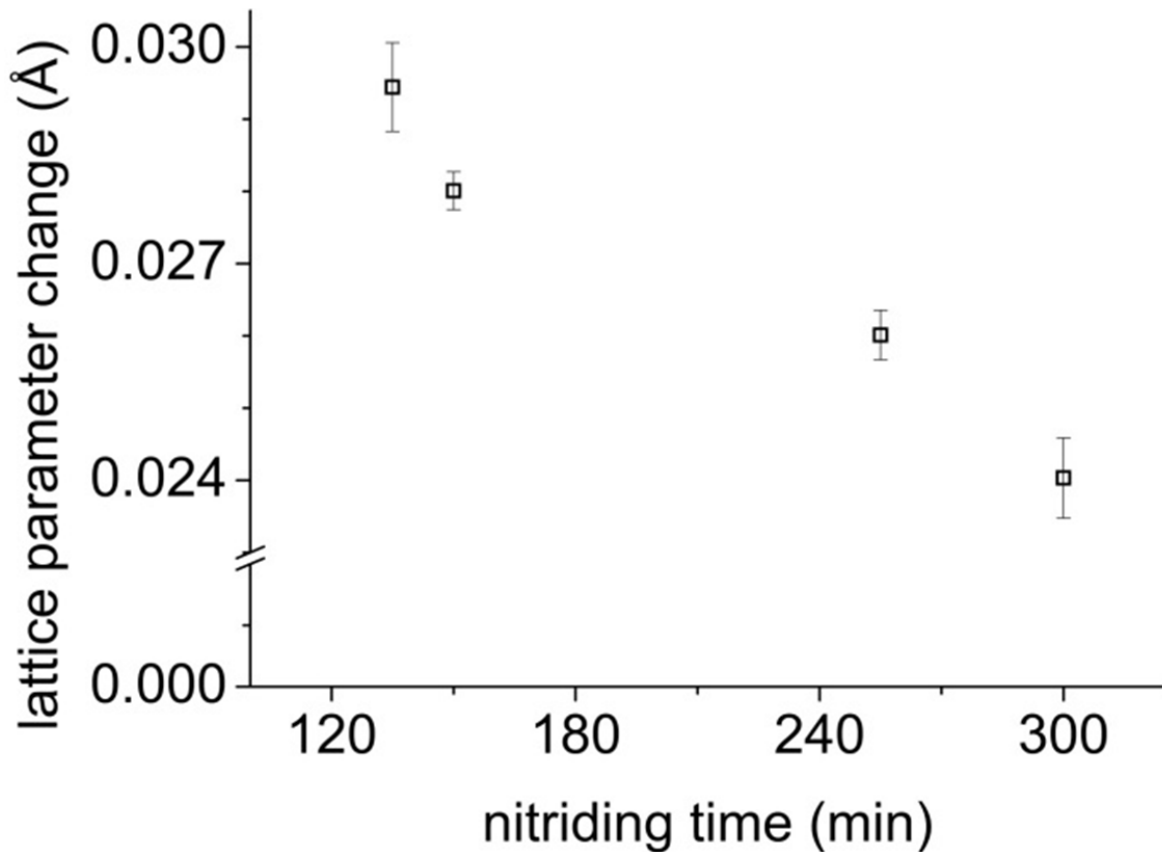


Fig. 4.8: Evolution of the lattice-parameter change as compared to the lattice-parameter of pure, unstrained α -Fe, determined from the 211 ferrite peak position of the CP main peak (later times present as a shoulder, cf. Fig. 4.7) of Fe-4.5 at.%Cr alloy, nitrided/aged at 500 °C with a nitriding potential of 0.1 atm^{-1/2} as function of nitriding/aging time.

The evolution of the 211 ferrite reflection upon further nitriding (i.e. aging) is shown as a function of nitriding time (i.e. aging) in Fig. 4.7. Two processes are discerned: i) the CP-main peak shifts (back) towards higher diffraction angles (see also Fig. 4.8) and its integrated intensity decreases with increasing treatment time until it has vanished at the finally observed stage after 300 min (see Fig. 4.9), and ii) the second peak at higher diffraction angle, centered at approximately the position of pure, unstrained α -Fe, increases in integrated intensity with increasing treatment time. Unlike the second peak present in the diffraction patterns of the nitrided and aged Fe-2.0 at.%Cr thin foils (Fig. 4.2) that is considerably broadened as compared to the main CP-peak, the second peak developing in the diffraction patterns of nitrided Fe-4.5 at.%Cr thin foils is relatively sharp (similar to the main CP-peak), from its initial appearance in the early stages of nitriding/coarsening, and shows only little change in broadening upon continued treatment.

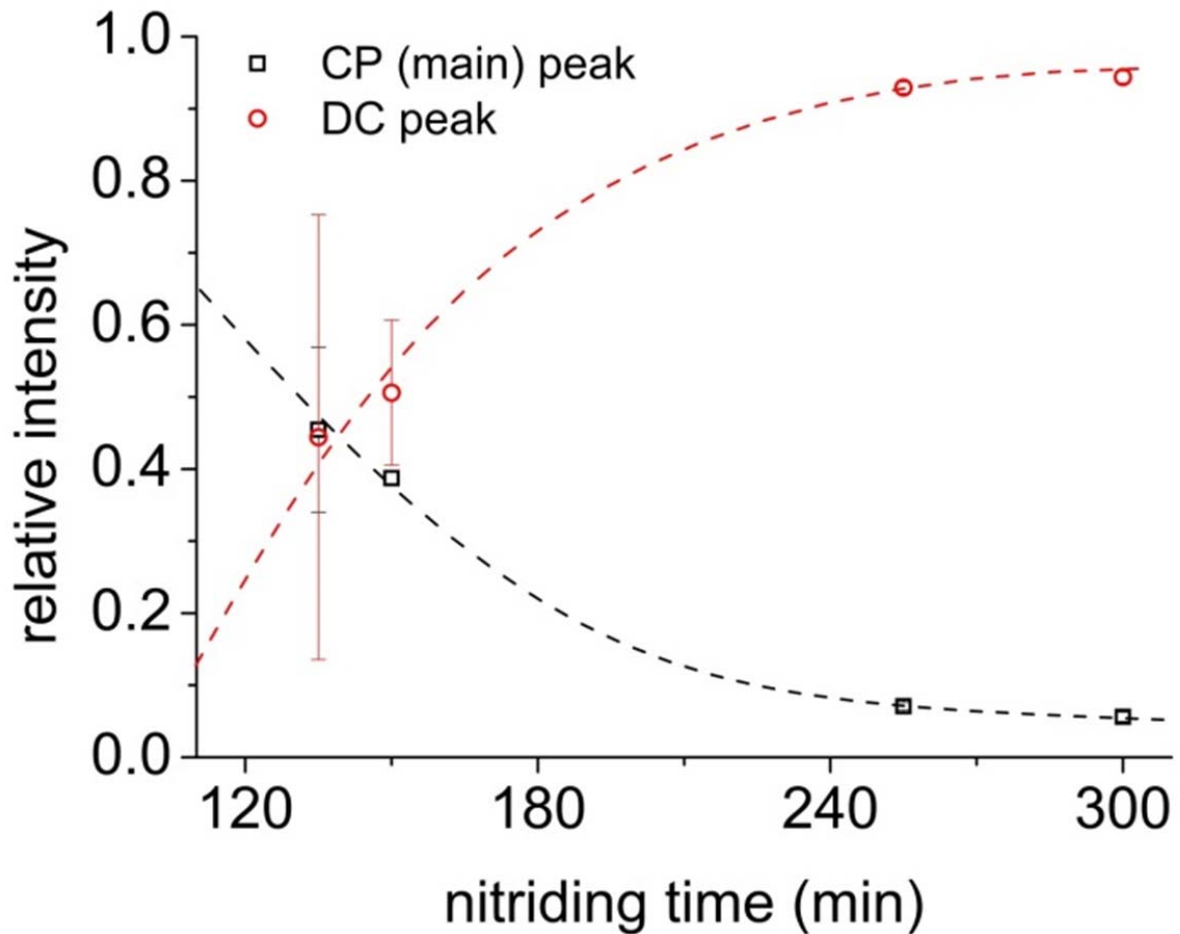


Fig. 4.9: Evolution of the relative intensities of the CP main peak and the DC peak determined from the 211 ferrite reflections of Fe-4.5 at.%Cr alloy, nitrided/aged at 500 °C with a nitriding potential of $0.1 \text{ atm}^{-\frac{1}{2}}$, as function of nitriding/aging time. Lines are drawn to guide the eye.

Corresponding light optical micrographs taken from cross sections prepared from the Fe-4.5 at.%Cr specimen after each nitriding step (Fig. 4.10) demonstrate the development of DC regions throughout the microstructure (note that already after 135 min., due to the large driving force for DC in this alloy, already a partial DC has occurred); the DC continues until the whole specimen has transformed to DC (see the microstructure as observed after 225 min in Fig. 4.10). It is concluded that the above described changes in the XRD patterns pertain to the DC process. After prolonged aging for another 72 h at 500°C with a nitriding potential of $0.1 \text{ atm}^{-\frac{1}{2}}$ to a total nitriding/aging time of 78 h, separate CrN reflections could be identified in the XRD pattern (see Fig. 4.11).

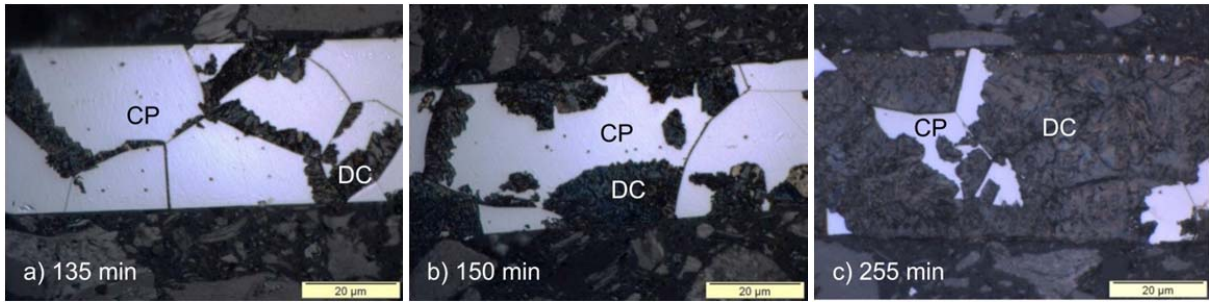


Fig. 4.10: Light optical micrographs taken from the cross-sections of a Fe-4.5 at.%Cr thin foil specimens after nitriding at 580 °C with a nitriding potential of $0.1 \text{ atm}^{-1/2}$ for the indicated nitriding (aging) times. The coarse lamellar DC microstructure is more prone to etchant attack, due to a large amount of incoherent interfaces, and thus shows a more pronounced etching contrast as compared to CP regions. Development of the DC regions within the diffracting volume of the specimen after nitriding for longer times is compatible with the gradual rise of a new ferrite reflection from the DC region and gradual disappearance of the ferrite reflection from the CP region (see Fig. 4.7).

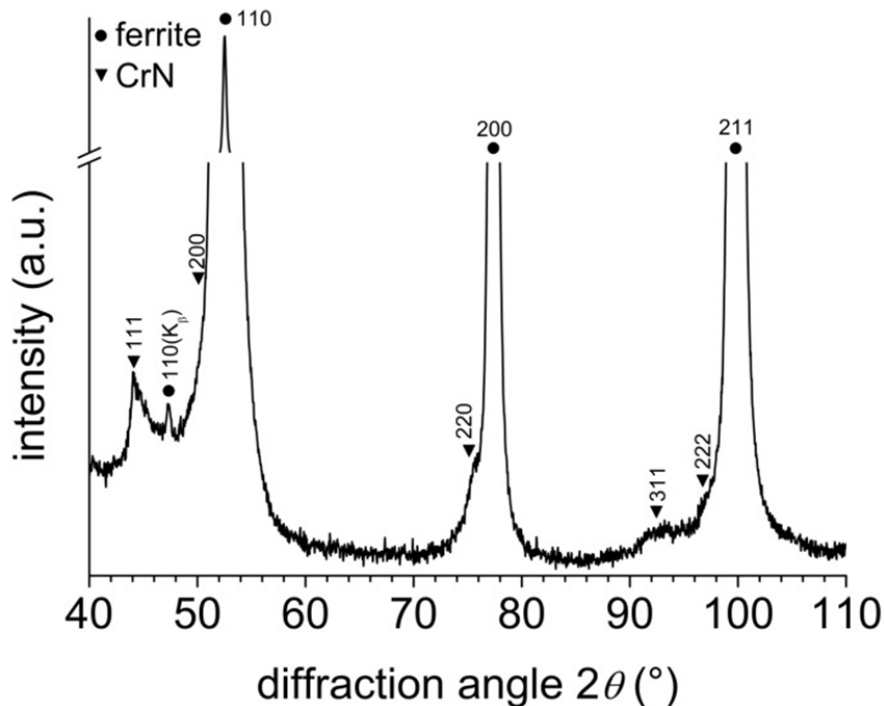


Fig. 4.11: Diffractogram (CoK_α radiation) recorded from the surface of an Fe-4.5 at.%Cr thin foil homogeneously nitrided at 500 °C with a nitriding potential of $0.1 \text{ atm}^{-1/2}$ for 78 h. The separate (see text in section 4.4.3) reflections of the ferrite matrix and the CrN precipitates have been indicated.

4.4 Discussion

4.4.1 Initial state

Before nitriding, the Fe-2.0 at.%Cr and Fe-4.5 at.%Cr alloys are single phase solid solutions of Cr in α -Fe. The substitutionally dissolved Cr atoms, that are slightly larger than the Fe atoms, induce an expansion of the ferrite lattice and thus a larger lattice parameter as compared to pure, unstrained α -Fe [154]; cf. the diffraction-peak positions of the Fe-Cr solid solution specimens (indicated as recr.) and of the pure α -Fe specimens (vertical line) (Fig. 4.2 and Fig. 4.7).

Table 4.1: Measured and predicted change of the lattice spacing of the {211} lattice planes of the ferrite matrix in fully nitrided Fe-2.0 at.%Cr (580 °C, 1 h, 0.1 atm^{-½}) and fully nitrided Fe-4.5 at.%Cr (500 °C, 135 min, 0.1 atm^{-½}) alloys: Δd_{CrN} is the calculated {211} lattice-plane spacing change of the ferrite matrix due to CrN precipitation (Chapter 2), $\Delta d_{dissolved\ N}$ corresponds to the calculated {211} lattice-plane spacing change of the ferrite matrix due to an equilibrium amount of dissolved N in ferrite under the present nitriding conditions [7], [99] and $\Delta d_{measured}$ corresponds to the measured lattice-plane spacing change of the {211} lattice planes of the ferrite matrix.

alloy	Δd_{CrN} [Å]	$\Delta d_{dissolved\ N}$ [Å]	$\Delta d_{total} = \Delta d_{CrN} + \Delta d_{dissolved\ N}$ [Å]	$\Delta d_{measured}$ [Å]
Fe-2.0 at.%Cr	0.0047	0.0009	0.0056	0.0053
Fe-4.5 at.%Cr	0.0105	0.0003	0.0108	0.0120

Upon nitriding of the Fe-2.0 at.%Cr and Fe-4.5 at.%Cr specimens the volume misfit between the ferrite matrix and the initially developing finely distributed, coherent nitride precipitates is accommodated fully elastically. In this condition, the ferrite matrix and the coherent nitride precipitates *diffract coherently* (Chapter 2 and Refs. [58], [59]); i.e. the observed ferrite reflections represent coherent diffraction by the whole assembly. The magnitude of the misfit-induced expansion of the assembly, and thus of the corresponding peak shift of the ferrite reflections towards lower diffraction angles, as compared to the unnitrided condition, depends on the volume fraction of precipitates, the precipitate/matrix (volume) misfit and the elastic properties of matrix and precipitates. Adopting the procedure given in Chapter 2, the thus predicted 211 lattice-plane spacing changes, Δd_{CrN} , for the specimens of the current study in this initial state (i.e. directly after homogeneous nitrogen saturation of the specimens; this is the state of the Fe-2.0 at.%Cr thin foil after 60 min of nitriding at 580 °C (Fig. 4.2) and of the CP microstructure in the

Fe-4.5 at.%Cr thin foil after 135 min of nitriding at 500 °C (Fig. 4.7) can be compared with the 211 lattice-plane spacing changes determined from the measured peak positions in Table 4.1.

A full comparison of measured and predicted lattice-parameter changes (diffraction-peak shifts) requires recognizing the following contributions to the lattice-parameter change:

i): The ferrite lattice contracts by the depletion of Cr from the solid solution during CrN precipitation: the {211} lattice-plane spacing changes Δd_{CrN} in Table 4.1 (due to elastic misfit accommodation; see above) have been given relative to pure α -Fe.

The following (minor) contributions occur, but have not been quantified:

ii): As the current specimens were not denitrided, an additional dilatation due to (equilibrium and excess) N dissolved in the ferrite matrix (for details about excess N see e.g. Ref. [10]) can occur for the specimens (as observed after cooling to room temperature). In Table 4.1, the effect on the {211} lattice-plane spacing by dissolution of the equilibrium amount of N in ferrite ($\Delta d_{\text{dissolved N}}$) has been given. For the Fe-2.0 at.%Cr specimen, the measured peak shift ($\Delta d_{\text{measured}}$) is a little smaller than would be expected taking into account the dilatation both by CrN precipitation and by dissolution of the equilibrium amount of N in ferrite (Δd_{total}). This suggests that due to the relatively high nitriding temperature of 580 °C, already after 1 h of nitriding some relaxation has occurred (i.e. the precipitation-induced misfit is only partially elastically accommodated). On the other hand, the Fe-4.5 at.%Cr specimen was nitrided at the relatively low temperature of 500 °C, and thus, less relaxation is expected. Indeed, the measured peak shift ($\Delta d_{\text{measured}}$) for this specimen is (even) larger than would be expected taking into account the dilatation both by CrN precipitation and by dissolution of the equilibrium amount of N in ferrite (Δd_{total}). This additional peak shift is likely due to the presence of excess N as indicated in [10].

iii): Precipitation of α'' -Fe₁₆N₂ from dissolved N will occur from N-supersaturated ferrite at room temperature (see e.g. Ref. [98], [155], [156]). This additional precipitation process at room temperature will also lead to additional line shifts and broadening changes [118], [131], [132]. However, the misfit between ferrite and α'' -Fe₁₆N₂ is considerably smaller ($\epsilon_V = 0.0300$ (lattice parameters of α'' -Fe₁₆N₂ from Ref. [156])) than the misfit between ferrite and CrN ($\epsilon_V = 0.1464$, see Chapter 2) and thus its influence on the measured lattice-parameter change is minimal.

iv): An additional misfit between CrN and ferrite results from the differences in thermal expansion coefficient of CrN precipitates and ferrite matrix ($\epsilon_T = 0.0065$ for cooling from 580 °C to

25 °C). Also this contribution to the lattice-parameter change can be neglected compared to the magnitude of the elastically accommodated volume misfit present after full initial precipitation of CrN in the alloys (see above).

In addition to the observed peak shifts due to elastic precipitate/matrix misfit accommodation, the asymmetric tail of the main reflection (towards higher diffraction angles) represents the severely distorted nature of the regions in the vicinity of the precipitates (Chapter 2 and Refs. [13], [78]).

4.4.2 Continuous Coarsening

The nitride precipitates in the Fe-2.0 at.%Cr alloy upon annealing show considerable growth in length from the initially, fully coherent state to the incoherent state, as evidenced by TEM (cf. Fig. 4.5a) and b)). The coarsening process is accompanied by a loss of elastic accommodation of the precipitate/matrix (volume) misfit and thereby the overall, long-range, elastic lattice expansion decreases (Fig. 4.3). This is accompanied by a “back”-shifting of the CP ferrite main peak towards the unstrained position as revealed in Fig. 4.2. Cr stays depleted from the ferrite matrix and thus does not contribute further to the peak shift as a function of aging time. Other (subordinate) causes of peak shift as a function of aging time are the following (cf. discussion in section 4.4.1):

- i): During relaxation of the precipitate/matrix volume misfit and the coarsening of the nitride platelets (reduction in interfacial area) the amount of excess N in the alloy decreases (desorption) and thus its (already minor) contribution to the peak shift decreases with increasing annealing time.
- ii): The thus decreased amount of dissolved N with increased annealing time can lead to a decreased development of α'' -Fe₁₆N₂ precipitates at room temperature. Also this (already minor) contribution to the peak shift decreases with increasing annealing time.
- iii): The minor contribution of the thermal misfit does not change. Its corresponding peak shift thus remains minimal (see section 4.4.1).

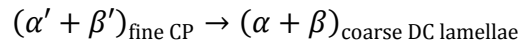
In an end stage of coarsening and apart from the immediate vicinity of the precipitates, the misfit will be (nearly) fully relaxed and thus the ferrite matrix shows a lattice spacing close to that of pure ferrite. Therefore, the emerging CC-peak develops at the approximate position of pure α -Fe. However, the heterogeneity of the relaxation process and its locally varying degree of completion involve the presence of a pronounced amount of microstrain and thus the occurrence of an appreciable amount of diffraction-line broadening as exhibited by the CC-peak. Ob-

viously, upon increasing (aging) time, the strain variation decreases leading to a sharpening of the corresponding reflection (Fig. 4.2).

The developing incoherency of the precipitate/matrix interface randomizes the phase relation of X-rays scattered by the matrix and those by the precipitates and thus incoherent diffraction of matrix and precipitates now occurs [58], [59]. Indeed, the TEM SADP in Fig. 4.5b) now reveals separate diffraction spots from matrix and precipitates. In the XRD patterns, individual precipitate reflections cannot be observed due to the low volume fraction.

4.4.3 Discontinuous Coarsening

If the alloy contains sufficient alloying element and if the misfit and the amount of precipitate/matrix interfacial area is high enough, then *discontinuous coarsening* is favored over the (usual) continuous coarsening. Indeed DC governs the coarsening process in the nitrided Fe-4.5 at.%Cr alloy (see Fig. 4.10). The overall DC reaction in the nitrided Fe-4.5 at.%Cr specimen can be expressed as (see Refs. [21], [150], [152]):



where, α' denotes the strained, N-supersaturated ferrite matrix, β' the strained, coherent CrN precipitates, α the relaxed ferrite lamellae without supersaturation and β the relaxed, coarse incoherent CrN precipitate lamellae. The energy difference of the continuously precipitated and discontinuously coarsened states, i.e. the driving force for DC, for the present specimens is comprised of three contributions [21]; reduction of the interfacial area (reduction of interfacial energy), the loss of ferrite matrix (nitrogen) supersaturation (i.e. loss of excess N; reduction in chemical energy), and the relaxation of the long-range strain-fields due to the coherent to incoherent transition (release of strain energy).

Actually, in specimens where DC can occur, both continuous and discontinuous coarsening take place simultaneously but with different reaction rates [19], [22], [23], [25]: The DC reaction can be rate controlled by diffusion of the atoms along the mobile grain boundary that sweeps through the specimen and in the wake of which the cellular microstructure develops, whereas the CC reaction is governed by volume diffusion processes, necessary for the growth and dissolution of precipitates. Consequently, the rate of the DC reaction is (much) higher than that of the CC reaction. Indeed, whereas an end stage of CC at 580 °C is reached after hundreds of hours, a final state of DC at 500 °C is reached after hundreds of minutes (cf. Fig. 4.2 and Fig. 4.7). Therefore, in addition to the development of relatively slowly relaxing and thus only partly relaxed regions surrounding the continuously coarsened precipitates, in advance of the reaction front of the DC reaction, fully relaxed matrix regions (ferrite lamellae) occur behind the DC reac-

tion front. Thus, in a specimen that undergoes DC, in principle two types of ferrite regions contribute to the second diffraction peak at higher diffraction angle (cf. section 4.3.2): i) the continuously coarsened regions (decreasing in volume upon continued aging) corresponding with a broad peak (cf. section 4.4.2), and ii) the fully stress-relieved ferrite in the discontinuously coarsened part (increasing in volume upon aging) corresponding with a sharp peak. At an end stage of aging (i.e. after 300 min of aging at 500 °C) the contribution of continuously coarsened regions has become minimal (cf. Fig. 4.10). Then, the emerging second peak is dominated by the discontinuously coarsened ferrite and is therefore sharp. Also, due to the presence of a clear boundary (see Refs. [23], [25]) between the ferrite in the continuously coarsened region and the ferrite in the discontinuously coarsened regions, both will always diffract *incoherently*. For the DC microstructure, i.e. with incoherently diffracting precipitates of relatively large dimensions, separate precipitate reflections of CrN and (DC-) ferrite matrix occur (see Fig. 4.11).

4.5 Conclusions

The interpretation of the behavior of the (X-ray) diffraction peaks recorded from ferrite in nitrided Fe-Me alloys (Me forms misfitting, coherent precipitates of MeN in early stages of nitriding), from the initial, fully continuously precipitated state to the continuously or discontinuously coarsened state, can be summarized as follows (see also schematic in Fig. 4.12):

1. In the initial, just fully nitrided state, the ferrite reflections have shifted towards lower diffraction angles as a result of the *elastic* accommodation of the precipitate-matrix misfit. The assembly of matrix and precipitate particles diffracts coherently. The magnitude of the CP-peak shift can be quantitatively predicted from the amount of precipitates and the degree of misfit. Additionally, the severely distorted regions surrounding the precipitates lead to a tail of the peaks towards higher diffraction angles.
2. Upon aging, coarsening of the initially coherent precipitates can occur in two distinctly different ways: continuous coarsening and discontinuous coarsening. Both processes can occur simultaneously. The higher the alloying element/precipitate content, the larger the contribution of the discontinuous coarsening.
3. Upon continuous coarsening the average precipitate-particle size increases under gradual loss of the coherency with the matrix, involving the development of a heterogeneous state of strain relaxation in the matrix: the CP-matrix diffraction maximum gradually shifts (back) towards higher diffraction angles due to the loss of the long-range matrix dilatation; the CC-reflection is strongly broadened due to the spatially varying state of relaxation/remaining lattice strain of the individual precipitates. As the volume fraction of the fully relaxed regions increases upon prolonged aging, the broadening of the CC-reflection de-

creases and its relative intensity increases upon approaching the fully coarsened state, when precipitates and matrix diffract incoherently.

4. Upon discontinuous coarsening, the matrix at the reaction front abruptly changes from misfit strained to fully relaxed, involving that already at the start of coarsening a sharp ferrite peak emerges at the position of pure unstrained ferrite. Upon increasing aging time, the relative intensity of this reflection increases, while that of the initially continuously precipitated and relatively very slowly continuously coarsening matrix decreases. Due to the comparatively large volume fraction of precipitates in alloys undergoing DC and the incoherent diffraction of matrix and precipitate lamellae of the relaxed DC microstructure, separate reflections of nitrides and ferrite can be detected.

Acknowledgements

The authors would like to thank Dr. E. Bischoff for the TEM investigations, Mr. W.-D. Lang for preparation of the TEM specimens and Mr. P. Kress for assistance with the nitriding experiments (all with Max Planck Institute for Intelligent Systems) and Prof. A. Leineweber (now with TU Bergakademie Freiberg) for valuable discussion.

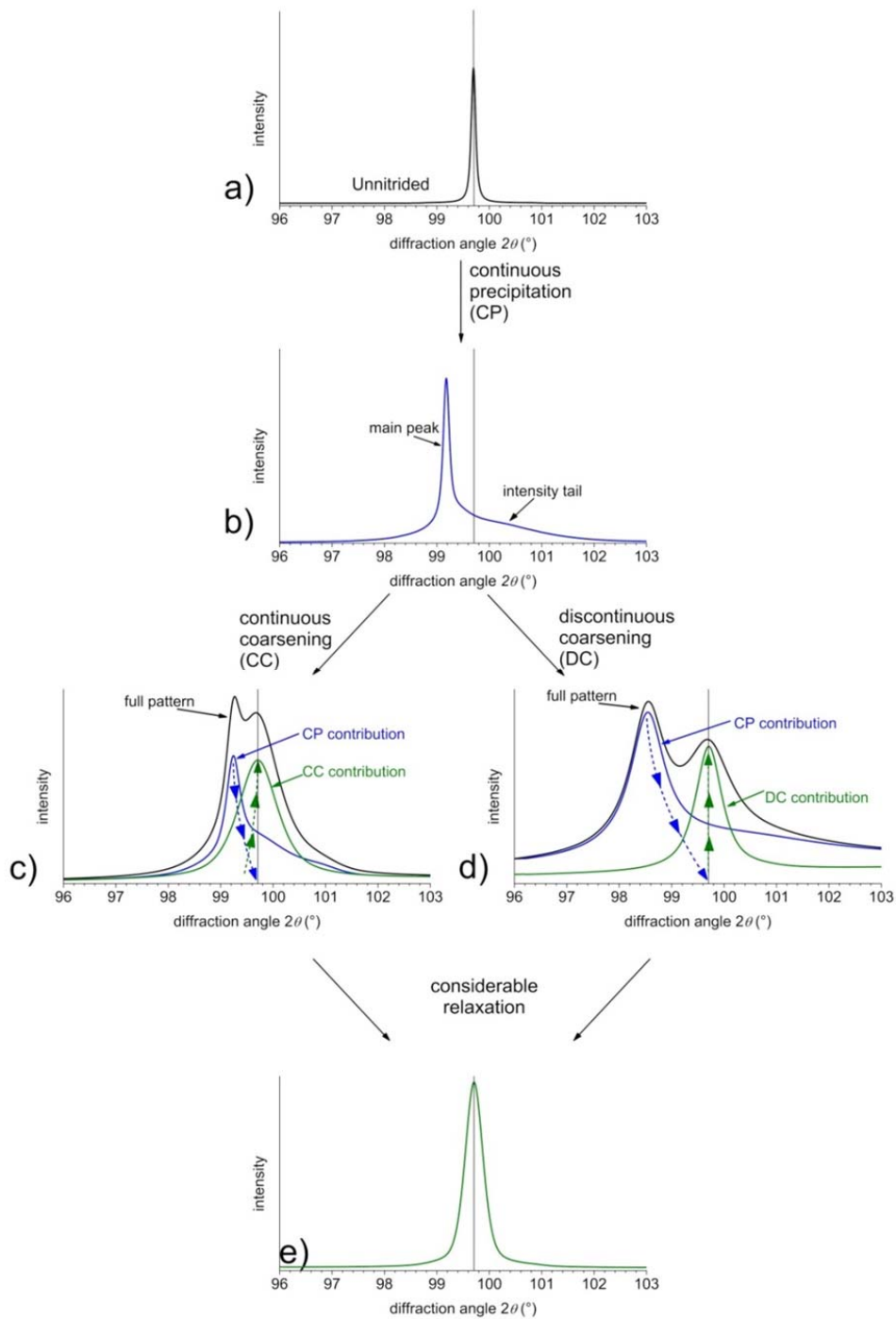


Fig. 4.12: Schematic presentation showing the evolution of the X-ray diffractogram of Fe-Me alloys upon nitriding and subsequent continuous and discontinuous coarsening, see section 4.5 for details. In all the diffractograms, the position of the pure α -Fe peak has been indicated with a vertical line. Arrows in c) and d) indicate the evolution of position and intensity of component peaks, together constituting the total diffraction profile, as a function of aging time.

Chapter 5

Alloying element nitride stability in nitrided iron-based alloys; denitriding of nitrided Fe-V alloys

T. Steiner, S.R. Meka, H. Göhring, E.J. Mittemeijer

Abstract

In view of the various types of absorbed nitrogen in nitrided iron-based alloys and the lack of accuracy in local composition analysis of the individual, nanosized nitride precipitates (e.g. by atom probe tomography) considerable interest exists to precisely determine the nitride composition by a so-called denitriding treatment to remove from the specimen the not strongly bonded nitrogen, i.e. the nitrogen not taken up in the nitrides. The present study proposes two routes to determine the nanonitride stoichiometry, which are demonstrated by experimental analysis of the denitriding behaviour of nitrided, model Fe-V alloys. Upon denitriding in hydrogen gas, after an initial fast loss of dissolved and excess nitrogen, an ongoing slow, but ultimately complete, loss of strongly bonded nitrogen takes place. The kinetics of nitrogen loss depends on the surface-to-volume ratio of the specimens, the (de-)nitriding temperature, and the specimen microstructure, e.g. discontinuously coarsened nitride particles dissociate more slowly. The minimal nitrogen activity in the gas atmosphere to stabilize the alloying element nitrides MeN in Fe- Me -N alloys is presented as calculated with the Thermo-Calc software. A strategy is offered to stabilize the alloying element nitrides and to determine the nitrogen content strongly bonded in the nitrides. On this basis for Fe-V alloys a nanonitride composition of VN is found, i.e. no significant amount of Fe is taken up in the nitrides.

5.1 Introduction

Nitriding is a thermochemical surface engineering process in which nitrogen from an outer atmosphere is introduced into the surface adjacent region of a metallic, usually ferritic Fe-based component [5], [8]. The inwardly diffusing nitrogen will interact with nitride forming alloying elements, Me , like, e.g., Ti [13], [14], [28], V [15]–[19], Cr [20]–[27], Mo [28]–[31], Al [32]–[35], [157], [158], Si [36]–[38] and Mn [39]–[43] allowing development of a range of nitrides [159]. Upon nitriding of ferritic Fe- Me alloys (with $Me = Ti, V, Cr, \dots$), initially the precipitation of fine, coherent, cubic NaCl-type MeN_y platelets, with their broad faces parallel to the $\{100\}_{\alpha-Fe}$ planes, occurs. This microstructure is referred to as continuously precipitated (CP). Prolonged nitriding of Fe- Me alloys can lead to the subsequent development of a coarsened lamellar microstructure via a discontinuous coarsening (DC) reaction leading to cells consisting of al-

ternating lamellae of MeN nitride and ferrite (see Refs. [21], [22] for $Me = Cr$, and Ref. [18] for $Me = V$).

In nitrided Fe- Me specimens of CP microstructure various types of nitrogen can be distinguished: (i) nitrogen strongly bonded in the crystal structure of the forming MeN nitrides; (ii) nitrogen dissolved in the ferrite matrix in equilibrium with the employed nitriding atmosphere. This includes the excess nitrogen dissolved in the ferrite matrix due to the expansion of the ferrite matrix by the precipitate-strain field, the so-called mobile excess nitrogen [9], [10]; (iii) adsorbed/segregated nitrogen: due to the usually nano-sized nature of the nitride precipitates and the corresponding, very large, coherent precipitate/matrix interfacial area, considerable nitrogen can be adsorbed at the precipitate-matrix interfaces; this is the so-called immobile excess nitrogen [9], [10]. In order to quantitatively describe the nitriding process (see, e.g., Refs. [9], [160]–[163]), knowledge of the respective amounts of excess nitrogen is required. Previous analyses of absorbed nitrogen of types (i)–(iii) have been performed in Refs. [26], [157], [158], [93], [64], [101], [164], [165].

Direct determination of the nitrogen content of individual nitride precipitates by local elemental analysis employing either (scanning) transmission electron microscopy in combination with energy dispersive X-ray spectroscopy or electron energy loss spectroscopy, or atom probe (tomography) is difficult due to the very small size of the finely distributed, nano-sized alloying element nitrides. Although these techniques allow establishment of the whether or not occurring coprecipitation of two (metallic) alloying elements in the form of ternary $(Me_1)_x(Me_2)_{1-x}N_y$ nitrides in ternary Fe- Me_1 - Me_2 alloys (Refs. [62], [65], [166] and Chapter 6), quantitative composition analysis by these methods is imprecise (see Refs. [29], [65], [166]–[171] and Chapter 6): for example, considerable amounts of Fe are seemingly (at least to a large extent) detected by atom probe tomography (APT) to be present inside the precipitates [166] and Chapter 6.

The respective amounts of strongly bonded nitrogen, equilibrium dissolved nitrogen, and the two types of excess nitrogen (dissolved and adsorbed/segregated) can be determined experimentally by recording so-called nitrogen-absorption isotherms [10], [157], [158], [93]. An alloy specimen that can be nitrided homogeneously, usually a thin foil of less than 200 μm thickness, is (pre-)nitrided to saturation, i.e. until no more nitrogen uptake occurs, to obtain a stable microstructure for the subsequent absorption-isotherm determination at a (somewhat) lower temperature. Subsequently, the specimen is denitrided, i.e. annealed at a low temperature (usually 400 to 480 $^{\circ}C$) in H_2 atmosphere (hydrogen reduction). This, ideally, leads to removal of the (equilibrium and excess) dissolved nitrogen and the interface adsorbed excess nitrogen and only the nitrogen strongly bonded in the nitrides remains in the specimen. By this method the

Me:N-stoichiometry (nitrogen of type (i)) of the forming alloying element nitrides can be determined (by weight measurements) from the nitrogen remaining in the specimen.

The nitrogen-absorption isotherm, as recorded after the above described denitriding, presents the maximum amount of nitrogen taken up by the specimen as function of the nitriding potential $r_N = \frac{p_{\text{NH}_3}}{p_{\text{H}_2}^{3/2}}$ (Ref. [172]; the nitriding potential is related to the nitrogen activity, see section 5.3.2). The nitrogen content shows a linear dependency on the applied nitriding potential; the slope of this straight line is given by the equilibrium constant of $\text{NH}_3 \rightleftharpoons [\text{N}]_\alpha + \frac{3}{2}\text{H}_2$, where $[\text{N}]_\alpha$ denotes the nitrogen dissolved in the matrix. The amount of mobile excess nitrogen (part of type (ii) nitrogen) is determined by the differences of the linear parts of the absorption isotherms of the nitrided alloy and pure iron [7]. The amount of immobile excess nitrogen (type (iii) nitrogen) can be obtained by comparison of the nitrogen content after denitriding and the intercept of the ordinate (i.e. at $r_N=0$) by the extrapolated linear part of the absorption isotherm.

The above discussed denitriding treatment in a H_2 -atmosphere cannot be applied to nitrides of relatively low thermodynamic stability, as e.g. Mo- or Mn-nitrides, as these nitrides may completely dissolve during this treatment (e.g. Ref. [28], [173]). The aim of the current study is (i) to test the stability of *Me*N nitrides of relatively high thermodynamic stability against a long time hydrogen reduction treatment and (ii) at the same time to propose and validate a denitriding method to correctly determine the stoichiometry of the alloying element nitrides in nitrided Fe-based alloys. To this end, Fe-V alloy was chosen as a model system due to high V-N interaction (see chapter 7 in Ref. [5]), the large solubility of V in ferrite [174] and a considerable amount of excess nitrogen occurring for this system [93]. The nitrogen content and the microstructure of nitrided and subsequently long-time denitrided Fe-2.23 at.%V thin foils was followed by weight measurements and electron probe micro-analysis (EPMA), and light optical microscopy, respectively. In order to better approach the final state of the denitriding process, powders instead of the usual foils were used as well. Powders have a much larger surface-to-volume ratio than thin foils and thus the escape of nitrogen from the specimen in a denitriding atmosphere is facilitated. It will be shown that ultimately complete dissolution of the VN-nitrides in the specimens occurs upon long-time hydrogen reduction. Against this background, the experimental strategy to prevent such dissolution of the nitrides is proposed.

5.2 Experimental

5.2.1 Specimen preparation

Fe-2.23 at.%V alloy was prepared by melting appropriate amounts of pure Fe (99.98 wt.%) and pure V (99.98 wt.%) in an Al₂O₃ crucible in an inductive furnace under a protective argon atmosphere (99.999 vol.%). After casting, the alloys had a cylindrical shape with a diameter of 10 mm and a length of 100 mm. The cast Fe-2.23 at.%V alloy rod was cold-rolled to sheets with a thickness of 1 mm. The obtained sheets were annealed for 2 h at 700 °C under flowing H₂ atmosphere to get a recrystallized grain structure and further cold-rolled to foils with a thickness of 0.2 mm and subsequently ground to a final thickness less than 100 μm. Subsequently, the specimens were annealed again at 700 °C for 2 h under flowing H₂ atmosphere to obtain a recrystallized grain structure. Thereafter, before nitriding, the thin foils were polished (last step: 1 μm diamond suspension) and cleaned with ethanol.

Fe-1.8 at.%V powder was procured from Nanoval GmbH&Co.KG, which had produced the Fe-V alloy powder from pure Fe (99.8 wt.%) and pure V (99.6 wt.%) by spray atomization of the alloy melt according to the Nanoval-process [92] under a high-velocity Ar-stream. The mean particle diameter of the Fe-1.8 at.%V powder was $d_{50} = 9.9 \mu\text{m}$.

The compositions of the cast Fe-2.23 at.%V alloy and the spray-atomized Fe-1.8 at.%V powder were determined by chemical analysis; the results have been gathered in Table 5.1. The contents of V and the contents of metal impurities (negligible) were determined by inductive coupled plasma optical emission spectroscopy (ICP-OES); the O and N contents were determined by carrier gas hot extraction and the C and S contents were determined by a combustion method.

Table 5.1: Alloying element contents of the Fe-V alloys used in this work. V contents were determined by inductive coupled plasma optical emission spectroscopy; C and S contents were determined by a combustion method; carrier gas hot extraction was applied for determination of O and N contents. Balance Fe.

alloy	V		O (wt.%)	N (wt.%)	C (wt.%)	S (wt.%)
	(at.%)	(wt.%)				
Fe-2.23 at.%V (foils)	2.23±0.02	2.04±0.05	0.050±0.004	<0.003	0.003±0.001	<0.001
Fe-1.8 at.%V (powders)	1.79±0.02	1.64±0.02	0.014±0.003	<0.002	0.004±0.002	<0.001

5.2.2 Nitriding and denitriding experiments

For nitriding, (i) the Fe-2.23 at.%V thin foils were suspended with a quartz fibre in a vertical quartz tube furnace and (ii) the Fe-1.8 at.%V powders were deposited onto a quartz half-tube slider and inserted into a horizontal quartz tube furnace. The furnaces have a temperature accuracy of ± 1 °C. Nitriding was performed in an ammonia/hydrogen gas flux (purity: H₂: 99.999 vol. %, NH₃: >99.998 vol. %) adjusted by mass flow controllers to the desired nitriding potential r_N [172]. The nitriding parameters employed in this study have been gathered in Table 5.2. All nitriding conditions have been chosen such that only a diffusion zone (ferrite with dissolved nitrogen and alloying element nitride particles) develops, i.e. other Fe-N phases such as iron-nitrides and Fe-N austenite do not develop [12]. Nitriding was terminated by removing the specimens from the hot zone of the furnace and cooling in the nitriding atmosphere (to maintain the nitrogen content of the specimen); cooling to room temperature required about 5 min.

The Fe-V thin foils (specimen weight of the order of 100 mg) were weighed before nitriding, after nitriding and after subsequent denitriding as a function of denitriding time using a Mettler Toledo UMX2 microbalance with an accuracy of ± 1 μ g.

5.2.3 Microstructural characterization

For metallographic investigations, (i) cross-sections of nitrided and denitrided specimens were prepared by cutting pieces from the foil specimens with a diamond wire saw, followed by embedding in Struers Polyfast (embedding temperature is about 180 °C; the heating time is about 5 min), and (ii) parts of the nitrided and denitrided powders were mixed with a small amount of embedding material and these mixtures were embedded. Cross-sections of foils and powder particles were then obtained by grinding and polishing of the embedded specimens (final polishing step: 1 μ m diamond suspension) and examined after subsequent etching with 1 % Nital (1 vol.% HNO₃ in ethanol) at room temperature for about 10 s. Light optical micrographs were taken using a Zeiss Axiophot microscope equipped with a digital camera (Olympus ColorView IIIu).

EPMA was performed on the cross-sections of nitrided and denitrided Fe-2.23 at.%V thin foils and of the nitrided and denitrided Fe-1.8 at.%V powder particles. For these measurements, a Cameca SX100 microprobe (acceleration voltage $U = 15$ kV, current $I = 100$ nA, spot size about 1 μ m) was used. To obtain the element contents at each measurement point, the intensities of the characteristic X-ray emission peaks were measured and divided by the corresponding intensities obtained from standard samples of pure Fe (for Fe-K _{β}), pure V (for V-K _{α}), and γ' -Fe₄N (for N-K _{α}). Elemental concentrations were calculated from the intensity ratios applying the $\Phi(\rho z)$ approach [94].

Table 5.2: Nitriding and denitriding treatments employed in the current work. The nitrogen activity is defined with respect to pure N₂-gas at a pressure of 1 atm and at the respective temperature (where $a_N = 1$).

alloy	treatment temperature [°C]		r_N =nitriding potential [atm ^{-½}]	nitrogen activity	total treatment time [h]
Fe-2.23 at.%V (thin foil in Fig. 5.1a))	500		0.1	25.26	16, 20
	denitriding	400	0	0	24, 28, 32, 36, 40, 44, 48, 52, 68, 84, 100, 116, 132, 148, 164, 180, 196, 268
		450	0	0	284, 300, 316, 332, 404, 524
Fe-2.23 at.%V (thin foil in Fig. 5.1b))	500		0.1	25.26	16, 32
	denitriding	450	0.01	1.43	104, 152
		450	0	0	224, 296, 368, 440, 512
Fe-1.8 at.%V (powders in Figs. 5.3a, d))	500		0.1	25.26	4, 17
	denitriding	400	0	0	8, 12, 20, 36, 52, 68
		400	0.01	0.74	8, 24, 40
Fe-1.8 at.%V (powders in Fig. 5.3c))	580		0.1	55.31	0.25, 0.5
	denitriding	400	0	0	4.25, 20.25
		580	0	0	4.25, 20.25

5.3 Results and discussion

5.3.1 Hydrogen reduction of nitrated Fe-V alloys

The nitrogen content of the Fe-2.23 at.%V thin foils after the nitrating treatment (16 h at 500 °C, implying homogeneous nitrating of the foil) is shown in Fig. 5.1 (at denitrating time = 0 h; see abscissa at top of the figure). The specimens were fully saturated with nitrogen after 16 h of nitrating as confirmed by additional nitrating treatments of 4 h (Fig. 5.1a) and 16 h (Fig. 5.1b)) showing no further nitrogen uptake.

The nitrogen content after nitrating is higher than that expected for precipitation of all V as VN plus the equilibrium amount of nitrogen dissolved in ferrite (approximately 0.08 at.% at the employed nitrating conditions [7]). Hence, a considerable amount of excess nitrogen is present. Upon ongoing (pre-)nitrating for times larger than necessary for homogeneous nitrating ($t > 16$ h at 500 °C, see Fig. 5.1), i.e. aging of the microstructure, the nitrogen content of the specimen slightly decreases, which can be attributed to coarsening of the precipitates: a decrease of precipitate-matrix interface area and less elastic accommodation of the precipitate/matrix misfit occurs upon coarsening, implying less capacity for adsorbed and dissolved excess nitrogen (see Chapter 2 and Chapter 4).

In Fe-Cr and Fe-V alloys of larger alloying element content (higher than about 2 at.% [18], [21]–[23], [25]) coarsening can occur either by the (slow) growth of the initially developed nitride particles (continuous coarsening (CC)), or by cellular transformation starting at a mobile interface/grain boundary (discontinuous coarsening (DC) [18], [21], [22], or, as in the case of Fe-Mo and Fe-Cr-Mo alloys, discontinuous precipitation (DP) (Ref. [31] and Chapter 6)) resulting in a microstructure of alternating ferrite and nitride lamellae. In the latter process the relaxation occurs (almost) completely during atomic rearrangement of the microstructure at the moving interface of the growing DC regions [150], [152]. Thus, practically no excess nitrogen is present in DC regions of the nitrated Fe-2.23 at.%V specimen (see Fig. 5.2b) and Ref. [18]). The release of excess nitrogen during DC can even lead to the development of iron nitrides (γ' -Fe₄N) at the CP/DC reaction front [48].

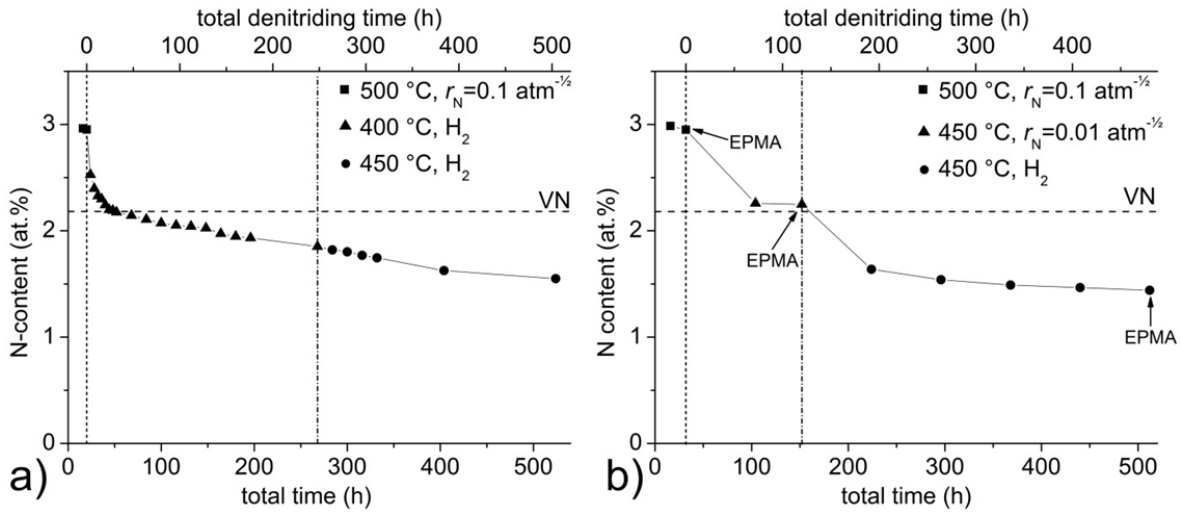


Fig. 5.1: a) The nitrogen content of Fe-2.23 at.%V thin foil after homogeneous nitriding for 20 h at 500 °C with a nitriding potential of $0.1 \text{ atm}^{-1/2}$ ($a_N=25.26$) (squares; at denitrifying time = 0 h: vertical dashed line), and as a function of subsequent time of denitrifying in flowing H_2 -atmosphere at 400 °C (triangles; until a denitrifying time of 248 h: vertical dash dotted line) and subsequently at 450 °C (circles; for denitrifying times > 248 h). b) The nitrogen content of Fe-2.23 at.%V thin foil after homogeneous nitriding for 32 h at 500 °C with a nitriding potential of $0.1 \text{ atm}^{-1/2}$ ($a_N=25.26$) (squares; at denitrifying time = 0 h: vertical dashed line) and as a function of subsequent “denitrifying” at 450 °C with a nitriding potential of $0.01 \text{ atm}^{-1/2}$ ($a_N=1.43$) (triangles; for denitrifying times up to 120 h: vertical dash dotted line) and subsequently as a function of denitrifying in flowing H_2 -atmosphere at 450 °C (circles; for denitrifying times > 120 h). Error bars of the nitrogen-content data, as determined by weight measurements (accuracy about $\pm 0.005 \text{ at.}\%$), are smaller than the size of the data points. Denitrifying in flowing H_2 leads to continuous loss of nitrogen, while “denitrifying” at $0.01 \text{ atm}^{-1/2}$ leads to a constant nitrogen content. Dashed horizontal line indicates the nitrogen content expected for full precipitation of all V as VN. Specimen conditions for which cross-sections were prepared and analysed by EPMA have been indicated in b) by black arrows (see Fig. 5.2).

Consistent with the above discussion, prenitriding at a higher temperature results in a lower nitrogen content (compare nitrogen contents of nitrified states, i.e. at denitrifying time = 0 h, in Fig. 5.3b)) of the nitrified specimens as larger precipitates are formed at higher temperature (see observations on Fe-Cr alloys in Ref. [20]).

Upon subjecting a Fe-2.23 at.%V thin foil, prenitrided at 500 °C with a nitriding potential of $0.1 \text{ atm}^{-1/2}$, to denitrifying in flowing H_2 at the lower temperature of 400 °C, initially a fast loss of nitrogen occurs to a level roughly corresponding to that expected for precipitation of all V in the

alloy as VN (Fig. 5.1a)). This suggests this (fast) loss of nitrogen concerns the less strongly bonded nitrogen, i.e. nitrogen of types (ii) and (iii) (see second paragraph of section 5.1). Upon continued treatment, the specimen continuously loses further nitrogen (i.e. the specimen then contains less nitrogen than necessary to bond all V as VN) but at a much slower rate, suggesting the loss of the (more) strongly bonded nitrogen of type (i). Close inspection of the nitrogen-concentration-depth profiles by EPMA (section 5.2.3), obtained after such denitriding for 360 h (Fig. 5.2e)), reveals that the decrease of nitrogen content is larger in the surface adjacent regions of the thin foil as compared to the specimen interior, indicating that the denitriding rate is faster closer to the surface. Indeed, the loss of nitrogen is very much faster upon denitriding of similarly nitrided and denitrided Fe-1.8 at.%V powders, which have a very high surface-to-volume ratio as compared to the Fe-2.23 at.%V thin foils (cf. Fig. 5.1 and Fig. 5.3a); note the different scales of the abscissae).

When the prenitriding was performed at the higher temperature of 580 °C (as compared to 500 °C; see above), a lower rate of nitrogen loss occurred upon subsequent denitriding at (the same as above) denitriding temperature of 400 °C (Fig. 5.3b)). The nitride particles precipitated at 580 °C are likely coarser than those precipitated at 500 °C, and thus, the release of (excess/dissolved) nitrogen is slower for the specimen nitrided at 580 °C (see discussion in the first paragraph of this section). On this basis it can also be understood that the DC regions, formed upon aging of the microstructure, retain a higher nitrogen content as compared to the surrounding CP regions upon denitriding in H₂, as clearly shown in Fig. 5.2f). Yet, after long-time denitriding (here 360 h) the nitrogen content of the DC regions has also become lower than that expected for all V precipitated as VN.

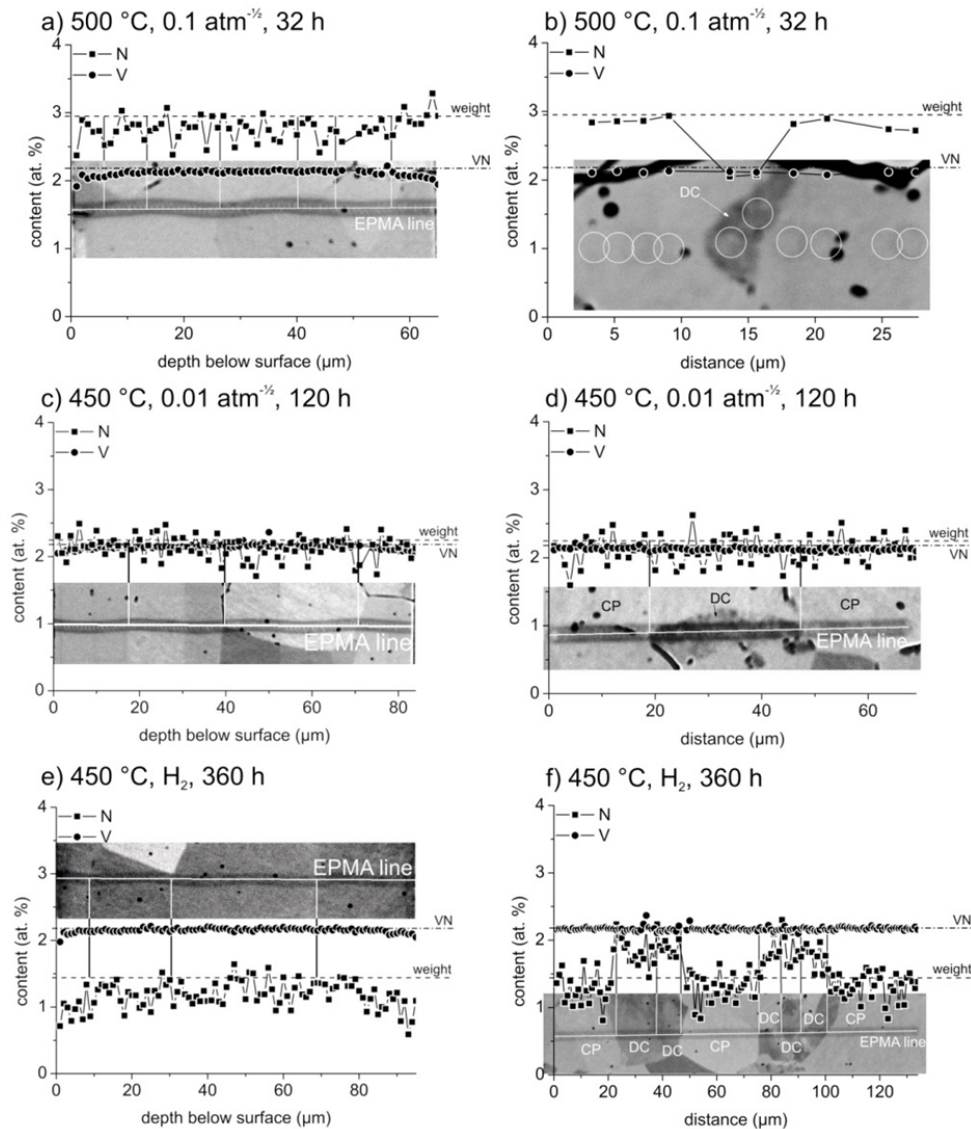


Fig. 5.2: EPMA line scans recorded across (surface to surface) the cross sections (a), c), e)) and through specific DC regions in the cross-sections (b), d), f)) of an Fe-2.23 at.%V alloy thin foil after a), b) nitriding at 500 °C for 32 h with a nitriding potential of $0.1 \text{ atm}^{-1/2}$ ($a_N=25.26$), and c), d) after subsequent “denitriding” at 450 °C for 120 h with a nitriding potential of $0.01 \text{ atm}^{-1/2}$ ($a_N=1.43$), and e), f) after subsequent denitriding at 450 °C for 360 h in flowing H_2 atmosphere (see arrows in Fig. 5.1). White horizontal lines indicate the position of the EPMA line scans. Vertical black and white lines indicate the positions of grain boundaries in (a), and c)-f)). White circles in b) indicate the locations of the EPMA measurements shown in the upper part of b). The dashed, horizontal lines indicate the nitrogen content calculated from the specimen weight change. The dash dotted, horizontal lines indicate the nitrogen content expected when all V in the alloy has precipitated as VN.

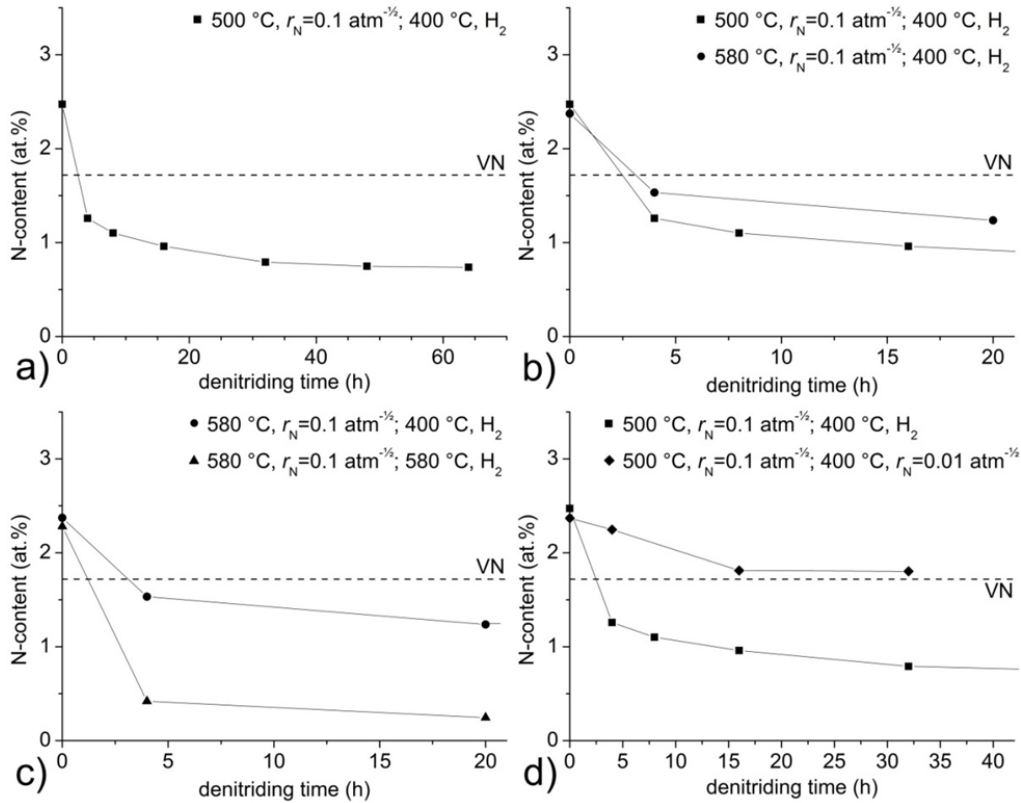


Fig. 5.3: a) Nitrogen content determined by chemical analysis of Fe-1.8 at.%V powders after homogeneous nitriding at 500 °C for 4 h with a nitriding potential of $0.1 \text{ atm}^{-1/2}$ ($a_N=25.26$) (at denitrating time = 0 h), and subsequent denitrating in flowing H₂-atmosphere at 400 °C, b) after homogeneous nitriding at 500 °C for 4 h with a nitriding potential of $0.1 \text{ atm}^{-1/2}$ ($a_N=25.26$) (at denitrating time = 0 h; squares) as compared to homogeneous nitriding at 580 °C for 15 min with a nitriding potential of $0.1 \text{ atm}^{-1/2}$ ($a_N=55.31$) (at denitrating time = 0 h; circles), and subsequent denitrating at 400 °C in flowing H₂-atmosphere, c) after homogeneous nitriding at 580 °C for 15 min with a nitriding potential of $0.1 \text{ atm}^{-1/2}$ ($a_N=55.31$) (at denitrating time = 0 h), and subsequent denitrating in flowing H₂-atmosphere at either (i) 400 °C (circles) or (ii) at 580 °C (triangles), d) after homogeneous nitriding at 500 °C for 4 h with a nitriding potential of $0.1 \text{ atm}^{-1/2}$ ($a_N=25.26$) (at denitrating time = 0 h), and subsequent “denitrating” at 400 °C with either (i) a nitriding potential of $0.01 \text{ atm}^{-1/2}$ ($a_N=0.74$) (diamonds) or (ii) in flowing H₂-atmosphere (squares). Error bars for the nitrogen-content data, as determined by chemical analysis (accuracy about $\pm 0.04 \text{ at.}\%$), are smaller than the size of the data points. The dashed horizontal lines indicate the nitrogen content expected for full precipitation of all V as VN.

If denitriding is performed at the same temperature as the nitriding temperature (580 °C in Fig. 5.3c)), the rate of nitrogen loss is relatively very fast and for the powder specimens an end stage of the denitriding process in flowing H₂ atmosphere can be attained: almost no nitrogen is present in the powder specimen after about 20 h of denitriding at 580 °C (Fig. 5.3c)).

In view of the thermodynamics of the system, it is no surprise that denitriding in H₂ in principle should lead to complete loss of all nitrogen in the specimen. The rate of nitrogen loss is determined by the surface-to-volume ratio of the nitrated solid (foil vs. powder specimen), the absolute value of the denitriding temperature, and the difference of the nitriding and subsequent denitriding temperatures. Further, as demonstrated in Fig. 5.1a, the (equilibrium and excess) dissolved nitrogen and excess nitrogen adsorbed at the nitride platelets faces are lost faster than nitrogen strongly bonded in the precipitates.

A number of studies have previously employed denitriding in flowing H₂-atmosphere of nitrated ferritic specimens [26], [157], [93], [64], [162], [165]. In most of these investigations, higher prenitriding temperatures and longer prenitriding times than in the current study were employed, e.g. prenitriding at 580 °C for 24 h with a nitriding potential of 0.104 atm^{-½} in Ref. [93]. Therefore, the microstructure likely consisted of relatively coarse nitride particles that are less prone to dissolution. Yet, in some of the previous studies [26], [93], the nitrogen content determined after denitriding was found to be a little lower than that expected for full precipitation of all alloying element as MeN in the employed alloys. This was attributed to an O-contamination of the specimens leading to a part of the alloying element being bonded as oxides, which is thus, as the oxides are generally more stable than the nitrides, inaccessible for the nitriding reaction. However, the O-content of the alloy was insufficient to explain the (small) amount of unreactive alloying element(s). It is therefore suggested that the observed small discrepancy might originate from the dissociation of a very small amount of the nitride particles during denitriding.

5.3.2 Strategy for denitriding; stabilization of nitrated microstructure

The above discussed, observed successive loss of the various types of nitrogen upon denitriding in a H₂-atmosphere suggests a possible strategy to determine the amount of nitrogen of type (i), i.e. the nitrogen strongly bonded in the nitrides: to stop denitriding once the initial fast loss of nitrogen of types (ii) and (iii) has completed, i.e. at the transition from fast to slow loss of nitrogen. However, the local rate of nitrogen loss depends on the depth below the surface (see discussion of Fig. 5.2e) in section 5.3.1) and therefore the determination of the time of transition from a fast to a slow rate of nitrogen loss becomes smeared, which obstructs precise determination of a time of transition. Moreover, determination of such a transition time is very labori-

ous, as the specimen weight has to be determined for a series of denitriding times; i.e. a series of experiments has to be performed.

Another (less laborious) procedure to preserve the nitrides in the specimen, upon denitriding to get rid of nitrogen of types (ii) and (iii), can be to maintain a small nitrogen activity in the gas phase such as to stabilize the nitride (MeN) phase. The stable phases occurring as function of the nitrogen activity (reference state: pure N_2 -gas at ($p_0=$) 1 atm at the temperature concerned here (450 °C or 580 °C)) and the molar fraction of alloying element Me have been calculated employing the Thermo-Calc software [175] with the TCFE7 database [176] for the Fe-Al-N, Fe-Cr-N, Fe-Mo-N, Fe-Ti-N, and Fe-V-N systems. The results have been gathered in Fig. 5.4.

The nitriding potential r_N (upper abscissa of Fig. 5.4) of an NH_3 - H_2 gas atmosphere with the same nitrogen activity a_N (reference state: pure N_2 -gas at ($p_0=$) 1 atm at the temperature concerned here (450 °C or 580 °C)) as the calculated activity of nitrogen in the solid phases (lower abscissa of Fig. 5.4) is given by [5]:

$$r_N = \frac{a_N}{K_N} = \frac{p_{NH_3}}{p_{H_2}^{3/2}} \quad (5.1)$$

where p_{NH_3} is the partial pressure of NH_3 , p_{H_2} is the partial pressure of H_2 , and K_N is the temperature dependent equilibrium constant of the nitriding reaction:



which can be calculated with the Gibbs energy functions for N_2 , H_2 , and NH_3 as given in Ref. [177]. Nitriding in an NH_3 - H_2 gas atmosphere is equivalent with nitriding in a (hypothetical) N_2 gas atmosphere of a partial pressure of N_2 given by $a_N^2 \cdot p_0$, with p_0 as the reference pressure (=1 atm, see above) [5].

Comparison of the five systems presented in Fig. 5.4, shows that the minimal nitrogen activity at which the concerned nitride phase in ferrite is stable, as indicated by the extent of the α -Fe(N)+ MeN two-phase field, roughly corresponds with the predicted trend of the interaction parameter, I , describing the strength of the Me -N interaction, as presented in Ref. [5]: Ti-N $I=1.7$, V-N $I=1.7$, Al-N $I=1.0$, Cr-N $I=0.8$, and Mo-N $I=0.2$ (the lowest value of a_N compatible with the presence of stable MeN in an α -Fe matrix occurs for $Me=Ti$). Note that according to these calculations hexagonal, wurtzite-type AlN has a slightly larger stability than cubic VN and hexagonal V_2N , whereas the interaction parameters of Al-N (1.0) and V-N (1.7) would suggest

the opposite. This is a straightforward consequence of the lower strain energy associated with the formation of VN (112 kJ/mol) as compared to that of AlN (272 kJ/mol); the role of strain energy is incorporated in the calculation of l , whereas the a_N calculations presented in Fig. 5.4 only pertain to the chemical energy differences.

With increasing *Me*-content of the alloy, the minimum nitrogen-activity to stabilize the forming nitride phase decreases, as the solubility product of the below reaction:



is surpassed at decreasing nitrogen activity. The occurrence of intermetallic phases (Fe_2Me Laves phases in the Fe-Ti and Fe-Mo systems) or of a nitride of smaller nitrogen content (Me_2N in Fe-Cr and Fe-V) involves a minimal nitrogen activity, to stabilize the initially developed nitride phase (MeN) in the α -Fe matrix at high nitrogen activity during (pre-)nitriding; this minimal nitrogen activity has the value pertaining to the α -Fe/ MeN /(Fe_2Me/Me_2N) three-phase equilibrium (at the temperature concerned), represented by the straight vertical lines in Figs. 5.4c-j). Accordingly, this specific minimal nitriding potential, to stabilize the initially forming nitride, is independent of the *Me*-content of the alloy, which is a direct consequence of Gibbs' phase rule.

The calculated minimal nitrogen activity required to stabilize the nitride phases are very low and technically difficult to control. At a nitrogen activity of 1, i.e. in pure N_2 gas at 1 atm at the temperature concerned (dashed vertical lines in Fig. 5.4) most alloying element nitrides are stable and one might thus propose denitriding in a, for the rest inert, gas atmosphere at 1 atm containing a certain, substantial amount of N_2 . However, according to Ref. [178] (see also chapter 1 in Ref. [5]), desorption of N_2 gas from *pure Fe* surfaces can be neglected at temperatures below 500 °C and thus the kinetics of nitrogen loss (also of the less strongly bonded types (ii) and (iii)) is very slow due to the slow N_2 desorption kinetics⁶. This also concerns the "forward", i.e. nitriding, reaction by nitrogen absorption from N_2 gas. Hence, for Fe-based Fe-*Me* specimens, in practice N_2 can be considered an inert gas at the common denitriding temperatures. In H_2 -containing atmospheres denitriding proceeds by the much faster formation of NH_3 [5], [178]. Thus, in order to establish a denitrided state in an experimentally viable time, denitriding needs to be performed in (NH_3 -) H_2 -atmospheres.

⁶ In this context it is worthwhile to refer to experiments where annealing of the comparatively very unstable Fe-nitrides γ' - Fe_4N_{1-x} and ϵ - Fe_3N_{1+x} was performed in inert gas or vacuum: *no* dissociation occurred (see Refs. [234], [235] for such annealing experiments with ϵ - Fe_3N_{1+x}/γ' - Fe_4N_{1-x} double layers on ferrite).

Employing the above consideration to the present alloy of Fe-2.23 at.%V at 450 °C, a minimal nitrogen activity of about 1.3×10^{-9} , corresponding to a $\text{NH}_3\text{-H}_2$ -atmosphere with a nitriding potential of $9.1 \times 10^{-12} \text{ atm}^{-1/2}$, is required to stabilize VN. As VN was found to dissociate upon annealing in flowing H_2 at 450 °C (see above, and Figs. 5.1 and 5.3), apparently not even this low nitriding potential is established in the continuously renewed H_2 -atmosphere by the NH_3 forming by denitriding of the specimen.

The general idea of applying a low nitrogen activity to stabilize the nitrides can now be adopted. In the nitriding furnace employed in this work, a $\text{NH}_3\text{-H}_2$ atmosphere with a nitriding potential as low as $0.01 \text{ atm}^{-1/2}$ ($a_{\text{N}}=1.426$ at 450 °C) can be controlled with good accuracy. As a consequence of this higher than required minimal nitrogen activity, some nitrogen will remain dissolved in the matrix upon denitriding: 0.003 at.% nitrogen at 450 °C and $0.01 \text{ atm}^{-1/2}$ in unstrained ferrite [7], and some unknown amount of excess nitrogen (dissolved and adsorbed) may occur. Yet this treatment, as a denitriding treatment to determine the amount of nitrogen incorporated in MeN , is appropriate as follows from the current experiments: the fixed nitrogen content, resulting by such “denitriding”, has become independent of treatment time for denitriding of Fe-2.23 at.%V foils for times beyond 72 h with $r_{\text{N}}=0.01 \text{ atm}^{-1/2}$ at 450 °C (Fig. 5.1b) and for denitriding of the Fe-1.8 at.%V powders for denitriding times beyond 20 h with $r_{\text{N}}=0.01 \text{ atm}^{-1/2}$ at 450 °C (Fig. 5.3d)). The nitrogen level attained in this case is also constant throughout the entire specimen depth (Fig. 5.2c)), and independent of precipitate size, as shown by the same nitrogen content in CP and DC regions of such samples (Fig. 5.2d)).

After the denitriding treatments discussed above, a nitrogen content slightly higher than that expected for all V being precipitated as VN is observed (2.25 at.% N for Fe-2.23 at.%V alloy (foils), 1.81 at.% N for Fe-1.8 at.%V alloy (powders)). This minimal difference may be due to either the above mentioned equilibrium dissolved nitrogen, plus (a very minimal amount of) excess nitrogen. Hence, the stoichiometry of the vanadium nitride is clearly given by VN: no Fe is contained in the nitrides as likely erroneously indicated by APT analysis (Refs. [29], [65], [166]–[168], [171] and Chapter 6), in agreement with results from earlier work in Ref. [93], where “less perfect” denitriding in pure H_2 was performed. On the basis of the results presented here, the method proposed, applying a low nitriding potential during denitriding, was very recently also successfully applied by the present authors for nitrides with a very low stability: Mo-containing nitrides in nitrided Fe-1 at.%Cr-1 at.%Mo alloy (Chapter 6).

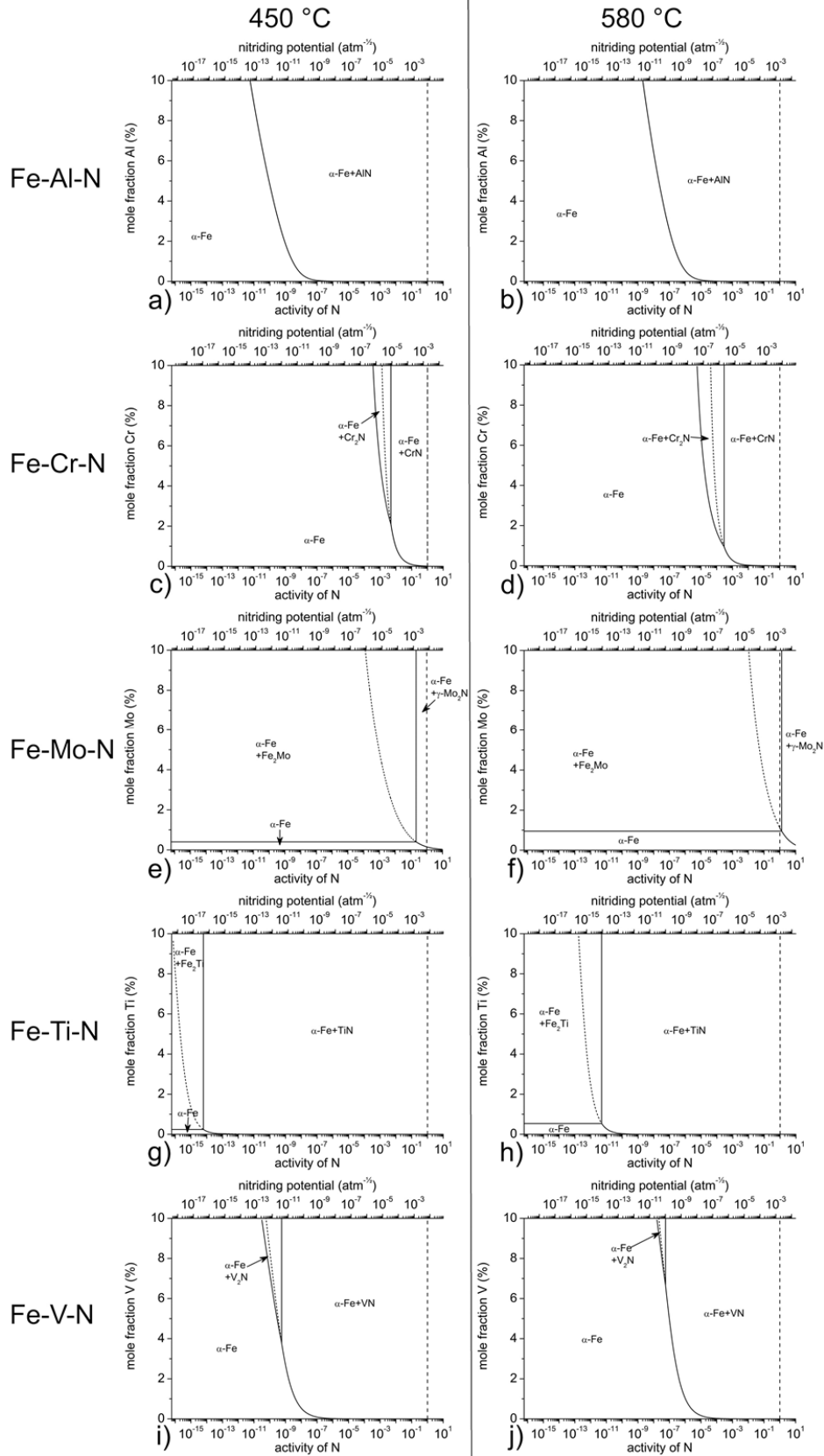


Fig. 5.4: Figure 1: Fe-*Me*-N phase diagrams (Nitrogen activity vs. *Me*-content) calculated at 450 °C (left) and at 580 °C (right) for the systems a), b) Fe-Al-N, c), d) Fe-Cr-N, e), f) Fe-Mo-N, g), h) Fe-Ti-N, and i), j) Fe-V-N by using the Thermo-Calc software [175] with the TCFE7 database [176]. The reference state for calculating the activity of nitrogen was chosen as pure N₂ gas at 1 atm at the temperature concerned. The nitriding potential of an NH₃-H₂ gas atmosphere (upper abscissa) with the same nitrogen activity (see Equation (5.1)) as the calculated activity of nitrogen in the solid phases (as given on the lower abscissa) was obtained employing the Gibbs energy functions for N₂, H₂, and NH₃ from the NIST-JANAF tables [177]. The short dashed lines indicate the metastable extensions of the α -Fe/ α -Fe+*Me*N equilibrium towards lower nitrogen activities. The vertical, dashed lines correspond to a nitrogen activity of 1 (i.e. that of pure N₂ at 1 atm at the temperature concerned).

5.4 Conclusions

Denitriding, as a method to derive from mass changes the stoichiometric composition of (nanosized) alloying element nitrides developed upon nitriding iron-based alloys, requires application of (gas) atmospheres of a minimal nitrogen activity.

Denitriding in a H₂-atmosphere, in principle and ultimately, leads to the full dissociation of the alloying element nitrides and loss of all nitrogen from the specimen.

The absolute value of nitrogen loss during denitriding (and the chance of arriving at a constant level of nitrogen pertaining to the amount of nitrogen contained in the alloying element nitrides) depends on:

- the surface-to-volume ratio of the solid (e.g. foil vs. powder particle);
- the (pre-)nitriding temperature;
- the denitriding temperature;
- the difference of nitriding and denitriding temperatures.

The rate of loss of nitrogen from the specimen during denitriding exposes two regimes:

- (i) an initial, fast denitriding due to loss of less strongly bonded nitrogen (dissolved nitrogen and nitrogen adsorbed/seggregated at the nitride-platelet faces), and
- (ii) a subsequent slow denitriding associated with the loss of strongly bonded nitrogen (in the alloying element nitride).

Successful denitriding, i.e. leaving only the strongly bonded nitrogen in the specimen, can be performed in two ways:

- (i) by application of a H₂-atmosphere and a denitriding time at the transition of high-rate of nitrogen loss to low-rate of nitrogen loss, or
- (ii) by application of a very low nitriding potential (say 0.01 atm^{-1/2}) leading to a final constant nitrogen level throughout the specimen.

The present analysis indicates that the composition of vanadium nitride developing in the (ferritic) matrix of Fe-V alloys upon nitriding is given by VN (i.e. it contains no significant amount of Fe).

Acknowledgements

The authors would like to thank Mr. P. Kress and Mr. G. Hörner for assistance with the nitriding experiments, Mr. S. Hammoud for assistance with chemical analysis (all with Max Planck Institute for Intelligent Systems), and Mrs. S. Haug for assistance with the EPMA experiments (both with Max Planck Institute for Solid State Research).

Chapter 6

Continuous and discontinuous precipitation in Fe-1 at.%Cr-1 at.%Mo alloy upon nitriding; crystal structure and composition of ternary nitrides

Tobias Steiner, Sai Ramudu Meka, Bastian Rheingans, Ewald Bischoff, Thomas Waldenmaier, Guma Yeli, Tomas L. Martin, Paul A.J. Bagot, Michael P. Moody, Eric J. Mittemeijer

Abstract

The internal nitriding response of a ternary Fe-1 at.%Cr-1 at.%Mo alloy, which serves as a model alloy for many CrMo-based steels, was investigated. The nitrides developing upon nitriding were characterized by X-Ray diffraction, Scanning Electron Microscopy, Electron Probe Microanalysis, Transmission Electron Microscopy, and Atom Probe Tomography. The developed nitrides were shown to be (metastable) ternary mixed nitrides, which exhibit complex morphological, compositional, and structural transformations as a function of nitriding time. Analogous to nitrided binary Fe-Cr and Fe-Mo alloys, in ternary Fe-Cr-Mo alloys initially continuous precipitation of fine, coherent, cubic, NaCl-type nitride platelets, here with the composition $(\text{Cr}_{1/2}, \text{Mo}_{1/2})\text{N}_{3/4}$, occurs, with the broad faces of the platelets parallel to the $\{100\}_{\alpha\text{-Fe}}$ lattice planes. These nitrides undergo a discontinuous precipitation reaction upon prolonged nitriding leading to the development of lamellae of a novel, hexagonal CrMoN_2 nitride along $\{110\}_{\alpha\text{-Fe}}$ lattice planes, and of spherical cubic, NaCl-type $(\text{Cr}, \text{Mo})\text{N}_x$ nitride particles within the ferrite lamellae. The observed structural and compositional changes of the ternary nitrides have been attributed to the thermodynamic and kinetic constraints for the internal precipitation of (misfitting) nitrides in the ferrite matrix.

6.1 Introduction

Many technologically important steels are based on the Fe-Cr-Mo(-C) system, due to superior hardenability, toughness, anti-corrosion properties, and microstructural stability at elevated temperatures, associated with the combined presence of Cr, Mo and C in these steels [1], [68], [179]. Further enhancement of the fatigue, wear and corrosion resistance of these steels can be achieved by nitriding, a thermochemical surface treatment process by which N is introduced into the surface adjacent regions of the steel components [5], [6], [8]. Cr is present in most nitriding steels due to its strong interaction with N leading to the formation of Cr-N-nitrides. Mo is usually added to nitriding steels to enhance the properties of the unnitrided core of the components. However, Mo does also interact with N, albeit relatively slowly [31]. Hence, in order to

optimize the nitriding response of the material to achieve desired property profiles, control and, to that end, understanding of the interaction of inwardly diffusing N with both alloying elements present in steel is necessary. This is the background for the present investigation of the nitriding behavior of Fe-1 at.%Cr-1 at.%Mo alloy.

Upon nitriding of binary Fe-Cr [20]–[23], [25], [180] and Fe-Mo [31], [181] alloys initially cubic, NaCl-type CrN and cubic, NaCl-type γ -Mo₂N (here 50 % of the octahedral-interstitial sublattice are not occupied by N), respectively, form as (semi-)coherent platelets with their broad faces parallel to the $\{100\}_{\alpha\text{-Fe}}$ lattice planes and with a Baker-Nutting (BN) orientation relationship (OR) [182] with the ferrite matrix. The kinetics of formation of CrN is considerably faster than that of γ -Mo₂N. This initial microstructure, composed of coherent nitrides finely dispersed in the ferrite matrix, is commonly referred to as *continuously precipitated (CP)*. Upon nitriding for prolonged time, Fe-Cr alloys with sufficiently high Cr-content undergo a *discontinuous coarsening (DC)* reaction [20]–[23], [25], [180], whereas in Fe-Mo alloys a *discontinuous precipitation (DP)* reaction of γ -Mo₂N to δ_3 -MoN occurs [31].

Information on the nitriding behavior of Fe-Cr-Mo-based technical alloys is scarce [183]–[185] and fundamental investigation on the nitriding behavior of ternary Fe-Cr-Mo alloys has not been carried out until now. The interaction of both Cr and Mo in a ternary Fe-Cr-Mo model alloy with the N introduced by a nitriding treatment is the focal point of the current work on the gaseous nitriding of a model Fe-1 at.%Cr-1 at.%Mo alloy (henceforth abbreviated as Fe-1Cr-1Mo). Some preliminary results of this project have been presented at a recent conference [186]. The here presented detailed characterization of the developing nitrides, employing X-ray diffraction (XRD), scanning electron microscopy (SEM), electron probe microanalysis (EPMA), transmission electron microscopy (TEM), and atom probe tomography (APT), reveals the sequential development of ternary nitrides.

6.2 Experimental

6.2.1 Specimen Preparation and Nitriding

The Fe-1Cr-1Mo alloy was prepared by melting elemental Fe (99.98 wt.%), Cr (99.99 wt.%), and Mo (99.95 wt.%) in an induction furnace under a protective Ar atmosphere, followed by casting into a Cu crucible. The surfaces of the cast were ground with SiC paper to remove surface contaminants. The cast slab was cold rolled to a sheet of 1 mm thickness. From this sheet, foils (dimensions 1 x 20 x 15 mm³) were cut. The surfaces of the foils were ground and polished. Results of the chemical analysis of the cast alloy are shown in Table 6.1.

Table 6.1: Composition of the Fe-1Cr-1Mo alloy used in this work. The Cr, Mo, Mn and Si contents were determined by inductive coupled plasma optical emission spectroscopy; the C content was determined by a combustion method; carrier gas hot extraction was applied for determination of the O and N contents.

element	Cr	Mo	Mn	Si	C	O	N	Fe
content [at. %]	1.01±0.01	0.98±0.01	<0.001	<0.02	0.010±0.001	0.021±0.004	<0.004	bal.

The foils were encapsulated in an Ar-filled quartz tube and recrystallized at 750 °C for 30 min. Before nitriding, the specimens were polished (last stage 1 µm diamond suspension) and cleaned, successively, with ethanol, acetone and isopropanol.

The foil specimens were nitrided in a vertical multizone quartz tube furnace (temperature accuracy ±1 K) in a flowing NH₃/H₂ gas mixture. High purity ammonia (>99.998 vol.%) and hydrogen (>99.999 vol.%) gases were used. The flow rates of the ammonia and hydrogen gases were adjusted with calibrated mass flow controllers to get a nitriding potential r_N of 0.1 atm^{-½}, $r_N = \frac{p_{\text{NH}_3}}{p_{\text{H}_2}^{3/2}}$, where p represents the partial pressure [172]. Nitriding was performed at 580 °C for total nitriding times in the range of 1 h to 504 h. For the denitriding treatments at 450 °C, r_N was adjusted to 0.01 atm^{-½} and the total denitriding time was 96 h. Note that under the employed nitriding conditions iron nitrides cannot develop (on the surface) upon nitriding pure iron [12]. The nitriding treatment was terminated by quenching the specimen into N₂-flushed water at room temperature. The Fe-1Cr-1Mo thin foils were weighed before nitriding, after nitriding and after subsequent denitriding using a Mettler Toledo UMX2 microbalance with an accuracy of ±1 µg. From the gain/loss in weight of the foils, the amount of N taken up/lost by the foils was calculated.

6.2.2 Microstructural Characterization

To identify the different nitride phases developed upon nitriding, X-ray diffractograms were recorded from the surface of the nitrided foil specimens using a PANalytical MPD diffractometer operating in Bragg-Brentano geometry, and applying Co-K_α radiation and a graphite monochromator in the diffracted beam. The diffraction-angle 2θ range of 10°-130° 2θ was scanned with a step size of 0.009° 2θ . During the measurement, the specimen was rotated around its surface normal to improve the crystallite statistics. For phase identification, the substance reference patterns in the ICDD database [97] were used. Rietveld refinement of the diffraction da-

ta for identification of a new ternary nitride was performed with the TOPAS (Bruker AG) software. A pseudo-Voigt function was employed for the peak shape [187], [188]. The height displacement of the specimen in the diffractometer circle [96] was determined from the positions of the four ferrite peaks in the measured 2θ -range.

For metallographic investigations, parts of the nitrated specimens were cut off normal to the specimen surface and a protective Ni plating was applied to these parts by electrodeposition in a Watts bath. Such Ni-plated pieces were embedded in Struers Polyfast. The embedded specimens were ground, polished (last stage 1 μm diamond suspension) and etched with 1 % Nital. A LEO 1530 VP scanning electron microscope (SEM) equipped with a field emission gun and an in-lens detector was employed in this study.

Elemental (Fe, N, Cr and Mo) concentration-depth profiles were recorded from the cross-sections employing a Cameca SX100 electron probe microanalysis (EPMA) system at 15 kV and a current of 100 nA. Characteristic X-ray emission peaks were measured and divided by the corresponding intensities obtained from standard samples of pure Fe (for Fe- K_{β}), pure Cr (for Cr- K_{α}), pure Mo (for Mo- L_{α}) and γ -Fe₄N (for N- K_{α}). Elemental concentrations were calculated from the intensity ratios employing the $\Phi(\rho z)$ approach [94].

For TEM investigations of the microstructure, rectangular pieces from the nitrated foils (edge length 3 mm) were cut and ground to discs of about 3 mm diameter. The discs were ground mechanically, dimpled and Ar-ion milled (3 kV, 8° ion angle of incidence, approx. 2 h, liq.-N₂ cooling). In order to obtain isolated nitride particles for TEM-based phase analysis, a nitrated thin foil (thickness approx. 200 μm) specimen was suspended in a solution of 2 vol.% HCl, 50 vol.% water, and 48 vol.% ethanol and electrolytically dissolved at 1.6 V for about 1 h. In order to remove the nitride particles from the specimen surface, the specimen was sonicated in the same electrolytic solution after every 15 min of the electrolytic dissolution. The thus obtained solution containing nitride particles was centrifuged for 2 h and the solution was discarded. Subsequently, the residue was rinsed with distilled water and ethanol, by ultrasonically suspending the residue in the liquid concerned and subsequent centrifuging. Finally, approx. 50 μl of a suspension of the residue, as produced by ultrasonic treatment in isopropanol, was placed onto a carbon-film for TEM analysis using a μl -syringe. After evaporation of the isopropanol, finely distributed nitride particles suitable for TEM analysis remained. A Zeiss 912 Omega TEM operating at an acceleration voltage of 120 kV and a Philips CM 200 TEM operating at 200 kV equipped with an EDAX energy dispersive X-ray (EDX) spectrometer were employed in this study.

6.2.3 Atom Probe Tomography

For APT analysis, the 1 x 20 x 15 mm³ foils (cf. section 6.2.1) were ground to a thickness of 0.6 mm and prepared for nitriding as described in section 6.2.1. The nitriding times employed, at 580 °C and a nitriding potential of 0.1 atm^{-½}, were 72 h to obtain a homogeneous CP microstructure, and 216 h to obtain a homogeneous DP microstructure. After the nitriding treatment, the foil specimens were sliced into small “matchsticks” of dimensions 0.6 x 0.6 x 15 mm³ by electrical discharge machining. The surfaces of the matchsticks were then ground and polished to dimensions of 0.5 x 0.5 x 15 mm³ with SiC-paper up to a final grid of P4000 and cleaned, successively, in acetone and isopropanol.

The matchsticks were then polished into needle-shaped specimens for APT by a standard two-stage electro-polishing method using 25 % perchloric acid and acetic acid with a voltage between 12-18 V in the first stage, and in the second stage 2 % perchloric acid and 2-Butoxyethanol with a voltage between 6-8 V [189]. APT investigations were carried out using a Cameca Local Electrode Atom Probe (LEAP) 3000X HR. The specimens were analyzed in pulsed-laser mode, applying laser pulse energies of 0.2-0.4 nJ. The specimen temperature and pulse fraction rate were set as 50 K and 200 kHz, respectively. The elemental distribution maps and quantitative information of the local chemistry of the precipitates were obtained from the reconstructed APT data by the Integrated Visualization & Analysis Software (IVAS) package which is based on the standard reverse projection algorithm [190]; for details see Ref. [189].

6.3 Results and evaluation

Upon nitriding an Fe-1Cr-1Mo alloy substrate, a nitrided zone develops in the surface adjacent region, as revealed by the more pronounced etching contrast of this region in light micrographs (LM) (cf. Ref. [186]). The nitride particles developing in the initially forming CP regions are too small to be revealed individually by LM or (conventional) SEM (see TEM analysis presented in section 6.3.1). Upon prolonged nitriding (after a time of the order of 10 hours at 580 °C), DP-regions develop in which a lamellar morphology of nitrides occurs which can be observed by LM and SEM.

6.3.1 Continuously precipitated nitrides; initial stages

X-ray diffractograms recorded from the surface of specimens nitrided at 580 °C for different times are shown in Fig. 6.1. After nitriding, all ferrite-matrix reflections have split into two peaks. The peak at lower diffraction angle emerges upon nitriding and is of higher relative integrated intensity after short nitriding times. With increasing nitriding time, the peak at higher diffraction angles increases in relative integrated intensity. No additional reflections pertaining to second (nitride) phases can be detected.

TEM bright-field (BF) micrographs reveal the initial formation of finely distributed, nano-sized platelets with their broad faces parallel to $\{100\}_{\alpha\text{-Fe}}$ lattice planes of the ferrite matrix (Fig. 6.2a). The corresponding $[001]_{\alpha\text{-Fe}}$ zone axis selected area electron diffraction patterns (SADPs) show, corresponding to the coherent nature of the nitride particles, pronounced streaking along $\langle 100 \rangle_{\alpha\text{-Fe}}$ directions owing to the small size and the misfit strain perpendicular to these directions (i.e. perpendicular to the platelet faces; Fig. 6.2b). Upon slight tilting of the specimen out of the $[001]_{\alpha\text{-Fe}}$ zone axis intensity maxima can be discerned on the streaks in the SADPs of the nitrided Fe-1Cr-1Mo alloy (Fig. 6.2c) at the positions expected for diffraction spots of a cubic NaCl-type nitride having a lattice parameter close to $\sqrt{2}$ times the lattice parameter of the ferrite matrix ($\sqrt{2} \cdot 2.8664 \text{ \AA} = 4.054 \text{ \AA}$); the lattice parameter of CrN is 4.14 Å (card 011-0065 in Ref. [97]), and that of $\gamma\text{-Mo}_2\text{N}$ is 4.163 Å (card 025-1366 in Ref. [97]). The position of these intensity maxima with respect to the diffraction spots of the ferrite matrix is compatible with a Baker-Nutting OR [182] of nitride precipitates and matrix (see Fig. 6.2d)).

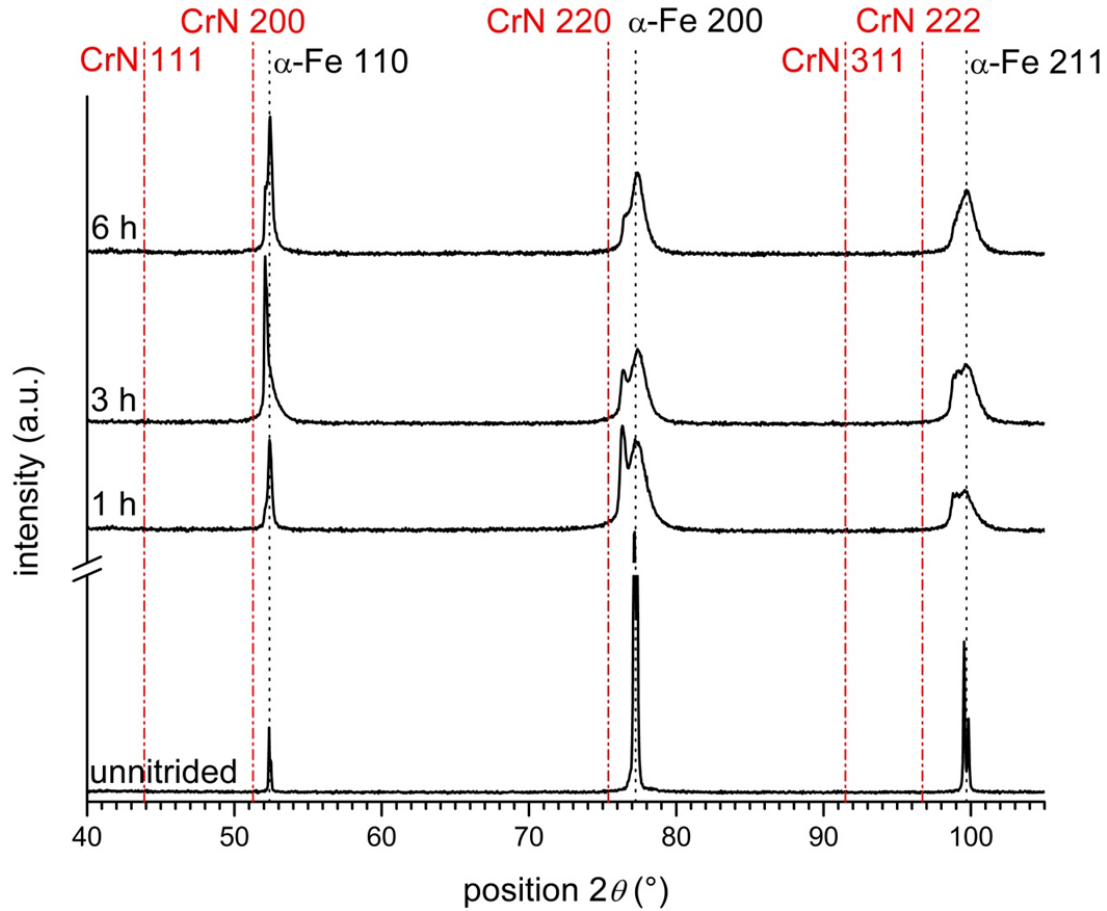


Fig. 6.1: XRD diffractograms (Co- K_{α}) recorded from the surface of Fe-1Cr-1Mo specimens nitrided at 580 °C with a nitriding potential of 0.1 atm^{-1/2} for the nitriding times indicated; full patterns were normalized with respect to their integrated intensities. The reflection positions expected for CrN have been indicated by red dash-dotted lines, those for pure α -Fe by black dotted lines (see Ref. [186]).

In order to find out, whether the precipitation of Cr and Mo has occurred either as separate binary nitrides or as a ternary mixed nitride, local composition analyses have been performed by APT. The spatial distribution of the elemental species found in the mass spectra is given in Fig. 6.3a. Evidently, the matrix is strongly depleted of the original alloying elements and the N-rich regions, i.e. the nitride platelets, are rich in both Cr and Mo. Iso-concentration surfaces enclosing regions of a combined Mo, Cr and N concentration larger than 4 at.% have been plotted for the analyzed tip to more or less separate the nitride particles from the matrix. These iso-concentration surfaces are presented in Fig. 6.3b, thereby highlighting the orientation and spatial distribution of the platelets. The morphology of the platelets is consistent with that observed by TEM (cf. Fig. 6.2 and Fig. 6.3a).

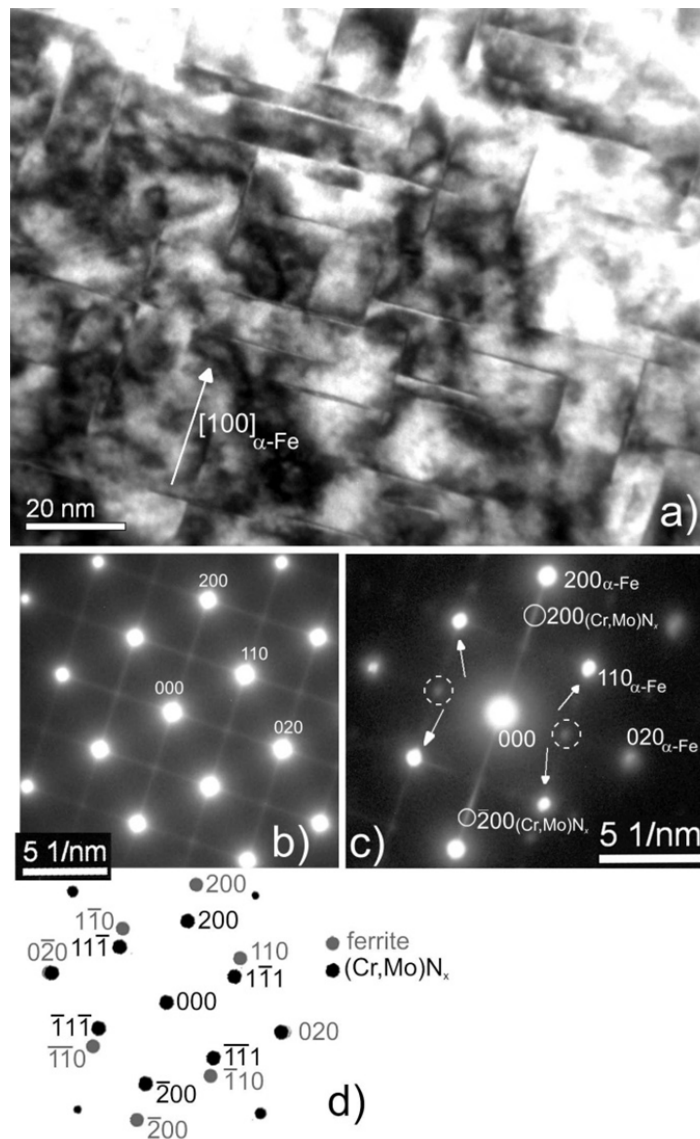


Fig. 6.2: a) TEM BF micrograph at a depth of 100 μm below the surface and b) the corresponding $[001]_{\alpha\text{-Fe}}$ electron beam direction/zone axis (ZA) SADP of the Fe-1Cr-1Mo specimen nitrided at 580 $^{\circ}\text{C}$ for 6 h with a nitriding potential of 0.1 $\text{atm}^{-\frac{1}{2}}$. Platelets occur along $\{001\}$ habit planes of the ferrite matrix. In the $[001]_{\alpha\text{-Fe}}$ zone axis SADP distinct streaking along $\langle 100 \rangle_{\alpha\text{-Fe}}$ directions is present. c) Slight tilting of the specimen out of the $[001]_{\alpha\text{-Fe}}$ zone axis reveals intensity maxima at $200_{(\text{Cr,Mo})\text{N}_x}$ positions on the streaks. Expected $111_{(\text{Cr,Mo})\text{N}_x}$ positions have been indicated with white arrows; dashed circled spots originate from magnetite Fe_3O_4 present on the TEM foil owing to unavoidable oxidation of the foil [33]. d) Schematic diffraction pattern of the ferrite matrix in $[001]_{\alpha\text{-Fe}}$ orientation and one variant of $(\text{Cr,Mo})\text{N}_x$ in a Baker-Nutting orientation relationship (see Ref. [186]).

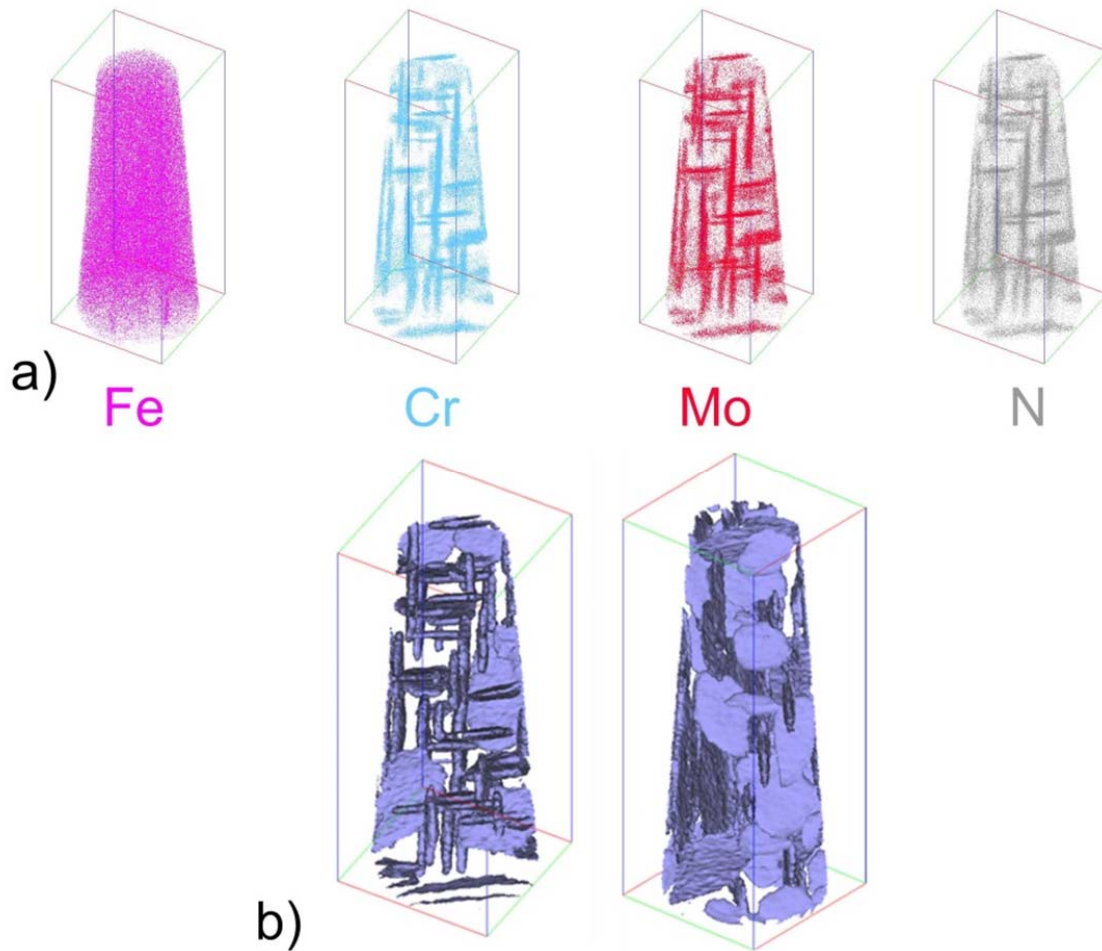


Fig. 6.3: a) Distribution of atomic species in an APT tip prepared from a Fe-1Cr-1Mo alloy specimen that was nitrided homogeneously at 580 °C for 72 h with a nitriding potential of $0.1 \text{ atm}^{-1/2}$. The size of the displayed box is $230 \times 93 \times 94 \text{ nm}^3$. Regions of increased contents of Cr, Mo, N species correspond to the ternary $(\text{Cr},\text{Mo})\text{N}_x$ nitrides platelets evidenced by TEM. Due to restrictions in the resolution of the APT technique, the platelets appear thicker (and longer) than as indicated by the TEM analysis. b) Compositional iso-concentration surfaces of $\text{Cr}+\text{Mo}+\text{N} = 4 \text{ at.}\%$, i.e. within these surfaces the sum of the Mo, Cr and N contents exceeds 4 at.%, see Table 6.2. Left and right figures differ by rotation around the tip axis and inclination of the tip out of the viewing plane (see also the colored lines of the display box).

Determination of the exact composition of the nitrides by APT can be problematic. The key limitations are:

- i. Peak overlap in the mass-to-charge-state ratio spectrum can potentially occur for N^+ and N_2^{2+} , although this is expected to be limited. More significant is the peak overlap between N_2^+ and Fe^{2+} in the spectrum [191], [192]. Close inspection of the mass spectrum originating from the nitrides alone (i.e. the volume inside the iso-concentration surfaces of 4 at.% Cr+Mo+N) indicates that the peak ratios at 28, 28.5 and 29 Da follow the natural abundances of the isotopes of Fe. It is therefore concluded that no significant evaporation of nitrogen could be detected in the form of N_2^+ .
- ii. Recent studies [65], [168] have shown that lateral surface diffusion of substitutional and interstitial atoms on the APT tip may affect the reconstruction of their original location on the tip thereby leading to inaccuracy in the determination of the composition of (small) second phase regions by APT. The electric field employed in the APT experiment is adjusted to give a steady evaporation of the Fe-based matrix. Thus, the effect of surface diffusion of the (heavier) substitutional species is likely not prominent and the co-enrichment of Cr and Mo (in the nitride) is certainly real. However, because the (surface) diffusion of light elements is considerably faster than that of heavier elements, the determination of their original location in the APT tip is more severely influenced by surface diffusion and quantitative determination of the N content of matrix and/or precipitates can be seriously affected. However, with reference to results in Ref. [65], the current experiments provide no evidence of significant surface migration of N.
- iii. The local magnification effect (LME) in APT can limit both spatial and chemical resolution in the analysis of precipitates within numerous alloy systems. Elements within the nitrides have a higher evaporation field than Fe in the surrounding matrix, i.e. a higher electric field must be applied to evaporate these nitride constituents from the surface of the APT tip, as compared to Fe. Thus, the preferential evaporation of the surrounding ferrite matrix, as compared to the evaporation of precipitates, results in a change of the shape of the surface of the tip in the vicinity of the platelets. This, in turn, leads to aberrations in the trajectories of ions emitted from these regions, which affects the spatial resolution of their reconstructed positions in the 3D APT image. Furthermore, the size and shape of the precipitates and their orientation in the specimen can influence the aberrations of the trajectories and thus the severity of the LME. For the very fine platelets in the current alloy, LME may therefore lead to erroneous detection of large amounts of Fe in the platelets (see Table 6.2). Earlier atom probe field ion microscopy

(APFIM) studies of nitrated Fe-Mo alloys [171], [181] also suggested the presence of considerable amounts of Fe in Mo-nitrides, whereas a study of nitrated Fe-Mo alloys based on Mössbauer spectroscopy [28] could not at all detect Fe in the nitrides. Furthermore, the aberrations by LME affect the observed shape of the precipitates: the width of the platelets appears thicker in Fig. 6.3a (APT) than in Fig. 6.2a (TEM).

The above discussion implies that the APT data do not allow a definitive conclusion about the whether or not presence of Fe in the precipitates. However, this limitation does not affect the accuracy of the value determined for the atomic *ratio* of Cr and Mo content in the precipitates. The measured atomic Cr:Mo ratio is approximately 1:0.9, as expected for an alloy containing equal atomic amounts of Cr and Mo (cf. section 6.2.1). Hence, from the above results and discussion it is concluded, at this stage of the analysis, that the developed, cubic NaCl-type nitrides can be described as ternary nitrides of composition $(\text{Cr}_{1/2}, \text{Mo}_{1/2})\text{N}_x$. Regarding the value of x and the effect of the possible presence of Fe in the nitride on the N-content, see in particular the next paragraph.

The precise stoichiometry of the developed ternary nitride was obtained as follows. A thin foil of Fe-1Cr-1Mo alloy was nitrated to full saturation (12 h at 580 °C) such that no further N-uptake occurred and before a significant (aging induced) DP reaction could take place (see section 6.3.2). Next, this specimen was denitrated (96 h at 450 °C) to remove all less strongly bonded N, i.e. the dissolved N and the excess N adsorbed on the platelet faces (for details about excess N see Ref. [10]), i.e. the N which is not strongly bound in alloying element nitrides⁷. The N-content left in such a denitrated foil was 1.53 at.%, which indicates a strongly-bonded N to alloying-element (Cr+Mo) ratio of 0.765, i.e. a composition of $(\text{Cr}_{1/2}, \text{Mo}_{1/2})\text{N}_{3/4}$ for the ternary NaCl-type nitride platelets in the CP regions of this alloy. This composition is in line with the assumption of “a continuous series of solid solutions” [193] of CrN and γ -Mo₂N. This suggests that the composition of the ternary, mixed nitride is given by a weighted sum of the ratios Cr:N 1:1 and Mo:N 2:1. Thus, for the current alloy with Cr/Mo=1, it follows Cr:Mo:N=1:1:(3/2). This implies that the composition of the present ternary nitride can be represented as $(\text{Cr}_{1/2}, \text{Mo}_{1/2})\text{N}_{3/4}$. As a matter of fact, in a recent parallel investigation by our group of a series of Fe-Cr-Mo alloys of

⁷ This treatment is the first step of a so-called absorption-isotherm analysis; see e.g. Ref. [93]. Denitrating of previously nitrated Fe-Mo specimens in pure, flowing H₂-atmosphere eventually causes all N to leave the specimen [28], i.e. the N-content becomes zero. This is a result of the low stability of Mo nitrides (see Chapter 5 and section 6.4). This effect can be prevented by applying a very low nitriding potential ($r_N^* = 0.01 \text{ atm}^{-1/2}$; see section 6.2.1) to stabilize the nitrides. This nitriding potential will also lead to a very small amount of N dissolved in ferrite (about 0.003 at.% for the conditions employed here [7]), leading to a very slight, negligible overestimation of the N-content incorporated in the nitrides.

varying Cr/Mo-ratio, the N-content in the nitrated zone was found to comply with the above described rule for the composition of the mixed CP nitrides (Chapter 7). This result is a strong indication that indeed no significant amount of Fe is incorporated in these nitrides.

Table 6.2: Composition of nitride particles as determined by APT in this study. The compositional analysis by APT is affected, especially, by the local magnification effect, which may lead to considerable, erroneous assignment of Fe from the surroundings to the nitrides (see section 6.3.1).

nitride precipitate	analysis method	Fe content (at.%)	Cr content (at.%)	Mo content (at.%)	N content (at.%)
CP-platelets	APT (Fig. 6.3b)*	89.7	3.45	3.00	3.82
DP-sphere	APT (Fig. 6.11a)°	31.5	26.8	11.0	30.8
DP-sphere	APT (Fig. 6.11b)°	28.7	30.4	9.45	31.4

* considering atoms inside the 4 at.% Mo-Cr-N-iso-concentration surface

° considering atoms inside the 20 at.% Mo-Cr-N-iso-concentration surface

Already previous denitriding experiments of a number of through nitrated, ferritic, Fe-based binary alloys [26], [157], [93], [165] and also a ternary Fe-Cr-Al alloy [63] indicated that the N-content remaining in the specimen after denitriding is compatible with the complete precipitation of all *Me* as *MeN*, or $(Me_1, Me_2)N$, respectively, implying (as above) that Fe is not significantly present in these nitrides. However, it might not be excluded that, if Fe is initially present in the nitrides, it may leave the nitrides during denitriding (if there exists a driving force for this effect). However, the mobility of Fe (in a nitride) at the relatively low denitriding temperature can be rather small. The initial incorporation of Fe into the nitrides would then simply be the consequence of Fe not being able to “go out of the way” fast enough. For a related discussion and results from our group on the composition of nitrides developing upon nitriding of Fe-Cr-Al alloy, see Ref. [166].

6.3.2 Discontinuously precipitated nitrides; later stages

Continued nitriding of Fe-1Cr-1Mo alloy specimens, i.e. after completed initial precipitation of Cr and Mo in the form of coherent nitride platelets as discussed in section 6.3.1, leads to distinct microstructural change: starting from the grain boundaries, regions with a lamellar microstructure are formed by a discontinuous transformation mechanism (this reaction begins after a nitriding time of the order of 10 hours at 580 °C). An SEM micrograph showing such a discontinuously transformed region growing into the grain interior (i.e. into a CP region) is shown in Fig. 6.4. At this stage of the nitriding treatment, the platelets in the as yet untransformed CP-region have now become visible (see the right-hand side of the SEM micrograph), as they have experienced considerable coarsening due to the long nitriding (=aging) time.

An EPMA line scan crossing transformed DP regions and (as yet untransformed) CP regions of nitrided Fe-1Cr-1Mo alloy (see Fig. 6.5), indicates a larger N-content (approx. 2.4 at.%) for the DP regions as compared to the surrounding CP region (approx. 2.1 at.%). Recognizing the same amounts of Cr and Mo in the CP and DP microstructures, i.e. no alloying element redistribution occurs between CP and DP regions, it follows that the nitrides in the DP region contain more N than the nitrides in the CP regions. The additional N is supplied from the nitriding atmosphere during the ongoing nitriding reaction; cf. discussion on DP of MoN upon nitriding of binary Fe-1Mo alloy in Ref. [31].

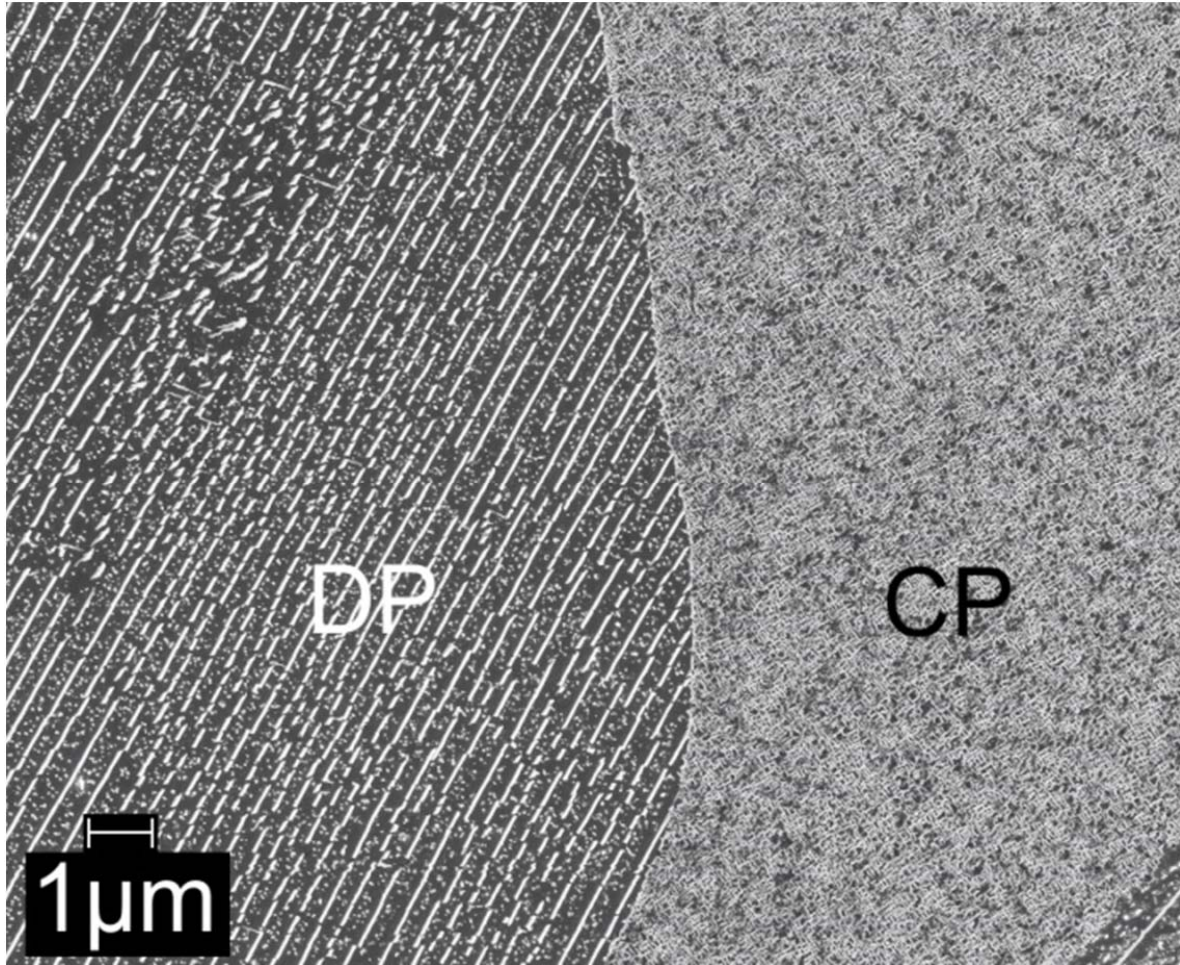


Fig. 6.4: SEM micrograph showing the microstructure as developed in the Fe-1Cr-1Mo alloy upon nitriding at 580 °C for 504 h with a nitriding potential of $0.1 \text{ atm}^{-1/2}$. The left part of the micrograph shows the lamellar microstructure: the CrMoN₂-nitride lamellae (white) and the ferrite lamellae (dark gray) with small spherical (Cr,Mo)N_x nitride particles (light gray) in the ferrite lamellae resulting by the DP reaction occurring upon prolonged nitriding (aging). The right part of the micrograph shows the CP microstructure with relatively coarse (as compared to the initial stage of nitriding) (Cr_{1/2}, Mo_{1/2})N_{3/4} platelets due to pronounced coarsening as a result of the prolonged time at elevated temperature.

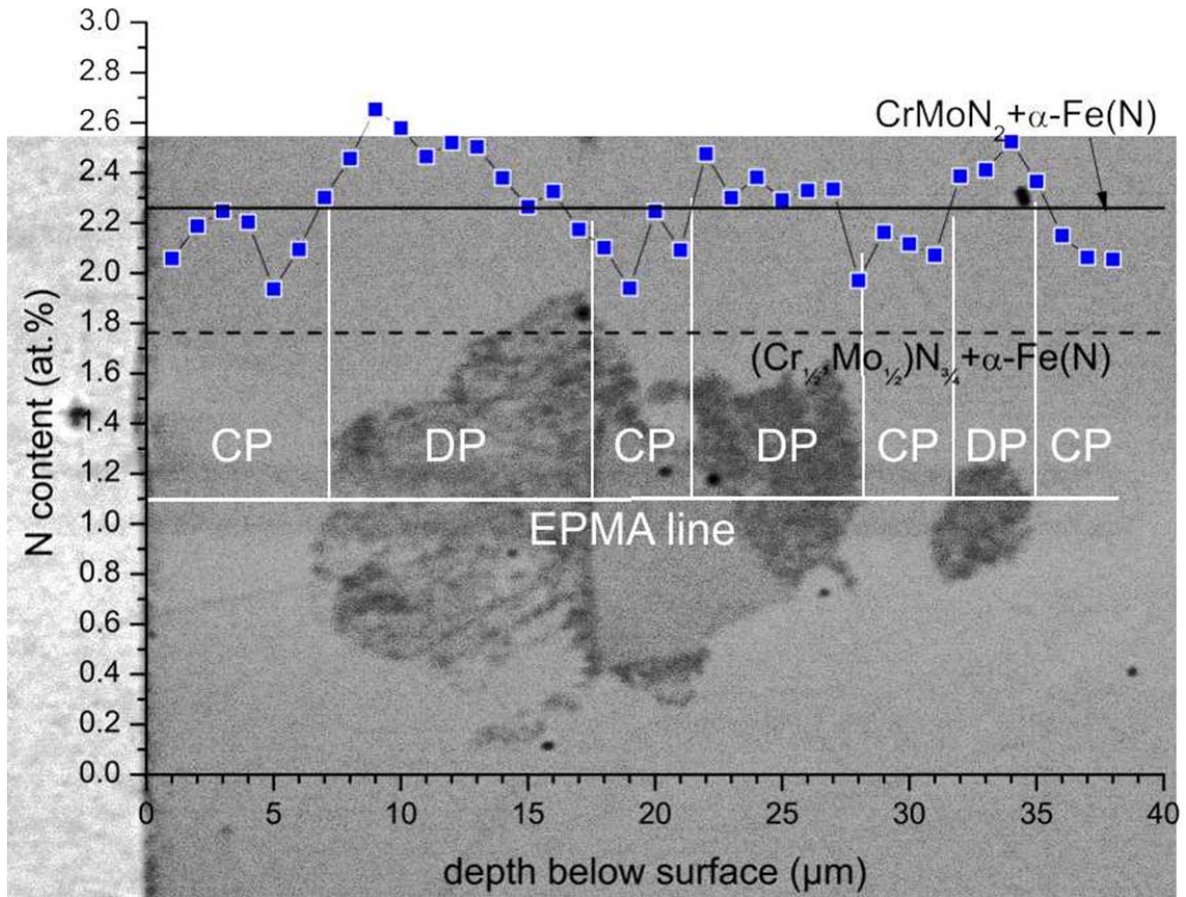


Fig. 6.5: EPMA line scan across a DP region in Fe-1Cr-1Mo alloy nitrided at 580 °C for 72 h with a nitriding potential of 0.1 atm^{-1/2}. The expected level of N-content for the case of precipitation of all Cr and Mo as (Cr_{1/2},Mo_{1/2})N_{3/4} plus the equilibrium N solubility of the ferrite matrix (1.76 at.% N; relevant for the CP microstructure) has been indicated by the dashed black line. The expected level of N-content for the case of precipitation of all Cr and Mo as CrMoN₂ plus the equilibrium N solubility of the ferrite matrix (2.23 at.% N; relevant for the DP microstructure) has been indicated by the full black line. Note that the presence of excess N particularly in the CP microstructure leads to a higher than expected N-content. The full horizontal white line indicates the position of the EPMA line scan; full vertical white lines indicate the positions of CP → DP reaction fronts crossed by the line scan.

The combined SEM, TEM and XRD analyses discussed below reveal the presence of three kinds of nitrides in the DP material:

- (i) Straight, parallel, plate-like lamellae identified as CrMoN_2 (up to several μm long but very thin (about 10 nm thickness); see below) with broad faces parallel to $\{110\}_{\alpha\text{-Fe}}$ planes of the ferrite matrix (Fig. 6.4, Fig. 6.6, Fig. 6.7, Fig. 6.8, Fig. 6.9);
- (ii) Spherical $(\text{Cr},\text{Mo})\text{N}_x$ particles in the ferrite lamellae between the CrMoN_2 lamellae (20-30 nm diameter; Fig. 6.4, Fig. 6.8, Fig. 6.10, Fig. 6.11);
- (iii) Undulating platelets: small undulating platelets of $\alpha''\text{-Fe}_{16}\text{N}_2$ with their broad faces overall parallel to $\{100\}_{\alpha\text{-Fe}}$ planes of the ferritic lamellae between the CrMoN_2 lamellae (Fig. 6.7, Fig. 6.11).

In the following, the structural and compositional details of the above types of nitrides are presented.

(i) DP-lamellae

X-ray diffractograms recorded from the surface of a Fe-1Cr-1Mo alloy specimen nitrided for prolonged treatment time (Fig. 6.6) show the presence of reflections of a new phase, in addition to the ferrite-matrix reflections, which emerged upon progress of the CP \rightarrow DP transition.

Comparison of the new reflections with diffraction patterns of known phases of the Fe-Cr-Mo-N system (see overview of the Fe-Cr-N, Fe-Mo-N and Cr-Mo-N systems given in section 6.4) to identify the developed nitrides was unsuccessful. However, the positions of the new peaks are close to those expected for CrWN_2 [194]. It has been suggested [195], that Mo can partially substitute W in the layered CrWN_2 structure, but pure CrMoN_2 was not synthesized until now (in an investigation of the precipitate phases forming in high-temperature steel materials [196], a ternary, layered, hexagonal Cr-Mo-nitride was proposed, although not fully characterized). Against this background, the crystal-structure data of CrWN_2 [194], with the W atoms fully substituted by Mo atoms, was used as a starting point for the Rietveld refinement of the lattice parameters of the accordingly proposed CrMoN_2 phase. The atomic positions of Cr, Mo, and N in CrMoN_2 were not refined, as the CrMoN_2 reflections are very weak in the diffraction pattern of the (bulk)⁸ nitrided specimen (Fig. 6.6). The results of the fitting are shown in Table

⁸ The isolated nitride powder (see section 6.2.2) showed a pronounced texture of the CrMoN_2 due to the plate morphology of the nitride lamellae (the plates lie on their faces, thus a strong 0001 texture occurs; see TEM results below), thereby prohibiting structural identification by Rietveld refinement of a corresponding X-ray diffractogram.

6.3:

the presence of such a CrMoN_2 phase is compatible with all but one of the new reflections (see Table 6.3 and Fig. 6.6); this very small unindexed reflection close to the 200 ferrite reflection in Fig. 6.6 could originate from a NaCl-type cubic nitride. This would suggest that not all $(\text{Cr}_{1/2}\text{Mo}_{1/2})\text{N}_{3/4}$ (the CP nitride (cf. section 6.3.1)) has transformed to CrMoN_2 (the DP nitride). This is the case indeed; see (ii) below. The hexagonal crystal structure of CrMoN_2 is illustrated in Fig. 6.12. It is built of alternating densely packed Cr and Mo layers separated by densely packed N layers. In this structure, Cr is coordinated by N octahedra and Mo is coordinated by N-trigonal prisms.

TEM BF micrographs and corresponding SADPs of the DP regions (Fig. 6.7) show that the CrMoN_2 lamellae have their broad faces parallel to $\{110\}_{\alpha\text{-Fe}}$ ferrite-matrix lattice planes, indicating a habit plane different from that of the fine CP platelets which have their broad faces parallel to $\{100\}_{\alpha\text{-Fe}}$ ferrite-matrix lattice planes. The SADP shows diffraction spots of the lamellae in addition to the ferrite-matrix reflections (verified by dark field micrographs made employing only the additional spots (not shown)). These lamellae diffraction spots can be indexed according to the CrMoN_2 crystal structure as determined by the XRD analysis (see above). The position of the 000/ spots of the hexagonal CrMoN_2 nitrides with respect to the 110 spots of the cubic ferrite matrix in SADPs with $[001]_{\alpha\text{-Fe}} / [\bar{1}100]_{\text{CrMoN}_2}$ electron beam/zone axis indicates that closest-packed planes of nitrides and matrix are parallel, i.e. $\{0001\}_{\text{CrMoN}_2} \parallel \{110\}_{\alpha\text{-Fe}}$.

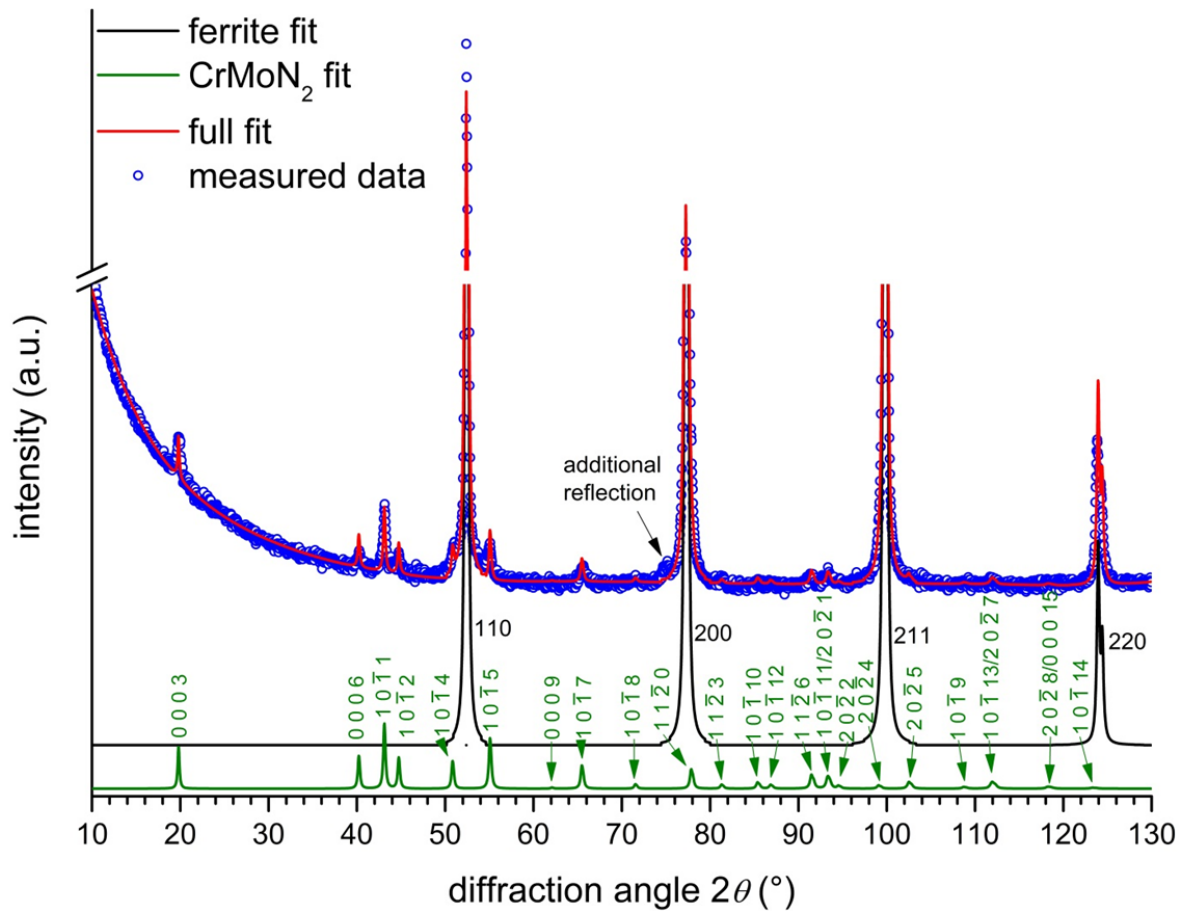


Fig. 6.6: XRD diffractogram ($\text{CoK}\alpha$) recorded from the surface of Fe-1Cr-1Mo alloy, nitrided at 580 °C for 504 h with a nitriding potential of $0.1 \text{ atm}^{-1/2}$. The fitted intensity curves for the ferrite (black) and CrMoN_2 (green) reflections are shown separately. The additional reflection at approx. $75^\circ 2\theta$ can be the NaCl-type 220 reflection of the coarsened spherical $(\text{Cr},\text{Mo})\text{N}_x$ particles in the DP ferrite lamellae (cf. Fig. 6.4).

Table 6.3: Structural data of and fitting results for the CrMoN₂ crystal-structure parameters. Atomic positions were not refined (see section 6.2.2).

refined structure data			
space group	R3m (160)		
a [Å]	2.8503(7)		
c [Å]	15.626(6)		
fitting criteria (figures of merit)			
R _{wp}	2.92		
R _{exp}	1.54		
GOF ($=\sqrt{\chi^2}$)	1.89		
atom positions [194]			
atom	x	y	z
Cr	0	0	0.825
Mo	0	0	0
N1	0	0	0.263
N2	0	0	0.407

Energy dispersive X-ray spectroscopy (EDX) spot analysis performed in the TEM of a freestanding lamella (Fig. 6.7b)) and of an electrolytically isolated lamella (cf. section 6.2.2; Fig. 6.9) shows that both lamellae contain the same amounts of Cr, Mo and N with a ratio of Mo/Cr>1, i.e. a higher amount of Mo than of Cr. Different values of the amounts of Cr, Mo and N in the nitride lamellae were obtained by evaluation of the EDX spectra if either the Mo K-lines or the Mo L-lines were considered, and therefore no quantitative composition data can be given. However, in both cases a Mo/Cr-ratio larger than one was obtained. As will be shown below, APT indirectly supports this indication of the TEM-EDX analysis, since characterization of the spherical particles shows that these particles exhibit a Mo/Cr-ratio smaller than one, as has to be expected if the lamellae indeed have a Mo/Cr-ratio larger than one and recognizing that in the alloy the Mo/Cr-ratio equals one.

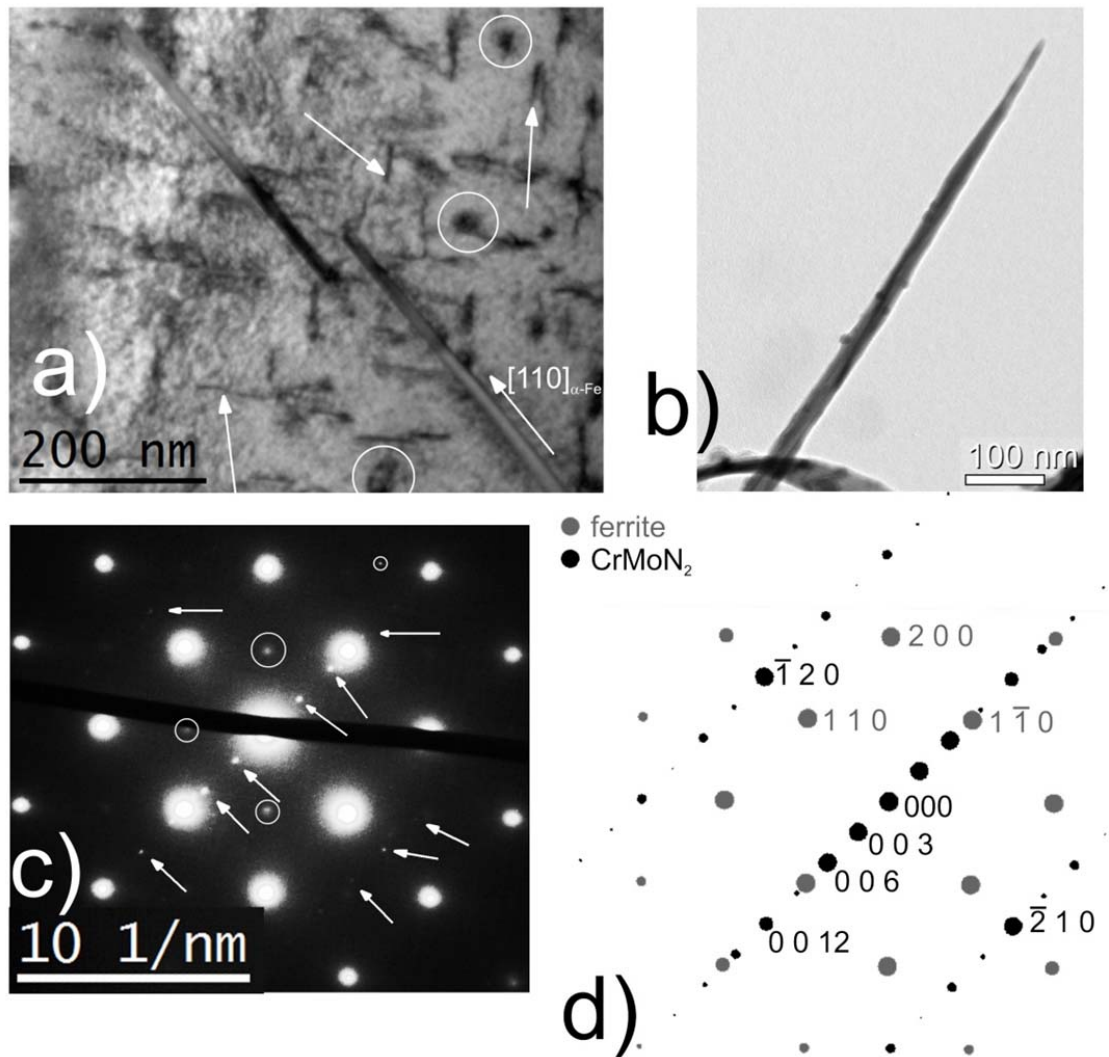


Fig. 6.7: (a) TEM bright field micrograph (BF) showing CrMoN_2 lamellae with their broad faces parallel to $\{110\}_{\alpha\text{-Fe}}$ ferrite lattice planes in Fe-1Cr-1Mo alloy nitrided at 580 °C for 72 h with a nitriding potential of 0.1 atm^{-1/2}. Some spherical (Cr,Mo) N_x particles in the ferrite lamellae have been indicated by white circles. Undulating appearing platelets in the ferrite lamellae (arrows), oriented along $\{100\}_{\alpha\text{-Fe}}$ ferrite planes, are $\alpha''\text{-Fe}_{16}\text{N}_2$ precipitates formed in the nitrogen supersaturated (after quenching) ferrite lamellae upon aging at low (RT) temperatures [38], [132]. (b) Free-standing CrMoN_2 lamella employed for EDX analysis: a Mo/Cr-ratio larger than 1 was observed (see discussion in section 6.3.2). (c) SADP (electron beam/zone axis $[001]_{\alpha\text{-Fe}}$) of a). The arrows indicate spots belonging to the CrMoN_2 phase; circled spots originate from unavoidable magnetite Fe_3O_4 present on the TEM foil. (d) Schematic diffraction pattern of the ferrite matrix and the CrMoN_2 nitride corresponding to a $[1\bar{1}00]_{\text{CrMoN}_2} / [001]_{\alpha\text{-Fe}}$ zone axis. The arrangement of the spots indicates $(0001)_{\text{CrMoN}_2} \parallel (110)_{\alpha\text{-Fe}}$.

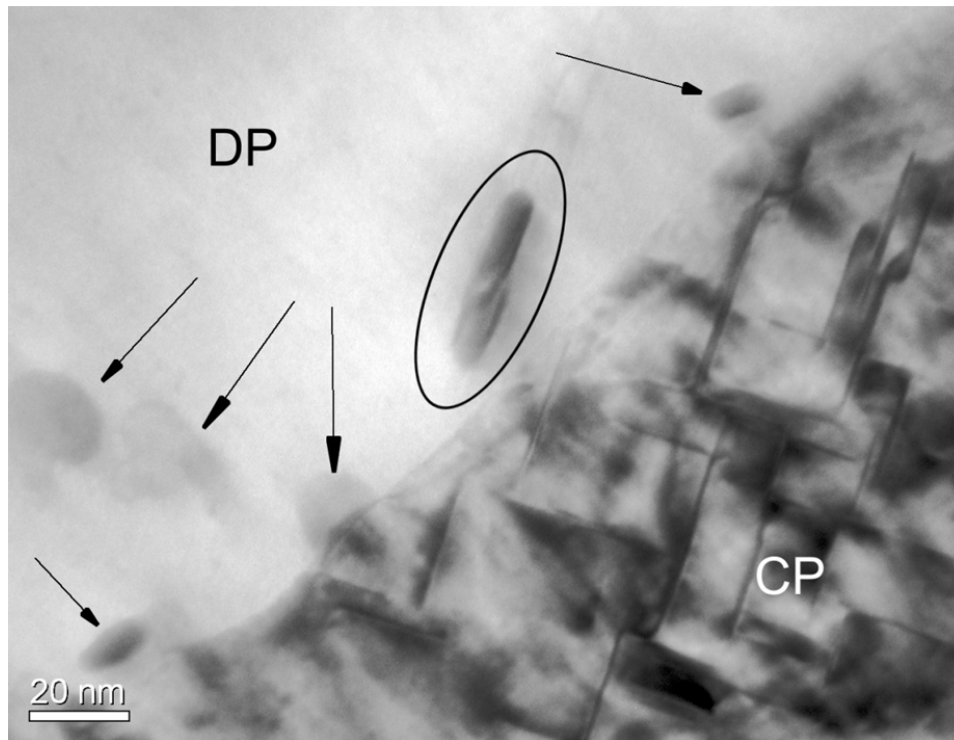


Fig. 6.8: TEM bright field (BF) micrograph at and around a CP/DP (ferrite lamella) interface in Fe-1Cr-1Mo alloy nitrided at 580 °C for 72 h with a nitriding potential of 0.1 atm^{-1/2}. Spherical particles have been indicated by arrows. Some spherical particles are visible very close to the interface. Black ellipse encloses an elongated particle with an elongation direction parallel to the long direction of a set of the former CP platelets. The electron-beam direction in the CP region is near to a [001]_{α-Fe}, ferrite zone axis, whereas the electron-beam direction in the DP region (ferrite lamella) corresponds with a high index ferrite direction.

(ii) Spherical precipitates

In SEM micrographs (Fig. 6.4), small particles are visible in the ferrite lamellae (between the CrMoN₂ lamellae). Close inspection of TEM-BF micrographs (Fig. 6.7a, Fig. 6.8, Fig. 6.9, and Fig. 6.10a and c) reveals the presence of these small, more or less spherical, particles as well. They appear to have no specific orientation relationship with the ferrite matrix; attempts to obtain a low index electron-beam/zone axis SADP for these particles in the ferrite lamellae were unsuccessful. Therefore, the nitride particles (and nitride lamellae) were isolated from the matrix in order to increase the volume fraction of nitrides in a sample for TEM analysis, as described in section 6.2.2. The particles deposited onto the CrMoN₂ lamellae faces (Fig. 6.9) and those forming larger agglomerates (Fig. 6.10) were found to be roughly spherical. The SADPs of

these agglomerates show diffraction spots on rings that are fully compatible with a NaCl-type crystal structure for the spherical particles (Table 6.4).

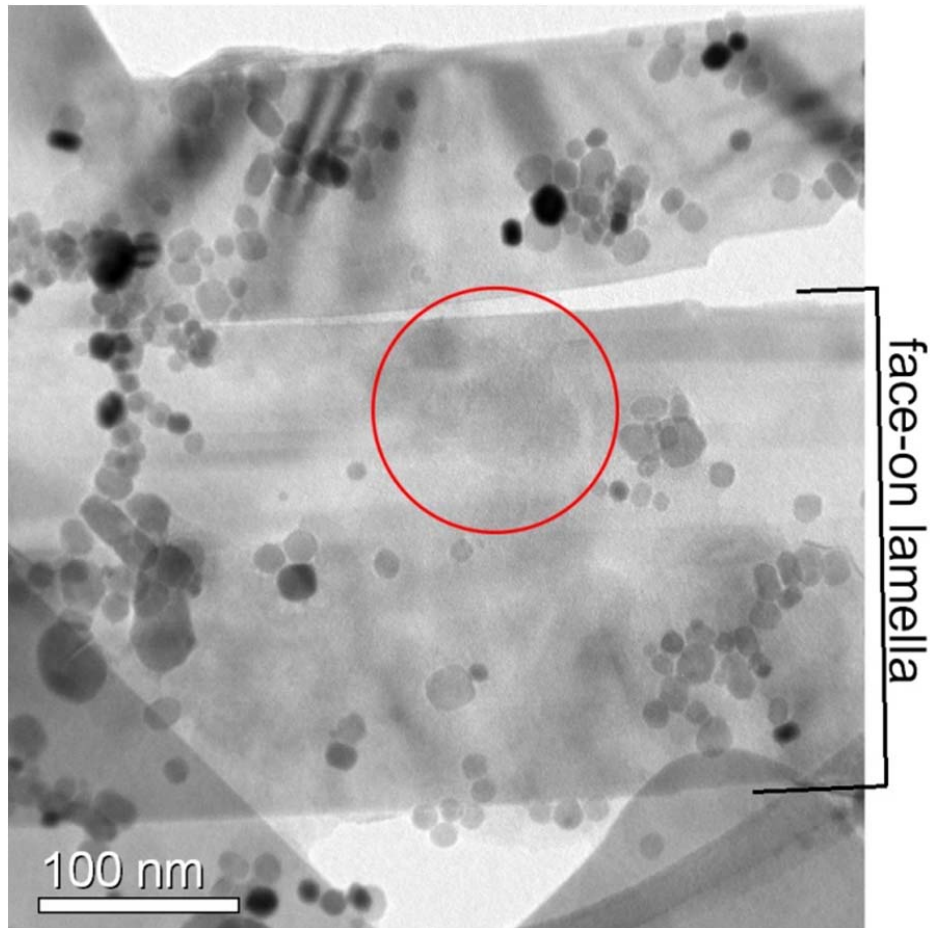


Fig. 6.9: TEM bright field (BF) micrograph of electrolytically isolated (i) CrMoN_2 lamella and (ii) spherical $(\text{Cr,Mo})\text{N}_x$ particles. The (dissolved) specimen was a thin foil (thickness approx. $200\ \mu\text{m}$, cf. section 6.2.2) that was homogeneously nitrified at $580\ ^\circ\text{C}$ for 72 h with a nitriding potential of $0.1\ \text{atm}^{-1/2}$ to have a fully DP microstructure. Spherical particles from the dissolved *ferrite* lamellae had deposited on the faces of the CrMoN_2 lamellae upon electrolytic dissolution. The red circle indicates the aperture position for EDX spot analysis: a Mo/Cr-ratio larger than 1 was observed (see discussion in section 6.3.2).

TEM-EDX analyses of some isolated particles (Fig. 6.10c) indicate the presence of Cr, Mo, and N with a ratio of $\text{Mo/Cr} < 1$, i.e. the spherical particles contain more Cr than Mo. Different values of the amounts of Cr, Mo and N in the nitride lamellae were obtained by evaluation of the EDX spectra if either the Mo K-lines or the Mo L-lines were considered, and therefore no quantitative composition data can be given. However, in both cases a Mo/Cr-ratio larger than one was

obtained. The Cr-enrichment in the spherical particles is confirmed by the elemental composition data obtained by the APT experiments shown in Fig. 6.11 and presented in Table 6.2: One spherical precipitate adjacent to the edge of the tip is shown in Fig. 6.11a; two spherical precipitates can be discerned in Fig. 6.11b. In order to separate the nitride particles from the matrix iso-concentration surfaces enclosing precipitate regions of a combined Mo, Cr and N concentration larger than 20 at.% were applied. The composition obtained of such defined precipitates is shown in Table 6.2.

Table 6.4: Lattice spacings for $(\text{Cr},\text{Mo})\text{N}_x$ NaCl-type nitride (i) as calculated with $a=4.15 \text{ \AA}$ (intermediate of the lattice parameter of CrN (4.14 \AA , card 011-0065 in Ref. [97]), and that of $\gamma\text{-Mo}_2\text{N}$ (4.163 \AA , card 025-1366 in Ref. [97]) and (ii) as measured from the (average) diameters of the SADP ring patterns due to diffraction by the spherical particles in Fig. 6.10b. The relative intensity of the calculated reflections has been given in a qualitative manner in brackets in the first column. The d-spacing ranges of the rings given in the last column have been provided with a measurement error range assessed at 3 pixels of the detector.

reflection of $(\text{Cr},\text{Mo})\text{N}_x$	calculated d-spacing [\AA] ($a=4.15 \text{ \AA}$)	observed d-spacing [\AA]
1 1 1 (moderate)	2.396	2.45 (2.69-2.33)
2 0 0 (strong)	2.075	2.06 (2.17-2.01)
2 2 0 (strong)	1.467	1.46 (1.50-1.41)
3 1 1 (moderate) 2 2 2 (moderate)	1.251 1.198	1.23 (1.26-1.19)
4 0 0 (weak)	1.038	1.05 (1.07-1.02)
3 3 1 (weak) 4 2 0 (moderate/strong)	0.952 0.928	0.93 (0.95-0.91)

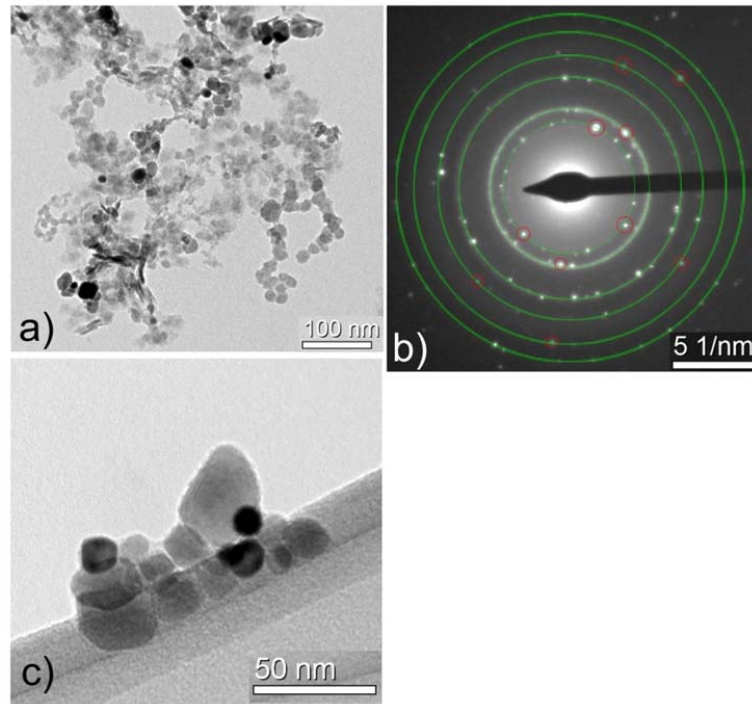


Fig. 6.10: (a) TEM bright field micrograph (BF) showing an agglomerate of spherical particles obtained by electrolytically dissolving the ferrite matrix. The (dissolved) specimen was a thin foil (thickness approx. 200 μm , cf. section 6.2.2) that was homogeneously nitrided at 580 $^{\circ}\text{C}$ for 72 h with a nitriding potential of 0.1 $\text{atm}^{-1/2}$ to have a fully DP microstructure. (b) The corresponding SADP. The diameters of the concentric rings can be indexed based on the NaCl-type crystal structure of $(\text{Cr},\text{Mo})\text{N}_x$. The corresponding d-spacings have been given in Table 6.4. The red circles indicate some reflections of low and higher order (111 and 222 (ring 1 and 4) and 200 and 400 (ring 2 and 5); cf. Table 6.4). The more homogeneous appearance of the second ring (d-spacing approx. 2.07 \AA) may originate from undissolved $\alpha\text{-Fe}$ in the agglomerate ($d_{110}(\alpha\text{-Fe})$ is 2.0268 \AA), or oxidation (of the nitride particles and/or the ferrite (see Fig. 6.2 and Fig. 6.7)). As also strong spots occur along the ring, this is concluded to be also a d-spacing of the spherical $(\text{Cr},\text{Mo})\text{N}_x$ particles. (c) Smaller agglomerates of the spherical particles on which EDX analysis was performed: a Mo/Cr-ratio smaller than 1 was observed (see discussion in section 6.3.2). The grey band is the C-film (see section 6.2.2).

(iii) Undulating platelets

The undulating platelets found in TEM BF micrographs (see arrows in Fig. 6.7a) resemble the morphology observed for α'' -Fe₁₆N₂ in ferrite [38], [49], [132]. The metal atoms in this nitride are arranged in a tetragonally distorted bcc lattice [156]; the nitrogen atoms occupy c-type octahedral interstices in an ordered way. These N atoms lead to only very weak superstructure spots in SADPs (note that the most intense, fundamental spots of α'' -Fe₁₆N₂ overlap with those of ferrite-matrix spots [140]). APT shows that the undulating platelets contain N (are N-rich as compared to the matrix) and Fe, and that Cr and Mo have not been taken up in these undulating platelets (see Fig. 6.11 a) and b)).

α'' -Fe₁₆N₂ is known to precipitate at room temperature or slightly elevated temperature from N-supersaturated ferrite [98], [155]. However, at the nitriding temperature of 580 °C employed in the current study, α'' -Fe₁₆N₂ is unstable. Hence, the presence of α'' -Fe₁₆N₂ precipitates within the Fe-lamellae is caused by aging (at RT) of the water-quenched (cf. section 6.2.1) nitrided specimens: quenching brought about retention of N-supersaturated ferrite at room temperature, and subsequent natural aging at room temperature causes the development of α'' -Fe₁₆N₂ nitride particles.

6.4 Discussion

Upon nitriding of binary Fe-Cr alloys, initially *continuous precipitation* of finely distributed, nano-sized, cubic NaCl-type CrN nitride platelets, with a Baker-Nutting orientation relationship (OR) with the ferrite matrix, occurs [20], [21], [23], [25], [180]. The precipitation of CrN platelets is very fast, due to a high (negative) Gibbs energy of formation of CrN (per mole N₂)⁹ (-129.1 kJ mol⁻¹ at 580 °C (853 K) and 1 atm). During prolonged treatment time and given a sufficiently high Cr-content of the alloy (more than approx. 2 at.% Cr [21]), these fine precipitates can undergo a *discontinuous coarsening* reaction leading to the development of relatively small colonies/cells of alternating CrN and ferrite lamellae [21]–[23], [25], [180]. Under the high activity of N imposed by the nitriding atmosphere, CrN represents the thermodynamically stable Cr-

⁹ The Gibbs energies of formation of the nitrides from the ferrite matrix ($\Delta G_{MeN,\alpha}^f$) presented here are determined by the Gibbs energies of formation of the nitrides from pure elemental Cr/Mo metal and N₂ gas (ΔG_{MeN}^f) (from Ref. [236]) and the activity of N at the current nitriding conditions (580 °C and 0.1 atm^{-3/2}) ($a_{N,\alpha}$) (from Ref. [177]) according to the formula $\Delta G_{MeN,\alpha}^f = \Delta G_{MeN}^f - RT \ln(a_{N,\alpha})$. The contributions of the dissolution of Cr and Mo in ferrite are neglected. See Ref. [237] for more details of such calculation.

nitride in nitrided binary, ferritic Fe-Cr alloys. No ternary phases have been reported for the Fe-Cr-N system [197].

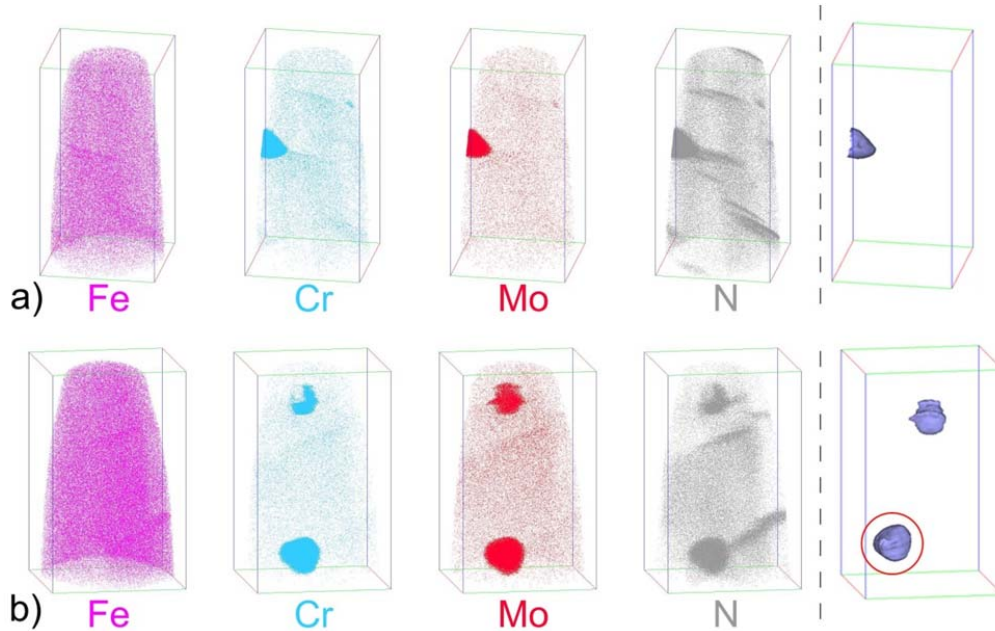


Fig. 6.11: (a) Distribution of atomic species (left) and compositional iso-concentration surfaces of Cr+Mo+N = 20 at.% (right) in an APT tip prepared from a (approx. 600 μm thick, c.f. section 6.2.3) Fe-1Cr-1Mo alloy specimen where the discontinuous precipitation reaction had (almost) completed after 216 h of nitriding at 580 $^{\circ}\text{C}$ with a nitriding potential of 0.1 $\text{atm}^{-\frac{1}{2}}$. The size of the displayed box is $164 \times 86 \times 86 \text{ nm}^3$. The region of increased contents of Cr, Mo and N species corresponds with either the tip (thin end) of a CrMoN_2 lamella or a spherical precipitate. Composition analysis indicates a higher content of Cr as compared to Mo in the nitride region (see Table 6.2). The N-rich regions, where neither Cr nor Mo are (significantly) enriched, correspond to the undulating $\alpha''\text{-Fe}_{16}\text{N}_2$ platelets revealed by TEM. (b) A second APT tip of the same material containing two spherical precipitates and several undulating platelets. Composition of the particle enclosed by a red circle is given in Table 6.2.

Upon nitriding of binary, ferritic Fe-Mo alloys, initially continuous precipitation of thin but (as compared to nitrided Fe-Cr alloys) long, nano-sized, cubic NaCl-type $\gamma\text{-Mo}_2\text{N}$ nitride platelets, with a Baker-Nutting OR with the ferrite matrix, occurs [31], [181]. Initially, the $\gamma\text{-Mo}_2\text{N}$ platelets form very slowly which can be ascribed to the low Gibbs energy of formation of $\gamma\text{-Mo}_2\text{N}$ (per mole N_2)⁹ ($-44.8 \text{ kJ mol}^{-1}$ at 580 $^{\circ}\text{C}$ (853 K) and 1 atm); the volume misfits of CrN and $\gamma\text{-Mo}_2\text{N}$ with the ferrite matrix are similar (51 – 53 %). The thermodynamically stable ni-

tride, hexagonal δ_3 -MoN (volume misfit ~67 %), forms from the earlier developed nitride, upon prolonged nitriding by a *discontinuous precipitation* reaction leading to relatively large transformed regions of parallel alternating δ_3 -MoN and ferrite lamellae [31]. For the system Fe-Mo-N, a cubic ternary η -Fe₃Mo₃N phase [198] and a WC-type hexagonal ternary FeMoN₂ phase [199] have been prepared by precursor synthesis from iron-molybdate powder (FeMoO₄, prepared from an aqueous solution) followed by reaction with pure flowing, gaseous ammonia at 650-700 °C.

The phase constitution of the ternary Cr-Mo-N system (at 1000 °C and 300 bar N₂) has been presented in Ref. [193]. Two types of nitride phases have been found: i) a cubic, NaCl-type γ -Mo₂N/CrN phase conceived as “a continuous series of solid solutions” of CrN and γ -Mo₂N. The N-content of the corresponding mixed nitride was found to decrease from 50 at.% for pure CrN to 33 at.% for pure γ -Mo₂N with increasing Mo content. The same phase was also observed in investigations on Cr-Mo-N thin films (prepared under non-equilibrium conditions [200], [201]; and

ii) a hexagonal (Cr,Mo)₂N phase, which can contain up to 55 at.% Mo at 1000 °C and 300 bar of N₂. Hexagonal, MoN-based phases [202]–[205] were not observed in the investigation of Ref. [193]. Other ternary nitrides of crystal structures different from the above mentioned ternary nitrides, and as found in other ternary transition metal nitride systems [206], [194], [199], [207], [208], have not been observed for the Cr-Mo-N system [193].

6.4.1 Continuous precipitation

Formation of ternary (Cr_{1/2},Mo_{1/2})N_{3/4} platelets

The present investigations on nitriding of Fe-1Cr-1Mo alloy showed that in the early stages of nitriding, similar to the case of nitrated Fe-Cr and Fe-Mo alloys, cubic NaCl-type (Cr_{1/2},Mo_{1/2})N_{3/4} nitride platelets develop (also with their broad faces parallel to {100}_{α-Fe} lattice planes of the ferrite matrix, and also with a Baker-Nutting OR with respect to the ferrite matrix). The nitriding time required to fully precipitate both Cr and Mo as NaCl-type ternary nitride in the ternary Fe-1Cr-1Mo alloy is much shorter than for the precipitation of Mo as NaCl-type binary nitride in the binary Fe-1Mo alloy [31]. The precipitation of Mo as nitride is evidently accelerated considerably by the presence of Cr. As indicated above for the binary systems, the binary NaCl-type nitrides CrN and γ -Mo₂N have considerably different Gibbs energies of formation (per mole N₂), which leads to the strongly differing precipitation kinetics of CrN (fast) and γ -Mo₂N (slow) for the respective binary systems upon nitriding. In the ternary system separate first, fast formation of Cr(-rich) nitrides and subsequent, slow formation of Mo(-rich) nitrides was not observed: instead, a ternary (Cr_{1/2},Mo_{1/2})N_{3/4}-nitride developed.

The preference for the formation of the ternary nitride phase over the development of separate binary CrN and γ -Mo₂N phases upon nitriding of Fe-1Cr-1Mo alloy could suggest that the ternary nitride is thermodynamically preferred. The investigation of the ternary Cr-Mo-N system discussed above (Ref. [193]) and the results obtained from Cr-Mo-N thin films synthesized under various conditions (see e.g. Refs. [200], [201]) indicate that, under specific conditions strongly different from those of the current experiments (see begin of section 6.4), development of the ternary, cubic NaCl-type (Cr,Mo)N_x nitride phase may be preferred thermodynamically over separate, binary cubic CrN and binary cubic γ -Mo₂N phases and then separate formation of binary nitrides is not to be expected. However, the cubic, NaCl-type (Cr_{1/2},Mo_{1/2})N_{3/4} phase formed in the present investigation, under the employed nitriding conditions, eventually transforms to the ternary hexagonal CrMoN₂ phase by a DP reaction, and thus does not represent a state of thermodynamic equilibrium.

The diffusion lengths of Cr⁵¹ ($\sqrt{2Dt} = 54$ nm/h at 580 °C in Fe-based ferrite [209], with D and t representing the tracer, self-diffusion diffusion coefficient and the diffusion time) and in particular Mo⁹⁹ ($\sqrt{2Dt} = 5$ nm/h at 580 °C in Fe-based ferrite [210]) are relatively small at the employed nitriding temperature. It can therefore be suggested that the supposedly initially forming CrN incorporates Mo (note the different Gibbs energies of formation of CrN and γ -Mo₂N; see begin of section 6.4): the system accepts a lesser gain in (release of) chemical Gibbs energy and a slightly larger volume misfit (for binary CrN: 51%, for binary γ -Mo₂N: 53%) than as possible by the development of the separate binary nitrides, which, according to this interpretation, is kinetically obstructed. A similar reasoning, preferred formation of mixed nitrides based on kinetic constraints, was given previously for the mixed nitrides formed in nitrided ternary Fe-Cr-Ti [64] and Fe-Cr-Al [61]–[63] alloys. Indeed, the mixed, cubic NaCl-type (Cr,Ti)N and (Cr,Al)N nitrides, as holds for the mixed (Cr,Mo)N_x nitride of the present study as well, were found to be metastable in these systems: decomposition into the separate binary nitrides can take place at elevated temperature [62], [211], [212].

The nitride-precipitate platelets are finely distributed and are (largely) coherent with the ferrite matrix (see Fig. 6.2). Upon nitriding, initially the elastic accommodation of the matrix/precipitate volume misfit causes long-range strains in the matrix which lead to an overall matrix expansion which causes the ferrite reflections to shift to lower diffraction angles (Chapter 2). A system composed of such fine nitride platelets and the ferrite matrix can diffract coherently, i.e. both matrix and nitride particles diffract as a single aggregate [59]. Furthermore, a compressive residual stress parallel to the surface results from the macroscopic misfit of the nitrided case and the unnitrided core causing a further peak shift to lower diffraction angles [56].

Upon continued nitriding, i.e. aging of the initially formed nitride platelets, in the precipitated regions not yet transformed by the DP reaction (cf. section 6.4.2; the DP reaction sets in after nitriding times of the order of 10 h at 580 °C) (mainly) increase of the precipitate size, i.e. continuous coarsening, occurs (Chapter 4). This is accompanied by plastic relaxation of the matrix/precipitate volume misfit and the development of a ferrite peak corresponding to the relaxed ferritic regions at higher diffraction angles (Chapter 4). In this stage, matrix and precipitates can diffract incoherently.

The matrix expansion, by elastic precipitate/matrix-misfit accommodation and macrostresses, and subsequent misfit relaxation are the origin of the presence of split ferrite reflections in the X-ray diffractograms (see Fig. 6.1): The lower angle peaks of the ferrite reflections originate from the expanded ferrite, representing coherent diffraction by the assembly ferrite matrix plus nitride platelets; the higher angle peaks of the ferrite reflections originate from the relaxed ferrite regions. Due to the ongoing relaxation, the contribution of the higher angle peak increases while that of the lower angle peak decreases with increasing nitriding time (see Fig. 6.1). The alloying element (Cr+Mo) content of the present alloy is not sufficiently high to observe reflections of the coarsened, but still small¹⁰, nitride platelets in X-ray diffractograms; yet, they are observed in TEM-SADPs (cf. diffractogram in Fig. 6.1 (for 6 h nitriding) and SADP in Fig. 6.2 (pertaining to 6 h of nitriding)).

6.4.2 Discontinuous precipitation

Under the currently employed nitriding conditions, the occurrence of a discontinuous reaction upon prolonged nitriding (of the order of 10 hours at 580 °C) with the accompanying formation of CrMoN₂ lamellae and the presence of (Cr,Mo)N_x spherical precipitates in the ferrite lamellae, indicates that the initial, complete precipitation of Cr and Mo as (Cr_{1/2},Mo_{1/2})N_{3/4} nitride (cf. section 6.4.1) represents an intermediate, thermodynamically metastable (see discussion in section 6.4.1) state. The system likely passes through this intermediate stage due to a large nucleation barrier for the continuous precipitation of the (equilibrium) hexagonal CrMoN₂ phase in the ferrite matrix (see below). In the DP regions, no further phase changes were observed in the current study even after prolonged nitriding/aging up to 504 h at 580 °C.

¹⁰ In the current alloy, at a depth of about 100 μm below the surface, the (initial) platelet dimensions after 1 h of nitriding are approximately 10 - 20 nm diameter and less than 1 nm thickness (TEM analysis performed in this project), and after 6 h of nitriding the dimensions have increased to 20 - 30 nm diameter and a few nm thickness (see Fig. 6.2).

Formation of ternary CrMoN_2 lamellae

Distinct formation of a lamellar microstructure by discontinuous coarsening (at the temperature considered) usually occurs in alloys with higher alloying element content and thus larger volume fraction of tiny, coherent nitride precipitates [21], [22] than in the current alloy. For example, a DC reaction occurs in nitrided binary Fe-Cr alloys only with Cr contents above approx. 2 at% Cr. The higher the volume fraction of the tiny precipitates the larger the driving force for coarsening [21]. The reaction proceeds by rearrangement of atoms at and along moving grain boundaries [150], the reaction fronts, where interfacial diffusion governs the atomic transport, allowing DC to proceed at relatively low temperatures (as compared to continuous coarsening where atomic transport proceeds by volume diffusion) [59].

In systems where the initially forming nitride phase of the CP platelets does not represent the most stable nitride, as is the case of nitrided binary Fe-Mo alloys [31] and the present nitrided ternary Fe-Cr-Mo alloy (in contrast with nitrided binary Fe-Cr alloys), an additional chemical driving force operates for the DP reaction (as compared to a DC reaction), as additional *chemical* Gibbs energy is released by the formation of the more stable phase. Therefore, the occurrence of a discontinuous precipitation reaction can occur at a lower volume fraction of precipitates than for the occurrence of a discontinuous coarsening reaction.

From a comparison of the morphologies of the discontinuously formed regions (lamellae of CrMoN_2 and ferrite) of the present nitrided ternary Fe-Cr-Mo alloy with those of the DC regions developing upon prolonged nitriding of binary Fe-Cr alloys (see e.g. Ref. [22]) and the DP regions of binary Fe-Mo alloys [31] it follows that the morphology of the lamellar regions in the present, nitrided Fe-Cr-Mo alloy is similar to that observed in the nitrided Fe-Mo alloys, again suggesting that a discontinuous *precipitation* reaction occurs in the Fe-1Cr-1Mo alloy. This can be related to the structural similarities of CrMoN_2 and $\delta_3\text{-MoN}$: both exhibit a hexagonal crystal structure and are oriented with their broad faces parallel to $\{110\}_{\alpha\text{-Fe}}$ ferrite lattice planes. However, due to the much faster initial precipitation of the cubic nitride, here $(\text{Cr}_{1/2}, \text{Mo}_{1/2})\text{N}_{3/4}$, in the ternary alloy as compared to the binary Fe-Mo alloy, the time required to transform the specimen microstructure according to DP is much shorter in the ternary Fe-1Cr-1Mo alloy. The volume misfits of $\delta_3\text{-MoN}$ and CrMoN_2 with the ferrite matrix, are ~67 % and ~56 %, respectively. This distinctly smaller volume misfit of CrMoN_2 with the ferrite matrix can be an (additional) important factor for the relatively fast DP in the ternary alloys. Note that the volume misfit of the *hexagonal*, ternary nitride is much larger than that of the ternary cubic nitride (see section 6.4.1) making its nucleation in the ferrite matrix more difficult and, indeed, initially precipitation of *cubic* ternary nitride occurs (see section 6.4.1 and beginning of section 6.4.2).

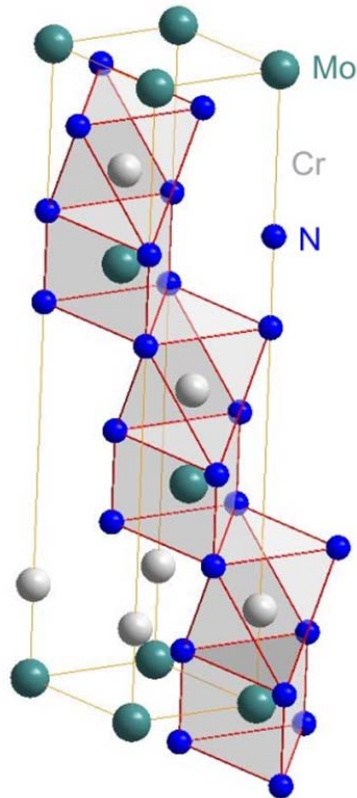


Fig. 6.12: Crystal structure of hexagonal CrMoN_2 . Coordination of the metal atoms by N has been indicated by polyhedra. Cr shows an octahedral coordination by N and Mo shows a trigonal prismatic coordination by N. The structure consists of alternating densely packed layers of Cr and Mo which are separated by densely packed N layers in a stacking sequence $(aA_{\text{Mo}}aA_{\text{Cr}})(bB_{\text{Mo}}bB_{\text{Cr}})(cC_{\text{Mo}}cC_{\text{Cr}})$, where capital letters denote close packed layers of metal atoms and small letters denote close packed N layers.

A consequence of dissolution of (a part of; cf. discussion below on the spherical ternary nitrides) the initial, cubic nitride, followed by demixing, i.e. formation of the hexagonal nitride and ferrite at the moving boundary, carried by grain-boundary diffusion, is the establishment of a microstructure consisting of alternating ferrite and nitride lamellae with an incoherent interface (see also Refs. [23], [25], [59]). Consequently, incoherent diffraction of matrix and precipitates can be expected and indeed separate reflections of the nitride phase can be observed in the X-ray diffractograms and the SADPs (cf. Fig. 6.6 and Fig. 6.7).

Formation of spherical ternary (Cr,Mo)N_x

The DP reaction in nitrided binary Fe-Mo alloys leads to the full transformation of all initially formed γ -Mo₂N to δ_3 -MoN [31]. Such full transformation to the DP nitride is not observed for the DP of CrMoN₂ from the initially formed $(\text{Cr}_{1/2}, \text{Mo}_{1/2})\text{N}_{3/4}$ in the nitrided ternary Fe-Cr-Mo alloys. While the DP reaction leads to a thermodynamically more stable microstructure, equilibrium in principle *cannot* be attained at a reaction front migrating with a velocity larger than zero [213], [214]. Thus, part of the alloying elements cannot be taken up (in time) at the reaction front into the developing CrMoN₂ lamellae. As an apparent consequence, more or less spherical (Cr,Mo)N_x particles appear in the ferrite lamellae. The possible mechanisms of formation of these spherical precipitates can then be discussed as follows:

- (i): All CP platelets dissolve at the DP reaction front. The Cr and Mo which cannot be incorporated (in time) into the forming CrMoN₂ lamellae remain dissolved and become incorporated in the ferrite lamellae where they subsequently *precipitate continuously* as (Cr,Mo)N_x. The precipitation of fine alloying element precipitates in the ferrite lamellae behind the discontinuous reaction front, was previously observed in Fe-Cr alloys with high Cr content [165]. However, the precipitation in the ferrite lamellae of the DC microstructure then occurred again in the form of fine platelets as in a CP microstructure. A spheroidization of these nitride platelets inside the ferrite matrix was not observed. As a matter of fact, the platelet shape of such cubic MeN nitrides is maintained even after long annealing times, also at elevated temperature (see e.g. Refs. [19], [215] and Chapter 4).
- (iia): All CP platelets dissolve at the DP reaction front. The Cr and Mo which cannot be incorporated (in time) into the forming CrMoN₂ lamellae *precipitate at the reaction front* as cubic (Cr,Mo)N_x. Being in contact with two (parent and product) ferrite grains of different crystallographic orientations and confined between the forming CrMoN₂ lamellae, the (Cr,Mo)N_x precipitates develop at the reaction front without a specific OR with the product ferrite (lamellae). Thus, the incoherent particles can assume a spherical shape to minimize their interfacial energy.
- (iib): Some CP nitride platelets do not dissolve at, and are “overrun” by, the DP reaction front and *coarsen at the reaction front* by taking up the alloying elements that cannot be incorporated (in time) into the forming CrMoN₂ lamellae. Being in contact with two (parent and product) ferrite grains of different crystallographic orientations and confined between the forming CrMoN₂ lamellae, the (Cr,Mo)N_x precipitates at the reaction cannot

realize the preferred OR with the product ferrite (lamellae). Thus, the incoherent particles can assume a spherical shape to minimize their interfacial energy.

The above discussion suggests cases (iia) and (iib) to be more likely. The high magnification TEM micrograph in Fig. 6.8 shows both spherical and elongated particles in the ferrite lamellae in close proximity of the interface. Thereby it cannot be decided whether new spherical precipitates form at the interface (case (iia)) or whether former CP platelets are “overrun” and grow (case (iib)). Note that no further transformation of the spherical particles to the CrMoN_2 structure was observed, suggesting that both nitride phases, cubic and hexagonal, may be stable under the employed nitriding conditions after redistribution of alloying elements by the DP reaction.

6.5 Conclusions

The nitride development upon nitriding of Fe-1 at.%Cr-1 at.%Mo alloy can be summarized as follows:

1. Initially finely distributed, nano-sized, coherent, NaCl-type $(\text{Cr}_{1/2}, \text{Mo}_{1/2})\text{N}_{3/4}$ nitride platelets, exhibiting a Baker-Nutting OR with the ferrite matrix, develop. These mixed nitrides contain vacancies on the N sublattice equal to half the amount of the number of Mo atoms.
2. The $(\text{Cr}_{1/2}, \text{Mo}_{1/2})\text{N}_{3/4}$ nitride forms as a, kinetically preferred, intermediate precipitate as compared to the thermodynamically stable CrMoN_2 phase:
 - i. The volume misfit with the matrix is much lower for $(\text{Cr}_{1/2}, \text{Mo}_{1/2})\text{N}_{3/4}$;
 - ii. The diffusion lengths of (Cr and) especially Mo are small and incorporation of Mo in the possibly initially developing CrN (much larger release of Gibbs energy (per mole N_2) than for $\gamma\text{-Mo}_2\text{N}$) already leads to substantial release of Gibbs energy of the system.
3. Upon continued nitriding, i.e. upon aging, CrMoN_2 nitride forms as lamellae by a discontinuous precipitation mechanism. CrMoN_2 has a complex hexagonal crystal structure, as indicated by Rietveld refinement, of alternating, densely packed Cr and Mo layers separated by densely packed N layers.
4. The transformation of the $(\text{Cr}_{1/2}, \text{Mo}_{1/2})\text{N}_{3/4}$ platelets to CrMoN_2 lamellae during the DP reaction is not complete; remaining alloying element develops as cubic $(\text{Cr}, \text{Mo})\text{N}_x$ as spherical particles contained in the ferrite lamellae (between the CrMoN_2 -lamellae).
5. The atomic Mo content of the CrMoN_2 lamellae is somewhat larger than the atomic Cr content, in correspondence and consistent with an atomic Mo content of the spherical $(\text{Cr}, \text{Mo})\text{N}_x$ particles somewhat smaller than the atomic Cr content, as indicated by both APT and TEM-EDX analyses.

6. The spherical $(\text{Cr,Mo})\text{N}_x$ particles likely develop at the DP reaction front, either by nucleation or by growth from the initial $(\text{Cr}_{1/2},\text{Mo}_{1/2})\text{N}_{3/4}$ platelets, and do not precipitate from the possibly remaining dissolved Cr, Mo, and N in the ferritic lamellae in the wake of the migrating reaction front.

Acknowledgements

The authors would like to thank Mr. W.-D. Lang for preparation of the TEM specimens, Mr. P. Kress for assistance with the nitriding experiments (all with Max Planck Institute for Intelligent Systems), Mrs. S. Haug for assistance with the EPMA experiments and Ms. S. Lacher for preparation of the APT matchsticks (both with Max Planck Institute for Solid State Research).

Chapter 7

Nitriding of ternary Fe-Cr-Mo alloys; role of the Cr/Mo-ratio

T. Steiner, S.R. Meka, E. Bischoff, T. Waldenmaier, E.J. Mittemeijer

Abstract:

Ternary Fe–Cr–Mo alloys, all containing about 2 at.% total alloying element content (Cr+Mo) but with atomic Cr/Mo-ratios ranging from 1.0 to 7.2, were nitrided at 580 °C, 550 °C, and 520°C. The nitrided zone was characterized by light microscopy, hardness measurements, electron probe microanalysis and X-ray diffraction. The alloying element nitrides forming in the nitrided zone were characterized by scanning and transmission electron microscopy. Initially, the continuous precipitation of finely distributed, “mixed”, cubic NaCl-type (Cr,Mo) N_y nitride platelets, exhibiting a Baker-Nutting orientation relationship with the ferrite matrix, occurs. The developing N-concentration-depth profiles indicate that alloys with a lower Cr/Mo-ratio show a slightly slower nitride-precipitation rate. The attainable surface hardness and the residual surface macrostress are of similar magnitudes for all Cr/Mo-ratios. Upon prolonged nitriding (= aging of the nitrided microstructure), a discontinuous transformation takes place leading to the formation of a coarsened lamellar microstructure. The nature of this discontinuous reaction changes from a discontinuous coarsening of the initial (Cr,Mo) N_y nitride platelets for alloys of high Cr/Mo-ratios to a discontinuous precipitation of hexagonal CrMoN₂ for alloys of low Cr/Mo-ratios. The latter reaction, as compared to the first one, is driven by a larger driving force and thus the extent of the discontinuous transformation increases considerably with decreasing Cr/Mo-ratio. A summarizing discussion on precipitation of “mixed” vs. separate nitrides is presented.

7.1 Introduction

The surface-dependent properties, e.g. wear, corrosion, and fatigue resistances, of many technological components can be pronouncedly improved by selective engineering of the surface-adjacent regions [4], [5]. Nitriding is a thermochemical surface treatment by which nitrogen is introduced into the workpiece [5], [8]. The nitrogen initially adsorbed at the surface may diffuse inwardly and react with alloying elements having an affinity for N [159], as e.g. Ti [13], [14], V[15]–[19], Al [32]–[35], Cr [20]–[27], and Mo [28]–[31], which is essential for the above mentioned property improvement. Nitriding of binary, ferritic Fe-based alloys containing one of the above mentioned alloying elements was subject of a number of investigations in order to arrive at fundamental understanding of the nitriding process in these materials.

Technical steels usually contain a larger number of alloying elements either added to achieve required properties of bulk material, e.g. strength and toughness, or present as a result of the steel-making process [179], [216]. Among the deliberately added alloying elements, addition of Cr result in improved hardenability, temperature stability, hardness, and corrosion resistance. These properties can be further enhanced by additionally alloying of the steel with Mo. Thus, both Cr and Mo are present in many commercial steel grades. These alloying elements can also bring about favorable properties in a nitriding treatment.

Upon nitriding of *binary* Fe-Cr and Fe-Mo alloys, both alloying elements are known to react with inwardly diffusing N to form finely distributed alloying element nitrides in the ferrite matrix of the binary Fe-based, Fe-Cr and Fe-Mo alloys, a microstructure commonly referred to as continuously precipitated (CP) [9], [20], [21], [23], [25], [29], [31]. Upon aging (as happening upon prolonged nitriding), the CP microstructure may transform to a coarse lamellar microstructure: in nitrided binary Fe-Cr alloys discontinuous coarsening (DC) takes place, whereas in nitrided binary Fe-Mo alloys discontinuous precipitation (DP) takes place, i.e. the initial (metastable) alloying element nitride is replaced by a (more) stable one. For further details on the nitriding reactions of binary Fe-Cr and Fe-Mo alloys, see section 7.4.1.

The nitriding behavior of only a few Fe-based *ternary* alloys has been investigated: The Fe-Cr-Al and Fe-Cr-Ti systems present a combination of strong [5], [32] nitride formers. It was found [61]–[64], [217] that both nitride forming elements are initially incorporated into a ternary, mixed, metastable, cubic NaCl-type (Me_1, Me_2)N nitride. A series of systems containing one of the strong nitride formers Cr, V and Ti next to the very weak nitride former Si showed no formation of mixed nitrides but sequential precipitation of nitrides [66], [215]: precipitation of Si-nitride commenced only after full precipitation of the Cr/V/Ti-nitride.

Against the above background an investigation of the nitriding response of the Fe-based Fe-Cr-Mo system, involving a stronger (Cr) and a weaker (Mo) nitride forming element, appears of both practical, technological and fundamental, scientific interest. The nitrides formed in a ternary Fe-1.01 at.%Cr-0.98 at.%Mo alloy were thoroughly characterized in the preceding publication Chapter 6: Initially, dissolved Cr and Mo react with the inwardly diffusing N to form a CP microstructure containing finely distributed, cubic NaCl-type ternary $(Cr_{1/2}, Mo_{1/2})N_{3/4}$ nitride platelets exhibiting a Baker-Nutting (BN) orientation relationship (OR) with the ferrite matrix. The cubic nitride is metastable and by a DP reaction, setting in upon prolonged nitriding (=aging of the already nitrided microstructure), the CP microstructure transforms to a microstructure composed of alternating lamellae of ferrite and the stable, hexagonal, Mo-enriched $CrMoN_2$

nitride. Inside the ferrite lamellae, spherical particles of stable, Cr-enriched cubic (Cr,Mo) N_y occur.

The purpose of the current study is to investigate the effect of a variable Cr/Mo-ratio of the Fe-Cr-Mo alloy, containing in total about 2 at.% (Cr+Mo), and thereby expose consequences of the difference in the Cr-N and Mo-N interactions for the nitride-precipitation mechanisms in the ternary alloy.

7.2 Experimental

7.2.1 Specimen preparation and nitriding

Cast slabs of Fe-Cr-Mo alloys were prepared by melting elemental Fe (purity 99.98 wt.%), Cr (99.99 wt.%) and Mo (99.95 wt.%) in an induction furnace under a protective Ar atmosphere. The casts were cold rolled to sheets of 1 mm thickness. From the rolled sheets, foils (dimensions 1 x 20 x 15 mm³) were cut. The surfaces of the foils were ground and polished (final stage 1 μ m diamond suspension). Results of the chemical analysis of the alloys have been gathered in Table 6.1. Note that not more than 1 at.% Mo can be dissolved in ferrite at 580 °C [218], which is why Cr/Mo-ratios lower than 1.0 were not investigated in the current study with a constant Cr+Mo content of 2 at.%.

Table 7.1: Alloying element contents and atomic Cr/Mo-ratios of the Fe-Cr-Mo alloys used in this work. Cr, Mo, Mn and Si contents were determined by inductive coupled plasma optical emission spectroscopy; C content was determined by a combustion method; carrier gas hot extraction was applied for determination of O and N contents. Balance Fe.

alloy	Cr [at.%]	Mo [at.%]	Mn [at.%]	Si [at.%]	C [at.%]	O [at.%]	N [at.%]	Cr/Mo -ratio
Fe-1.04Cr- 1.01Mo	1.04±0.01	1.01±0.01	<0.001	<0.02	0.010±0.001	0.021±0.004	<0.004	1.0
Fe-1.31Cr- 0.74Mo	1.31±0.01	0.74±0.01	<0.001	<0.02	0.009±0.001	0.018±0.004	<0.004	1.8
Fe-1.57Cr- 0.50Mo	1.58±0.02	0.50±0.01	<0.001	<0.02	0.007±0.001	0.021±0.004	<0.004	3.1
Fe-1.81Cr- 0.25Mo	1.81±0.02	0.25±0.01	<0.001	<0.02	0.007±0.002	0.018±0.007	<0.004	7.2

The foil specimens were encapsulated in an Ar-filled quartz tube and recrystallized at 750 °C for 30 min. Before nitriding, the surfaces of the specimens were polished (last stage 1 µm diamond suspension) and cleaned, successively, with ethanol, acetone and isopropanol.

The foil specimens were nitrided in a vertical multizone quartz tube furnace (temperature accuracy ±1 K) in a flowing NH₃/H₂ gas mixture. High purity ammonia (>99.998 vol.%) and hydrogen (>99.999 vol.%) gases were used. The flow rates of the gases were adjusted with calibrated mass flow controllers. The flow rates of the ammonia and hydrogen gases were adjusted to achieve a nitriding potential $r_N = \frac{p_{\text{NH}_3}}{p_{\text{H}_2}^{3/2}}$, where p represents the partial pressure [172], of 0.1 atm^{-½}. Nitriding was performed for nitriding times of 1, 3, 6, 62 and 144 h at 580 °C, 1, 4, and 8 h at 550 °C, and 2, 7, and 16 h at 520 °C. Note that under the employed nitriding conditions iron nitrides cannot develop (on the surface) upon nitriding pure iron [12]. The nitriding treatment was terminated by quenching the specimen into N₂ flushed water at room temperature. Specimens were weighed before and after nitriding using a Mettler Toledo UMX2 microbalance with an accuracy of ±1 µg. From the gain/loss in weight of the foils, the amount of N taken up/lost by the specimens was calculated.

7.2.2 Microstructural characterization

For metallographic investigations, parts of the nitrided foils were cut off normal to the foil surface and a protective Ni plating was applied to these parts by electrodeposition in a Watts bath [219], [220]. These Ni plated pieces were embedded in Struers Polyfast. The embedded specimens were ground, polished (last stage 1 µm diamond suspension) and etched with 1 % Nital. Light microscopy (LM) images were taken from cross sections with a Zeiss Axiophot microscope equipped with a Colorview Illu CCD camera. Scanning electron microscopy (SEM) images were taken using a LEO 1530 VP SEM equipped with a field emission gun and an inlens detector.

Elemental (Fe, N, Cr and Mo) concentration-depth profiles were recorded from the cross-sections employing a Cameca SX100 electron probe microanalysis (EPMA) system operating at 15 kV and a current of 100 nA. Characteristic X-ray emission peaks were measured and divided by the corresponding intensities obtained from standard specimens of pure Fe (for Fe-K_β), pure Cr (for Cr-K_α), pure Mo (for Mo-L_α) and pure γ'-Fe₄N (for N-K_α). Elemental concentrations were calculated from the intensity ratios employing the $\Phi(\rho z)$ approach [94]. Three depth profiles were recorded on each specimen cross-section; the profiles used in the evaluation repre-

sent the average of the three measured values for the elemental content at each depth below the surface.

For transmission electron microscopy (TEM) investigations of the microstructure, rectangular pieces from the nitrided foils (edge length 3 mm) were cut and subsequently ground to round discs of about 3 mm diameter. These discs were polished mechanically, dimpled and Ar-ion milled (3 kV acceleration voltage, 8° ion angle of incidence with respect to the plane of the surface, for approximately 2 h, liq.-N₂ cooling). Bright field (BF) and dark field (DF) diffraction contrast images and selected area diffraction patterns (SADP) were recorded employing a Philips CM 200 TEM operating at 200 kV and equipped with a Gatan CCD camera.

X-ray diffraction (XRD) patterns were recorded from the surface of the foil specimens using a PANalytical Multipurpose Diffractometer (MPD) operating in Bragg-Brentano geometry, and employing Co-K α radiation selected by a graphite monochromator in the diffracted beam [56]. The diffraction-angle (2θ) range of 10°-110° 2θ was scanned with a step size of 0.03° 2θ . During the measurement the specimen was rotated around its surface normal to improve the crystallite statistics. For phase identification, the substance reference patterns in the ICDD database [97] were used.

For residual stress determination, $\sin^2\psi$ measurements [60] were performed applying a PANalytical Materials Research Diffractometer (MRD) equipped with an Eulerian cradle, operating in parallel beam geometry and employing Co-K α radiation selected by a graphite monochromator in the diffracted beam [56]. The 211 ferrite-matrix reflection was recorded in the 2θ -range from 93-107° 2θ with a step size of 0.05° 2θ at ψ -angles from 0 to 80° in steps of 10°. The thus recorded 211 ferrite-matrix peaks were fitted utilizing the PANalytical X'Pert HighScore (Version 3.0.5) software employing a linear background and two peaks, one for the ferrite-main reflection and one for the broad tail and/or continuous coarsening (CC) ferrite peak (see discussion of XRD results in section 7.3.3). Each peak is described by two pseudo-Voigt functions, one for each (α_1 and α_2) component of the employed Co-K α radiation. The peak positions obtained for the K α_1 -pV function of the ferrite-main peak were employed in the $\sin^2\psi$ -analysis [60] for a rotationally symmetric state of planar stress. The diffraction (X-ray) elastic constants for the 211 ferrite reflection, calculated according to the Eshelby-Kröner grain-interaction model [60], with the single crystal data of pure ferrite, have been adopted as given in Ref. [221].

7.3 Results and discussion

7.3.1 Morphology

The microstructures of the various Fe-Cr-Mo alloys of different Cr/Mo-ratio after nitriding at 550 °C for 8 h are shown in the LM images presented in Fig. 7.1. The nitrided zone exhibits a more pronounced etching contrast than the unnitrided core due to the formation of alloying element nitrides in association with depletion of dissolved alloying elements from the matrix. As indicated in Fig. 7.1 by dashed lines, the nitrided zone is of comparable thickness for the four alloys investigated (as also indicated by EPMA results shown in Fig. 7.8). The alloys of lower Cr/Mo-ratio exhibit a more pronounced grain-boundary etching.

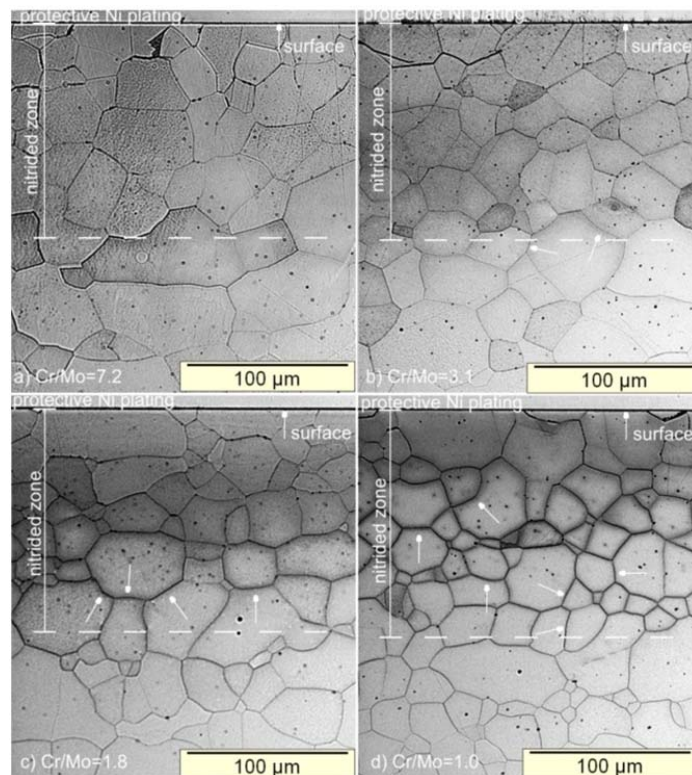


Fig. 7.1: Light optical micrographs taken from the etched cross-section of a) Fe-1.81Cr-0.25Mo, b) Fe-1.57Cr-0.50Mo, c) Fe-1.31Cr-0.74Mo, and d) Fe-1.04Cr-1.01Mo alloy specimens nitrided at 550 °C for 8 h with a nitriding potential of 0.1 atm^{-½}. The nitrided zone has been indicated by white dashed lines (see also EPMA results in Fig. 7.8) and the surface by a white arrow. Formation of misfitting alloying element nitrides in association with the depletion of dissolved Cr and Mo from the matrix leads to the more pronounced etching of the ferritic matrix in the nitrided zone as compared to the specimen core. White arrows in the lower part of the nitrided zone indicate regions of pronounced grain-boundary etching (see text).

The nitrogen-content depth profile, as determined by EPMA, is shown for the nitrided alloy with a Cr/Mo-ratio of 1.0 in Fig. 7.2. This nitrogen-content depth profile shows features similar for all investigated alloys: the surface-adjacent region exhibits an N-concentration plateau of height compatible with complete precipitation of all originally dissolved Cr and Mo as nitride (see section 7.3.2 for a detailed discussion). The pronounced etching observed at the grain boundaries in the nitrided zone (Fig. 7.1) is accompanied by an increased N-content at these locations suggesting a preferred precipitation of alloying element nitrides at grain boundaries (see also section 7.3.2).

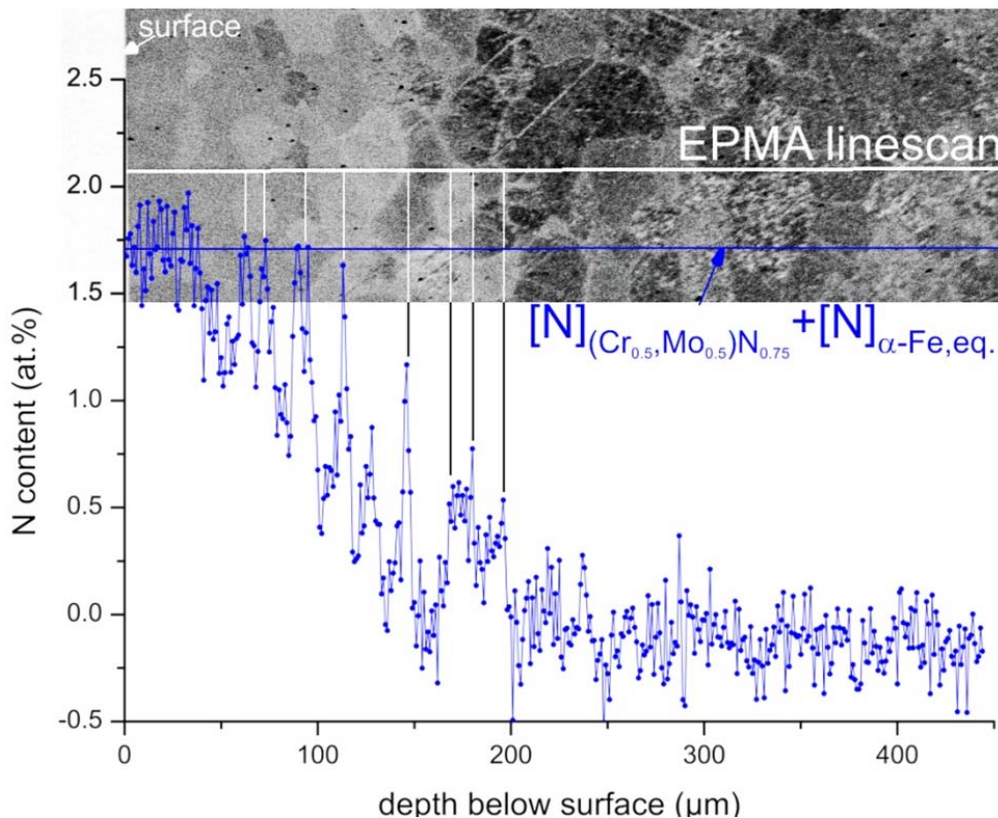


Fig. 7.2: A single (not averaged; cf. section 6.2.2) EPMA N-concentration-depth profile recorded on the cross-section of a Fe-1.04Cr-1.01Mo alloy specimen nitrided at 550 °C for 8 h with a nitriding potential of $0.1 \text{ atm}^{-\frac{1}{2}}$. The location of the EPMA line-scan has been indicated by a horizontal white line. The expected N-content for full precipitation of all Cr and Mo as $(\text{Cr}_{\frac{1}{2}}, \text{Mo}_{\frac{1}{2}})\text{N}_{\frac{3}{4}}$ plus the equilibrium amount of N dissolved in ferrite for the given nitriding conditions has been indicated by a blue horizontal line. A plateau of constant N-concentration approximately corresponding to the expected level of N is evidenced close to the specimen surface (in a depth range of $\sim 25 \mu\text{m}$). Grain boundaries in the deeper nitrided region (below the plateau region) are indicated by vertical lines and correspond to regions of increased N-content.

TEM BF and DF diffraction contrast images (Fig. 7.3) of the nitrided region of the Fe-Cr-Mo alloys demonstrate that finely distributed, nano-sized nitride platelets, with their broad faces parallel to the $\{100\}_{\alpha\text{-Fe}}$ planes of the ferrite matrix, have formed in all alloys. In the corresponding SADPs (see insets in Fig. 7.3), streaking occurs along $\langle 100 \rangle_{\alpha\text{-Fe}}$ directions, as a result of the small size of the cubic NaCl-type $(\text{Cr},\text{Mo})\text{N}_y$ nitride platelets being largely coherent with the ferrite matrix (Chapter 6). The nitride platelets exhibit similar sizes and morphology, practically independent of the Cr/Mo-ratio.

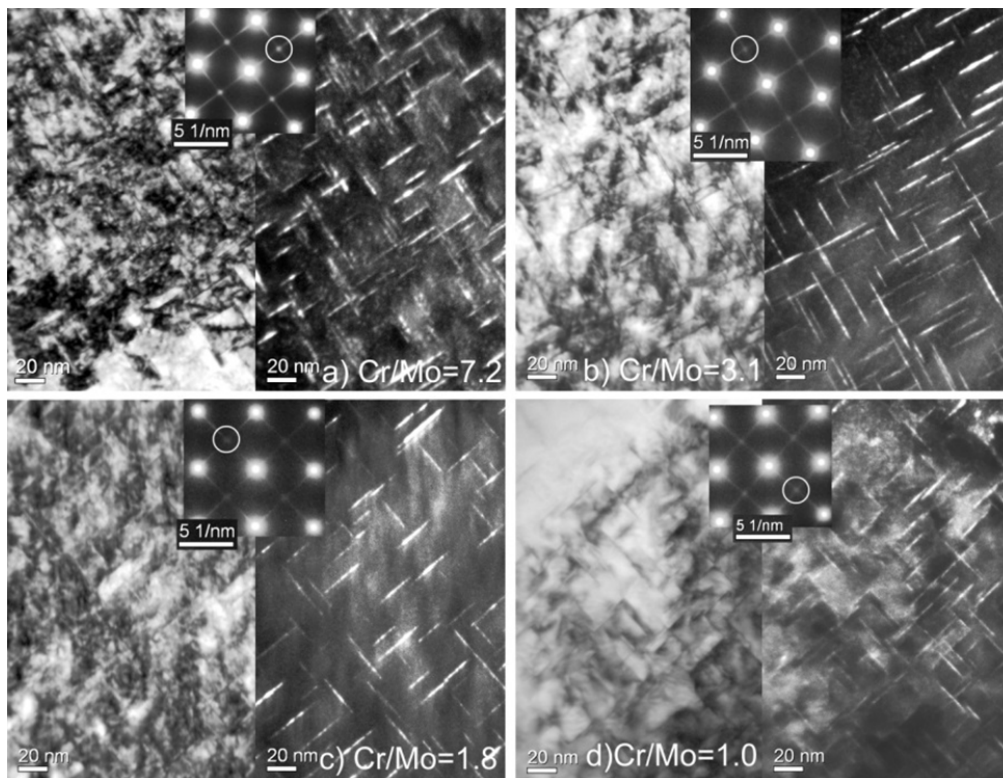


Fig. 7.3: TEM bright field micrographs (left parts of the figures), corresponding $[001]_{\alpha\text{-Fe}}$ zone axis SADPs (inset), and dark field micrographs (right parts of the figures) obtained by positioning the aperture as indicated by white circles in the SADPs of Fe-Cr-Mo alloy specimens with the indicated Cr/Mo-ratios nitrided at $580\text{ }^{\circ}\text{C}$ for 6 h with a nitriding potential of $0.1\text{ atm}^{-1/2}$. The TEM specimens/foils were taken from a depth of about $100\text{ }\mu\text{m}$ below the surface. Platelets with broad faces parallel to $\{100\}_{\alpha\text{-Fe}}$ lattice planes and of approximately similar size are present in all alloys. In the SADPs streaking occurs along $\langle 100 \rangle_{\alpha\text{-Fe}}$ directions, compatible with a Baker-Nutting orientation relationship of NaCl-type nitride precipitates with the platelet faces parallel to $\{100\}_{\alpha\text{-Fe}}$. The dark field images evidence that the streaks correspond with the nitride platelets. The 220 magnetite (Fe_3O_4) spots (at the intersection of the streaks) emerge due to unavoidable oxidation of the TEM foil surfaces (cf. Ref. [33]).

Upon prolonged nitriding (=aging for the nitrided regions), all investigated Fe-Cr-Mo alloys (partially) undergo a “discontinuous” reaction, as evidenced by the development of regions with dark etching contrast in the nitrided region close to the specimen surface after 72 h of nitriding (Fig. 7.4). The extent of the discontinuous transformation shows a strong dependence on the Cr/Mo-ratio of the alloy: in alloys with a high Cr/Mo-ratio a minimal amount of discontinuous transformation had occurred (Fig. 7.4a), whereas in the alloy with the lowest Cr/Mo-ratio the entire surface adjacent microstructure had transformed discontinuously (Fig. 7.4d). After *through* nitriding for 144 h at 580 °C, practically the entire specimen of the alloy with a (the lowest) Cr/Mo-ratio of 1.0 had transformed discontinuously to the lamellar microstructure (Fig. 7.5). Note that in this stage of the discussion a distinction between discontinuous coarsening and discontinuous precipitation (see section 6.1) cannot be made (but see what follows).

The discontinuously transformed regions form by the movement of reaction fronts starting from grain boundaries of the microstructure [150], [152]. The transformed regions consist of alternating, parallel ferrite-matrix and alloying-element-nitride lamellae. As shown by the SEM micrographs presented in Fig. 7.6, the morphology of the transformed regions and of the developing nitride lamellae vary with the Cr/Mo-ratio: in alloys of higher Cr/Mo-ratio the discontinuously transformed regions consist of multiple packages of parallel, short and wavy nitride lamellae (Fig. 7.6a). This morphology is similar to that resulting from a DC reaction in nitrided binary Fe-Cr alloys [22], [23]. In alloys of lower Cr/Mo-ratio the discontinuously transformed regions show very long, straight, parallel lamellae extending through the entire transformed regions. In a previous investigation of the nitride phases in nitrided Fe-1.01 at.%Cr-0.98 at.%Mo-alloy (i.e. Cr/Mo \approx 1.0) such long straight lamellae have been shown to be of hexagonal CrMoN₂ formed by a DP reaction (Chapter 6).

The hardness of the discontinuously transformed regions is distinctly lower than/ roughly half of that of the (initial) CP regions (see Fig. 7.7).

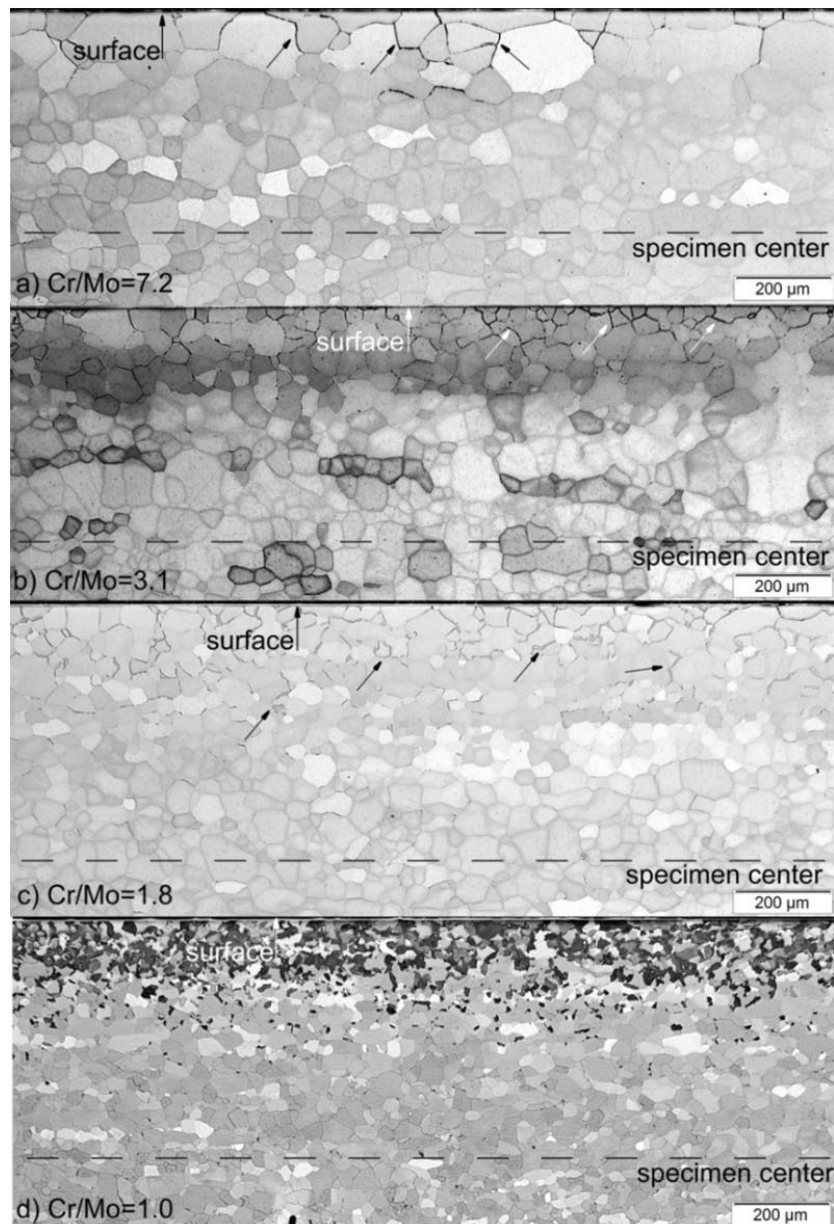


Fig. 7.4: Light optical micrographs taken from the etched cross-sections of a) Fe-1.81Cr-0.25Mo, b) Fe-1.57Cr-0.50Mo, c) Fe-1.31Cr-0.74Mo, and d) Fe-1.04Cr-1.01Mo alloy specimens nitrided at 580 °C for 72 h with a nitriding potential of $0.1 \text{ atm}^{-1/2}$. The centers of the approximately 0.9 mm thick specimens have been indicated by dashed black lines. In the surface-adjacent regions of the specimens of higher Cr/Mo-ratios, some grain boundaries (indicated by arrows) were etched pronouncedly and appear black (a) and b)) while for the specimens of lower Cr/Mo-ratios (c) and d)) pronouncedly etched and dark appearing regions, starting from grain boundaries, can be observed. Such regions have a lamellar microstructure, as revealed especially in SEM micrographs (Fig. 7.6).

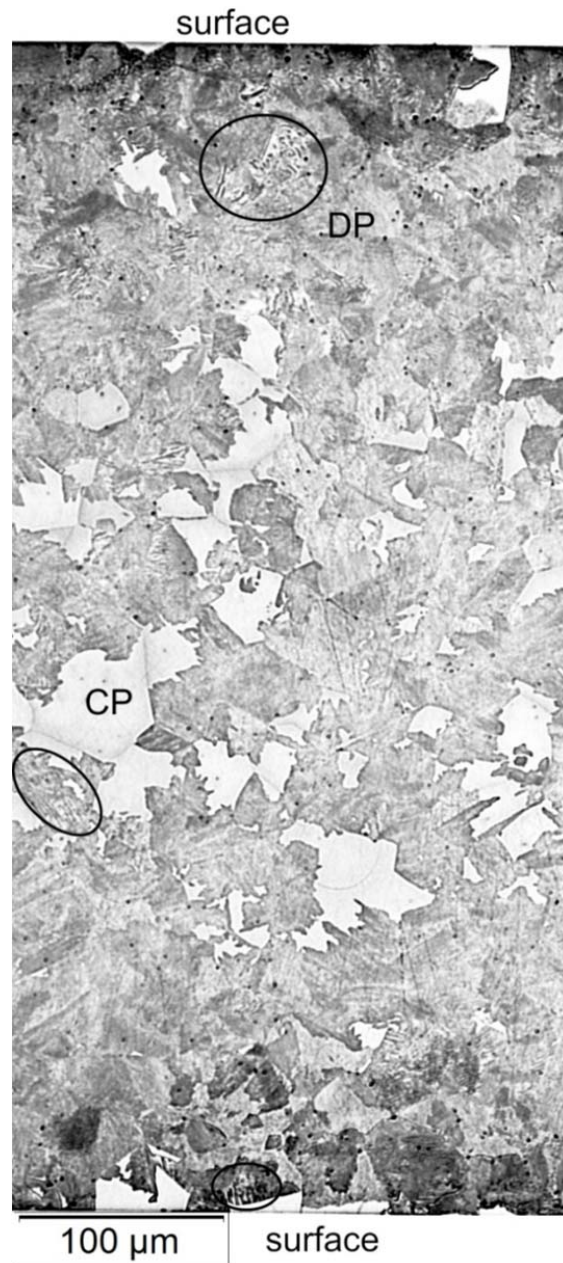


Fig. 7.5: Light optical micrograph taken from the entire etched cross-section of an Fe-1.04Cr-1.01Mo alloy specimen, through nitrided at 580 °C for 144 h with a nitriding potential of $0.1 \text{ atm}^{-1/2}$. Regions exhibiting the lamellar DP-microstructure (see also Fig. 7.6) appear darker due to their stronger response to etching. At locations where the lamellae of the DP microstructure have been cut at a shallow angle with respect to the surface of the cross-section, they can be resolved by light microscopy: see the regions enclosed by black circles. The few bright appearing regions correspond with the remaining regions of the initially forming CP microstructure (see Fig. 7.1).

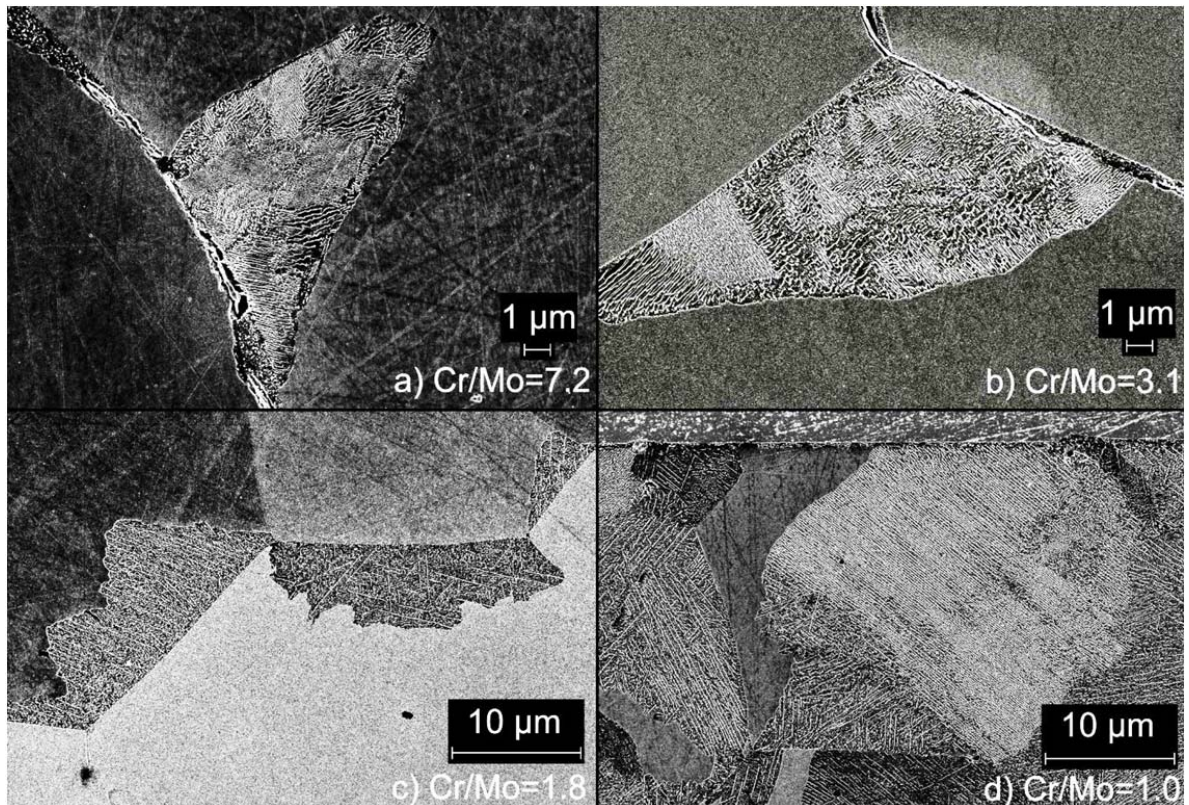


Fig. 7.6: SEM micrographs taken from the etched cross-sections of a) Fe-1.81Cr-0.25Mo, b) Fe-1.57Cr-0.50Mo, c) Fe-1.31Cr-0.74Mo, and d) Fe-1.04Cr-1.01Mo alloy specimens nitrided at 580 °C for 72 h with a nitriding potential of $0.1 \text{ atm}^{-\frac{1}{2}}$.

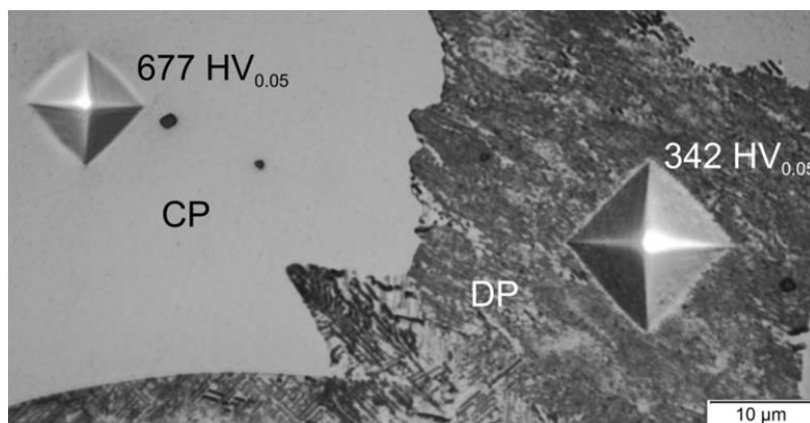


Fig. 7.7: Light optical micrograph taken from the etched cross-section of an Fe-1.04Cr-1.01Mo alloy specimen nitrided at 580 °C for 72 h with a nitriding potential of $0.1 \text{ atm}^{-\frac{1}{2}}$. As follows from the microhardness testing indents shown in the micrograph, the lamellar DP regions are considerably softer than the adjacent CP regions.

7.3.2 Nitrogen uptake

The average N-concentration-depth profiles measured on the cross-sections of the Fe-Cr-Mo alloy specimens nitrided at 580 °C for 6 h, 550 °C for 8 h and 520 °C for 16 h with a nitriding potential of $0.1 \text{ atm}^{-\frac{1}{2}}$ (determined as described in section 6.2.2) are shown in Fig. 7.8 (N-concentration-depth profiles of the other nitrided specimens have been compiled in the supplementary data.) In the surface-adjacent regions (of depth range $\sim 25 \mu\text{m}$) of in particular the specimens with a high Cr/Mo-ratio an N-plateau of approximately constant N-concentration occurs. With decreasing Cr/Mo-ratio, the N-concentration level of this plateau decreases.

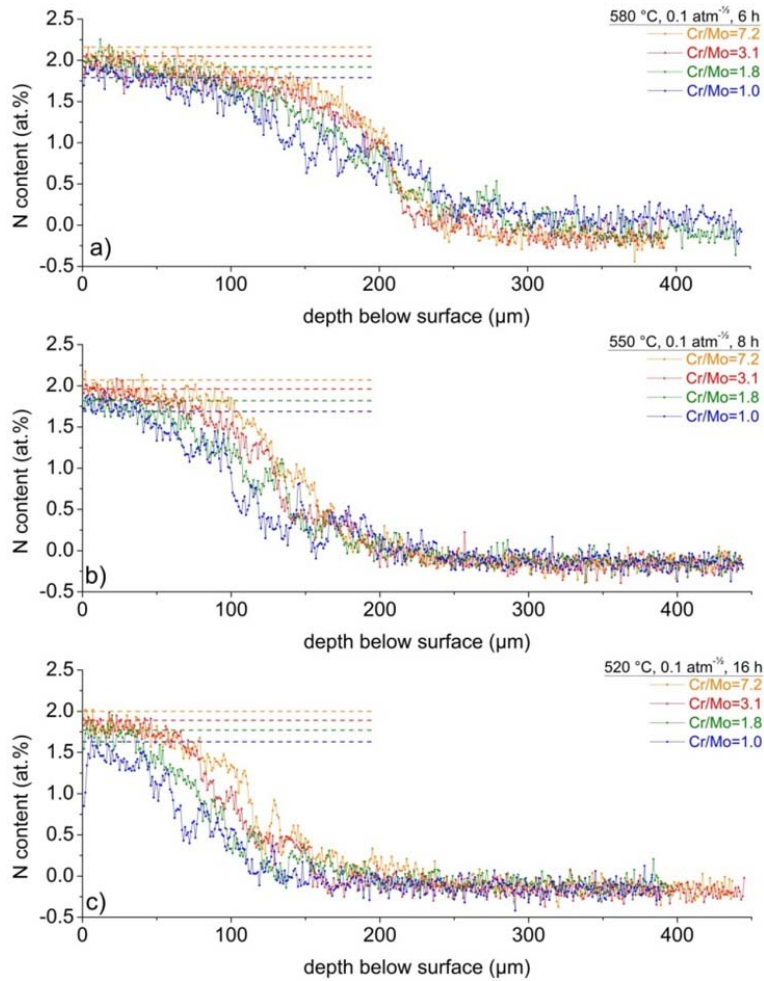


Fig. 7.8: N-concentration-depth profiles determined by EPMA (average of three measured profiles, see section 6.2.2) on the cross-sections of Fe-Cr-Mo alloy specimens nitrided with a nitriding potential of $0.1 \text{ atm}^{-\frac{1}{2}}$ a) at 580 °C for 6 h, b) at 550 °C for 8 h, and c) at 520 °C for 16 h. Expected levels of N-content (precipitation of all Cr and Mo as $(\text{Cr}_z, \text{Mo}_{1-z})\text{N}_{\frac{1+z}{2}}$ plus the equilibrium amount of dissolved N in ferrite) have been indicated by dashed lines.

Table 7.2: Inclination of the EPMA N-concentration-depth profiles in the transition regions from nitrided case to unnitrided core of Fe-Cr-Mo alloy specimens nitrided with a nitriding potential of $0.1 \text{ atm}^{-\frac{1}{2}}$ at 580 °C for 6 h, 550 °C for 8 h, and 520 °C for 16 h. The inclination was determined by a linear least-squares fit to the data points $\pm 70 \text{ }\mu\text{m}$ around the “nitrided depth”. Errors indicate the standard deviation of the linear fit.

nitriding treatment	inclination of the N-content-depth profile [$\text{at.}\% \mu\text{m}^{-1}$]			
	Fe-1.04Cr-1.01Mo	Fe-1.31Cr-0.74Mo	Fe-1.57Cr-0.50Mo	Fe-1.81Cr-0.25Mo
580 °C, 6 h, $0.1 \text{ atm}^{-\frac{1}{2}}$	-0.0065 ± 0.0003	-0.0110 ± 0.0002	-0.0141 ± 0.0004	-0.0157 ± 0.0004
550 °C, 8 h, $0.1 \text{ atm}^{-\frac{1}{2}}$	-0.0122 ± 0.0004	-0.0126 ± 0.0003	-0.0141 ± 0.0003	-0.0159 ± 0.0003
520 °C, 16 h, $0.1 \text{ atm}^{-\frac{1}{2}}$	-0.0127 ± 0.0003	-0.0141 ± 0.0003	-0.0156 ± 0.0003	-0.0139 ± 0.0003

The initially forming nitride platelets of the CP microstructure were shown to be of ternary, cubic NaCl-type $(\text{Cr},\text{Mo})\text{N}_y$ (Chapter 6) with an N-deficiency ($y < 1$), with respect to the (hypothetically fully occupied N-sublattices of the) $(\text{Cr},\text{Mo})\text{N}$ NaCl-type crystal structure, due to the presence of vacancies on the N-sublattice (as in binary $\gamma\text{-Mo}_2\text{N}$, see also Ref. [222]). It will be assumed in the following, that the amount of N to be expected in the mixed ternary $(\text{Cr},\text{Mo})\text{N}_y$ follows from a linear interpolation of the stoichiometry of CrN (1:1) and $\gamma\text{-Mo}_2\text{N}$ (2:1), thus giving the general formula $(\text{Cr}_z, \text{Mo}_{1-z})\text{N}_{\frac{1+z}{2}}$, where $z = \frac{x_{\text{Cr}}}{x_{\text{Cr}} + x_{\text{Mo}}}$, with x_i as the molar fraction of the alloying element i in the unnitrided state. Thus it follows for Cr/Mo = 1: $\frac{x_{\text{Cr}}}{x_{\text{Mo}}} = 1$; $z = \frac{1}{2}$ and the composition of the “ideal” nitride would be $(\text{Cr}_{\frac{1}{2}}, \text{Mo}_{\frac{1}{2}})\text{N}_{\frac{3}{4}}$, with 25 % vacancies on the N sublattice; in good agreement with data from Chapter 6. Accordingly, the amount of N required for full precipitation of all Cr and Mo as $(\text{Cr}_z, \text{Mo}_{1-z})\text{N}_{\frac{1+z}{2}}$ is then expected to decrease with the Cr/Mo-ratio of the alloy. On this basis, and by adding to these amounts of N the (very minor) amount of N dissolved in the ferrite matrix [7], predictions for the maximal amount of N taken up at saturation were obtained. These predicted values can be compared with the N-concentration values of the surface-adjacent plateau. Data for the latter were determined by averaging the N-content, as determined by EPMA, within $25 \text{ }\mu\text{m}$ of the specimen surface. These experimental data for the (maximal) N-content can be compared with the above-indicated predictions for the various Fe-Cr-Mo-alloys: see Fig. 7.9 (see also dashed lines in Fig. 7.8). In view of the experimental inaccuracy (Fig. 7.8) a good correspondence of experimental and predicted values is obtained indicating that the stoichiometry of the nitride is well described by the formu-

la $(Cr_z, Mo_{1-z})N_{\frac{1+z}{2}}$, and also that only a minimal amount of excess N occurs (for details about excess N, see Ref. [10]).

The evolution of the “nitrided depth” (defined here as the depth at which the N-concentration is half that of the surface-adjacent region, i.e. the “nitrided depth” corresponds to the penetration of N into the specimen if the N-concentration depth profile would be of perfectly rectangular shape) as function of the nitriding time and temperature for the various Fe-Cr-Mo alloys is shown in Fig. 7.10¹¹.

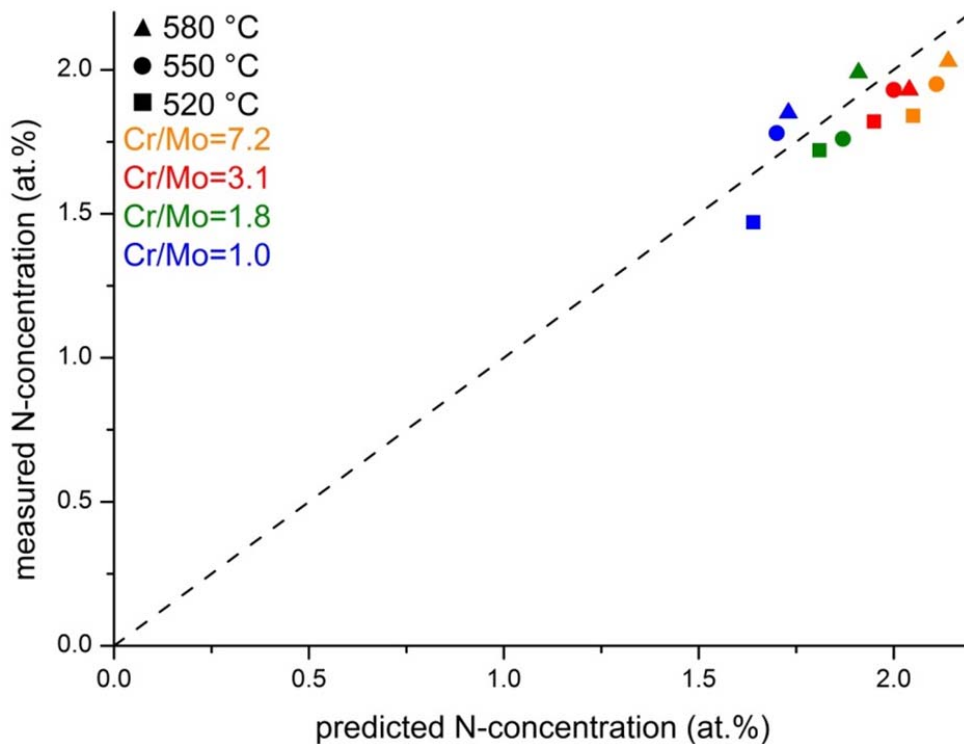


Fig. 7.9: N-concentration of the surface-adjacent N-plateau (as measured for the first 25 μm) of the Fe-Cr-Mo alloy specimens nitrided with a nitriding potential of $0.1 \text{ atm}^{-\frac{1}{2}}$ at 580 °C for 6 h, at 550 °C for 8 h, and at 520 °C for 16 h versus the expected N-concentration at the employed nitriding conditions for the respective alloy (precipitation of all Cr and Mo as $(Cr_z, Mo_{1-z})N_{\frac{1+z}{2}}$ plus the equilibrium amount of N dissolved in ferrite). The dashed line corresponds with (hypothetical) perfect coincidence of measured and expected N-contents.

¹¹ Note that the occurrence of pronounced grain-boundary precipitation (see section 7.3.1) in the low Cr/Mo-ratio alloys leads to a larger scatter in the N-concentration especially in the depth range of the transition region (i.e. the region between the fully nitrided plateau and the unnitrided core). Therefore, the averaging over three individual depth profiles, measured for each specimen, was employed (see section 6.2.2).

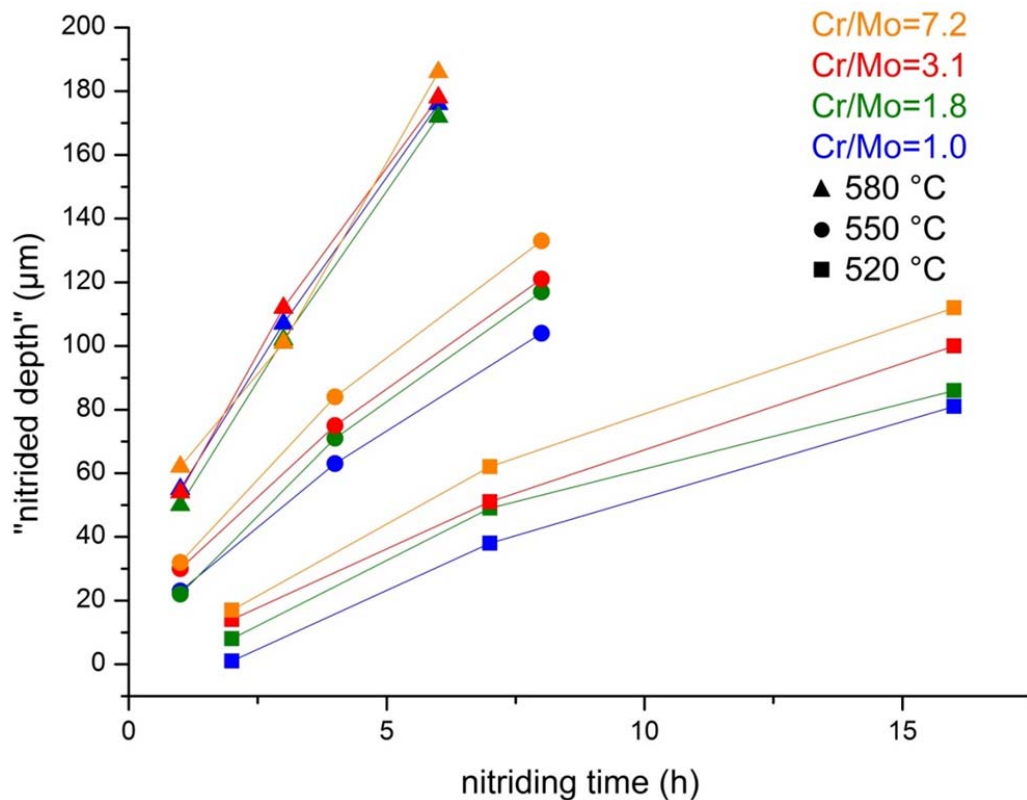


Fig. 7.10: The “nitrided depth” of Fe-Cr-Mo alloy specimens nitrided with a nitriding potential of $0.1 \text{ atm}^{-1/2}$ at the indicated nitriding temperature as function of nitriding time. The “nitrided depth” was determined by integrating the N-concentration-depth curves (see Fig. 7.8 and the supplementary data) and dividing by the N-content measured as the average of the first 10 data points in the vicinity of the surface (i.e. the “nitrided depth” corresponds to the penetration of N into the specimen if the N-concentration depth profile would be of perfectly rectangular shape).

At the highest nitriding temperature of 580 °C, the nitrided depth for all four alloys is nearly the same. For the lower nitriding temperatures of 550 °C and 520 °C, the nitrided depth is larger for alloys with a higher Cr/Mo-ratio, implying a deeper penetration of N into the specimens. Together with the finding of a higher plateau level of N-content for alloys of a higher Cr/Mo-ratio (see above), this implies a higher N-uptake rate for the alloys of higher Cr/Mo-ratios.

With decreasing Cr/Mo-ratio, the development of a clear plateau of constant N-concentration near the surface regions becomes less outspoken: alloys of low Cr/Mo-ratio show a more gradual decrease of the N-content with depth. As a measure for the inclination/steepness of the N-concentration-depth profile in the transition region from nitrided case to unnitrided core, a linear function was fitted by least squares refinement to the EPMA data points $\pm 70 \text{ }\mu\text{m}$ around

the nitrided depth (as defined above). The values for the slope of that line are presented in Table 7.2. It follows that the lower the Cr/Mo-ratio of the alloy, the less inclined/less steep the N-concentration-depth profile in the transition region at all nitriding temperatures, which is indicative of a so-called *Me-N* interaction becoming weaker [8], [32] with decreasing Cr/Mo-ratio. Hence, although the nitrogen-uptake rate is lower for lower Cr/Mo-ratios (see above), the inward diffusing nitrogen can reach larger depths for lower Cr/Mo-ratios under the same nitriding conditions (see below for the related discussion of the core-hardness increase).

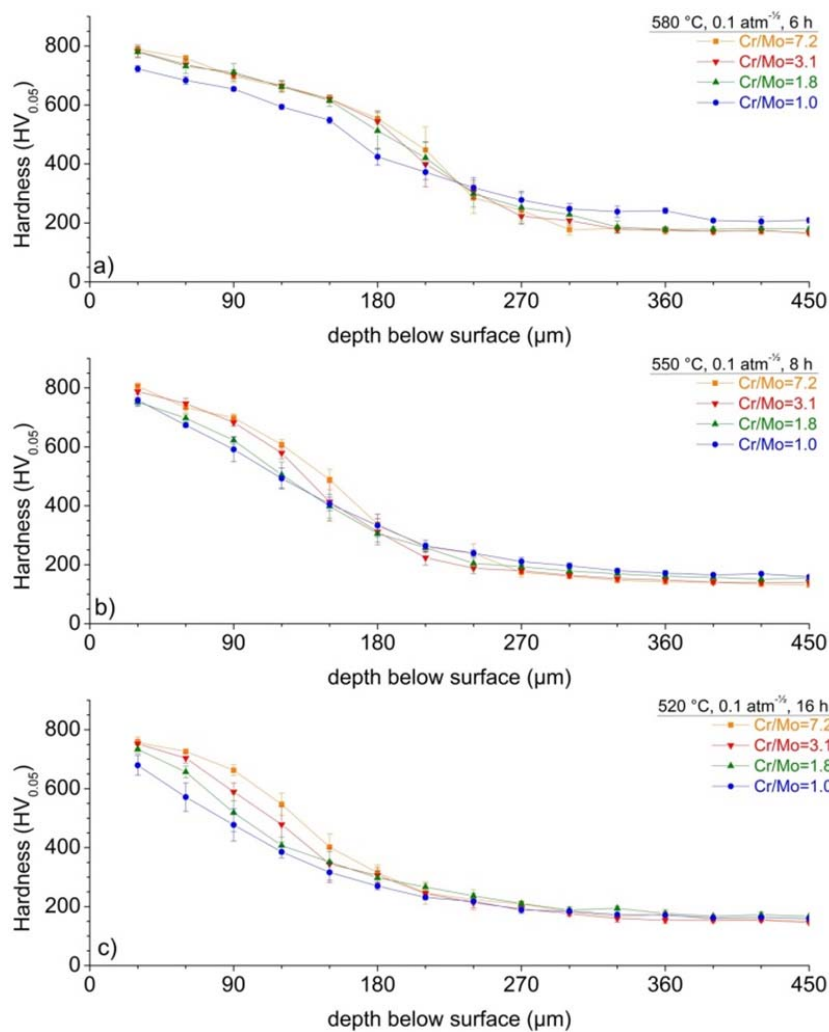


Fig. 7.11: Hardness-depth profiles determined on the cross-sections of Fe-Cr-Mo alloy specimens nitrided with a nitriding potential of 0.1 atm^{-3/2} a) at 580 °C for 6 h, b) at 550 °C for 8 h, and c) at 520 °C for 16 h. The data points represent the average of 5 individual measurements; error bars indicate the standard deviation of the measurements.

The hardness-depth profiles determined on cross-sections of the nitrided Fe-Cr-Mo alloys (Fig. 7.11) reflect the trends revealed by the measured N-concentration depth profiles (hardness-depth profiles of the other nitrided specimens have been compiled in the supplementary data). The higher the Cr/Mo-ratio, the higher the attainable surface hardness and the steeper the hardness-depth profile in the transition region. The shape of the hardness-depth profile follows from the shape of the N-concentration-depth profiles. The hardness of the nitrided zone is determined mainly by the volume fraction of nitride particles and the particle-size distribution, i.e. for a certain amount of second phase a finer distribution of particles is expected to be associated with a higher hardness [59]. In the various Fe-Cr-Mo alloys (i) an equal volume fraction of nitrides (about 3 vol.%) is expected to precipitate upon nitriding as the content of (metallic) alloying elements in the alloys is practically the same (2 at.% total) and the crystal structure of the precipitating nitride is the same for all investigated alloys (see section 7.3.1), and (ii) the distribution and size of the precipitates, as determined by TEM, is also practically the same (Fig. 7.3). It can be concluded that similar hardness increases upon completion of nitriding (as in the surface region) can be expected, in agreement with the observations.

A striking feature of the hardness-depth profiles is the apparent increase in core hardness of the specimens with nitriding time (see Table 7.3). This increase is of the order of what can be expected as a consequence of the presence of dissolved N in ferrite (note that the corresponding N-concentration is too small to be detected by EPMA). If an ideally weak *Me-N* interaction would prevail (as observed, for example, upon nitriding binary Fe-Si alloy specimens [38]) the nitrogen concentration in the core of the specimen can be predicted crudely as similar to that brought about by diffusion of N in pure ferrite. Such concentration profiles can be calculated straightforwardly (see Ref. [223]). Then, adopting the relation between hardness increase and dissolved nitrogen content presented in Ref. [224], a predicted value for the increase in core hardness is obtained. Such predicted values can be compared with the experimentally observed ones in Table 7.3. It can be concluded that the increase of hardness in the core is indeed about that expected for an amount of dissolved nitrogen which has arrived there by inward diffusion. Strikingly, the experimental hardness increase at the core increases with decreasing Cr/Mo-ratio, which is compatible with the above conclusion that the inwardly diffusing nitrogen reaches larger depths for lower Cr/Mo-ratios.

Table 7.3: The core hardness (as $HV_{0.05}$, i.e. application of a load of 50 g, with a loading duration of 10 s) increases as measured for the Fe-Cr-Mo specimens nitrided at conditions indicated in the first column. The calculated N-contents in the center of a corresponding (0.9 mm thick) pure Fe foil [223] for nitriding conditions as for the Fe-Cr-Mo specimens are given in the sixth column. The last column shows the hardness increases as predicted from the calculated dissolved N-content in pure iron [224].

nitriding treatment	measured core hardness increase [$HV_{0.05}$]				predicted hardness increase of pure Fe containing the calculated N-content at the center of 0.9 mm thick pure Fe [$\Delta HV_{0.05}$]
	Fe-1.04Cr-1.01Mo	Fe-1.31Cr-0.74Mo	Fe-1.57Cr-0.50Mo	Fe-1.81Cr-0.25Mo	
580 °C, 1 h, 0.1 atm ^{-½}	+20	+16	+18	+14	+7
580 °C, 3 h, 0.1 atm ^{-½}	+44	+40	+33	+32	+38
580 °C, 6 h, 0.1 atm ^{-½}	+92	+71	+68	+66	+65
550 °C, 1 h, 0.1 atm ^{-½}	±0	±0	±0	±0	+2
550 °C, 4 h, 0.1 atm ^{-½}	+20	+32	+16	+21	+24
550 °C, 8 h, 0.1 atm ^{-½}	+47	+53	+37	+34	+41
520 °C, 2 h, 0.1 atm ^{-½}	±0	±0	±0	±0	+2
520 °C, 7 h, 0.1 atm ^{-½}	+27	+33	+25	+20	+16
520 °C, 16 h, 0.1 atm ^{-½}	+51	+61	+55	+49	+30

7.3.3 X-ray diffraction and residual stress evolution

The XRD patterns of the unnitrided and nitrided Fe-Cr-Mo alloys show that the alloys are fully ferritic before and after nitriding. No separate reflections due to alloying element nitrides can be observed in the diffraction patterns of the nitrided specimens. Initially the fine, cubic NaCl-type nitrides diffract coherently with the ferrite matrix, which expands due to the elastic accommodation of the precipitate/matrix misfit (Ref. [10], Chapter 2, and Chapter 4). The latter effect causes the diffraction peak of the aggregate (matrix + precipitates) to shift to a lower diffraction angle (Chapter 4). Further, the macroscopic misfit of the nitrided case (experiencing volume expansion) and the unnitrided core induces a residual compressive macrostress in the nitrided zone (see below) parallel to the surface (see e.g. Ref. [27]) causing further peak shift towards lower diffraction angle (the experimentally determined 211 reflections of all nitrided alloys have been compiled in the supplementary data).

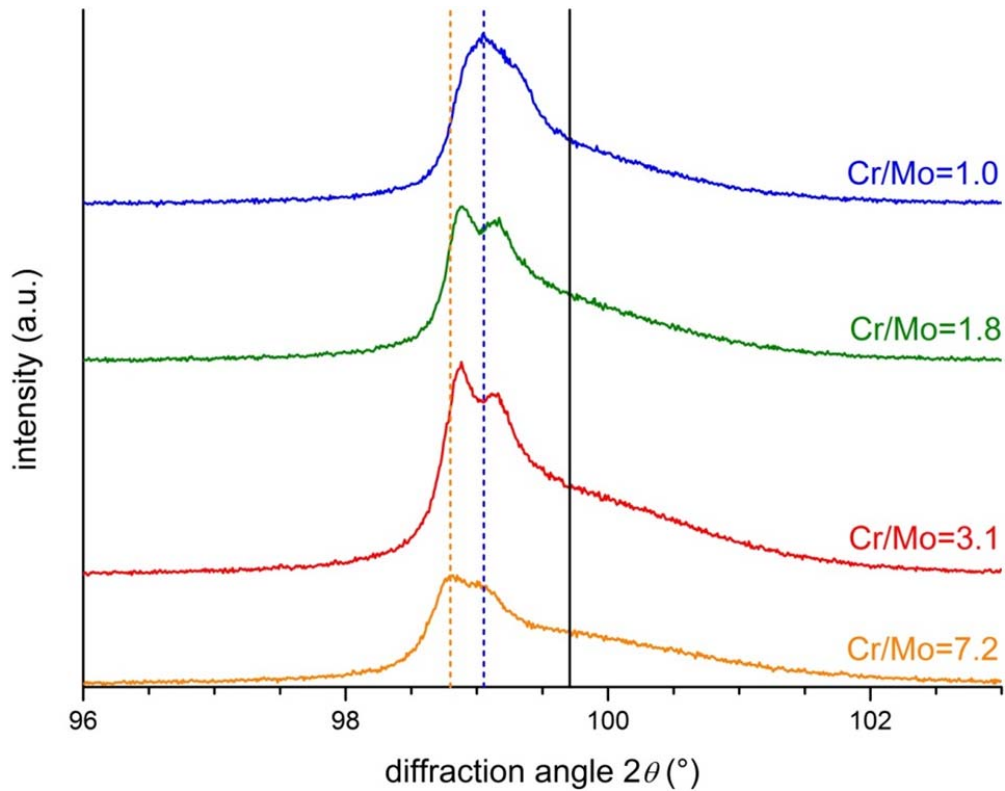


Fig. 7.12: Evolution of the Co- K_α -211 ferrite–matrix diffraction-line profile, recorded from the surfaces of Fe-Cr-Mo alloy specimens nitrided for 1 h at 550 °C with a nitriding potential of $0.1 \text{ atm}^{-1/2}$. The K_α -peak position for pure, unstrained ferrite (α -Fe) has been indicated by the full black vertical line. The vertical colored dashed lines indicate the main ferrite peak positions of the nitrided Fe-1.81Cr-0.25Mo alloy (yellow) and the nitrided Fe-1.04Cr-1.01Mo alloy (blue).

When comparing the XRD patterns recorded from Fe-Cr-Mo alloy specimen of different Cr/Mo-ratios, after nitriding at 550 °C for 1 h with a nitriding potential of $0.1 \text{ atm}^{-1/2}$ (see Fig. 7.12), it is clear that the initial shift of the ferrite peak towards lower diffraction angle is more pronounced for alloys of a higher Cr/Mo-ratio. This is a consequence of the faster progress of the nitriding reaction in alloys of a higher Cr/Mo-ratio (see results and discussion in section 7.3.2).

Upon prolonged nitriding, the “oldest” nitride platelets in the surface adjacent regions begin to coarsen, in association with relaxation of the misfit-strain fields surrounding the precipitates (Chapter 4). This process of continuous coarsening (CC) can be tracked by the development of a broad reflection at the position of (now) more or less unstrained ferrite, while the peak originating from the expanded CP ferrite, with the nitrided precipitates in their initial state, decreases in relative intensity.

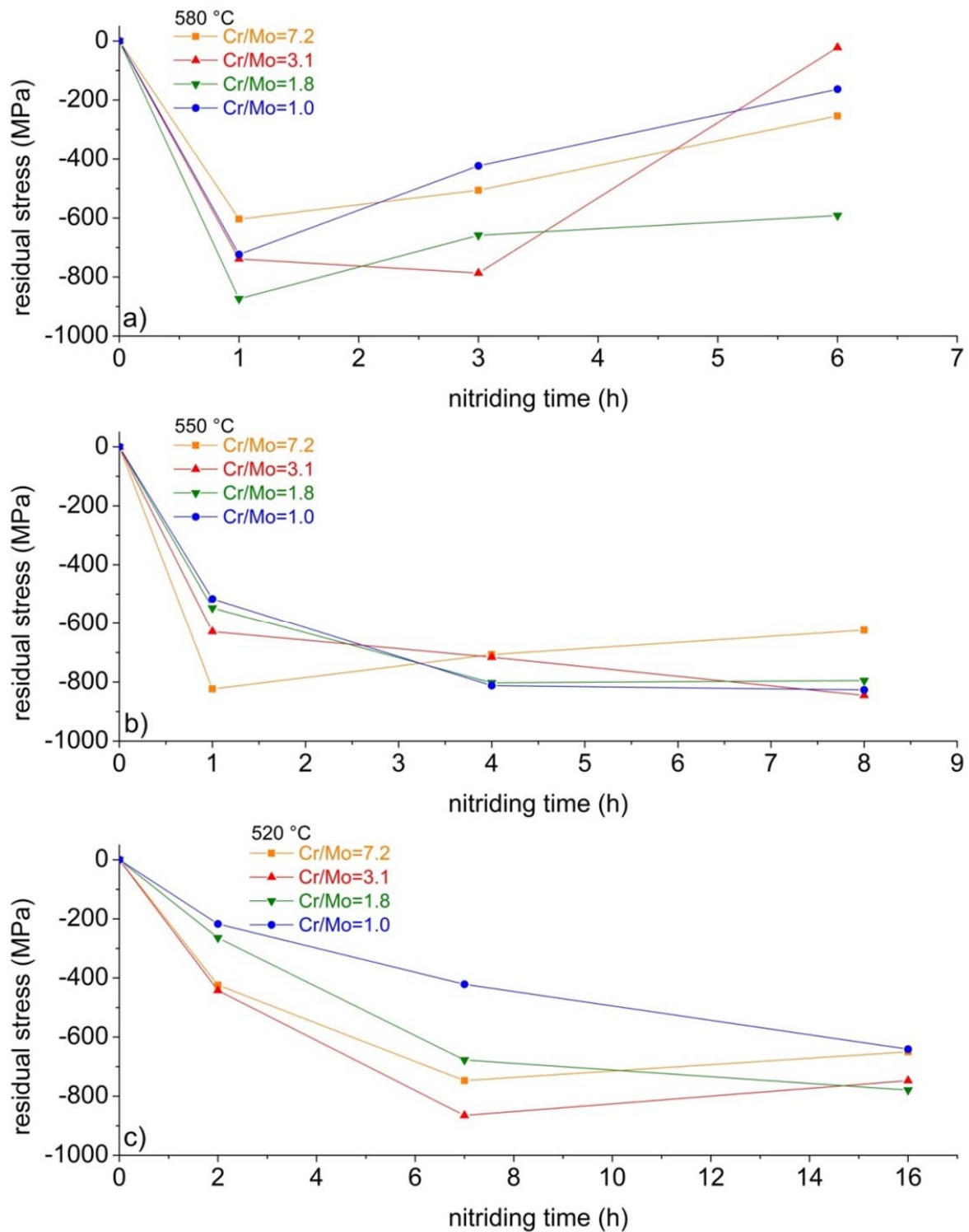


Fig. 7.13: Residual surface macrostress parallel to the surface as function of nitriding time as determined by XRD (see section 6.2.2) for Fe-Cr-Mo specimens nitrided with a nitriding potential of $0.1 \text{ atm}^{-1/2}$ at a nitriding temperature of a) 580 °C, b) 550 °C, and c) 520 °C.

The values of the residual macrostress in the surface region developing upon nitriding of the present Fe-Cr-Mo alloys are shown in Fig. 7.13 as function of nitriding time for the nitriding temperatures employed in this study. At 520 °C, the development of the compressive stress in alloys of lower Cr/Mo-ratio is relatively slow due to the slower nitride precipitation in these alloys (cf. section 7.3.2) leading to a slower increasing tendency to expand laterally for the nitrided case. With continued nitriding, aging of the precipitated nitrides leads to their coarsening and thus to relaxation of their volume misfit with the ferrite matrix by either CC or DC/DP, which brings about a decrease of the compressive stress (as the case-core misfit becomes accommodated plastically instead of elastically). The relaxation processes are faster at higher temperatures, and thus relaxation of the compressive stress at 550 °C and 580 °C can be more pronounced, as observed, despite the shorter nitriding times employed at these temperatures as compared to 520 °C. As the tendency for discontinuous transformation increases with decreasing Cr/Mo-ratio (cf. section 7.3.1) a faster relaxation of macrostresses is expected for a lower Cr/Mo-ratio, and at 580 °C, where pronounced DP occurs.

7.4 General discussion

First what is known about the nitriding behavior of binary Fe-Cr and binary Fe-Mo systems is briefly summarized in section 7.4.1. On this basis, the results presented above on the nitriding response of the ternary Fe-Cr-Mo system are discussed in section 7.4.2.

7.4.1 Nitriding of binary Fe-Cr and Fe-Mo alloys

Binary Fe-Cr

Upon nitriding of binary Fe-Cr alloys, inwardly diffusing N reacts with dissolved Cr to form finely-distributed, nano-sized nitride platelets of NaCl-type CrN with a BN-OR with the ferrite matrix [9], [20], [21], [23], [25]. The formation of these precipitates leads to high hardness and residual stresses in the nitrided region [9], [20]–[22], [24], [27]. The nitriding reaction progresses relatively fast and step-like N-concentration-depth profiles develop. Thus, Cr is considered a relatively strong nitride former (see the classification in Refs. [5], [32]).

Upon prolonged nitriding (=aging of the nitrided microstructure) for a Cr-content above approximately 2 at.%, the microstructure of finely distributed nitrides in the ferrite matrix experiences a discontinuous *coarsening* (DC) process [20], [21]. Mobile grain boundaries sweep through the microstructure and Fe, Cr and N are rearranged at the reaction front to form a coarse lamellar structure consisting of alternate lamellae of CrN and ferrite in the wake of the moving boundaries [9], [20], [23], [25]. The driving force for this reaction is the reduction of the interfacial area (reduction of interfacial energy), the loss of ferrite-matrix (nitrogen) supersaturation (i.e. loss of

excess N; reduction in chemical energy), and the relaxation of the long-range strain-fields due to the coherent to incoherent transition (release of strain energy) [21]. The formation of such microstructures is associated with loss of mechanical strength [27], as, for example, expressed by the loss of hardness due to a coarser microstructure and the loss of compressive residual macrostress due to plastic accommodation of the case/core misfit [27], [217].

Binary Fe-Mo

Upon nitriding of binary Fe-Mo alloys, Mo reacts with inwardly diffusing N to form relatively long but very thin nitride platelets of NaCl-type γ -Mo₂N (containing 50 % vacancies on the N sublattice) with a BN-OR with the ferrite matrix [28], [31]. The formation of these precipitates leads to a high hardness and residual stresses in the nitrided region ([30]; see also results obtained for the nitrided maraging steel presented in Ref. [162]). As compared to Fe-Cr alloys, the nitriding reaction is relatively slow and very shallow N-concentration-depth profiles develop [30]. Thus Mo is considered a weak nitride former (see the classification in Refs. [5], [32]).

Upon prolonged nitriding (=aging of the nitrided microstructure) the initially developing CP microstructure, consisting of γ -Mo₂N platelets in the ferrite matrix, experiences a discontinuous *precipitation* (DP) process [31]. Mobile grain boundaries sweep through the microstructure and Fe, Mo and N are rearranged at the reaction front to form a coarse lamellar microstructure consisting of alternating lamellae of hexagonal δ -MoN and ferrite. The MoN lamellae develop with their broad faces parallel to the $\{110\}_{\alpha\text{-Fe}}$ ferrite matrix planes and have a Burgers OR with the ferrite matrix. Due to the stoichiometry change of the nitride (Mo₂N to MoN), DP regions in the nitrided Fe-Mo alloys exhibit an increased N-content. In addition to the contributions to the driving force as would occur for a purely DC reaction (see below), an additional chemical Gibbs energy contribution occurs in the case of the DP reaction due to the transition of the metastable (under the nitriding conditions employed) molybdenum-nitride modification (γ -Mo₂N) to the stable one (δ -MoN). The formation of the coarse lamellar microstructure is associated with the loss of mechanical strength [31], [225], as expressed by loss of hardness due to a coarser microstructure.

7.4.2 Nitriding of ternary Fe-Cr-Mo alloys

Continuous precipitation

In the preceding study (Chapter 6) it was shown, that the nitrides formed in the initial CP microstructure are of mixed, ternary nature and thus both Cr and Mo are incorporated in the nitrides developing in Fe-Cr-Mo alloys upon nitriding. Since the overall alloying element content of the four investigated alloys is fixed at about 2 at.% and the morphology and density of the nitrides is

practically the same for all investigated alloys of varying Cr/Mo-ratio, the hardness and the residual stress of the nitrified zone (before significant DC/DP occurs, see below) are about the same, i.e. are independent of the Cr/Mo-ratio.

The kinetics of formation of the ternary Cr-Mo-nitrides (nitrogen-uptake rate) appears to be more or less similar to that observed for the formation of CrN in binary Fe-Cr alloys of similar alloying element content (cf. nitriding treatments of the current study with those of Ref. [21]), but, as discussed in the following, a distinct dependence on the Cr/Mo-ratio occurs.

The Cr/Mo-ratio of the nitrified Fe-Cr-Mo alloys has a distinct effect on the amount of N taken up in the nitrides formed: the developing NaCl-type nitride can be conceived as a solid solution of CrN and Mo₂N (which contains vacancies on the N sublattice). For the N-concentration, as measured in the N-saturated surface-adjacent region, this leads to the conclusion that the mixed nitride can be well described by the formula (Cr_z, Mo_{1-z})N _{$\frac{1+z}{2}$} for the Cr/Mo-ratio given by $\frac{z}{1-z}$. A smaller amount of N is thus required for the precipitation of all alloying element as nitride for a lower Cr/Mo-ratio alloy. One might then expect faster nitrogen saturation at lower Cr/Mo-ratio. However, the opposite is observed: with decreasing Cr/Mo-ratio the nitride-precipitation reaction becomes slower (see Fig. 7.10 and Table 7.2, as well as the discussion in section 7.3.2). Further, at lower Cr/Mo-ratios the precipitation occurs initially preferentially at grain boundaries before the bulk of the grains becomes nitrified by the progressing nitriding front (Fig. 7.2). The slower nitride-precipitation kinetics and preferred grain-boundary precipitation for a lower Cr/Mo-ratio of the alloy suggest that the development of the mixed nitride becomes more difficult with decreasing Cr/Mo-ratio. This may hint at a larger nucleation barrier [59] owing to (i) a lesser chemical driving force for the formation of (Cr,Mo)N_y with increasing Mo content of the nitride (indeed, it holds for the Gibbs energy of formation (per mole N₂)¹² at 550 °C (823 K) and 1 atm for CrN and γ-Mo₂N: -131.4 kJ mol⁻¹ for CrN, -47.4 kJ mol⁻¹ for γ-Mo₂N) and (ii) a (slightly) larger volume misfit of the (Cr,Mo)N_y nitride with the ferrite matrix with increasing Mo-content of the nitride (volume misfit for binary CrN: 51 %; volume misfit for binary γ-Mo₂N: 53 %). Further, the development of the mixed nitride may become slower with increasing Mo content of the nitride as a consequence of the slower diffusivi-

¹² The Gibbs energies of formation of the nitrides from the ferrite matrix ($\Delta G_{MeN,\alpha}^f$) presented here represent the Gibbs energies of formation of the nitrides from pure elemental Cr/Mo metal and N₂ gas (ΔG_{MeN}^f) (data from Ref. [236]) and the activity of N at the current nitriding conditions (580 °C and 0.1 atm^{-3/2}) ($a_{N,\alpha}$) (data from Ref. [177]) by the formula $\Delta G_{MeN,\alpha}^f = \Delta G_{MeN}^f - RT \ln(a_{N,\alpha})$. The contributions of the dissolution of Cr and Mo in ferrite thus are and can be neglected. See Ref. [237] for more details of such calculations.

ty of Mo as compared to that of Cr ($\sqrt{2Dt}= 2$ nm/h for Mo⁹⁹ and $\sqrt{2Dt}= 30$ nm/h for Cr⁵¹ in Fe-based ferrite at 550 °C (823 K), with D as the tracer, self-diffusion coefficient [209], [210] and t as the time).

The above discussion suggests that, because the diffusion of Mo and the diffusion of Cr are very slow compared to that of N ($\sqrt{2Dt}= 216$ nm/h for N in ferrite at 550 °C (823 K), with D as the intrinsic diffusion coefficient [226] and t as the time), and the diffusion of Mo is distinctly slower than that of Cr (see above data), the Mo atoms are “dragged” into the very first developing NaCl-type CrN precipitates before they have the chance to precipitate as the separate binary (γ -Mo₂N) nitride or the ternary equilibrium (CrMoN₂; see below) nitride. This happens at the cost of only a little more misfit-strain energy than in the case of precipitation of pure CrN (see above data). The system thus, by the precipitation of the metastable, mixed nitride, accepts the gain (=release) of a smaller-than-maximum amount of Gibbs energy, as an intermediate solution: (Cr,Mo)N_y precipitates develop in the very first stage of precipitation.

It may be argued that the similarity of the crystal structures of CrN, TiN, VN, (cubic) AlN, and γ -Mo₂N (all of NaCl-type crystal structure) is indicative of the observed possibility to develop mixed nitrides to be conceived as solid “solutions” of the binary boundary nitrides: (Cr,Al)N [61]–[63], (Cr,Ti)N [64], (Cr,V)N [65], and (Cr,Mo)N_y (Chapter 6) were observed upon nitriding ternary Fe- Me_1 - Me_2 alloys and also in a quaternary Fe-Cr-Mo-V alloy, mixed (Cr,Mo,V)N nitrides were found to develop [225]. Strikingly, in the case of Si as one of the (two) alloying elements with affinity for N, no such mixed nitrides appear (the crystal structure of Si₃N₄ has no resemblance with the NaCl-type crystal structure): indeed in the Fe-Cr/V/Ti-Si systems first CrN/VN/TiN precipitate before Si precipitates as Si₃N₄ [66].

This dominance of the similarity of nitride crystal structure for binary boundary nitrides, as a predictor for the occurrence of mixed nitrides, appears even more clear considering that the difference in Me -N interaction parameter I (for its definition and calculations, see Ref. [5]) for Si-N ($I=0.4$) and Cr-N ($I=0.8$) is smaller than for Cr-N ($I=0.8$) and Mo-N ($I=0.2$). However, if the Me_1 -N and Me_2 -N interactions become very different, albeit the crystal structures of the binary boundary nitrides are similar, it may be expected that separate precipitates of the binary nitrides can occur and indeed this is what is observed for the Fe-based Fe-V-Al [65] (V-N: $I=1.7$;

Al-N (cubic modification¹³): $I=0.7$), Fe-Ti-Al [65] (Ti-N: $I=1.7$; Al-N (cubic modification¹³): $I=0.7$), and Fe-Ti-Mo [67] (Ti-N: $I=1.7$; Mo-N: $I=0.2$) alloys.

Discontinuous transformations

As suggested by the extent (Fig. 7.4) and morphology (Fig. 7.6) of the discontinuously transformed regions in Fe-Cr-Mo alloys nitrided for prolonged nitriding (=aging) time and as follows from the crystal structure and composition of the nitride lamellae (cf. section 7.3.1), a transition from a discontinuous *coarsening* reaction to a discontinuous *precipitation* reaction occurs with decreasing Cr/Mo-ratio of the alloy.

It appears likely that a minimal amount of Mo must be present in the initial, metastable $(\text{Cr},\text{Mo})\text{N}_y$ nitride to overcome (by a sufficient release of chemical Gibbs energy) energy barriers associated with the development of a different crystal structure and composition of the nitride, so that the DP reaction is only observed at lower Cr/Mo-ratios. The additional chemical driving force available for the DP reaction by the replacement of the metastable mixed nitrides $(\text{Cr}_z, \text{Mo}_{1-z})\text{N}_{\frac{1+z}{z}}$ by the stable nitride (CrMoN_2) , as compared to the DC reaction, considerably increases the discontinuously transformed fraction of the microstructure with decreasing Cr/Mo-ratio: the alloy with a Cr/Mo-ratio as low as 1.8 already shows considerable extent of the DP reaction and the clear development of the long, straight CrMoN_2 lamellae in the DP regions (see section 7.3.1). This becomes even more pronounced at the Cr/Mo-ratio of 1.0.

It should be remarked that for alloys of low Cr/Mo-ratio part of the alloying element nitrides remain precipitated (in ferrite) as mixed nitrides of cubic, NaCl-type crystal structure, as $(\text{Cr},\text{Mo})\text{N}_y$ (see Chapter 6). Their presence can be discussed as follows. The DP reaction takes place at a grain boundary sweeping through the matrix. If, at the reaction front, there is not enough time to complete the transformation to CrMoN_2 , which is a matter of principle for any boundary moving with a speed faster than nil [213], and also because of the lack of additional N (additional to that contained in the initial $(\text{Cr},\text{Mo})\text{N}_y$ nitride and necessary to form CrMoN_2 nitrides), that has to be transported to the interface by diffusion, then the remainder of Cr and Mo remain dissolved in the ferrite lamellae. Upon (later) arrival of further N

¹³ As the cubic modification of AlN is metastable, its Gibbs energy of formation from the elements is unknown. An estimate was made in Ref. [237] based on the kinetics of nitriding of Fe-2 at.%Al alloy and this value was used here to calculate the interaction parameter of cubic AlN. Note that the dissolution of Me in ferrite is neglected for the calculations of the interaction parameter in Ref. [5], and thus the contribution of the dissolution of 2 at.% Al in ferrite to the estimate in Ref. [237] was subtracted for the present calculation. Thus, strictly speaking, all interaction parameters presented here pertain to dilute Fe-Me-N alloys.

this dissolved Cr and Mo precipitate, either at the reaction front or in the ferrite lamellae. Another possibility is that not all $(\text{Cr},\text{Mo})\text{N}_y$ platelets dissolve at the reaction front, they are “over-run” and remain in the ferrite matrix and coarsen into a spherical shape.

7.5 Conclusions

The following conclusions can be drawn about the role of the Cr/Mo-ratio on the nitriding behavior of Fe-Cr-Mo alloys:

1. Upon nitriding Fe-Cr-Mo alloys, a nitrated zone develops that shows a continuously precipitated (CP) microstructure consisting of finely distributed, cubic NaCl-type $(\text{Cr},\text{Mo})\text{N}_y$ nitride platelets exhibiting a Baker-Nutting orientation relationship with the ferrite matrix.
2. The nitride precipitation kinetics of alloys of lower Cr/Mo-ratio is slower due to (i) a lesser chemical driving force and a larger volume misfit of more Mo-rich $(\text{Cr},\text{Mo})\text{N}_y$, and (ii) a diffusivity of Mo smaller than that of Cr.
3. As consequence of conceiving the mixed $(\text{Cr},\text{Mo})\text{N}_y$ nitride as a solid “solution” of CrN and $\gamma\text{-Mo}_2\text{N}$, the N-content at saturation of the specimen is compatible with a composition of the ternary, mixed NaCl-type nitride according to the general formula $(\text{Cr}_z, \text{Mo}_{1-z})\text{N}_{\frac{1+z}{2}}$, where $z = \frac{x_{\text{Cr}}}{x_{\text{Cr}}+x_{\text{Mo}}}$ and the Cr/Mo-ratio of the alloy of is given by $\frac{z}{1-z}$.
4. Upon prolonged nitriding (=aging of the nitrated microstructure), the nitrated Fe-Cr-Mo alloys undergo a discontinuous transformation leading to the formation of a coarsened lamellar microstructure associated with a loss of hardness and residual stress. The nature of this reaction changes from a discontinuous coarsening (DC) of $(\text{Cr},\text{Mo})\text{N}_y$ at high Cr/Mo-ratio to a discontinuous precipitation (DP) of CrMoN_2 at low Cr/Mo-ratio.
5. The extent of the discontinuous transformation increases significantly with decreasing Cr/Mo-ratio, as consequence of the additional chemical contribution to the driving force of the discontinuous transformation by the development of the stable CrMoN_2 nitride during the discontinuous precipitation reaction.
6. The occurrence of mixed $(\text{Me}_1, \text{Me}_2)\text{N}$ nitrides in Fe-based Fe- Me_1 - Me_2 -alloy systems, with Me_1 and Me_2 having affinity for N, requires (i) similarity of crystal structures of the binary bounding Me_1 - and Me_2 -nitrides, and (ii) a not (too) large difference of the Me_1 -N and Me_2 -N interactions. On this basis, the present results and those published before can be generalized as follows:
 - “mixed” nitride precipitation in the systems Fe-Cr-Al [61]–[63], Fe-Cr-Ti [64], Fe-Cr-Mo (Chapter 6) and Fe-Cr-V [65] (similar crystal structures for the binary bounding nitrides, modest Me -N interaction-parameter difference),

- separate nitride precipitation in the systems Fe-Ti-Al [65], Fe-V-Al [65], and Fe-Ti-Mo [67] (similar crystal structures for the binary bounding nitrides, large Me -N interaction-parameter difference),
 - separate nitride precipitation in the systems Fe-Cr-Si [66], Fe-V-Si [66], and Fe-Ti-Si [66] (different crystal structures).
7. In case “mixed” nitrides development occurs, the slower diffusing of the two alloying elements Me_1 and Me_2 , say Me_2 , is “dragged” into the first developing Me_1 -nitride, before it can precipitate as a more stable or even equilibrium Me_2 -nitride.

Acknowledgements

The authors would like to thank Dr. M. Jung for calculation of the diffusion depth profiles, Mr. W.-D. Lang for preparation of the TEM specimens, Mr. P. Kress for assistance with the nitriding experiments (all with Max Planck Institute for Intelligent Systems), Mrs. S. Haug for assistance with the EPMA experiments (with Max Planck Institute for Solid State Research)

Chapter 8

Summary

X-ray diffraction has become a standard method of microstructural analysis. However, in systems with a complex microstructure, the interpretation of the measured diffractograms may not be very straightforward. The influence of the precipitation of fine alloying element nitrides and the changes in precipitation morphology that occur upon continued nitriding on the shape and position of XRD peaks have been identified as a result of this work.

In Chapter 2, the shape and position of the ferrite XRD peaks of homogeneously nitrided Fe-Cr thin foils and Fe-V powders is tracked as a function of the degree of nitride precipitation. Initially the ferrite matrix peaks shift towards lower diffraction angles which indicates a considerable expansion of the ferrite lattice. This lattice expansion is compared to the predicted expansion of the assembly consisting of ferrite matrix and precipitate particles considering the full elastic accommodation of the misfit originating from the precipitation. To correctly predict the peak shift of the XRD peaks of the assembly (which diffracts as the ferritic matrix), coherent diffraction of matrix and precipitates must be occurring, i.e. constructive interference occurs between the X-rays scattered by the matrix and those scattered by the precipitates. If other contributions to the peaks shift, i.e. due to residual stress (from an inhomogeneously nitrided microstructure), and due to dissolved and excess N, are removed, very good agreement of the predicted and measured lattice parameter changes is obtained. In addition to the peak shifts, a tail of intensity towards higher diffraction angles accompanies the peaks of the diffracting assembly. From the evaluation of the relative position of the tail and the corresponding peak and the evolution of its relative intensity as function of the order of reflection it is concluded that this tail originates due to scattering of the severely distorted regions in the immediate vicinity of the nitride platelets.

In Chapter 3 the developed elastic misfit accommodation model is applied to literature lattice parameter data for nitrided Fe-Cr and Fe-V alloys, nitrided and aged Fe-Cr alloys, α'' -Fe₁₆N₂ precipitation in N-supersaturated pure Fe, Cu-Co thin films, and Si precipitation in Al-Si alloys. Considering (i) the type of misfit in the system (thermal or precipitation-induced), (ii) the type of misfit accommodation (elastic or plastic), and (iii) the type of diffraction (coherent or incoherent) good to very good agreement of experimental and predicted lattice parameter changes is obtained.

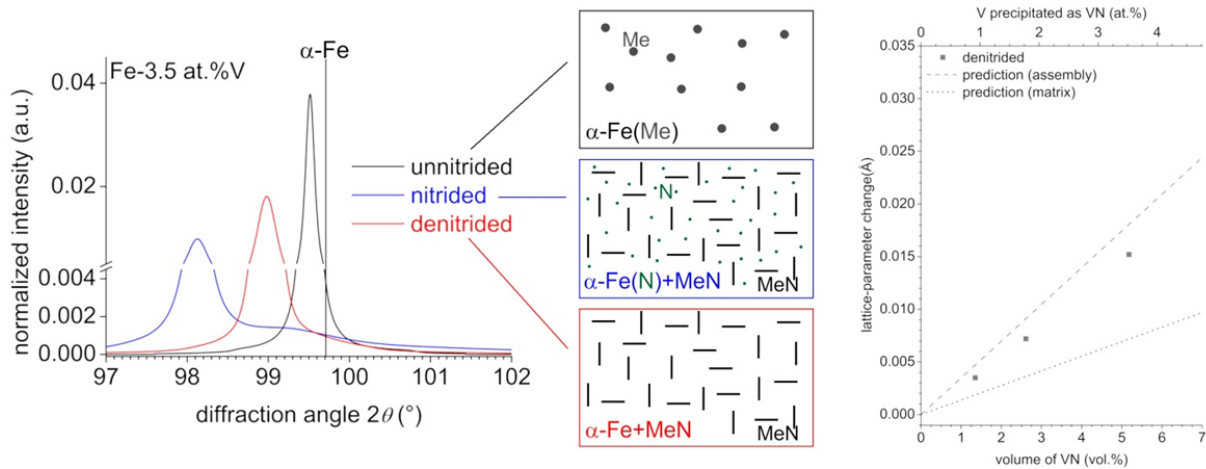


Fig. 8.1: Graphical summary of Chapter 2 showing the evolution of ferrite peaks upon nitriding, the various contributions to the peak shift and the comparison to model predictions.

Upon ongoing nitriding, the above described full elastic accommodation of the precipitate/matrix-misfit can relax plastically in order to reduce the energy of the system. Two main mechanisms operate in the nitrided microstructure: continuous or discontinuous coarsening. The effect of both processes on the shape and position of the XRD peaks of ferrite was tracked on homogeneously nitrided Fe-Cr thin foils in Chapter 4. It is shown that the gradual plastic accommodation of the precipitate/matrix volume misfit by continuous coarsening leads to a “back-“shifting of the ferrite peaks towards their unstrained position at higher diffraction angles. Further, precipitates and matrix begin to diffract incoherently in the relaxed regions as the precipitates grow. This leads to the emergence of a separate ferrite peaks near the position of unstrained ferrite in the diffractogram, which increases in relative intensity upon ongoing nitriding/aging. If relaxation occurs by discontinuous coarsening, the complete relaxation by atomic rearrangement at the interface leads to a separate peak of relaxed ferrite emerging directly at the position of unstrained ferrite. Upon ongoing discontinuous coarsening, the relative intensity of this peak increases. Due to the higher volume fraction of CrN in the alloys where discontinuous coarsening occurs, the occurrence of incoherent, i.e. separate, diffraction of ferrite matrix and CrN precipitates after coarsening allows to observed CrN peaks in the diffractogram, whereas in the alloy with lower Cr-content separate CrN spots can only be observed by TEM. The correlation of microstructural evolution upon nitriding and the XRD (ferrite) peaks is presented for the first time in a summarizing way (see also Fig. 8.2).

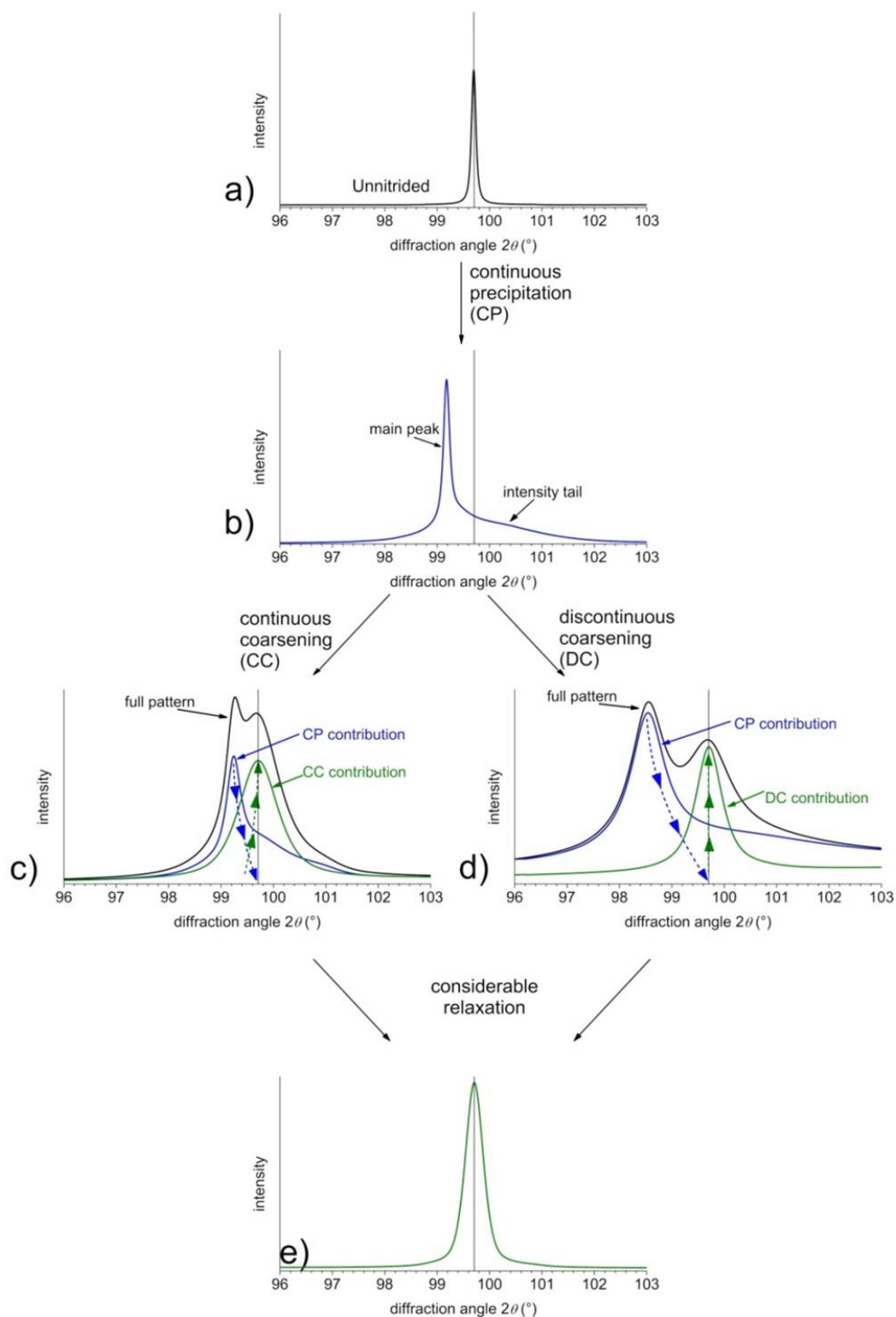


Fig. 8.2: Schematic presentation showing the evolution of the X-ray diffractogram of Fe-Me alloys upon nitriding and subsequent continuous and discontinuous coarsening.

The denitriding behavior of nitrided Fe-Me alloys, on the example of nitrided Fe-V alloy thin foils and powders, is investigated in Chapter 5. In flowing H₂ atmosphere, ultimately the complete loss of all N in the specimen occurs during denitriding. The loss of N as function of time reveals two regimes of N-loss: (i) initially fast loss of less strongly bonded (equilibrium and excess) dissolved N and interface adsorbed N occurs, followed by (ii) the slow loss of N strongly bound in alloying element nitrides. The rate of N-loss depends on the surface to volume ratio of the solid, the absolute values of nitriding and denitriding temperatures, and the difference between nitriding and denitriding temperatures. The N-activity required to stabilize the alloying element nitrides in ferrite are calculated with the Thermo-Calc software. Based on this knowledge, a strategy to denitride Fe-base alloys while retaining the alloying element nitrides is proposed and experimentally validated.

The precipitation of finely distributed alloying element nitrides is the main strengthening mechanism in the diffusion zone of nitrided parts. Various alloying elements having an affinity for N show considerably different nitriding behavior. Cr shows a strong N-affinity and therefore readily precipitates in the presence of N. However, Mo has a weak strength of interaction with N and reacts only slowly. In order to better understand the nitriding behavior of nitrided steels containing both Cr and Mo, the nitriding behavior of ternary Fe-Cr-Mo model alloys is investigated in this thesis.

In Chapter 6 it is shown that upon nitriding a ternary Fe-1 at.%Cr-1 at.%Mo alloy, initially fast precipitation of nano-sized, coherent, cubic NaCl-type, ternary mixed (Cr_{1/2}Mo_{1/2})N_{3/4} nitride platelets occurs, i.e. Cr and Mo react simultaneously with inwardly diffusing N. The formation of this mixed nitride is driven by the low diffusivity of Mo in ferrite, such that Mo is incorporated into the developing CrN instead of forming separate binary γ -Mo₂N. Upon continued nitriding, the cubic (Cr_{1/2}Mo_{1/2})N_{3/4} nitride platelets are transformed by a discontinuous precipitation reaction. The nitride that develops in this way is found to be a novel, hexagonal layered, ternary CrMoN₂ nitride which forms as lamellae in the wake of moving grain boundaries. However, the precipitation of this nitride is not complete and small spherical, cubic NaCl-type (Cr,Mo)N_y nitride particles are found in the ferrite lamellae after the discontinuous precipitation. These spherical particles likely develop at the reaction front of the discontinuous precipitation reaction by precipitation of alloying elements that cannot be incorporated into the forming CrMoN₂ lamellae (in time).

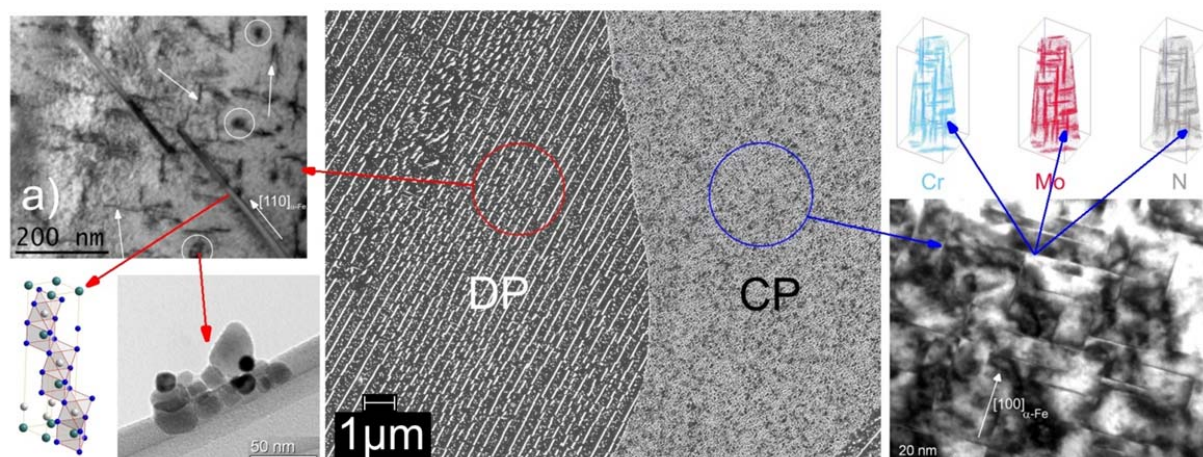


Fig. 8.3: Graphical summary of Chapter 6 showing main features of the continuously precipitated (CP) microstructure (blue, $(\text{Cr}_{1/2}, \text{Mo}_{1/2})\text{N}_{3/4}$ nitride platelets) and the discontinuously precipitated (DP) microstructure (red, CrMoN_2 nitride lamellae and spherical $(\text{Cr,Mo})\text{N}_y$ particles).

An investigation of four Fe-Cr-Mo alloys of fixed total (Cr+Mo) alloying element content but with varying Cr/Mo-ratio from 1.0 to 7.2 is presented in Chapter 7. Initially, the precipitation of fine $(\text{Cr,Mo})\text{N}_y$ nitride platelets occurs in all four alloys. With decreasing Cr/Mo-ratio the nitride precipitation kinetics become slower, as more Mo-rich $(\text{Cr,Mo})\text{N}_y$ has a slightly larger volume misfit to the ferrite matrix and a lower chemical driving force, and the diffusivity of Mo in ferrite is considerably slower than that of Cr. The slower nitride precipitation kinetics influence the shape of the N-concentration- and hardness-depth profiles such that with decreasing Cr/Mo-ratio, more shallow profiles occur. Furthermore, in alloys with low Cr/Mo-ratio, pronounced grain boundary precipitation occurs, as dissolved N is present throughout the entire specimen. As less N is immediately bound in nitrides forming in the surface adjacent regions in alloys with lower Cr/Mo-ratio, these alloys show a more pronounced hardness increase in the core. It follows from the evaluation that the stoichiometry of the mixed ternary nitride can be conceived as a solid “solution” of CrN and $\gamma\text{-Mo}_2\text{N}$, and the ternary nitride composition is given by $(\text{Cr}_z, \text{Mo}_{1-z})\text{N}_{\frac{1+z}{2}}$, where $z = \frac{x_{\text{Cr}}}{x_{\text{Cr}} + x_{\text{Mo}}}$ (the Cr/Mo-ratio of the alloy of is given by $\frac{z}{1-z}$). Prolonged nitriding of the ternary Fe-Cr-Mo alloys leads to a discontinuous transformation of the initial microstructure. The nature and extent of this transformation strongly depends on the Cr/Mo-ratio of the alloy. In alloys of high Cr/Mo-ratio, a minimal extent of discontinuous coarsening occurs. The nature of the discontinuous transformation changes to a discontinuous precipitation reaction with decreasing Cr/Mo-ratio. This is due to the fact that at low Cr/Mo-ratios the hexagonal CrMoN_2 nitride becomes stable. The increased chemical driving force for the precipitation of CrMoN_2 considerably increases the extent of discontinuous precipitation in low Cr/Mo-ratio

alloys as compared to the discontinuous coarsening occurring in high Cr/Mo-ratio alloys. From a comparison of the nitrides forming in various ternary Fe- Me_1 - Me_2 alloys it is concluded that the development of mixed ternary nitrides can be expected if (i) the crystal structures of the binary boundary nitrides are compatible, and (ii) the interaction parameters of the two nitride forming elements are comparable.

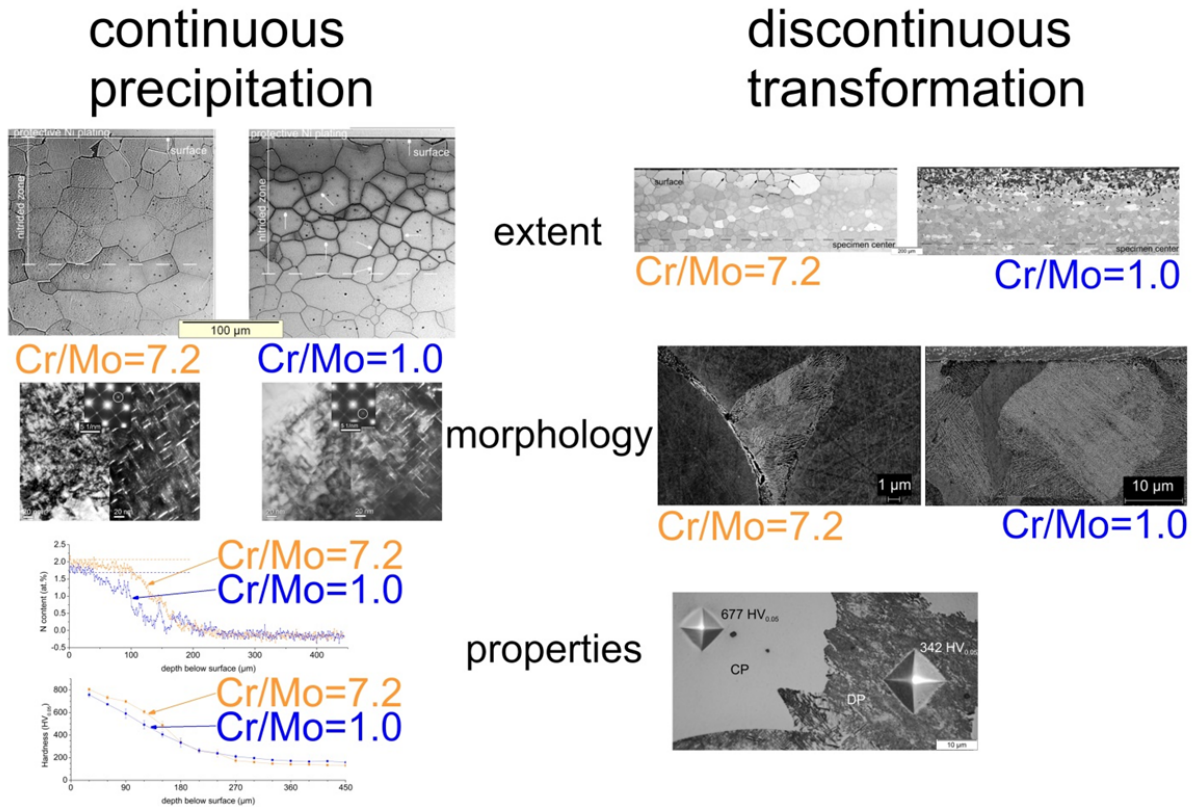


Fig. 8.4: Graphical summary of Chapter 7 showing the influence of the Cr/Mo-ratio on the extent of the nitriding reaction (top), morphology of the developing nitrides (middle) and the properties (N-content and hardness) (bottom) of the continuously precipitated (CP) microstructure (left), and the discontinuously transformed regions (right).

Chapter 9

Zusammenfassung in deutscher Sprache

Röntgenbeugung stellt heutzutage eine Standardmethode zur Analyse der Mikrostruktur von Materialien dar. Diffraktogramme, die von sehr komplexen Mikrostrukturen erzeugt werden, sind jedoch häufig nicht leicht zu interpretieren. Der Zusammenhang zwischen der Ausscheidung feiner Legierungselementnitridteilchen sowie deren morphologische Veränderungen beim fortgesetzten Nitrieren und der Form und Position der Röntgenreflexe wird in dieser Arbeit identifiziert.

In Kapitel 2 wird die Form und Position der Ferritreflexe von homogen nitrierten dünnen Fe-Cr Folien und Fe-V Pulvern als Funktion des Ausscheidungsgrades der Nitride verfolgt. Zunächst tritt eine Verschiebung der Ferritmatrixreflexe zu niedrigeren Beugungswinkeln auf, was auf eine starke Aufweitung des Ferritgitters hindeutet. Diese Gitteraufweitung wird mit der für das Gesamtsystem aus Ferritmatrix und Ausscheidungsteilchen vorhergesagten Aufweitung verglichen. Zur richtigen Vorhersage der Reflexverschiebungen des Gesamtsystems (das wie die Ferritmatrix beugt), muss die kohärente Beugung von Matrix und Ausscheidungen berücksichtigt werden, d.h. es findet konstruktive Interferenz der von Matrix und Ausscheidungen gebeugten Röntgenstrahlen statt. Wenn weitere mögliche Beiträge zu einer Reflexverschiebung entfernt werden, wie sie durch in inhomogen nitriertem Material vorhandene Eigenspannungen sowie durch gelösten und Exzess-Stickstoff hervorgerufen werden, wird eine sehr gute Übereinstimmung von berechneten und gemessenen Gitterparametern gefunden. Zusätzlich zu den Reflexverschiebungen tritt am Fuß der Gesamtsystemreflexe ein Intensitätsband zu höheren Beugungswinkel auf. Aus dem Verhalten des relativen Abstandes zwischen Intensitätsband und dem jeweiligen Reflex sowie der relativen Intensität des Intensitätsbandes mit steigender Beugungsordnung konnte geschlossen werden, dass das Intensitätsband durch die Streuung in den stark verzerrten Bereichen um die Ausscheidungsplättchen hervorgerufen wird.

In Kapitel 3 wird das in Kapitel 2 entwickelte Modell zur elastischen Fehlpassungsakkommodation auf Literaturdaten für Gitterparameterveränderungen von nitrierten Fe-Cr- und Fe-V-Legierungen, von nitrierten und gealterten Fe-Cr-Legierungen, von stickstoffüberstättigtem Reineisen, hervorgerufen durch α -Fe₁₆N₂-Ausscheidung, von Cu-Co Dünnschichtsystemen, und von Al-Si-Legierungen, hervorgerufen durch Si-Ausscheidung, angewandt. Unter Berücksichtigung von (i) der Art der Fehlpassung im System (thermisch oder durch Ausscheidungsvorgänge induziert), (ii) der Art der Fehlpassungsakkommodation (elastisch oder plastisch), und (iii) den Beugungsbedingungen (kohärente oder inkohärente Beugung) kann eine gute bis sehr gute

Übereinstimmung von gemessenen und berechneten Gitterparameterveränderungen erzielt werden.

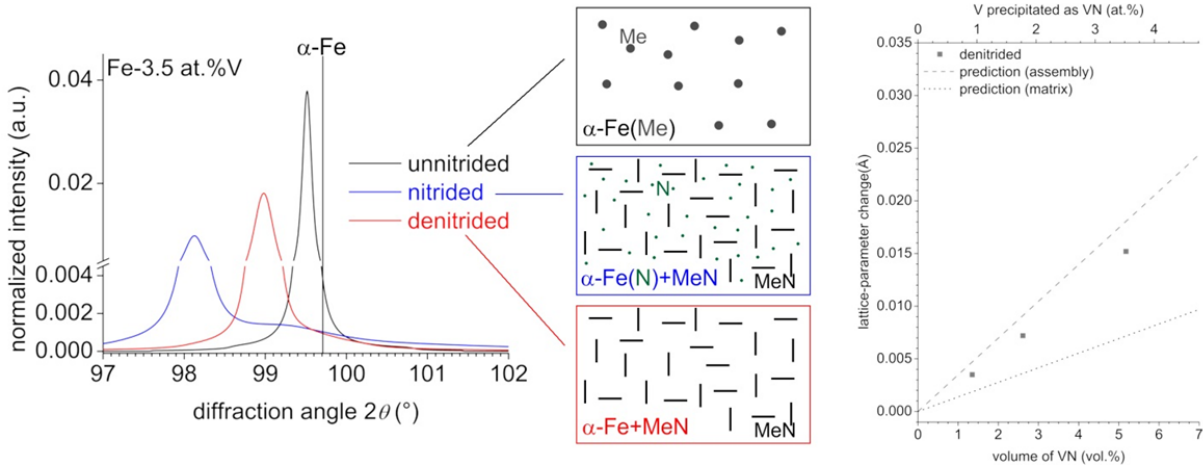


Fig. 9.1: Bildliche Zusammenfassung von Kapitel 2, welche die Entwicklung der Ferritreflexe während des Nitrierens, die jeweiligen Beiträge zur Reflexverschiebung und der Vergleich mit den Modellvorhersagen zeigt.

Beim weiteren Nitrieren beginnt die zuvor angenommene rein elastische Fehlpassungsaufnahme plastisch zu relaxieren um die Energie im System zu reduzieren. Es treten im nitrierten Gefüge zwei Hauptrelaxationsmechanismen auf: kontinuierliche oder diskontinuierliche Vergrößerung. Die Auswirkung beider Relaxationsmechanismen auf die Form und Position der Röntgenbeugungsreflexe der Ferritmatrix wird in Kapitel 4 an homogen nitrierten, dünnen Fe-Cr Folien verfolgt. Es wird gezeigt, dass plastische Akkommodation der Ausscheidungs-Matrix-Volumenfehlpassung durch kontinuierliche Vergrößerung zu einer Rückverschiebung der Ferritreflexe zu höheren Beugungswinkeln, ihrer Position im ungedehnten Zustand, stattfindet. Außerdem beginnen Matrix und die wachsenden Ausscheidungen in den relaxierten Bereichen inkohärent zu beugen. Dies führt dazu, dass ein separater Ferritreflex in der Nähe der Position von ungedehntem, reinen Ferrit im Diffraktogramm auftritt, dessen relative Intensität mit zunehmendem Nitrieren/Altern ansteigt. Wenn die Relaxation über diskontinuierliche Vergrößerung abläuft, tritt wegen der vollständigen Relaxation durch die atomare Umordnung an der Grenzfläche ein separater Ferritreflex direkt an der Position von reinem Ferrit auf. Mit fortschreitender diskontinuierlicher Vergrößerung nimmt die relative Intensität dieses Reflexes zu. Durch den höheren Volumenanteil an CrN in den Legierungen in denen diskontinuierliche Vergrößerung auftritt, führt das Auftreten von inkohärenter Beugung von Ferritmatrix und CrN-Ausscheidungen zum Auftreten von CrN-Reflexen im Röntgendiffraktogramm, während in den Legierungen mit niedrigerem Cr-Gehalt nur im Transmissionselektronenbeugungsbild separate

CrN-Reflexe beobachtet werden können. Der Zusammenhang zwischen der Entwicklung der Mikrostruktur und den (Ferrit-)Reflexen während des Nitrierens wird erstmals zusammenfassend dargestellt (siehe Fig. 9.2).

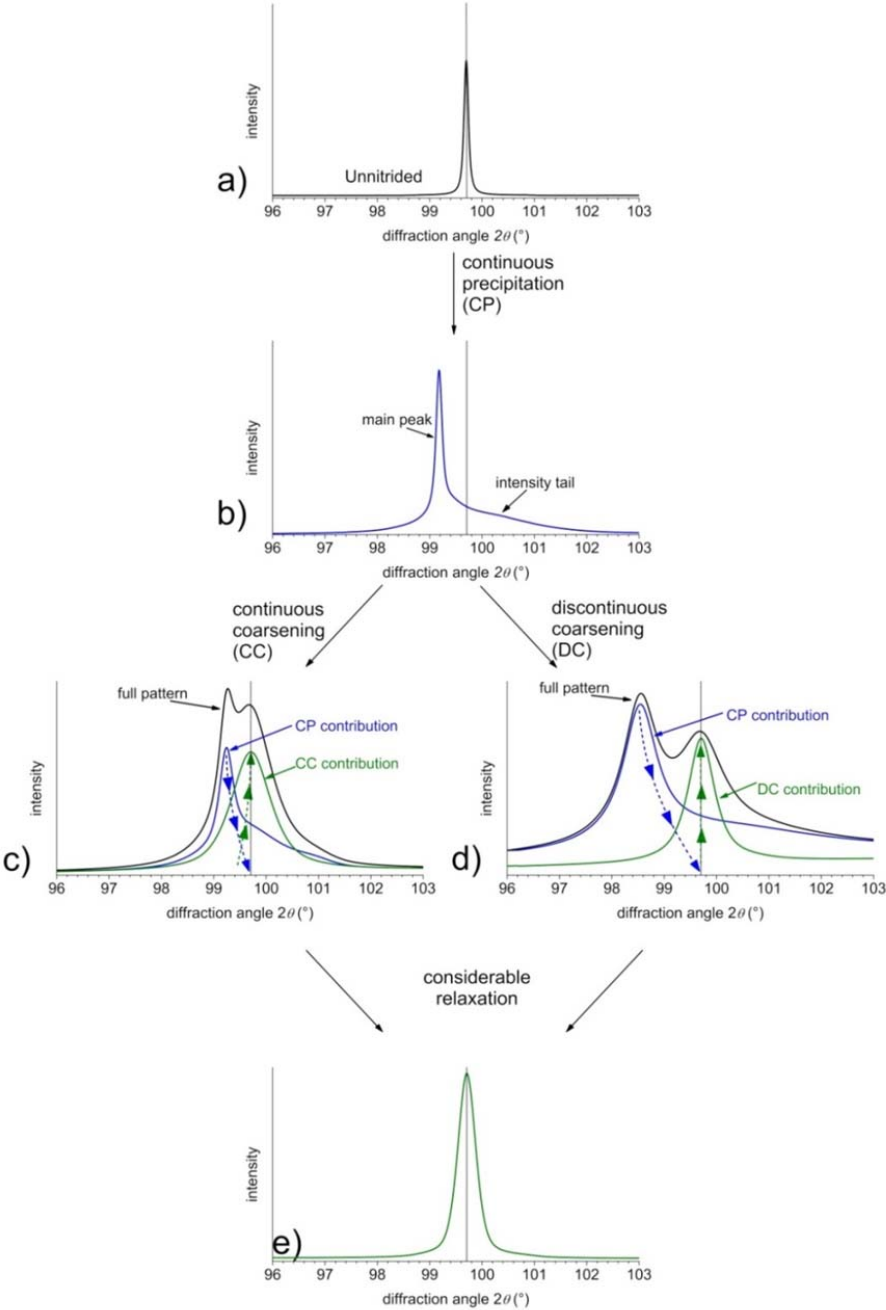


Fig. 9.2: Schematische Darstellung der Entwicklung der Röntgenbeugungsreflexe von Fe-Me-Legierungen während des Nitrierens und anschließenden Alterns durch kontinuierliche und diskontinuierliche Vergrößerung.

Das Denitrierverhalten nitrierter Fe-Me-Legierungen wird in Kapitel 5 am Beispiel nitrierter dünner Fe-V Folien und Pulver untersucht. Beim Denitrieren in strömender H₂-Atmosphäre wird die letztendlich vollständige Entfernung des gesamten Stickstoffs aus der Probe beobachtet. Der Stickstoffverlust geschieht in zwei Stufen: (i) zunächst wird in kurzer Zeit der weniger stark gebundene, gelöste (Gleichgewichts- und Exzess-) Stickstoff sowie der an Grenzflächen adsorbierte Stickstoff entfernt, (ii) anschließend wird der (relativ) fest in Nitriden gebundene Stickstoff freigesetzt. Die Stickstofffreisetzungsrates hängt vom Oberflächen-zu-Volumen-Verhältnis des Feststoffs, den absoluten Nitrier- und Denitriertemperaturen, sowie von der Differenz von Nitrier- und Denitriertemperatur ab. Die Stickstoffaktivität, die zur Stabilisierung der Nitride im Ferrit nötig ist, wird mit Hilfe der Thermo-Calc Software berechnet. Basierend auf diesem Wissen wird eine Denitrierstrategie unter Erhaltung der Nitride entworfen und validiert.

Die Ausscheidung fein verteilter Legierungselementnitride ist der hauptsächliche Verstärkungsmechanismus in der Diffusionszone von nitrierten Bauteilen. Die verschiedenen Legierungselemente, die eine Wechselwirkung mit Stickstoff eingehen, zeigen sehr unterschiedliches Nitrierverhalten. Cr zeigt eine starke Affinität zu Stickstoff und scheidet sich daher in Anwesenheit von Stickstoff schnell als Nitrid aus. Mo zeigt hingegen nur eine schwache Affinität zu Stickstoff und reagiert daher nur langsam. Um das Nitrierverhalten von Stählen, die sowohl Cr als auch Mo enthalten, besser zu verstehen, werden nitrierte ternäre Fe-Cr-Mo-Modelllegierungen in dieser Arbeit untersucht.

In Kapitel 6 wird gezeigt, dass beim Nitrieren einer ternären Fe-1 at.%Cr-1 at.%Mo-Legierung, zunächst die rasche Ausscheidung von nanometer-großen, kohärenten ternären (Cr_{1/2},Mo_{1/2})N_{3/4}-Mischnitriden vom NaCl-Typ auftritt, d.h. Cr und Mo reagieren gleichzeitig mit dem eindiffundierenden Stickstoff. Die Bildung dieses Mischnitrids wird durch die langsame Diffusivität von Mo in Ferrit hervorgerufen, welche bewirkt, dass sich Mo in das entstehende CrN einlagert anstatt separates binäres γ -Mo₂N zu bilden. Bei weiterem Nitrieren wandeln die (Cr_{1/2},Mo_{1/2})N_{3/4}-Plättchen über eine diskontinuierliche Ausscheidungsreaktion um. Das sich dabei als Lamelle bildende Nitrid wurde als das bisher unbekannte, hexagonale, ternäre CrMoN₂ Schichtnitrid identifiziert. Die Umwandlung in dieses Nitrid läuft jedoch nicht vollständig ab, sodass auch nach der diskontinuierlichen Umwandlung kleine, sphärische (Cr,Mo)N_γ-Nitridpartikel vom NaCl-Typ innerhalb der Ferritlamellen beobachtet wurden. Die sphärischen Partikel bilden sich wahrscheinlich an der Reaktionsfront der diskontinuierlichen Ausscheidungsreaktion durch die Ausscheidung von Legierungselementen, die nicht (rechtzeitig) in die sich bildenden CrMoN₂-Lamellen aufgenommen werden können.

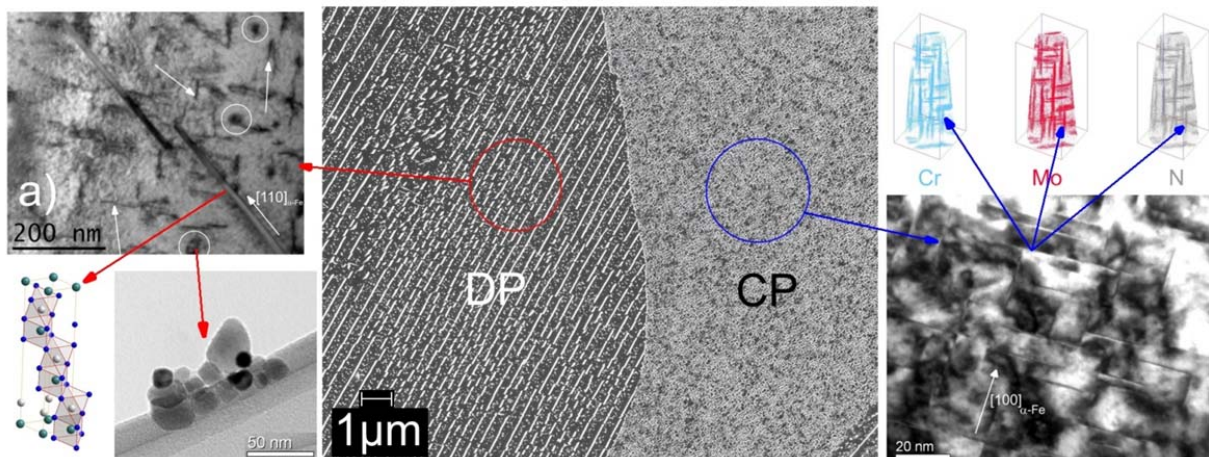


Fig. 9.3: Bildliche Zusammenfassung von Kapitel 6, in der die Hauptmerkmale des Gefüges mit kontinuierlichen Ausscheidungen (CP) (blau, $(\text{Cr}_{1/2}, \text{Mo}_{1/2})\text{N}_{3/4}$ Nitridplättchen) und des diskontinuierlich ausgeschiedenen (DP) Gefüges (rot, CrMoN_2 Nitridlamellen und sphärische $(\text{Cr}, \text{Mo})\text{N}_y$ Partikel) gezeigt sind.

Die Untersuchung von vier Fe-Cr-Mo-Modelllegierungen mit festem Gesamtlegierungselementgehalt (Cr+Mo) aber von 1.0 bis 7.2 variierendem Cr/Mo-Verhältnis wird in Kapitel 7 vorgestellt. Zunächst findet in allen vier Legierungen die Ausscheidung von feinen $(\text{Cr}, \text{Mo})\text{N}_y$ -Nitridplättchen statt. Mit sinkendem Cr/Mo-Verhältnis wird jedoch die Ausscheidungskinetik langsamer, da Mo-reicheres $(\text{Cr}, \text{Mo})\text{N}_y$ eine etwas größere Volumenfehlpassung zur Ferritmatrix und seine Bildung eine geringere chemisch Triebkraft aufweist und die Diffusivität von Mo im Ferrit deutlich langsamer ist als die von Cr. Die langsamere Ausscheidungskinetik der Nitride beeinflusst die Form der Stickstoffkonzentrations- und Härte-Tiefenprofile, sodass bei niedrigem Cr/Mo-Verhältnis flachere Tiefenprofile entstehen. Weiterhin tritt mit sinkendem Cr/Mo-Verhältnis die Nitridausscheidung deutlich bevorzugt an den Korngrenzen auf, da gelöster Stickstoff im gesamten Probenquerschnitt vorhanden ist. Da weniger Stickstoff an der Oberfläche als Nitrid abgebunden wird zeigen diese Legierungen einen größeren Kernhärteanstieg. Aus der Auswertung der Nitridstöchiometrie des ternären Mischnitrids folgt, dass dieses als feste „Lösung“ von CrN und $\gamma\text{-Mo}_2\text{N}$ aufgefasst werden kann, sodass die Zusammensetzung des ternären Nitrids durch die Formel $(\text{Cr}_z, \text{Mo}_{1-z})\text{N}_{\frac{1+z}{2}}$, mit $z = \frac{x_{\text{Cr}}}{x_{\text{Cr}} + x_{\text{Mo}}}$ gegeben ist (das atomare Cr/Mo-Verhältnis ist dann $\frac{z}{1-z}$). Weiteres Nitrieren der ternären Fe-Cr-Mo-Legierungen führt zu einer diskontinuierlichen Umwandlung des zuvor gebildeten Gefüges. Art und Ausmaß der diskontinuierlichen Umwandlung hängen stark vom Cr/Mo-Verhältnis der Legierung ab. Bei hohem Cr/Mo-Verhältnis der Legierung findet nur eine minimale diskontinuierliche Vergrößerung statt. Die Art der diskontinuierlichen Reaktion wandelt sich zu einer diskontinuierlichen Ausscheidung mit

sinkendem Cr/Mo-Verhältnis, da dieses zu einer Stabilisierung von CrMoN_2 führt. Der erhöhte chemische Beitrag der Bildung von CrMoN_2 zur Triebkraft der diskontinuierlichen Ausscheidung erhöht auch das Ausmaß der Umwandlung im Vergleich zur reinen diskontinuierlichen Vergrößerung bei hohem Cr/Mo-Verhältnis. Durch den Vergleich der sich in ternären Fe- Me_1 - Me_2 -Legierungen bildenden Nitridphasen konnte der Schluss gezogen werden, dass zur Entstehung ternäre Mischnitride (i) die Kristallstrukturen der Nitride in den binären Randsystemen kompatibel sein müssen, sowie (ii) eine ähnlich Stärke der Wechselwirkung der beiden Legierungselemente mit Stickstoff gegeben sein muss.

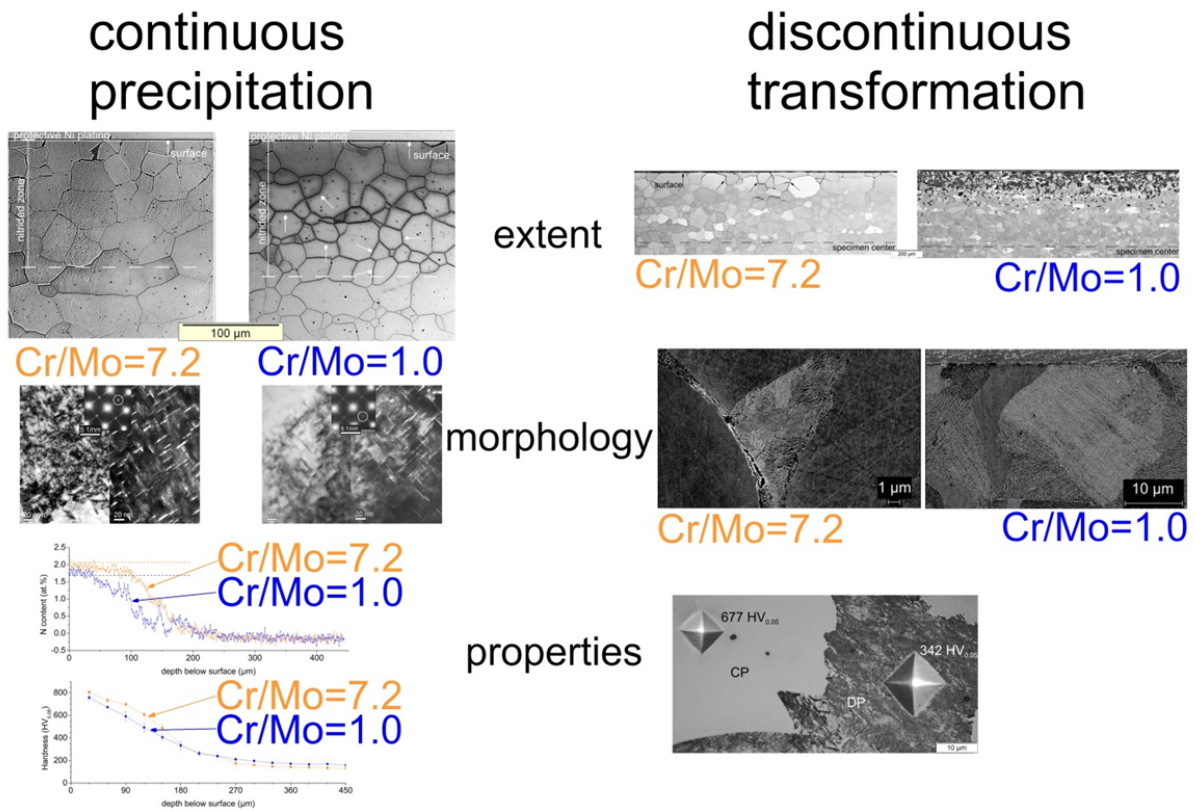


Fig. 9.4: Bildliche Zusammenfassung von Kapitel 7, die den Einfluss des Cr/Mo-Verhältnisses auf das Ausmaß (oben), die Ausscheidungsmorphologie (Mitte), sowie die Eigenschaften (Stickstoffgehalt und Härte) (unten) der kontinuierlichen Ausscheidung (links) und des diskontinuierlich umgewandelten Gefüges (rechts) zeigt.

References

- [1] Stahlinstitut VdEh, Ed., *Steel A Handbook for Materials Research and Engineering; Vol. 1: Fundamentals, and Vol. 2: Applications*. Düsseldorf: Springer Verlag and Verlag Stahleisen, 1984.
- [2] H. K. D. H. Bhadeshia, *Bainite in Steels*, 3rd ed. Maney Publishing, 2015.
- [3] D. E. Boyce, P. R. Dawson, B. Sidle, and T. Gnäupel-Herold, "A multiscale methodology for deformation modeling applied to friction stir welded steel," *Comput. Mater. Sci.*, vol. 38, pp. 158–175, 2006.
- [4] C. M. Cotell, J. A. Sprague, and F. A. Smidt, Eds., *ASM Handbook Volume 5: Surface Engineering*. Materials Park: ASM International, 1994.
- [5] E. J. Mittemeijer and M. A. J. Somers, Eds., *Thermochemical Surface Engineering of Steels*, 1st Ed. Woodhead Elsevier, 2015.
- [6] C. H. Knerr, T. C. Rose, and J. H. Filkowski, *ASM Handbook, Volume 4: Heat Treating: Gas Nitriding*. Materials Park: ASM International, 1991.
- [7] J. Stein, R. E. Schacherl, M. Jung, S. R. Meka, B. Rheingans, and E. J. Mittemeijer, "Solubility of nitrogen in ferrite; the Fe–N phase diagram," *Int. J. Mater. Res.*, vol. 104, pp. 1053–1065, 2013.
- [8] E. J. Mittemeijer, "Fundamentals of Nitriding and Nitrocarburizing," in *ASM Handbook, Volume 4A, Steel Heat Treating Fundamentals and Processes*, vol. 4A, J. Dosset and G. E. Totten, Eds. ASM International, 2013, pp. 619–646.
- [9] R. E. Schacherl, P. Graat, and E. J. Mittemeijer, "The nitriding kinetics of iron-chromium alloys; the role of excess nitrogen: Experiments and modelling," *Metall. Mater. Trans. A*, vol. 35, pp. 3387–3398, 2004.
- [10] M. A. J. Somers, R. M. Lankreijer, and E. J. Mittemeijer, "Excess nitrogen in the ferrite matrix of nitrided binary iron-based alloys," *Philos. Mag. A*, vol. 59, pp. 353–378, 1989.
- [11] K. H. Jack, "The Occurrence and the Crystal Structure of α "-Iron Nitride; a New Type of Interstitial Alloy Formed during the Tempering of Nitrogen-Martensite," *Proc. R. Soc. Lond. A. Math. Phys. Sci.*, vol. 208, pp. 216–224, 1951.
- [12] E. Lehrer, "Über das Eisen-Wasserstoff-Ammoniak-Gleichgewicht," *Zeitschrift für Elektrochemie und Angew. Phys. Chemie*, vol. 36, pp. 383–392, 1930.
- [13] D. S. Rickerby, S. Henderson, A. Hendry, and K. H. Jack, "Overview no. 51 Structure and thermochemistry of nitrided iron-titanium alloys," *Acta Metall.*, vol. 34, pp. 1687–1699, 1986.
- [14] D. S. Rickerby, A. Hendry, and K. H. Jack, "Low-temperature aging of nitrided Fe-Ti alloys," *Acta Metall.*, vol. 34, pp. 1925–1932, 1986.
- [15] M. Pope, P. Grieveson, and K. H. Jack, "Nitride precipitation in ferritic iron-vanadium alloys," *Scand. J. Metall.*, vol. 2, pp. 29–34, 1973.

-
- [16] S. Bor and Ö. E. Atasoy, "The nitriding of Fe-V alloys," *Metall. Trans. A*, vol. 8, pp. 975–979, 1977.
- [17] J.-D. Kamminga and G. C. A. M. Janssen, "Calculation of nitrogen depth profiles in nitrided Fe-Mn and Fe-V," *Surf. Coatings Technol.*, vol. 200, pp. 909–912, 2005.
- [18] S. S. Hosmani, R. E. Schacherl, and E. J. Mittemeijer, "Nitriding behavior of Fe–4wt%V and Fe–2wt%V alloys," *Acta Mater.*, vol. 53, pp. 2069–2079, 2005.
- [19] N. E. Vives Díaz, S. S. Hosmani, R. E. Schacherl, and E. J. Mittemeijer, "Nitride precipitation and coarsening in Fe–2.23at.% V alloys: XRD and (HR)TEM study of coherent and incoherent diffraction effects caused by misfitting nitride precipitates in a ferrite matrix," *Acta Mater.*, vol. 56, pp. 4137–4149, 2008.
- [20] B. Mortimer, P. Grieveson, and K. H. Jack, "Precipitation of nitrides in ferritic iron alloys containing Chromium," *Scand. J. Metall.*, vol. 1, pp. 203–209, 1972.
- [21] P. M. Hekker, H. C. F. Rozendaal, and E. J. Mittemeijer, "Excess nitrogen and discontinuous precipitation in nitrided iron-chromium alloys," *J. Mater. Sci.*, vol. 20, pp. 718–729, 1985.
- [22] R. E. Schacherl, P. C. J. Graat, and E. J. Mittemeijer, "Gaseous nitriding of iron-chromium alloys," *Zeitschrift für Met.*, vol. 93, pp. 468–477, 2002.
- [23] M. Sennour, P. H. Jouneau, and C. Esnouf, "TEM and EBSD investigation of continuous and discontinuous precipitation of CrN in nitrided pure Fe-Cr alloys," *J. Mater. Sci.*, vol. 9, pp. 4521–4531, 2004.
- [24] M. Sennour, C. Jacq, and C. Esnouf, "Mechanical and microstructural investigations of nitrided Fe-Cr layers," *J. Mater. Sci.*, vol. 39, pp. 4533–4541, 2004.
- [25] G. Miyamoto, A. Yonemoto, Y. Tanaka, T. Furuhashi, and T. Maki, "Microstructure in a plasma-nitrided Fe–18 mass% Cr alloy," *Acta Mater.*, vol. 54, pp. 4771–4779, 2006.
- [26] S. S. Hosmani, R. E. Schacherl, and E. J. Mittemeijer, "Nitrogen absorption by Fe–1.04at.%Cr alloy: uptake of excess nitrogen," *J. Mater. Sci.*, vol. 43, pp. 2618–2624, 2008.
- [27] N. E. Vives Díaz, R. E. Schacherl, L. F. Zagonel, and E. J. Mittemeijer, "Influence of the microstructure on the residual stresses of nitrided iron–chromium alloys," *Acta Mater.*, vol. 56, pp. 1196–1208, 2008.
- [28] G. P. Huffman and H. H. Podgurski, "Mössbauer study of nitrided Fe-Mo and Fe-Ti alloys," *Acta Metall.*, vol. 23, pp. 1367–1379, 1975.
- [29] R. Wagner and S. S. Brenner, "Morphology and chemistry of internally nitrided Fe-3at.% Mo," *Acta Metall.*, vol. 26, pp. 197–206, 1978.
- [30] M. M. Yang and A. D. Krawitz, "Resistometric study of Fe-V and Fe-Mo nitrided by constant activity aging," *Metall. Trans. A*, vol. 15, pp. 1545–1554, 1984.
-

-
- [31] H. Selg, E. Bischoff, S. R. Meka, R. E. Schacherl, T. Waldenmaier, and E. J. Mittemeijer, "Molybdenum-Nitride Precipitation in Recrystallized and Cold-Rolled Fe-1 at. pct Mo Alloy," *Metall. Mater. Trans. A*, vol. 44, pp. 4059–4070, 2013.
- [32] M. H. Biglari, C. M. Brakman, M. A. J. Somers, W. G. Sloof, and E. J. Mittemeijer, "On the internal nitriding of deformed and recrystallized foils of Fe-2 at% Al," *Zeitschrift für Met.*, vol. 84, pp. 124–131, 1993.
- [33] M. H. Biglari, C. M. Brakman, and E. J. Mittemeijer, "Crystal structure and morphology of AlN precipitating on nitriding of an Fe-2at.% Al alloy," *Philos. Mag. A*, vol. 72, pp. 1281–1299, 1995.
- [34] M. Sennour and C. Esnouf, "Contribution of advanced microscopy techniques to nano-precipitates characterization: case of AlN precipitation in low-carbon steel," *Acta Mater.*, vol. 51, pp. 943–957, 2003.
- [35] S. R. Meka, E. Bischoff, S. S. Hosmani, and E. J. Mittemeijer, "Interrelationships of defects, nitride modification and excess nitrogen in nitrided Fe-4.75 at.% Al alloy," *Int. J. Mater. Res.*, vol. 105, pp. 1057–1066, 2014.
- [36] G. R. Booker and J. Norbury, "A New Nitride Precipitate in Iron-Silicon Alloys," *Nature*, vol. 184, pp. 1311–1312, 1959.
- [37] E. J. Mittemeijer, M. H. Biglari, A. J. Böttger, N. M. van der Pers, W. G. Sloof, and F. D. Tichelaar, "Amorphous precipitates in a crystalline matrix; precipitation of amorphous Si₃N₄ in α -Fe," *Scr. Mater.*, vol. 41, pp. 625–630, 1999.
- [38] S. R. Meka, K. S. Jung, E. Bischoff, and E. J. Mittemeijer, "Unusual precipitation of amorphous silicon nitride upon nitriding Fe–2at.%Si alloy," *Philos. Mag.*, vol. 92, pp. 1435–1455, 2012.
- [39] J. Baird, "Precipitation of nitrides in iron-manganese-nitrogen alloys," *J. Iron Steel Inst.*, pp. 1122–1130, 1966.
- [40] J. F. Enrietto, "The Solubility and Precipitation of Nitrides in Alpha-Iron Containing Manganese," *Trans. Metall. Soc. AIME*, vol. 224, pp. 43–48, 1961.
- [41] M. Gouné, A. Redjaïmia, T. Belmonte, and H. Michel, "Identification and characterization of a novel Mn–N nitride formed in Fe–Mn–N alloy," *J. Appl. Crystallogr.*, vol. 36, pp. 103–108, 2003.
- [42] M. Gouné, T. Belmonte, A. Redjaïmia, P. Weisbecker, J. . Fiorani, and H. Michel, "Thermodynamic and structural studies on nitrided Fe–1.62%Mn and Fe–0.56%V alloys," *Mater. Sci. Eng. A*, vol. 351, pp. 23–30, 2003.
- [43] S. R. Meka, A. Chauhan, T. Steiner, E. Bischoff, P. K. Ghosh, and E. J. Mittemeijer, "Generating duplex microstructures by nitriding; nitriding of iron based Fe–Mn alloy," *Mater. Sci. Technol.*, 2015, doi: 10.1179/1743284715Y.0000000098.
- [44] J. L. Meijering, "Internal Oxidation in Alloys," in *Advances in Materials Research*, H. Herman, Ed. New York: John Wiley and Sons, Inc., 1971, pp. 1–82.
-

-
- [45] J. W. Christian, *The Theory of Transformations in Metals and Alloys*. Elsevier, 2002.
- [46] E. J. Mittemeijer, M. V. Rooyen, M. van Rooyen, I. Wierszylowski, H. C. F. Rozendaal, and P. F. Colijn, "Tempering of Iron--Nitrogen Martensite," *Zeitschrift für Met.*, vol. 74, pp. 473–483, 1983.
- [47] B. Schwarz, H. Göhring, S. R. Meka, R. E. Schacherl, and E. J. Mittemeijer, "Pore Formation Upon Nitriding Iron and Iron-Based Alloys: The Role of Alloying Elements and Grain Boundaries," *Metall. Mater. Trans. A*, vol. 45, pp. 6173–6186, 2014.
- [48] S. R. Meka and E. J. Mittemeijer, "Abnormal Nitride Morphologies upon Nitriding Iron-Based Substrates," *JOM*, vol. 65, pp. 769–775, 2013.
- [49] K. Han, A. J. Böttger, H. W. Zandbergen, and E. J. Mittemeijer, "Microstructural changes during tempering of Fe-N martensite: formation of α '' -nitride," *Philos. Mag. A*, vol. 82, pp. 715–733, 2002.
- [50] E. J. Mittemeijer, A. B. P. Vogels, and P. J. Schaaf, "Morphology and lattice distortions of nitrated iron and iron-chromium alloys and steels," *J. Mater. Sci.*, vol. 15, pp. 3129–3140, 1980.
- [51] Y. Tomio, S. Kitsuya, K. Oh-ishi, K. Hono, G. Miyamoto, and T. Furuhashi, "Plasma Nitriding Behavior of Fe-C-M (M = Al, Cr, Mn, Si) Ternary Martensitic Steels," *Metall. Mater. Trans. A*, vol. 45, pp. 239–249, 2013.
- [52] R. G. Baker and J. Nutting, "The tempering of a Cr-Mo-V-W and a Mo-V steel," *Iron Steel Inst. Spec. Rep.*, vol. 64, pp. 1–22, 1959.
- [53] W. Pitsch and A. Schrader, "Die Ausscheidungsform des ϵ -Karbids im Ferrit and im Martensit beim Anlassen," *Arch. für das Eisenhüttenwes.*, vol. 29, pp. 715–721, 1958.
- [54] W. Burgers, "On the process of transition of the cubic-body-centered modification into the hexagonal-close-packed modification of zirconium," *Physica*, vol. 36, pp. 561–586, 1934.
- [55] H. Selg, E. Bischoff, R. E. Schacherl, J. Schwarzer, and E. J. Mittemeijer, "Microstructural and surface residual stress development during low-temperature gaseous nitriding of Fe-3.07at.%Mo alloy," *HTM J. Heat Treat. Mater.*, vol. 66, pp. 94–99, 2011.
- [56] E. J. Mittemeijer and U. Welzel, Eds., *Modern Diffraction Methods*. Weinheim: Wiley VCH, 2013.
- [57] M. A. Krivoglaz, *X-Ray and Neutron Diffraction in Nonideal Crystals*. Berlin, Heidelberg: Springer Berlin Heidelberg, 1996.
- [58] J. G. M. van Berkum, R. Delhez, T. H. de Keijser, and E. J. Mittemeijer, "Diffraction-Line Broadening due to Strain Fields in Materials; Fundamental Aspects and Methods of Analysis," *Acta Crystallogr. Sect. A Found. Crystallogr.*, vol. 52, pp. 730–747, 1996.
- [59] E. J. Mittemeijer, *Fundamentals of Materials Science*. Berlin, Heidelberg: Springer Berlin Heidelberg, 2011.
-

-
- [60] U. Welzel, J. Ligot, P. Lamparter, A. C. Vermeulen, and E. J. Mittemeijer, "Stress analysis of polycrystalline thin films and surface regions by X-ray diffraction," *J. Appl. Crystallogr.*, vol. 38, pp. 1–29, 2005.
- [61] K. S. Jung, R. E. Schacherl, E. Bischoff, and E. J. Mittemeijer, "Nitriding of ferritic Fe–Cr–Al alloys," *Surf. Coatings Technol.*, vol. 204, pp. 1942–1946, 2010.
- [62] A. R. Clauss, E. Bischoff, R. E. Schacherl, and E. J. Mittemeijer, "Phase transformation of mixed Cr_{1-x}Al_xN nitride precipitates in ferrite," *Philos. Mag.*, vol. 89, pp. 565–582, 2009.
- [63] A. R. Clauss, E. Bischoff, S. S. Hosmani, R. E. Schacherl, and E. J. Mittemeijer, "Crystal Structure and Morphology of Mixed Cr_{1-x}Al_xN Nitride Precipitates: Gaseous Nitriding of a Fe-1.5 Wt Pct Cr-1.5 Wt Pct Al Alloy," *Metall. Mater. Trans. A*, vol. 40, pp. 1923–1934, 2009.
- [64] K. S. Jung, S. R. Meka, R. E. Schacherl, E. Bischoff, and E. J. Mittemeijer, "Nitride Formation and Excess Nitrogen Uptake After Nitriding Ferritic Fe-Ti-Cr Alloys," *Metall. Mater. Trans. A*, vol. 43, pp. 934–944, 2011.
- [65] G. Miyamoto, S. Suetsugu, K. Shinbo, and T. Furuhashi, "Surface Hardening and Nitride Precipitation in the Nitriding of Fe-M1-M2 Ternary Alloys Containing Al, V, or Cr," *Metall. Mater. Trans. A*, vol. 46, pp. 5011–5020, 2015.
- [66] B. Schwarz, P. J. Rossi, L. Straßberger, F. Jörg, S. R. Meka, E. Bischoff, R. E. Schacherl, and E. J. Mittemeijer, "Coherency strain and precipitation kinetics: crystalline and amorphous nitride formation in ternary Fe–Ti/Cr/V–Si alloys," *Philos. Mag.*, vol. 94, pp. 3098–3119, 2014.
- [67] S. Henderson, "Solute interactions in nitrided iron alloys," Ph. D. Thesis, University of Newcastle upon Tyne, 1976.
- [68] *Metals Handbook, Volume 1: Properties and Selection: Irons, Steels, and High-Performance Alloys*. Materials Park: ASM International, 1990.
- [69] Y. C. Liu, F. Sommer, and E. J. Mittemeijer, "Abnormal austenite–ferrite transformation behaviour in substitutional Fe-based alloys," *Acta Mater.*, vol. 51, pp. 507–519, 2003.
- [70] S. Loewy, B. Rheingans, S. R. Meka, and E. J. Mittemeijer, "Unusual martensite-formation kinetics in steels: Observation of discontinuous transformation rates," *Acta Mater.*, vol. 64, pp. 93–99, 2014.
- [71] M. Villa, K. Pantleon, and M. A. J. Somers, "Evolution of compressive strains in retained austenite during sub-zero Celsius martensite formation and tempering," *Acta Mater.*, vol. 65, pp. 383–392, 2014.
- [72] S. R. Meka, E. Bischoff, B. Rheingans, and E. J. Mittemeijer, "Octapod-shaped, nanosized, amorphous precipitates in a crystalline ferrite matrix," *Philos. Mag. Lett.*, vol. 93, pp. 238–245, 2013.
-

References

- [73] S. J. Song, F. Liu, and Z. H. Zhang, "Analysis of elastic–plastic accommodation due to volume misfit upon solid-state phase transformation," *Acta Mater.*, vol. 64, pp. 266–281, 2014.
- [74] R. Abbaschian and R. Reed-Hill, *Physical Metallurgy Principles*. Cengage Learning, 2008.
- [75] M. F. Ashby and L. M. Brown, "Diffraction contrast from spherically symmetrical coherency strains," *Philos. Mag.*, vol. 8, pp. 1083–1103, 1963.
- [76] M. F. Ashby and L. M. Brown, "On diffraction contrast from inclusions," *Philos. Mag.*, vol. 8, pp. 1649–1676, 1963.
- [77] T. C. Bor, A. T. W. Kempen, F. D. Tichelaar, E. J. Mittemeijer, and E. Van der Giessen, "Diffraction-contrast analysis of misfit strains around inclusions in a matrix: VN particles in α -Fe," *Philos. Mag. A*, vol. 82, pp. 971–1001, 2002.
- [78] R. Kuzel, B. He, and C. Houska, "Characterization of severe matrix distortions during phase separation from the redistribution of diffracted intensities," *J. Mater. Sci.*, vol. 32, pp. 2451–2467, 1997.
- [79] A. Guinier, *X-Ray Diffraction in Crystals, Imperfect Crystals, and Amorphous Bodies*. California: Freeman, 1963.
- [80] A. G. Khachaturyan, *Theory of Structural Transformations in Solids*. New York: John Wiley and Sons, Inc., 1893.
- [81] M. R. Ahmadi, E. Povoden-Karadeniz, B. Sonderegger, K. I. Öksüz, A. Falahati, and E. Kozeschnik, "A model for coherency strengthening of large precipitates," *Scr. Mater.*, vol. 84–85, pp. 47–50, 2014.
- [82] P. H. Leo, J. S. Lowengrub, and Q. Nie, "On an elastically induced splitting instability," *Acta Mater.*, vol. 49, pp. 2761–2772, 2001.
- [83] E. J. Mittemeijer, P. van Mourik, and T. H. De Keijser, "Unusual lattice parameters in two-phase systems after annealing," *Philos. Mag. A*, vol. 43, pp. 1157–1164, 1981.
- [84] P. Van Mourik, E. J. Mittemeijer, and T. H. De Keijser, "On precipitation in rapidly solidified aluminium-silicon alloys," *J. Mater. Sci.*, vol. 18, pp. 2706–2720, 1983.
- [85] P. van Mourik, T. H. De Keijser, and E. J. Mittemeijer, "Misfit Strains and Excess Vacancies in Liquid-Quenched and Solid-Quenched AlSi Alloys on Aging," in *Rapidly Solidified Materials*, 1985, pp. 341–350.
- [86] J. Eshelby, "Distortion of a crystal by point imperfections," *J. Appl. Phys.*, vol. 25, pp. 255–261, 1954.
- [87] J. Eshelby, "The continuum theory of lattice defects," *Solid state Phys.*, vol. 3, pp. 79–144, 1956.
- [88] L. Vegard, "Die konstitution der mischkristalle und die raumfüllung der atome," *Zeitschrift für Phys.*, vol. 5, pp. 17–26, 1921.

-
- [89] J. W. Morris, "The Khachaturyan theory of elastic inclusions: Recollections and results," *Philos. Mag.*, vol. 90, pp. 3–35, 2010.
- [90] M. Fährmann, P. Fratzl, and O. Paris, "Influence of coherency stress on microstructural evolution in model Ni-Al-Mo alloys," *Acta Metall. Mater.*, vol. 43, pp. 1007–1022, 1995.
- [91] W. Johnson and J. W. Cahn, "Elastically induced shape bifurcations of inclusions," *Acta Metall.*, vol. 32, pp. 1925–1933, 1984.
- [92] M. Stobik, "Nanoval Metal Powder - Market Requirements and Powder Characteristics," *Adv. Eng. Mater.*, vol. 2, pp. 547–548, 2000.
- [93] S. S. Hosmani, R. E. Schacherl, and E. J. Mittemeijer, "Nitrogen uptake by an Fe–V alloy: Quantitative analysis of excess nitrogen," *Acta Mater.*, vol. 54, pp. 2783–2792, 2006.
- [94] J. L. Pouchou and F. Pichoir, "A new model for quantitative X-ray microanalysis," *Rech. Aerosp.*, vol. 3, pp. 167–192, 1984.
- [95] R. Delhez and E. J. Mittemeijer, "An improved α 2 elimination," *J. Appl. Crystallogr.*, vol. 8, pp. 609–611, 1975.
- [96] A. J. C. Wilson, *Elements of X-ray crystallography*. Reading, Mass.: Addison-Wesley, 1970.
- [97] ICDD, "JCPDS-international Centre for Diffraction Data, PCPDFWIN," *JCPDS-international Cent. Diffr. Data, PCPDFWIN*, 2002.
- [98] E. J. Mittemeijer, A. B. P. Vogels, and P. Van Der Schaaf, "Aging at room temperature of nitrated α -iron," *Scr. Metall.*, vol. 14, pp. 411–416, 1980.
- [99] H. Wriedt and L. Zwell, "Lattice dilatation of alpha-Iron by Nitrogen," *Trans. Metall. Soc. AIME*, vol. 224, pp. 1242–1246, 1962.
- [100] W. B. Pearson and G. V. Raynor, *A Handbook of Lattice Spacings and Structures of Metals and Alloys*. Elsevier Ltd., 1958.
- [101] H. H. Podgurski and F. N. Davis, "Thermochemistry and nature of nitrogen absorption in nitrogenated Fe-Ti alloys," *Acta Metall.*, vol. 29, pp. 1–9, 1981.
- [102] H. Wawra, "Kröner-limits of elastic moduli of materials of technical importance. Part II: elastic moduli of elements as function of temperature (in German)," *Zeitschrift für Met.*, vol. 69, pp. 518–523, 1978.
- [103] J. Grossman, A. Mizel, M. Côté, M. Cohen, and S. Louie, "Transition metals and their carbides and nitrides: Trends in electronic and structural properties," *Phys. Rev. B*, vol. 60, pp. 6343–6347, 1999.
- [104] D. Dzivenko, A. Zerr, N. Guignot, M. Mezouar, and R. Riedel, "Compressibility of cubic vanadium mononitride," *EPL (Europhysics Lett.)*, vol. 92, p. 66001, 2010.
- [105] Z. S. Basinski, W. Hume-Rothery, and A. L. Sutton, "The Lattice Expansion of Iron," *Proc. R. Soc. A Math. Phys. Eng. Sci.*, vol. 229, pp. 459–467, 1955.
-

-
- [106] G. V. Samsonov, *Plenum Press Handbooks of High-Temperature Materials: No. 2 Properties Index*. New York: Plenum Press, 1964.
- [107] M. J. Starink, P. van Mourik, and B. M. Korevaar, "Misfit Accommodation in a Quenched and Aged Al-Cu Alloy with Silicon Particles," *Metall. Trans. A*, vol. 24, pp. 1723–1731, 1993.
- [108] M. Thompson, C. Su, and P. Voorhees, "The equilibrium shape of a misfitting precipitate," *Acta Metall. Mater.*, vol. 42, pp. 2107–2122, 1994.
- [109] D. A. Porter and K. E. Easterling, *Phase Transformations in Metals and Alloys*. London: Van Nostrand Reinhold, 1982.
- [110] Z. Guo and W. Sha, "Quantification of precipitate fraction in Al–Si–Cu alloys," *Mater. Sci. Eng. A*, vol. 392, pp. 449–452, 2005.
- [111] Y. Wang and A. G. Khachaturyan, "Shape instability during precipitate growth in coherent solids," *Acta Metall. Mater.*, vol. 43, pp. 1837–1857, 1995.
- [112] N. Ratel, G. Bruno, P. Bastie, and T. Mori, "Plastic strain-induced rafting of γ' precipitates in Ni superalloys: Elasticity analysis," *Acta Mater.*, vol. 54, pp. 5087–5093, 2006.
- [113] N. Ratel, M. Kawauchi, T. Mori, I. Saiki, P. J. Withers, and T. Iwakuma, "Application of anisotropic inclusion theory to the deformation of Ni based single crystal superalloys: Stress–strain curves determination," *Mech. Mater.*, vol. 42, pp. 237–247, 2010.
- [114] A. J. Ardell, "The effects of elastic interactions on precipitate microstructural evolution in elastically inhomogeneous nickel-base alloys," *Philos. Mag.*, vol. 94, pp. 2101–2130, 2014.
- [115] Y. Ni and A. G. Khachaturyan, "Phase field approach for strain-induced magnetoelectric effect in multiferroic composites," *J. Appl. Phys.*, vol. 102, p. 113506, 2007.
- [116] P. van Mourik, T. De Keijser, N. Van der Pers, and E. J. Mittemeijer, "On misfit-induced lattice spacine variations in two-phase alloys: The case of cooling-induced microstrains in the al-matrix of fully aged AlSi alloys," *Scr. Metall.*, vol. 22, pp. 1547–1551, 1988.
- [117] T. Mura, *Micromechanics of defects in solids*. The Hague: Martinus Nijhoff Publishers, 1987.
- [118] E. J. Mittemeijer and A. van Gent, "Unusual lattice parameters in two-phase systems; the case of aged nitrogen-ferrite," *Scr. Metall.*, vol. 18, pp. 825–828, 1984.
- [119] J. Zhou, J. Duszczuk, and B. M. Korevaar, "As-spray-deposited structure of an Al-20Si-5Fe Osprey preform and its development during subsequent processing," *J. Mater. Sci.*, vol. 26, pp. 5275–5291, 1991.
- [120] A. Müller, T. Gnäupel-Herold, and W. Reimers, "Small Lattice Mismatches in Highly Imperfect Single Crystals: A Probe into Phase Specific Strains and Stresses," *Phys. status solidi*, vol. 159, pp. 375–396, 1997.
-

-
- [121] G. Timmermans and L. Froyen, "Calculation of the effect of alloy characteristics on the permanent expansion of cold compacted hypereutectic Al-Si-Fe-X powder after thermal treatment," *Scr. Mater.*, vol. 40, pp. 743–750, 1999.
- [122] N. G. Chechenin, A. R. Chezan, C. B. Craus, D. O. Boerma, L. Niesen, P. M. Bronsveld, and J. T. M. De Hosson, "Precipitate formation in low-temperature nitrided cold-rolled Fe₉₄Ni₄Ti₂ and Fe₉₃Ni₄Cr₃ films," *Metall. Mater. Trans. A*, vol. 33, pp. 3075–3087, 2002.
- [123] G. Bruno, G. Schumacher, H. C. Pinto, and C. Schulze, "Measurement of the Lattice Misfit of the Nickel-Base Superalloy SC16 by High-Energy Synchrotron Radiation," vol. 34, pp. 193–197, 2003.
- [124] H. Lu, P. Kadolkar, K. Nakazawa, T. Ando, and C. A. Blue, "Precipitation Behavior of AA2618," *Metall. Mater. Trans. A*, vol. 38, pp. 2379–2388, 2007.
- [125] D. Rafaja, V. Klemm, G. Schreiber, M. Knapp, and R. Kužel, "Interference phenomena observed by X-ray diffraction in nanocrystalline thin films," *J. Appl. Crystallogr.*, vol. 37, pp. 613–620, 2004.
- [126] A. Leineweber and E. J. Mittemeijer, "Notes on the order-of-reflection dependence of microstrain broadening," *J. Appl. Crystallogr.*, vol. 43, pp. 981–989, 2010.
- [127] S. S. Quek, Y. Xiang, and D. J. Srolovitz, "Loss of interface coherency around a misfitting spherical inclusion," *Acta Mater.*, vol. 59, pp. 5398–5410, 2011.
- [128] P.-A. Geslin, B. Appolaire, and A. Finel, "Investigation of coherency loss by prismatic punching with a nonlinear elastic model," *Acta Mater.*, vol. 71, pp. 80–88, 2014.
- [129] J. Van Berkum, R. Delhez, T. H. De Keijser, E. J. Mittemeijer, and P. van Mourik, "Note on relaxation of cooling-induced strains in two-phase AlSi-alloys at room temperature," *Scr. Metall. Mater.*, vol. 25, pp. 2255–2258, 1991.
- [130] C. Michaelsen, "On the structure and homogeneity of solid solutions: The limits of conventional X-ray diffraction," *Philos. Mag. A*, vol. 72, pp. 813–828, 1995.
- [131] E. J. Mittemeijer, "Gitterverzerrungen in nitriertem Eisen und Stahl," *HTM Härtereitechnische Mitteilungen*, vol. 36, pp. 57–65, 1981.
- [132] P. Ferguson and K. H. Jack, "Quench-aging and strain-aging of nitrogen-ferrite," in *Proceedings of the Heat Treatment Conference*, 1981, pp. 158–163.
- [133] C. J. Smithells, *Metals Reference Book*, 8th edn. Elsevier, 2004.
- [134] Y. Wang, J. Zhang, H. Xu, Z. Lin, L. L. Daemen, Y. Zhao, and L. Wang, "Thermal equation of state of copper studied by high P-T synchrotron x-ray diffraction," *Appl. Phys. Lett.*, vol. 94, p. 071904, 2009.
- [135] a. Taylor and R. W. Floyd, "Precision measurements of lattice parameters of non-cubic crystals," *Acta Crystallogr.*, vol. 3, pp. 285–289, 1950.
-

References

- [136] O. Madelung, U. Rössler, and M. Schulz, Eds., *Landolt-Börnstein - Group III Condensed Matter, Vol. 41A1a: Group IV Elements, IV-IV and III-V Compounds. Part a - Lattice Properties*, Berlin/Heidelberg: Springer-Verlag, 2001.
- [137] R. B. Roberts, "Thermal expansion reference data: silicon 300-850 K," *J. Phys. D. Appl. Phys.*, vol. 14, pp. L163–L166, 1981.
- [138] D. S. Rickerby and A. Hendry, "Strengthening of nitrided Fe-Ti alloys," *Acta Metall.*, vol. 34, pp. 1911–1923, 1986.
- [139] A. E. Berkowitz, J. R. Mitchell, M. J. Carey, A. P. Young, S. Zhang, F. E. Spada, F. T. Parker, A. Hutten, and G. Thomas, "Giant magnetoresistance in heterogeneous Cu-Co alloys," *Phys. Rev. Lett.*, vol. 68, pp. 3745–3748, 1992.
- [140] M. J. van Genderen, A. Böttger, R. J. Cernik, and E. J. Mittemeijer, "Early stages of decomposition in iron-carbon and iron-nitrogen martensites: Diffraction analysis using synchrotron radiation," *Metall. Trans.*, vol. 24, pp. 1965–1973, 1993.
- [141] D. J. Dyson, *X-Ray and Electron Diffraction Studies in Materials Science*, 1st ed. London: Maney Publishing, 2004.
- [142] J. W. Cahn, *Concise Encyclopedia of Materials Characterization*. Amsterdam: Elsevier, 2005.
- [143] M. Ladd and R. Palmer, *Structure Determination by X-ray Crystallography*, 5th edn. Boston, MA: Springer US, 2013.
- [144] V. Daniel and H. Lipson, "An X-ray study of the dissociation of an alloy of copper, iron and nickel," *Proc. R. Soc. Lond. A. Math. Phys. Sci.*, vol. 181, pp. 368–378, 1943.
- [145] L. Zwell and a. W. Danko, *Applications of X-ray Diffraction Methods to Quantitative Chemical Analysis*, vol. 9, 1975.
- [146] H. Ledbetter and M. Austin, "Internal strain (stress) in an SiC-Al particle-reinforced composite: an X-ray diffraction study," *Mater. Sci. Eng.*, vol. 89, pp. 53–61, 1987.
- [147] J. Luo, K. Tao, H. Yin, and Y. Du, "Studies on quantitative x-ray diffraction characterization of phase depth profiles," *Rev. Sci. Instrum.*, vol. 67, pp. 2859–2862, 1996.
- [148] J. Epp, H. Surm, O. Kessler, and T. Hirsch, "In situ X-ray phase analysis and computer simulation of carbide dissolution of ball bearing steel at different austenitizing temperatures," *Acta Mater.*, vol. 55, pp. 5959–5967, 2007.
- [149] W. Tirry and D. Schryvers, "Quantitative determination of strain fields around Ni₄Ti₃ precipitates in NiTi," *Acta Mater.*, vol. 53, pp. 1041–1049, 2005.
- [150] D. B. Williams and E. P. Butler, "Grain boundary discontinuous precipitation reactions," *Int. Mater. Rev.*, vol. 26, pp. 153–183, 1981.
- [151] F. Findik, "Discontinuous (cellular) precipitation," *J. Mater. Sci. Lett.*, vol. 7, pp. 79–83, 1998.

-
- [152] I. Manna, S. K. Pabi, and W. Gust, "Discontinuous reactions in solids," *Int. Mater. Rev.*, vol. 46, pp. 53–91, 2001.
- [153] S. J. B. Kurz, S. R. Meka, N. Schell, W. Ecker, J. Keckes, and E. J. Mittemeijer, "Residual stress and microstructure depth gradients in nitrided iron-based alloys revealed by dynamical cross-sectional transmission X-ray microdiffraction," *Acta Mater.*, vol. 87, pp. 100–110, 2015.
- [154] A. Sutton and W. Hume-Rothery, "CXLI. The lattice spacings of solid solutions of titanium, vanadium, chromium, manganese, cobalt and nickel in α -iron," *Philos. Mag.*, vol. 46, pp. 1295–1309, 1955.
- [155] L. Dijkstra, "Precipitation phenomena in the solid solutions of Nitrogen and Carbon in alpha Iron below the eutectoid temperature," *Trans. Am. Inst. Min. Metall. Eng.*, vol. 185, pp. 252–260, 1949.
- [156] K. H. Jack, "Results of further X-ray structural investigations of the iron-carbon and iron-nitrogen systems and of related interstitial alloys," *Acta Crystallogr.*, vol. 3, pp. 392–394, 1950.
- [157] M. H. Biglari, C. M. Brakman, E. J. Mittemeijer, and S. Van Der Zwaag, "Analysis of the nitrogen absorption isotherms of cold-rolled Fe-2 at.% Al specimens with different AlN precipitate dimensions," *Philos. Mag. A*, vol. 72, pp. 931–947, 1995.
- [158] H. H. Podgurski, R. Oriani, F. Davis, J. Li, and Y. Chou, "Nitrogenation of Fe-Al alloys. Pt. 2. The Adsorption and solution of nitrogen in nitrogenated Fe-Al alloys," *Trans. Metall. Soc. AIME*, vol. 245, pp. 1603–1608, 1969.
- [159] D. H. Jack and K. H. Jack, "Invited review: carbides and nitrides in steel," *Mater. Sci. Eng.*, vol. 11, pp. 1–27, 1973.
- [160] J. L. Meijering, "Internal Oxidation of Alloys," in *Advances in Materials Research, Vol. 5*, H. Herman, Ed. New York: Wiley-Interscience, John Wiley & Sons, Inc., 1971, pp. 1–82.
- [161] H. P. Van Landeghem, M. Gouné, and A. Redjaïmia, "Nitride precipitation in compositionally heterogeneous alloys: Nucleation, growth and coarsening during nitriding," *J. Cryst. Growth*, vol. 341, pp. 53–60, 2012.
- [162] H. Selg, S. R. Meka, M. Kachel, R. E. Schacherl, T. Waldenmaier, and E. J. Mittemeijer, "Nitriding behaviour of maraging steel: experiments and modelling," *J. Mater. Sci.*, vol. 48, pp. 4321–4335, 2013.
- [163] M. Jung, S. R. Meka, B. Rheingans, and E. J. Mittemeijer, "Coupling inward diffusion and precipitation kinetics; the case of nitriding iron-based alloys," Accepted for publication in *Metall. Mater. Trans. A*, 2015.
- [164] D. H. Jack, "The structure of nitrided iron-titanium alloys," *Acta Metall.*, vol. 24, pp. 137–146, 1976.
-

-
- [165] S. S. Hosmani, R. E. Schacherl, L. Lityńska-Dobrzyńska, and E. J. Mittemeijer, "The nitrogen-absorption isotherm for Fe–21.5 at. % Cr alloy: dependence of excess nitrogen uptake on precipitation morphology," *Philos. Mag.*, vol. 88, pp. 2411–2426, 2008.
- [166] M. Akhlaghi, S. R. Meka, E. A. Jäggle, S. J. B. Kurz, E. Bischoff, and E. J. Mittemeijer, "Low temperature nitriding of recrystallized and cold-rolled ferritic Fe-Cr-Al alloy," Submitted for publication.
- [167] P. Jessner, R. Danoix, B. Hannover, and F. Danoix, "Investigations of the nitrided subsurface layers of an Fe-Cr-model alloy.," *Ultramicroscopy*, vol. 109, pp. 530–534, 2009.
- [168] B. Gault, F. Danoix, K. Hoummada, D. Mangelinck, and H. Leitner, "Impact of directional walk on atom probe microanalysis," *Ultramicroscopy*, vol. 113, pp. 182–191, 2012.
- [169] D. C. Joy, A. D. Romig, and J. I. Goldstein, Eds., *Principles of Analytical Electron Microscopy*. Boston, MA: Springer US, 1986.
- [170] C. Ginter, L. Torchane, J. Dulcy, M. Gantois, A. Malchère, C. Esnouf, and T. Turpin, "A new approach to hardening mechanisms in the diffusion layer of gas nitrided α -alloyed steels . Effects of chromium and aluminium: experimental and simulation studies," *La Metall. Ital.*, vol. 7–8, pp. 29–35, 2006.
- [171] S. S. Brenner and S. R. Goodman, "FIM-atom probe analysis of thin nitride platelets in Fe-3 at.% Mo," *Scr. Metall.*, vol. 5, pp. 865–870, 1971.
- [172] E. J. Mittemeijer and J. T. Slycke, "Chemical potentials and activities of nitrogen and carbon imposed by gaseous nitriding and carburising atmospheres," *Surf. Eng.*, vol. 12, pp. 152–162, 1996.
- [173] J. H. Driver, D. C. Unthank, and K. H. Jack, "Substitutional-interstitial G.P. zones in nitrided Fe-Mo alloys," *Philos. Mag.*, vol. 26, pp. 1227–1231, 1972.
- [174] O. Madelung, Ed., *Landolt-Börnstein - Group IV Physical Chemistry, Vol. 5E: Phase Equilibria, Crystallographic and Thermodynamic Data of Binary Alloys: Fe-V (Iron-Vanadium) Phase diagram Crystal structure*, vol. e. Berlin/Heidelberg: Springer-Verlag, 1995.
- [175] J.-O. Andersson, T. Helander, L. Höglund, P. Shi, and B. Sundman, "Thermo-Calc & DICTRA, computational tools for materials science," *Calphad*, vol. 26, pp. 273–312, 2002.
- [176] Thermo-Calc Software TCFE7 Steels/Fe-alloys database version 7 .
- [177] M. W. J. Chase, *NIST-JANAF Thermochemical Tables*, 4th ed. American Chemical Society, 1998.
- [178] H. J. Grabke, "Kinetik und Mechanismen der Oberflächenreaktionen bei der Auf-Entkohlung und Auf- und Entstickung von Eisen in Gasen," *Arch. für das Eisenhüttenwes.*, vol. 46, pp. 75–81, 1975.
- [179] E. Houdremont and H. J. Wiester, *Handbuch der Sonderstahlkunde*, Dritte Aufl. Berlin/Göttingen/Heidelberg: Springer Verlag Berlin Heidelberg, 1956.
-

-
- [180] G. Miyamoto, Y. Tomio, H. Aota, K. Oh-ishi, K. Hono, and T. Furuwara, "Precipitation of nanosized nitrides in plasma nitrided Fe-M (M = Al, Cr, Ti, V) alloys," *Mater. Sci. Technol.*, vol. 27, pp. 742–746, 2011.
- [181] J. Driver and J. Papazian, "The electron and field ion metallography of zones in nitrided Fe-Mo alloys," *Acta Metall.*, vol. 21, pp. 1139–1149, 1973.
- [182] R. G. Baker and J. Nutting, "Precipitation Processes in Steels," *Iron Steel Inst. Spec. Rep.*, vol. 64, p. 1–22, 1959.
- [183] A. Molinari, T. Bacci, P. Campestrini, M. Pellizzari, and B. Tesi, "Plasma nitriding of Fe–Cr–Mo sintered steels," *Powder Metall.*, vol. 42, pp. 119–125, 1999.
- [184] A. Molinari, B. Tesi, T. Bacci, and T. Marcu, "Plasma nitriding and nitrocarburising of sintered Fe–Cr–Mo and Fe–Cr–Mo–C alloys," *Surf. Coatings Technol.*, vol. 140, pp. 251–255, 2001.
- [185] J. Kazior and C. Janczur, "Thermochemical treatment of Fe–Cr–Mo alloys," *Surf. Coatings Technol.*, vol. 152, pp. 333–337, 2002.
- [186] T. Steiner, S. R. Meka, E. Bischoff, T. Waldenmaier, and E. J. Mittemeijer, "Internal nitriding of ternary Fe–Cr–Mo alloys; nitride development," in *Proceedings - European Conference on Heat Treatment and 21st IFHTSE Congress*, 2014, pp. 53–61.
- [187] P. Thompson, D. E. Cox, and J. B. Hastings, "Rietveld refinement of Debye–Scherrer synchrotron X-ray data from Al₂O₃," *J. Appl. Crystallogr.*, vol. 20, pp. 79–83, 1987.
- [188] R. A. Young and P. Desai, "Crystallite size and microstrain indicators in Rietveld refinement," *Arch. Nauk. o Mater.*, vol. 10, pp. 71–90, 1989.
- [189] B. Gault, M. P. Moody, J. M. Cairney, and S. P. Ringer, *Atom Probe Microscopy*. Springer Science & Business Media, 2012.
- [190] B. Gault, D. Haley, F. de Geuser, M. P. Moody, E. a Marquis, D. J. Larson, and B. P. Geiser, "Advances in the reconstruction of atom probe tomography data.," *Ultramicroscopy*, vol. 111, pp. 448–457, 2011.
- [191] A. Martinavičius, R. Danoix, M. Drouet, C. Templier, B. Hannoyer, and F. Danoix, "Atom probe tomography characterization of nitrogen induced decomposition in low temperature plasma nitrided 304L austenitic stainless steel," *Mater. Lett.*, vol. 139, pp. 153–156, 2015.
- [192] M. Fonović, A. Leineweber, O. Robach, E. A. Jäggle, and E. J. Mittemeijer, "The Nature and Origin of 'Double Expanded Austenite' in Ni-Based Ni-Ti Alloys Developing Upon Low Temperature Gaseous Nitriding," *Metall. Mater. Trans. A*, vol. 46, pp. 4115–4131, 2015.
- [193] P. Ettmayer, A. Vendl, and R. Kieffer, "Investigations of the Cr–Mo–N system," *High Temp. - High Press.*, vol. 10, pp. 699–702, 1978.
- [194] K. S. Weil and P. Kumta, "Chemical Synthesis and Structural Investigation of a New Ternary Nitride, CrWN₂," *J. Solid State Chem.*, vol. 128, pp. 185–190, 1997.
-

-
- [195] K. S. Weil, P. Kumta, and J. Grins, "Exploration of Cation Substitution in the Layered Compound CrWN₂," *MRS Proc.*, vol. 755, pp. 283–288, 2002.
- [196] H. Beattie and F. Ver Snyder, "Microconstituents in High Temperature Alloys," *Trans. Am. Soc. Met.*, vol. 45, pp. 397–428, 1953.
- [197] G. Effenberg and S. Ilyenko, *Landolt-Börnstein Group IV Physical Chemistry, Vol. 11D3: Ternary Alloy Systems: Cr-Fe-N*, Berlin, Heidelberg: Springer Berlin Heidelberg, 2008.
- [198] R. N. Panda and N. S. Gajbhiye, "Electronic and magnetic properties of Fe₃Mo₃N," *J. Alloys Compd.*, vol. 256, pp. 102–107, 1997.
- [199] R. N. Panda and N. S. Gajbhiye, "Chemical synthesis and magnetic properties of nanocrystalline FeMoN₂," *J. Cryst. Growth*, vol. 191, pp. 92–96, 1998.
- [200] P. Hones, R. Sanjinés, F. Lévy, and O. Shojaei, "Electronic structure and mechanical properties of resistant coatings: The chromium molybdenum nitride system," *J. Vac. Sci. Technol. A Vacuum, Surfaces, Film.*, vol. 17, pp. 1024–1030, 1999.
- [201] B. Gu, J. P. Tu, X. H. Zheng, Y. Z. Yang, and S. M. Peng, "Comparison in mechanical and tribological properties of Cr–W–N and Cr–Mo–N multilayer films deposited by DC reactive magnetron sputtering," *Surf. Coatings Technol.*, vol. 202, pp. 2189–2193, 2008.
- [202] A. Y. Ganin, L. Kienle, and G. V. Vajenine, "Synthesis and characterisation of hexagonal molybdenum nitrides," *J. Solid State Chem.*, vol. 179, pp. 2339–2348, 2006.
- [203] P. Etmayer, "Das System Molybdän-Stickstoff," *Monatshefte für Chemie*, vol. 101, pp. 127–140, 1970.
- [204] A. Bezinge, K. Yvon, and J. Muller, "High-pressure high-temperature experiments on δ -MoN," *Solid State Commun.*, vol. 63, pp. 141–145, 1987.
- [205] C. L. Bull, P. F. McMillan, E. Soignard, and K. Leinenweber, "Determination of the crystal structure of δ -MoN by neutron diffraction," *J. Solid State Chem.*, vol. 177, pp. 1488–1492, 2004.
- [206] D. S. Bem and H.-C. Zur Loye, "Synthesis of the New Ternary Transition Metal Nitride FeWN₂ via Ammonolysis of a Solid State Oxide Precursor," *J. Solid State Chem.*, vol. 104, pp. 467–469, 1993.
- [207] K. S. Weil and P. N. Kumta, "Synthesis of ternary transition metal nitrides using chemically complexed precursors," *Mater. Sci. Eng. B*, vol. 38, pp. 109–117, 1996.
- [208] P. S. Herle, "Synthesis of new transition metal nitrides, MWN₂ (M= Mn, Co, Ni)," *J. Alloys Compd.*, vol. 217, pp. 22–24, 1995.
- [209] H. Bakker, *Landolt-Börnstein - Group III Condensed Matter, Vol. 26: Diffusion in Solid Metals and Alloys: 4 Self-diffusion in binary alloys and intermediate phases (tables): Ag-Al - Cu-Sn*, New Series. Springer Verlag Berlin Heidelberg, 1990.
- [210] H. Nitta, K. Miura, and Y. Iijima, "Self-diffusion in iron-based Fe–Mo alloys," *Acta Mater.*, vol. 54, pp. 2833–2847, 2006.
-

-
- [211] P. H. Mayrhofer, H. Willmann, and A. E. Reiter, "Structure and phase evolution of Cr–Al–N coatings during annealing," *Surf. Coatings Technol.*, vol. 202, pp. 4935–4938, 2008.
- [212] R. Forsén, M. Johansson, M. Odén, and N. Ghafoor, "Decomposition and phase transformation in TiCrAlN thin coatings," *J. Vac. Sci. Technol. A Vacuum, Surfaces, Film.*, vol. 30, pp. 061506–1–8, 2012.
- [213] J. W. Cahn, "The kinetics of cellular segregation reactions," *Acta Metall.*, vol. 7, pp. 18–28, 1959.
- [214] G. A. López, P. Zieba, W. Gust, and E. J. Mittemeijer, "Discontinuous precipitation in a Cu–4.5 at.-%In alloy," *Mater. Sci. Technol.*, vol. 19, pp. 1539–1545, 2003.
- [215] B. Schwarz, S. R. Meka, R. E. Schacherl, E. Bischoff, and E. J. Mittemeijer, "Nitriding of iron-based ternary Fe–V–Si alloy: The precipitation process of separate nitrides," *Acta Mater.*, vol. 76, pp. 394–403, 2014.
- [216] Verein Deutscher Eisenhüttenleute, *Steel: A Handbook for Materials Science and Engineering*. Berlin, Heidelberg, New York, Tokyo, Düsseldorf: Springer, Verein Deutscher Eisenhüttenleute, 1991.
- [217] A. R. Clauss, E. Bischoff, R. E. Schacherl, and E. J. Mittemeijer, "The microstructure of the diffusion zone of a gaseously nitrided Fe–1.5 wt-%Cr–1.5 wt-%Al alloy," *Mater. Sci. Technol.*, vol. 26, pp. 297–308, 2010.
- [218] A. Fernández Guillermet, in: *Phase Diagrams of Binary Iron Alloys; Fe–Mo*. Materials Park, Ohio: Materials Information Soc., 1993.
- [219] P. F. Colijn, E. J. Mittemeijer, and H. C. F. Rozendaal, "Light-Microscopical Analysis of Nitrided or Nitrocarburized Iron and Steels," *Zeitschrift für Met.*, vol. 74, pp. 620–627, 1983.
- [220] A. Wells, "Metallographic analysis of compound layers on ferritic nitrocarburized plain low carbon steel," *J. Mater. Sci.*, vol. 20, pp. 2439–2445, 1985.
- [221] V. Hauk, *Structural and Residual Stress Analysis by Nondestructive Methods*. Amsterdam: Elsevier, 1997.
- [222] L. Toth, *Transition metal carbides and nitrides*, vol. 7. Academic Press New York and London, 1971.
- [223] H. C. F. Rozendaal, E. J. Mittemeijer, P. F. Colijn, and P. J. Van Der Schaaf, "The development of nitrogen concentration profiles on nitriding iron," *Metall. Mater. Trans. A*, vol. 14, pp. 395–399, 1983.
- [224] M. Nikolussi, A. Leineweber, and E. J. Mittemeijer, "Nitrogen diffusion through cementite layers," *Philos. Mag.*, vol. 90, pp. 1105–1122, 2010.
- [225] C. W. Kang, S. R. Meka, R. E. Schacherl, and E. J. Mittemeijer, "Microstructure and Kinetics of Nitride Precipitation in a Quaternary Iron-Based Model Fe-2.82 at. pct Cr-0.13 at. pct Mo-0.18 at. pct V Alloy," *Metall. Mater. Trans. A*, vol. 46, pp. 328–336, 2014.
-

-
- [226] A. D. LeClaire, *Landolt-Börnstein - Group III Condensed Matter, Vol. 26: Diffusion in Solid Metals and Alloys: 8.2 Diffusion tables for C, N, and O in metals*, vol. 26. Berlin/Heidelberg: Springer-Verlag, 1990.
- [227] L. Cheng, A. Böttger, T. H. De Keijser, and E. J. Mittemeijer, "Lattice parameters of iron-carbon and iron-nitrogen martensites and austenites," *Scr. Metall. Mater.*, vol. 24, pp. 509–514, 1990.
- [228] A. Leineweber, H. Jacobs, F. Hüning, H. Lueken, and W. Kockelmann, "Nitrogen ordering and ferromagnetic properties of ϵ -Fe₃N," *J. Alloys Compd.*, vol. 316, pp. 21–38, 2001.
- [229] M. A. J. Somers, B. J. Kooij, L. Maldzinski, E. J. Mittemeijer, A. A. Van Der Horst, A. M. Van Der Kraan, and N. M. Van Der Pers, "Thermodynamics and long-range order of interstitials in an h.c.p. lattice: nitrogen in ϵ -Fe₂N_{1-z}," *Acta Metall.*, vol. 45, pp. 2013–2025, 1997.
- [230] M. Widenmeyer, T. C. Hansen, and R. Niewa, "Formation and Decomposition of Metastable α' -Fe₁₆N₂ from in situ Powder Neutron Diffraction and Thermal Analysis," *Zeitschrift für Anorg. und Allg. Chemie*, vol. 639, pp. 2851–2859, 2013.
- [231] S. Eriksson, "Röntgenundersökningar över systemet järn-krom-kväve," *Jernkontorets Ann.*, pp. 530–546.
- [232] W. Paszkowicz, S. Podsiadło, and R. Minikayev, "Rietveld-refinement study of aluminium and gallium nitrides," *J. Alloys Compd.*, vol. 382, pp. 100–106, 2004.
- [233] S. K. Jackson, R. C. Layland, and H. Loye, "The simultaneous powder X-ray and neutron diffraction refinement of two eta-carbide type nitrides, Fe₃Mo₃N and Co₃Mo₃N, prepared by ammonolysis and by plasma nitridation of oxide precursors," *J. Alloys Compd.*, vol. 291, pp. 94–101, 1999.
- [234] T. Liapina, A. Leineweber, and E. J. Mittemeijer, "Nitrogen redistribution in ϵ/γ' -iron nitride compound layers upon annealing," *Scr. Mater.*, vol. 48, pp. 1643–1648, 2003.
- [235] T. Liapina, A. Leineweber, and E. J. Mittemeijer, "Phase transformations in iron-nitride compound layers upon low-temperature annealing: Diffusion kinetics of nitrogen in ϵ - and γ' -iron nitrides," *Metall. Mater. Trans. A*, vol. 37, pp. 319–330, 2006.
- [236] I. Barin, *Thermochemical Data of Pure Substances*. Weinheim, Germany: Wiley-VCH Verlag GmbH, 1995.
- [237] M. H. Biglari, C. M. Brakman, E. J. Mittemeijer, and S. van der Zwaag, "The kinetics of the internal nitriding of Fe-2 at. pct Al alloy," *Metall. Mater. Trans. A*, vol. 26, no. April, pp. 765–776, 1995.

Supplements

Supplement 1: Crystal structure parameters for Fe-N phases.

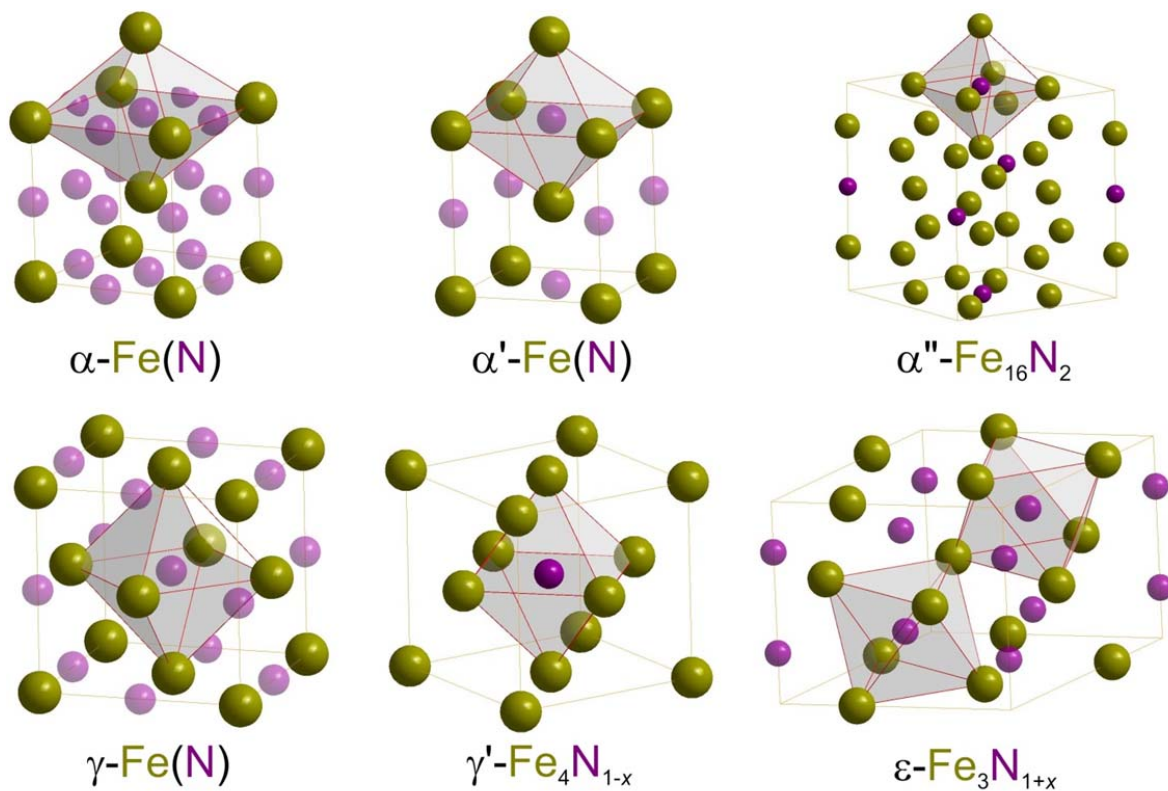
phase	space group	lattice parameters [Å]	atom position				Ref.
			atom	x	y	z	
α -Fe(N) (ferrite)	$Im\bar{3}m$ (229)	$2.8664+0.0079*x_N$	Fe1 N1	0 0	0 0	0 $\frac{1}{2}$	[98]
γ -Fe(N) (austenite)	$Fm\bar{3}m$ (225)	$3.562+0.0093*x_N$	Fe1 N1	0 $\frac{1}{2}$	0 $\frac{1}{2}$	0 $\frac{1}{2}$	[227]
α' -Fe(N) (martensite)	$I4/mmm$ (139)	$a=2.8664-0.0018*x_N$ $c=2.8664+0.0263*x_N$	Fe1 N1	0 0	0 0	0 $\frac{1}{2}$	[227]
γ' -Fe ₄ N _{1-x}	$Pm\bar{3}m$ (221)	3.6468	Fe1 Fe2 N1	0 0 $\frac{1}{2}$	0 $\frac{1}{2}$ $\frac{1}{2}$	0 $\frac{1}{2}$ $\frac{1}{2}$	[97]
ϵ -Fe ₃ N _{1+x}	$P6_322$ (182)	$a=4.4709+0.673*\frac{x_N}{1-x_N}$ $c=4.2723+0.318*\frac{x_N}{1-x_N}$	Fe1 N1	0.328 $\frac{1}{3}$	0 $\frac{2}{3}$	0 $\frac{1}{4}$	[228] [229]
α'' -Fe ₁₆ N ₂	$I4/mmm$ (139)	$a=5.7176$ $c=6.288$	Fe1 Fe2 Fe3 N1	0 $\frac{1}{2}$ $\frac{1}{4}$ 0	0 0 $\frac{1}{4}$ 0	0.208 $\frac{1}{4}$ 0 $\frac{1}{2}$	[230]

Supplement 2: Crystal structure parameters for alloying-element nitride phases.

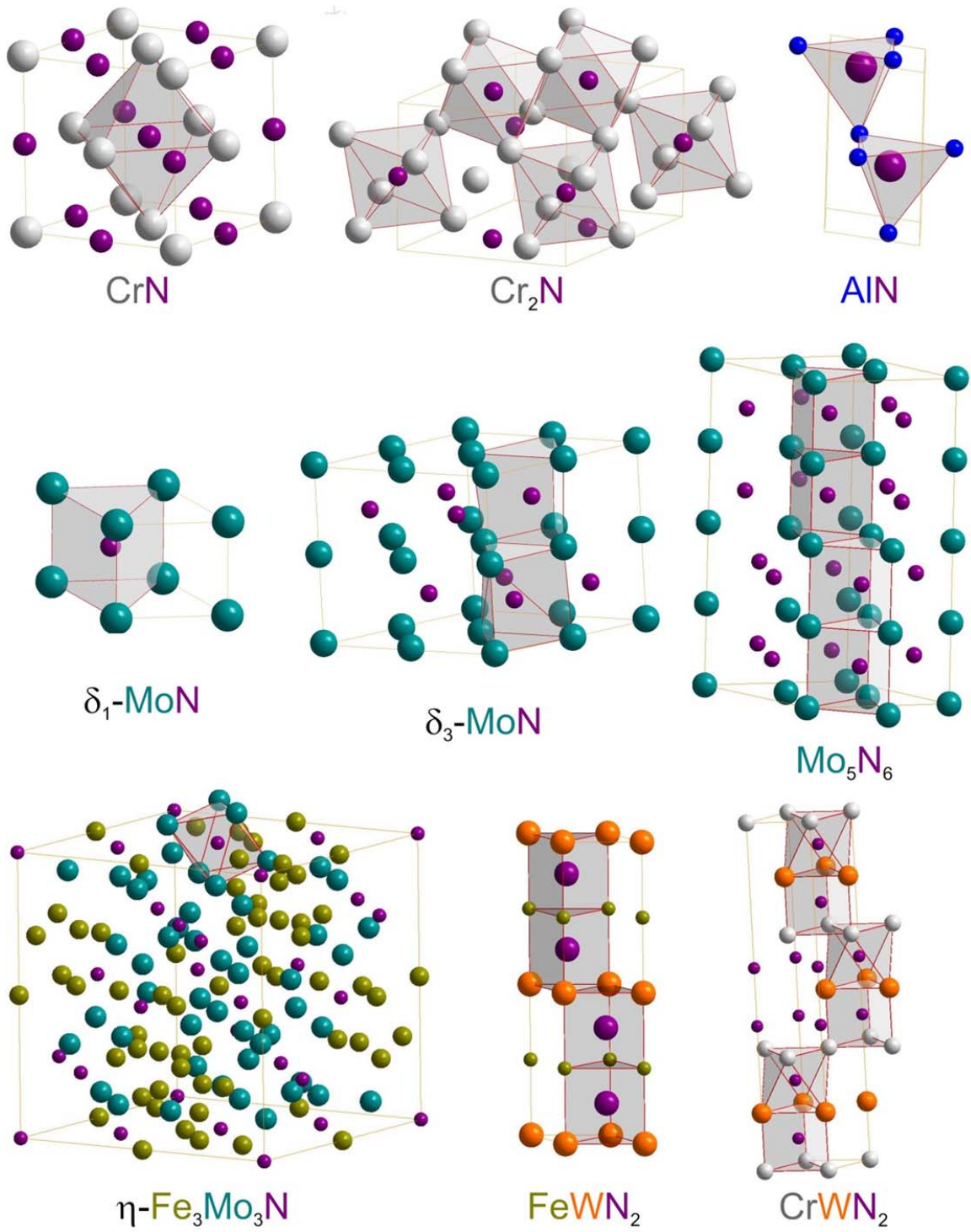
nitride	space group	lattice parameters [Å]	atom position				Ref.
			atom	x	y	z	
CrN (TiN, VN, cubic AlN, γ -Mo ₂ N (50% N vacancies))	Fm $\bar{3}$ m (225)	4.14	Cr1 N1	0 0	0 0	0 $\frac{1}{2}$	[97]
Cr ₂ N	P $\bar{3}$ 1m (162)	$a=4.795$ $c=4.469$	Cr1 N1 N2	$\frac{1}{3}$ 0 $\frac{1}{3}$	0 0 $\frac{2}{3}$	$\frac{3}{4}$ $\frac{1}{2}$ 0	[231]
AlN	P6 ₃ mc (186)	$a=3.112$ $c=4.9809$	Al1 N1	$\frac{1}{3}$ $\frac{1}{3}$	$\frac{2}{3}$ $\frac{2}{3}$	0 0.387	[232]
δ_1 -MoN	P $\bar{6}$ m2 (187)	$a=2.868$ $c=2.610$	Mo1 N1	0 $\frac{1}{3}$	0 $\frac{2}{3}$	0 $\frac{1}{2}$	[202]
δ_3 -MoN	P6 ₃ mc (186)	$a=5.7356$ $c=5.6281$	Mo1 Mo2 N1 N2	0 0.488 $\frac{1}{3}$ 0.166	0 0.512 $\frac{2}{3}$ 0.836	-0.009 -0.007 0.757 0.263	[202]

Cont. from p. 58.

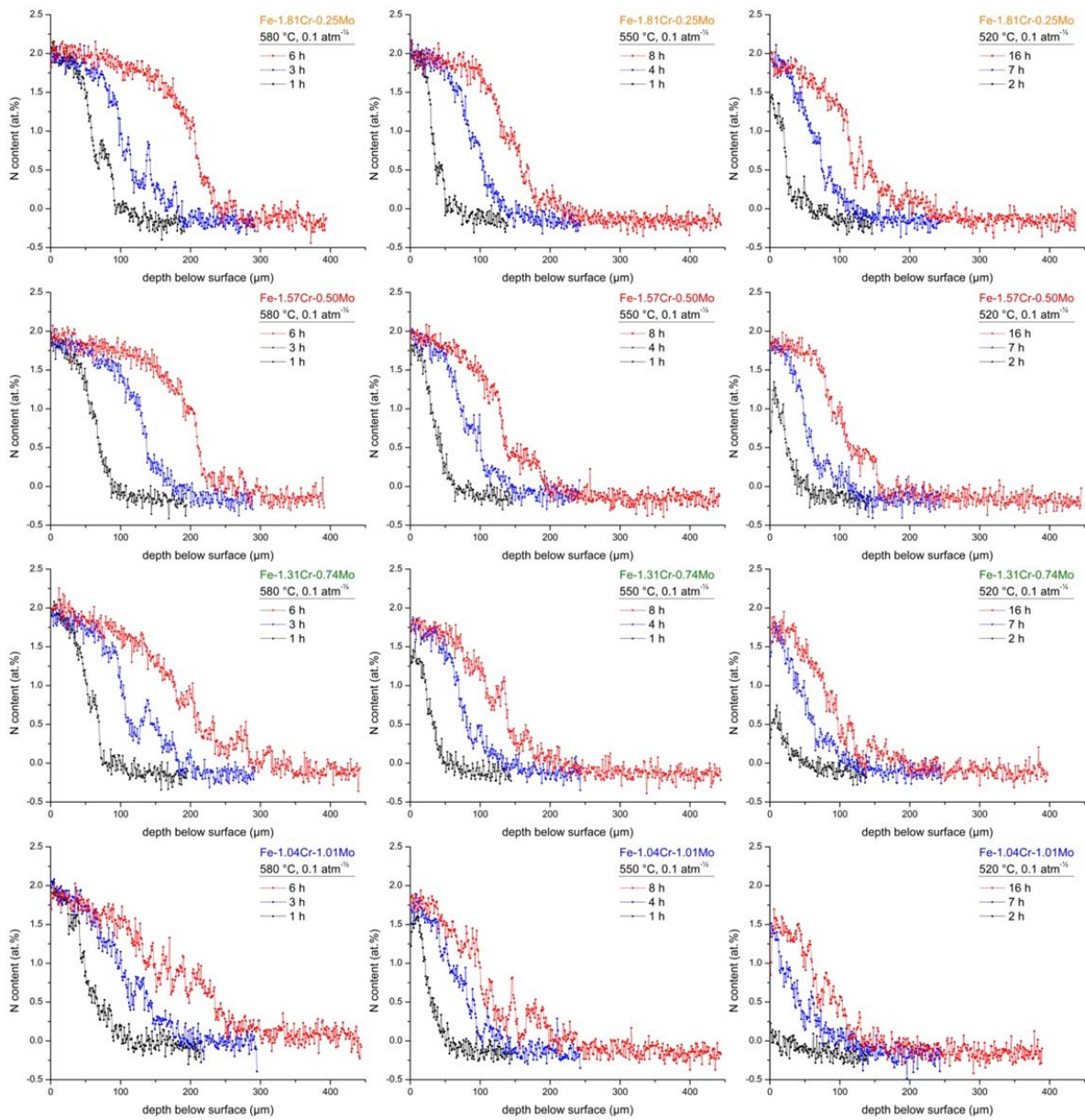
nitride	space group	lattice parameters [Å]	atom position				Ref.
			atom	x	y	z	
Mo ₅ N ₆	P6 ₃ /m (176)	$a=5.7356$ $c=5.6281$	Mo1	0	0	$\frac{1}{4}$	[202]
			Mo2	0	0	0	
			Mo3	$\frac{1}{3}$	$\frac{2}{3}$	$\frac{1}{4}$	
			Mo4	$\frac{2}{3}$	$\frac{1}{3}$	$\frac{1}{4}$	
			Mo5	$\frac{1}{3}$	$\frac{2}{3}$	0.003	
			N1	-0.013	0.356	0.124	
η -Fe ₃ Mo ₃ N	Fd3mz (227)	11.0859	Mo1	0.321	$\frac{1}{8}$	$\frac{1}{8}$	[233]
			Fe1	0.294	0.294	0.294	
			Fe2	$\frac{1}{2}$	$\frac{1}{2}$	$\frac{1}{2}$	
			N1	0	0	0	
FeWN ₂ (FeMoN ₂)	P6 ₃ /mmc (194)	$a=2.87$ $c=10.96$	Fe1	0	0	$\frac{1}{4}$	[206]
			W1	0	0	0	
			N1	$\frac{1}{3}$	$\frac{2}{3}$	$\frac{1}{8}$	
CrWN ₂ (CrMoN ₂)	R3mhr (160)	$a=2.852$ $c=15.63$	Cr1	0	0	0.852	[194]
			W1	0	0	0	
			N1	0	0	0.263	
			N2	0	0	0.407	



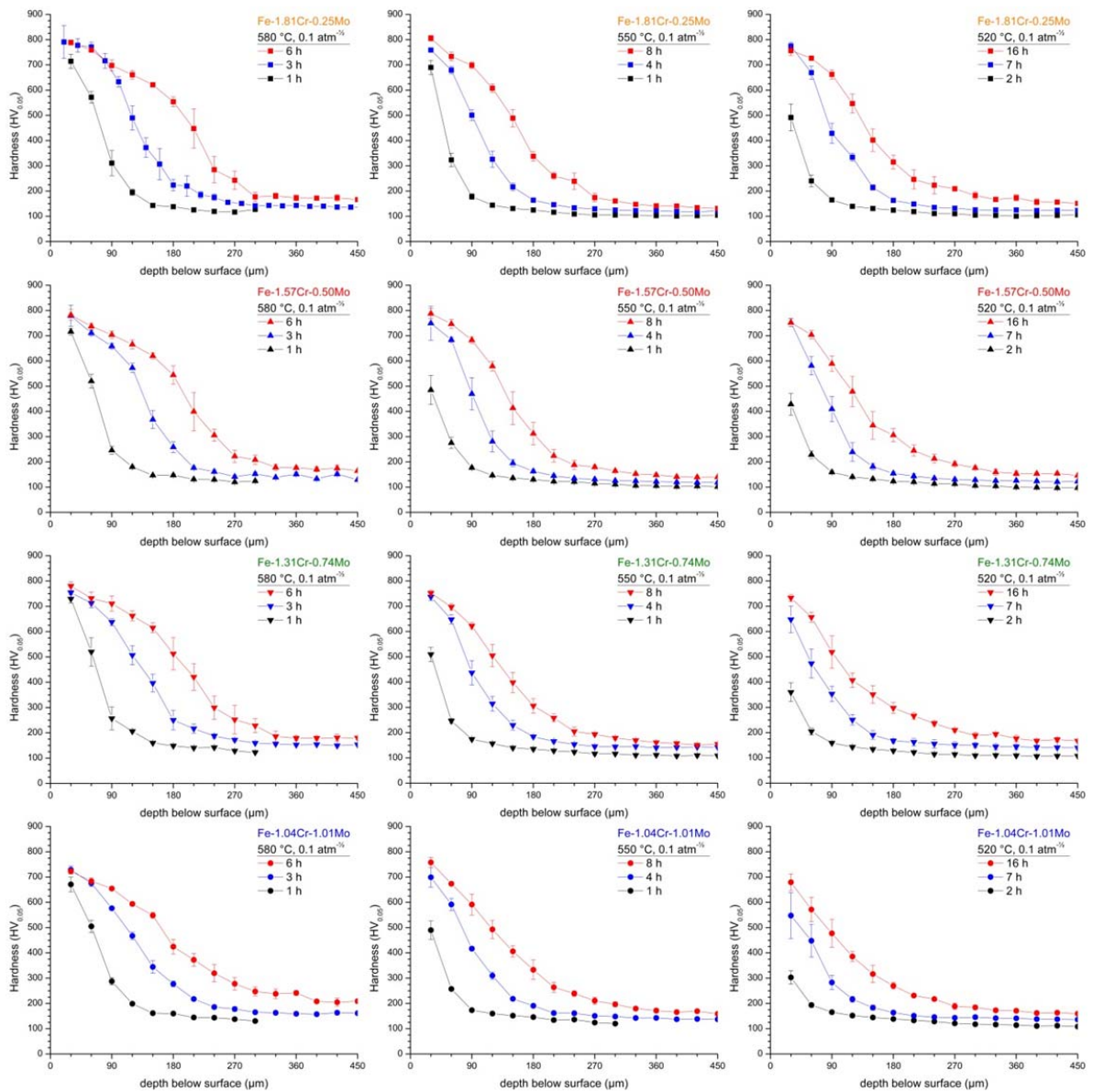
Supplement 3: Crystal structures of Fe-N phases presented in Supplement 1. The coordination of N by Fe is indicated by polyhedra. Sites for interstitially dissolved N in α -Fe(N) (ferrite), martensite (α' -Fe(N)) and austenite (γ -Fe(N)) are represented by transparent N-atoms. These sites are occupied randomly.



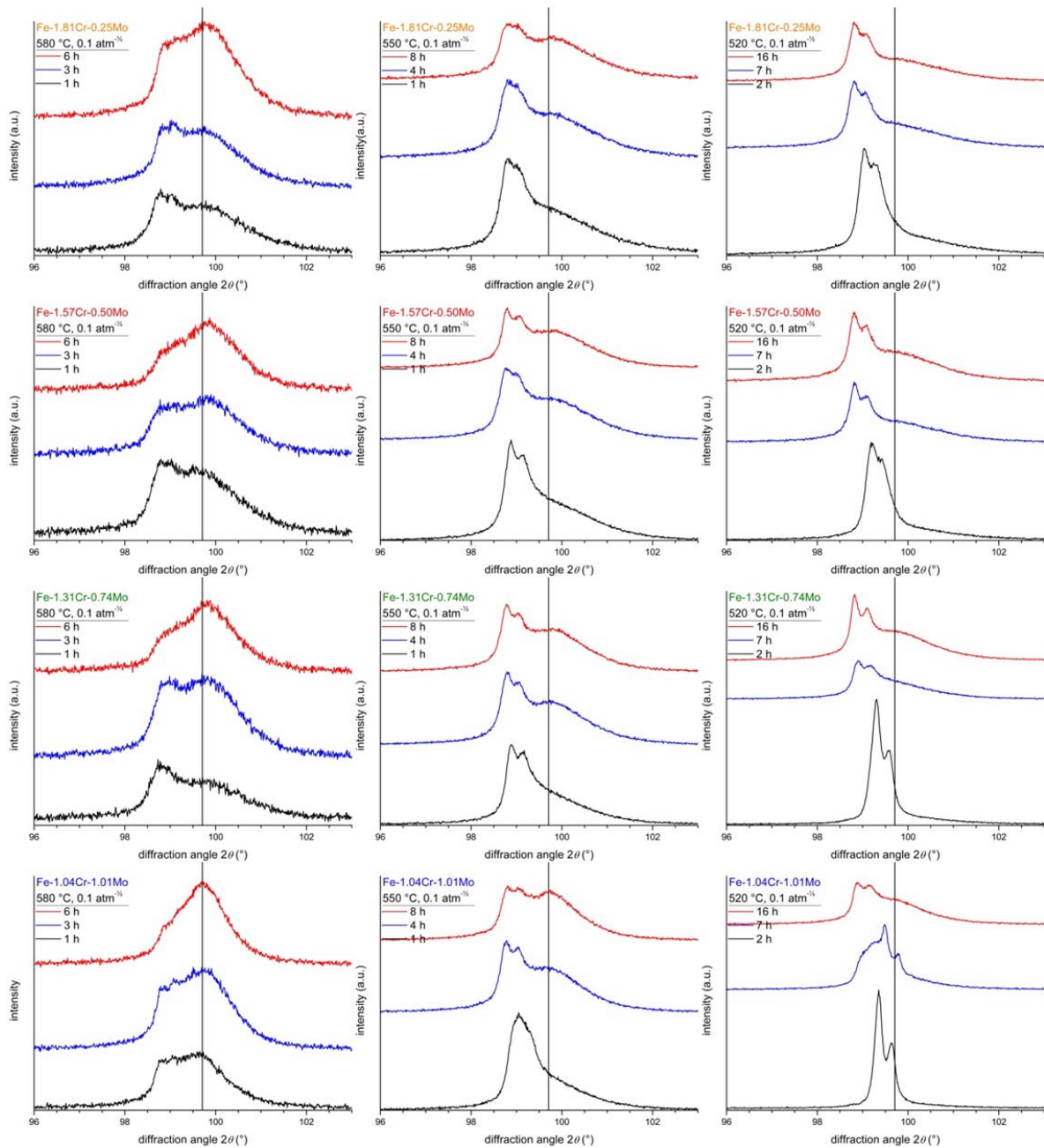
Supplement 4: Crystal structures of alloying element nitride phases, as presented in Supplement 2. The coordination of N by the metal atoms is indicated by polyhedra.



Supplement 5: N-concentration-depth profiles determined by EPMA (average of three measured profiles, see section 6.2.2) on the cross-sections of nitrided Fe-Cr-Mo alloy specimens. Nitriding conditions of the specimens corresponding to the respective profile are given in the figure legends.



Supplement 6: Hardness-depth profiles determined on the cross-sections of nitrided Fe-Cr-Mo alloy specimens. Nitriding conditions of the specimens corresponding to the respective profile are given in the figure legends. The data points represent the average of 5 individual measurements; error bars indicate the standard deviation of the measurements.



Supplement 7: Evolution of the Co- K_{α} -211 ferrite–matrix diffraction-line profile, recorded from the surfaces of nitrided Fe-Cr-Mo alloy specimens. Nitriding conditions of the specimens corresponding to the respective profile are given in the figure legends. The K_{α} -peak position for pure, unstrained ferrite (α -Fe) has been indicated by the full black vertical line.

Danksagung

Die vorliegende Arbeit entstand im Zeitraum von Dezember 2012 bis Dezember 2015 am Institut für Materialwissenschaft der Universität Stuttgart, dem Max Planck Institut für Intelligente Systeme (ehemals Max Planck Institut für Metallforschung) in Stuttgart, und in Kooperation mit dem Zentralbereich Forschung und Voraentwicklung der Robert Bosch GmbH in Schwieberdingen und Renningen. Obwohl ich vielen aus diesen Abteilungen zu Dank verpflichtet bin, können doch nicht alle, die zum Gelingen dieser Arbeit beigetragen haben, hier namentlich erwähnt werden.

Zunächst möchte ich meinem Doktorvater, Herrn Prof. Dr. Ir. E. J. Mittemeijer für die Ermöglichung der Arbeit danken. Seine immenser wissenschaftlicher Überblick, die ausführlichen Diskussionen und Ermutigungen, doch nochmal genauer hinzusehen, nochmal darüber nachzudenken, haben die vielen Beobachtungen erst zu den Ergebnissen gemacht, die nun hier vorliegen.

Mein Dank gilt weiterhin Herrn Prof. Dr. J. Bill für die freundliche Übernahme des Mitberichts dieser Arbeit, sowie Herrn Prof. Dr. T. Schleid für die Bereitschaft zur Übernahme des Prüfungsvorsitzes.

Des Weiteren gilt mein Dank meinen beiden täglichen Betreuern, am Max Planck Institut Dr. S. Meka, und bei der Robert Bosch GmbH Dr. T. Waldenmaier, die mir immer motivierend zur Seite standen. Mit viel Geduld haben sie die verrückten von den guten Ideen getrennt und mir einen spannenden Einblick in die wissenschaftliche und technologische Bedeutung des Themas ermöglicht.

Ohne gute Kollegen wäre solche eine Dissertation nicht möglich gewesen, daher gilt mein Dank auch Maryam, Holger, Zoltan, Gabor, Sarah, Bastian und Paul. Außerdem bin ich Prof. Dr. A. Leineweber und Dr. E. Bischoff für die sehr hilfreichen Diskussionen dankbar.

Zu guter Letzt, aber sicherlich nicht am geringsten, gilt mein Dank meinen Freunden und meiner Familie, deren Rückhalt außerhalb der täglichen Arbeit ebenfalls maßgeblich zu deren Erfolg beigetragen hat.

Curriculum Vitae

Persönliche Daten

Name Tobias Steiner
geboren am 25. Februar 1989 in Hamburg
Nationalität Deutsch

Schulbildung

1995-1997 Hohbuchsule Reutlingen, Deutschland
1997-2000 Collégio Visconde de Pôrto Seguro, Valinhos, Brasilien
2000-2005 Johannes Kepler Gymnasium, Reutlingen, Deutschland
2005-2007 Deutsche Schule Shanghai, PR China, mit Abschluss Abitur

Universitäre Ausbildung

2007-2012 Studium der Werkstoffwissenschaften,
Universität Stuttgart

Juni – Dezember 2012 Diplomarbeit am Max Planck Institut für Intelligente Systeme und Institut für Materialwissenschaft, Universität Stuttgart. Thema der Diplomarbeit: *„Nitriding of Ti and Ti-Al alloys“*

Promotion

Seit Dezember 2012 Wissenschaftlicher Mitarbeiter mit dem Ziel der Promotion zum Dr. rer. nat. bei der Robert Bosch GmbH, in Kooperation mit dem Max Planck Institut für Intelligente Systeme (ehemals Metallforschung), Abteilung von Prof. Dr. Ir. E.J. Mittemeijer und dem Institut für Materialwissenschaft, Universität Stuttgart. Thema der Promotion: *„Internal precipitation of nitrides in Iron-based alloys“*

List of Publications

- *“Lattice-parameter change induced by accommodation of precipitate/matrix misfit; misfitting nitrides in ferrite”*, M. Akhlaghi, T. Steiner, S.R. Meka, A. Leineweber and E.J. Mittemeijer, 2015, Acta Mater., 98, 254-262. (Chapter 2 of this thesis)
- *“Misfit Induced Changes of Lattice Parameters in Two-Phase Systems: Coherent/Incoherent Precipitates in a Matrix”*, M. Akhlaghi, T. Steiner, S.R. Meka and E.J. Mittemeijer, 2015, accepted for publication in J. Appl. Cryst. (Chapter 3 of this thesis)
- *“Diffraction-line shifts and broadenings in continuously and discontinuously coarsening precipitate-matrix systems; coarsening of initially coherent nitride precipitates in a ferrite matrix”*, T. Steiner, M. Akhlaghi, S.R. Meka, and E.J. Mittemeijer, 2015, J. Mat. Sci., 50, 7075-7086. (Chapter 4 of this thesis)
- *“Alloying element nitride stability in nitrated iron-based alloys; denitriding of nitrated Fe-V alloys”*, T. Steiner, S.R. Meka, H. Göhring and E.J. Mittemeijer, submitted for publication in Mater. Sci. Techn. (Chapter 5 of this thesis)
- *“Continuous and discontinuous precipitation in Fe-1 at.%Cr-1 at.%Mo alloy upon nitriding; crystal structure and composition of ternary nitrides”*, T. Steiner, S.R. Meka, B. Rheingans, E. Bischoff, T. Waldenmaier, G. Yeli, T.L. Martin, P.A.J. Bagot, M.P. Moody and E.J. Mittemeijer, submitted for publication in Philos. Mag. (Chapter 6 of this thesis)
- *“Nitriding of ternary Fe-Cr-Mo alloys; role of the Cr/Mo-ratio”*, T. Steiner, S.R. Meka, E. Bischoff, T. Waldenmaier and E.J. Mittemeijer, submitted for publication in Surf. Coat. Techn. (Chapter 7 of this thesis)
- *“Generating duplex microstructures by nitriding; nitriding of iron based Fe-Mn alloy”*; S.R. Meka, A. Chauhan, T. Steiner, E. Bischoff, P.K. Ghosh and E.J. Mittemeijer, 2015, Mat. Sci. Techn.
- *“Internal Nitriding of Fe-Cr-Mo Alloys; Precipitation of mixed nitrides and role of the Cr/Mo-ratio”*, T. Steiner, S.R. Meka, T. Waldenmaier and E.J. Mittemeijer, 2015, Proceedings of the ‘ASM Heat Treat 2015’ Conference, Detroit, USA.
- *“Internal Nitriding of Fe-Cr-Mo alloys; nitride precipitation”*; T. Steiner, S.R. Meka, E. Bischoff, T. Waldenmaier and E.J. Mittemeijer, 2014, Proceedings of the ‘European Conference on Heat Treatment and 21st IFHTSE Conference’, Munich, Germany

Awards

- Tom Bell Young Author Award 2014, 21st IFHTSE Conference, Munich, Germany
- Best Poster Award 2014, 21st IFHTSE Conference, Munich, Germany

Erklärung über die Eigenständigkeit der Dissertation

Ich versichere, dass ich die vorliegende Arbeit mit dem Titel

Internal precipitation of nitrides in Iron-based alloys

selbständig verfasst und keine anderen als die angegebenen Quellen und Hilfsmittel benutzt habe; aus fremden Quellen entnommene Passagen und Gedanken sind als solche kenntlich gemacht.

Declaration of Authorship

I hereby certify that the dissertation entitled

Internal precipitation of nitrides in Iron-based alloys

is entirely my own work except where otherwise indicated. Passages and ideas from other sources have been clearly indicated.

Name/Name: Tobias Steiner

Datum/Date: _____

Unterschrift/Signed: _____